Orbital ordering in the layered manganites

Thomas . W. Beale

Orbital Ordering in the Layered Manganites

Thomas A. W. Beale

A thesis submitted in partial fulfillment of the requirements for the degree of Doctor of Philosophy

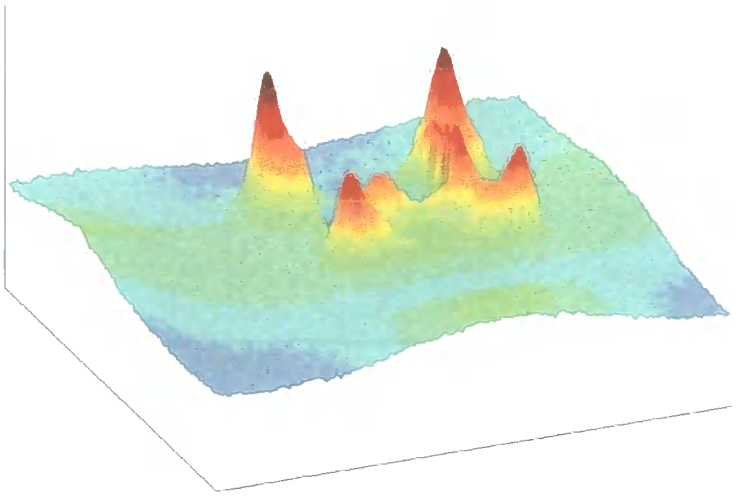

Department of Physics

University of Durham

2006

to my parents

I declare that no part of this material has previously been submitted for a degree to this or any other University

Publication List

1. *Orbital Bi-Stripes in Highly Doped Bilayer Manganites*

   T.A.W. Beale, P.D. Spencer, P.D. Hatton, S.B. Wilkins, M. v. Zimmerman, S.D. Brown, D. Prabhakaran, and A.T. Boothroyd

   Physical Review B **72**, 064432 (2005)

2. *Observation of Orbital Ordering in Weakly Jahn-Teller Distorted* $LaSr_2Mn_2O_7$

   S.B. Wilkins, N. Stojić, T.A.W. Beale, N. Binggeli, P. Bencock, P. Abbamonte, J. Mitchel, P.D. Hatton and M. Altarelli

   Journal of Physics: Condensed Matter Accepted

3. *Resonant Soft X-Ray Scattering Investigation of Orbital and Magnetic Ordering in* $La_{0.5}Sr_{1.5}MnO_4$

   S.B. Wilkins, N. Stojić, T.A.W. Beale, N. Binggeli, C.W.M. Castleton, P. Bencock, D. Prabahkaran, A.T. Boothroyd, P. D. Hatton and M. Altarelli.

   Physical Review B **71**, 245102 (2005)

4. *Direct Observation of Orbital Ordering in Layered Manganites*

   P.D. Hatton, S.B. Wilkins, T.A.W. Beale,T.K. Johal, D. Probhakaran and A.T. Boothroyd.

   Journal of Superconductivity In Press

5. *Probing Orbital Order with Soft X-rays: The Case of the Manganites*

   S.B. Wilkins, T.A.W. Beale, P.D. Hatton, J.A. Purton, P. Bencok, D. Prabhakaran and A.T. Boothroyd.

   New Journal of Physics **7**, 80 (2005)

6. *Resonant Soft X-ray Scattering - A New Probe of Charge, Spin, and Orbital Ordering in the Manganites.*

   P.D. Hatton, S.B.Wilkins, T.A.W. Beale, T.K. Johal, D. Prabhakaran and A.T. Boothroyd.

   Journal of Magnetism and Magnetic Materials **290-291** 891 (2005)

7. *Soft X-ray Diffraction - in Extremis*

   P.D. Hatton, S.B. Wilkins, T.A.W. Beale, J.A. Purton, D. Prabhakaran and A.T. Boothroyd.

   Journal of Synchrotron Radiation **12** 434 (2005)

8. *Resonant Soft Energy X-ray Diffraction of Charge, Spin, and Orbital Ordering*

   P.D. Hatton, S.B. Wilkins, T.A.W. Beale, T. Johal, P. Bencok, D. Prabahkaran and A.T. Boothroyd.

   Advances in Solid State Physics **44**, 467 (2004)

9. *Charge Ordering and Structural Distortions at Low Temperature in* $La_{2-2x}Sr_{1+2x}Mn_2O_7$ *(*$x = 0.475$ *and* 0.5*)*

   S.B. Wilkins, P.D. Spencer, T.A.W. Beale, P.D. Hatton, M. von Zimmerman, S.D. Brown, D. Prabhakaran and A.T. Boothroyd.

   Physical Review B **67**, 205110 (2003)

Abstract

Thesis Title: Orbital Ordering in the Layered Manganites

Author: Thomas A. W. Beale

The interaction between the long range correlations of electrons and the encompassing crystal structure is a key aspect of solid state physics. This thesis studies the long range interactions of the $3d$ orbitals in the single and bilayered manganites. Orbital ordering and the omnipresent Jahn-Teller distortions appear at low temperatures in these samples, accompanied by a real-space charge order.

The results display different aspects of these long range order phenomena in $La_{0.5}Sr_{1.5}MnO_4$, $Nd_{1-x}Sr_{1+x}MnO_4$ where $0.66 \geq x \geq 0.8$, and $La_{2-2x}Sr_{1+2x}Mn_2O_7$where $0.5 \geq x \geq 0.7$ using different techniques of x-ray diffraction. High energy x-ray diffraction is optimised to detect structural aspects in materials, and as such is sensitive to the Jahn-Teller distortions. Resonant scattering at the Mn K edge is used to study both the structural and the more specific charge and orbital ordering. Finally, soft x-ray resonant diffraction at the Mn L edge is used as a specialised technique for looking at the magnetic and orbital ordering.

A small crystal field distortion is always observed to be present in the orbitally ordered materials, however the size of the distortion is very large in the single layer $La_{0.5}Sr_{1.5}MnO_4$, and very small in the bilayer $LaSr_2Mn_2O_7$. Despite this, orbital ordering is observed in both materials. Combining experimental data with theoretical models, suggests that integer charge ordering occurs on the MnO_6 octahedra in both materials within the orbitally ordered regime.

Acknowledgements

The very nature of x-ray diffraction experiments requires a large number of people. Beamlines have to be constructed, and maintained, and then run by users 24 hrs a day. As such I am indepted to a large community in the production of this thesis.

Before thanking the staff at each beamline, I would like to start with the crystal growers. This is often an under-appreciated task. Without samples the majority of condensed matter investigation would cease, not only are these samples used for x-ray diffraction, but also many other techniques. It is not uncommon for the same sample to have been subject to a multitude of experiments. As such, I would like to thank D. Prababhakaran and Andrew Boothroyd at Oxford University, and John Mitchell at Argonne National Laboratory.

Closest to home, I would like to thank the staff of beamlines 5U.1 and 1.1 at the SRS Daresbury, in particular Mark Roper for constructing the soft x-ray chamber, John Purton and Tarnjit Johal for assistance on 5U.1, and Ian Kirkman on 1.1.

Crossing the channel, I would like to thank Martin von Zimmermann for his extensive help while using beamline BW5 at HASYLAB, and Thomas Brücker for the use of his cryomagnet. At the ESRF there is an army of personnel who have assisted in my experiments. On beamline ID08, I would like to that Stephan Sanescu, Peter Bencok and Nick Brookes. Appreciation also goes to the ID15 team, including Thomas Buslaps and Veijo Honkimaki. Finally at the ESRF I would like to thank the BM28 'XMAS' team, including in Grenoble, Simon Brown, Paul Thompson, David Paul, and at Warwick, Malcom Cooper and Sandra Beaufoy. In addition I would like to thank Anita Stadler at the ESRF Travel Office.

I am delighted to be able to thank Natasa Stojić, Nadia Binggeli, Christopher Castleton and Massimo Altarelli, at the Abdus Salam International Centre for Theoretical Physics, in Trieste. The results presented in Part II of this thesis are almost meaningless without some theoretical interpretation, and the interaction between experimentalists and theorists in this area of physics is getting more and more important. As an experimentalist, working with theorists, is enlightening. Firstly I quickly realised that I am most definitely an experimentalist, and to try and do the theory would be madness. Secondly you realise that there are

people who are interested in your results, and how much experimental detail you (possibly mistakenly) take for granted. Thirdly (hopefully) you manage to get some agreement in the results, and lastly, it is fantastic to travel and not be on an experiment!

The other side of the Atlantic, I would like to thank Peter Abbamonte and George Sawaski for their construction of beamline X1B at NSLS.

Back to Durham I would like to thank all the support staff that have helped, in particular the Clare and Joanne in the Finance office, who have tolerated frequent requests for air tickets and copies of receipts from months previously. Also John Dobson, who has maintained an ageing rotating anode diffractometer, with an unabating sense of humour. I would particularly like to thank Philip Spencer and Stuart Wilkins, who I have worked with both at Durham and on experiment. Philip has an unmatched memory, which is extremely advantageous when attempting to track down an elusive reference, or even remember which samples we studied 6 months previously. He is also an extremely dedicated experimentalist, and has undertaken more than his fair share of unsociable working hours on a beamline. Stuart spent the first six months of my PhD at Durham, whereupon he moved to ID20 at the ESRF. He has since proved to be an invaluable resource while conducting an experiment in Grenoble, always willing to come and help out, with everything from polishing crystals, to hardware problems or calculating azimuthal dependence simulations. He is perhaps most useful though for recovery, when something really unexpected happens and the rest of us are clueless as to 'how to get back'! In addition he has been collaborating with Peter and myself on the soft x-ray diffraction studies, accompanying us on beamtime at SRS and NSLS.

Finally I would like to thank my Supervisor, Prof. Peter Hatton. He has provided me with guidance and assistance throughout my scientific research, and for his efforts, has suffered near continuous abuse from his current and former students, especially when a certain football team looses again... His assistance has been invaluable, especially as I am still alive after attempting to keep up with his parallel skis on the slopes of Trois Valleés.

I would like to thank my parents, and Claire, who despite my regular absence on experiments, still married me.

Contents

Chapter 1

Introduction

1.1 Thesis Outline

This thesis describes results obtained through x-ray scattering from transition metal oxides. Transition metal oxides are one of the most important range of compounds. With the relatively recent discoveries of high temperature superconductivity [1] and colossal magnetoresistance [2], human exploitation of their properties can only increase. Despite the importance of the transition metal oxides there are many properties that are far from fully understood. This thesis aims to study a very small section of these oxides, namely the manganites, and in particular the long range correlation effects that occur.

This introduction summarises to the reader previous work conducted on the layered manganites. More detailed references to specific papers will be made in each chapter. There is also a brief outline of the theoretical understanding of resonant magnetic scattering, the results of which form the main bulk of this thesis. The remainder of this thesis is then divided into two parts. Part I looks at high energy and resonant K-edge x-ray diffraction. Both these techniques are mature and have been used to investigate a multitude of systems, from biological viruses and amorphous liquids to actinide elements. Within Part I, chapter 2 introduces the single layered manganite $(La,Nd)_{1-x}Sr_{1+x}MnO_4$, and shows x-ray scattering results from K edge diffraction and also high energy (100 keV) x-ray diffraction. Chapters 3 and 4 look at the bilayer manganite $La_{2-2x}Sr_{1+2x}Mn_2O_7$, chapter 3 looking at the orbital structure where $x > 0.5$ and chapter 4 looking at the effects of high magnetic fields on the ordering in the case of $x = 0.4$ and $x = 0.5$.

Part II concentrates on the recent technique of soft x-ray diffraction. Diffraction from single crystals at the transition metal L edge was first published in 2003. Since then there have been results from manganites, nickelates and cuprates. This second part describes some new results from the manganite series. Part II comprises of chapter 5, introducing soft x-ray

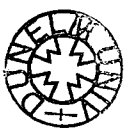

diffraction and outlining the major advantages as well as looking at the technical difficulties. Chapters 6 and 7 then look at orbital and magnetic ordering using soft x-ray diffraction, the former from the single layered $La_{0.5}Sr_{1.5}MnO_4$, and the latter from the bilayer $LaSr_2Mn_2O_7$.

1.2 Ordering in the Manganites

Wollan and Koehler[3] and Goodenough [4] first brought the manganites to the attention of condensed matter physicists in 1955. Wollan and Koehler conducted a neutron powder diffraction study of $La_{1-x}Ca_xMnO_3$, determining the range of magnetic ordering throughout the stoichiometric range. Goodenough followed up this paper with theoretical predictions for the origin of the magnetic ordering, and additionally, predicted an orbital and charge ordered state. Since the advent of synchrotron radiation the use of resonant diffraction has led to an wealth of papers discussing the state of long range ordering in the manganites, and other transition metal oxides.

The Ruddleston-Popper compounds follow the chemical formula $(La,Sr)_{n+1}Mn_nO_{3n+1}$. Figure 1.1 shows the crystal structure of these crystals for $n = \infty, 1, 2$. The $n = \infty$ ([La,Sr]MnO_3) crystals were the first to be studied, both theoretically and experimentally, in fact even now the majority of theoretical studies still concentrate on the $n = \infty$ group. This group however presents significant problems when it comes to studying single crystals. Although many studies have been conducted the samples suffer hugely from twinning, due to the $\sqrt{2}a \approx c$. This means that high quality single crystals are very hard to grow, and so are in limited availability, especially for a range of dopants. These cubic systems are also arguable the most complicated. As n is increased the systems reduce in dimensionality, becoming more two-dimensional. This is caused by the insertion of spacer layers of [La,Sr]O between the MnO layers.

1.2.1 The Single Layer Manganites

One of the earliest studies of single crystals of the single layer MnO_4 manganite was by Moritomo *et al.* [5]. Single crystals of $La_{1-x}Sr_{1+x}MnO_4$ were grown using the floating zone method, and characterised by x-ray diffraction. This determined an $I4/mmm$ tetragonal crystal structure (known as the K_2NiF_4 structure). The c lattice parameter was observed to change with doping level, ranging from 13.17 Å for $x = 0$ to 12.40 Å for $x = 0.6$. This agrees with a much earlier study by Rao *et al.* [6] on polycrystalline samples.

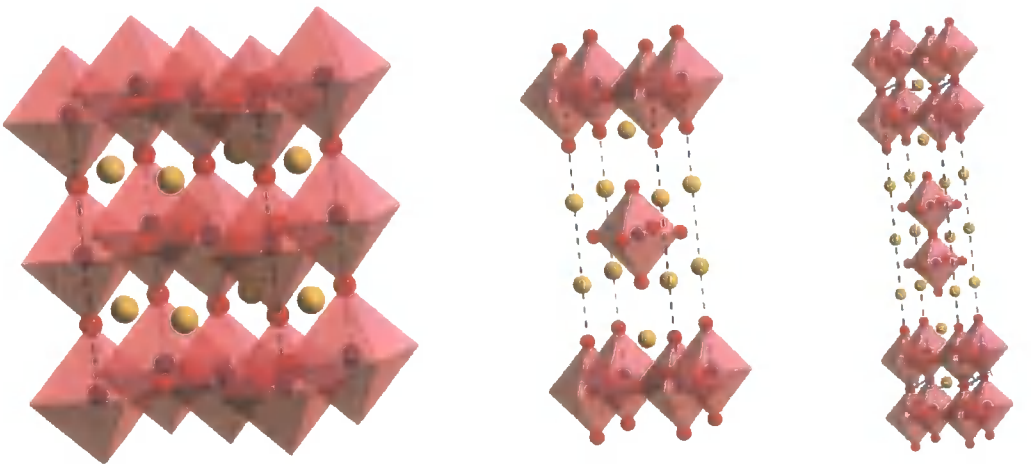

Figure 1.1: The crystal structure of $La_{1-x}Sr_xMnO_3$; $n = \infty$ (left), $La_{1-x}Sr_{1+x}MnO_4$; $n = 1$ (centre) and $La_{2-2x}Sr_{1+2x}Mn_2O_7$; $n = 2$ (right). The pink shading represents the MnO_6 octahedra, with a purple sphere representing Mn in the centre. The red spheres represent O, and the yellow represent La/Sr.

In addition to the structural determination by x-ray diffraction, Moritomo and co-workers reported the electrical resistivity, magnetic susceptibility, and examined the sample using electron diffraction. The electrical resistivity shows kinks in the curves for the samples with $x = 0.5$ and $x = 0.6$ but not for $x = 0.7$ or $x \leq 0.4$. They associated the anomaly in the resistivity curves as due to the formation of a periodic arrangement of holes in the MnO_2 sheets, in samples where $x \approx 0.5$. This is the first mention of a Charge Ordered (CO) state. This theory is supported by the electron diffraction patterns at 100 K which show the presence of superlattice spots (Fig. 1.2). It is speculated that these extra spots occur because of a lattice modulation induced by the charge ordering. The spots are not evident at 300 K. The magnetic susceptibility of $La_{1-x}Sr_{1+x}MnO_4$ showed a significant increase below approximately 100 K. This occurred for doping levels $0.2 \leq x \leq 0.5$. This Curie-Weiss like increase was proposed to indicate the onset of a spin-glass state below this temperature.

A year after this study, Sternlieb *et al.* [7] published an exemplary neutron scattering study on the superlattice peaks observed in $La_{0.5}Sr_{1.5}MnO_4$ by Moritomo. Through using neutrons, Sternlieb was able to observe both the charge order superlattice peaks, and peaks arising from the magnetic ordering in the system. Charge order superlattice peaks were observed with a wavevector of $(\frac{1}{2},\frac{1}{2},0)$ (Fig. 1.3) from the Bragg peaks and magnetic superlattice peaks at wavectors of $(\frac{1}{4},\frac{1}{4},\frac{1}{2})$ from Bragg peaks (Fig. 1.4). The temperature dependence of both of these wavevectors was reported. Sternlieb and co-workers were thus

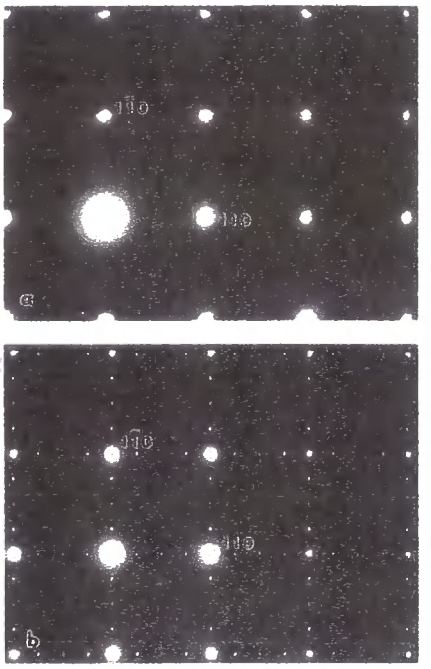

Figure 1.2: [001] zone-axis electron diffraction patterns observed at (a) 300 K and (b) 110 K for $La_{0.5}Sr_{1.5}MnO_4$ ($x = 0.5$). The presence of superlattice spots is evident at 110 K (lower figure).*Figure from Moritomo et al.* [5] describing $La_{0.5}Sr_{1.5}MnO_4$.

able to construct a model of the system, where the $\sqrt{2}a \times \sqrt{2}a \times 2c$ charge order unit cell orders at the charge order transition temperature (T_{co}) $\sim$ 217 K, and the $2\sqrt{2}a \times 2\sqrt{2}a \times 2c$ magnetic unit cell orders at the Néel temperature (T_N) $\sim$ 110 K.

Moritomo and co-workers published a second study, looking at the effects of replacing the La with Nd [8]. This suggested that a complete substitution of the La ion destroyed the charge ordering. This is in contrast to measurements on the nickelates, where a change in the atomic radius is seen to have little effect.

The first observation of the superlattice peaks by resonant x-ray scattering was undertaken by Murakami *et al.* [9]. Murakami recognised that on the Mn^{3+} ions the e_g electron had an orbital degree of freedom, available to occupy either in the $3x^2 - y^2$ or $3z^2 - r^2$ orbital. Murakami observed superlattice peaks at ($\frac{1}{4}$,$\frac{1}{4}$,0) type positions that displayed a resonance at the Mn K edge (Fig. 1.5). This was attributed to a direct observation of the orbital ordering in the sample. Murakami measured the temperature dependence of this orbital order peak, and the charge order peak at ($\frac{1}{2}$,$\frac{1}{2}$,0) positions, and found the orbital order transition temperature (T_{oo}) was equal to the charge order transition temperature. In addition, this was higher than T_N observed by Sternlieb [7]. In addition to the energy dependence of

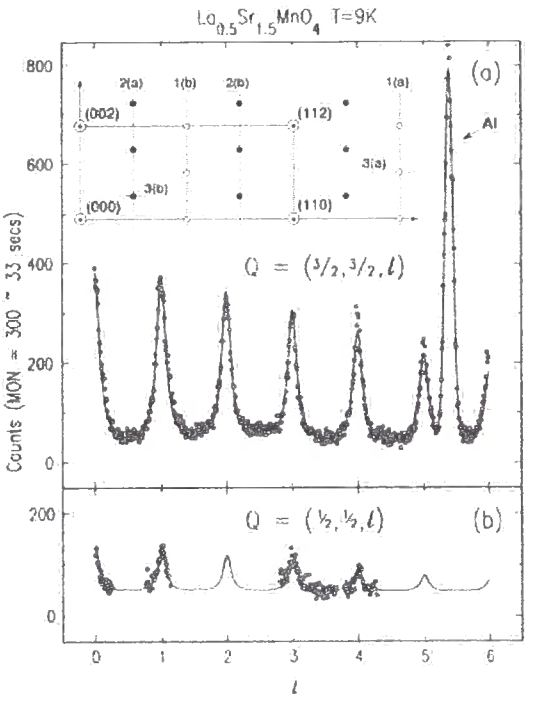

Figure 1.3: Structural scattering along (a) $\mathbf{q} = (\frac{3}{2}, \frac{3}{2}, l)$ and (b) $\mathbf{q} = (\frac{1}{2}, \frac{1}{2}, l)$. Inset the $\mathbf{q} = (hhl)$ scattering plane. Nuclear reflections are allowed at $h + k + l = 2n$. Light (dark) circles are structural (magnetic) peaks. *Figure from Sternlieb et al.* [7].

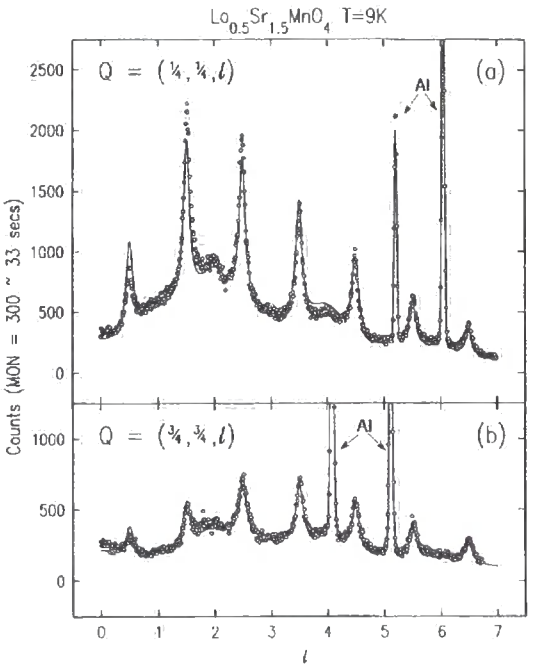

Figure 1.4: Magnetic data: (a) $\mathbf{q} = (\frac{1}{4}, \frac{1}{4}, l)$ and (b) $\mathbf{q} = (\frac{3}{4}, \frac{3}{4}, l)$. *Figure from Sternlieb et al.* [7].

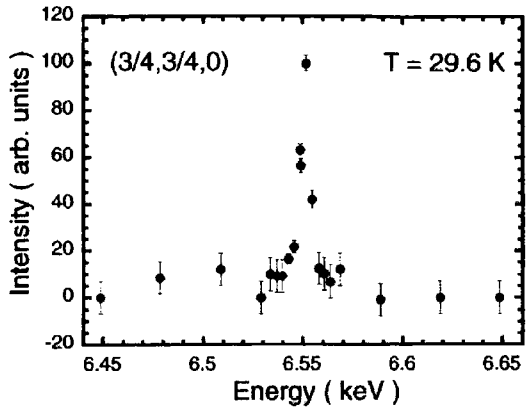

Figure 1.5: Energy dependence of the orbital-ordering superlattice reflection (3/4,3/4,0) near the manganese K-absorption edge at $T = 29.6$ K. *Figure from Murakami et al.* [9] *describing* $La_{0.5}Sr_{1.5}MnO_4$.

the orbital order peak, Murakami measured an azimuthal dependence of the orbital order peak. This displays a sinusoidal azimuthal dependence (Fig. 1.6), in agreement with the orbitals being spatially anisotropic. The energy dependence measured by Murakami does indeed suggest that the reflection originated from the anomalous scattering term from the Mn ions, and is not simply charge scattering. The scattering however was observed at the Mn K edge. This is sensitive to the $4p$ electron shells, and not directly to the $3d$ orbitals. As such, despite Murakami's claims, it seems unlikely that this is a *direct* observation of orbital ordering in the manganites. In fact, Murakami did postulate that the scattering was a result of an electric dipole transition, and stated "*The dipole transitions would correspond to the 1s core levels to the 4p band, which is hybridized with the polarized 3d band.*" Murakami did not attempt to suggest in which of the two orbitals the e_g electron resides, as either produces the same azimuthal dependence.

Murakami's observation of orbital ordering stimulated interest in the layered manganites. Ishikawa *et al.* [10] looked at the optical response of the sample through the charge / orbital order transition. By looking at the reflective optical spectra in the 1-3 eV range, anisotropy due to the orbital ordering could be observed. This was complicated by the existence of different orbital domains occurring with a 90° rotation to each other. The reflectivity spectra in the optical phonon range (0-0.1 eV) showed an additional phonon mode appearing at 0.07 eV below $T_{co/oo}$. This is not expected from the charge order pattern, and suggests the occurrence of an orbital order transition.

Tokunaga *et al.* [11] looked at the high-field magnetisation and magnetoresistance of

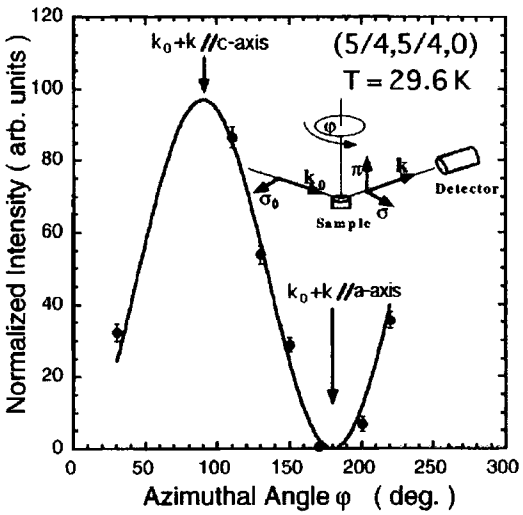

Figure 1.6: Azimuthal-angle dependence of the intensity of the OO superlattice reflection (5/4,5/4,0) normalised by the fundamental reflection (1,1,0) at $E = 6.552$ keV, $T = 29.6$ K. The solid curve is a calculated intensity. *Figure from Murakami et al.* [9] *describing* $La_{0.5}Sr_{1.5}MnO_4$. (*Polarisation analysis was not used, the calculation in the paper suggests that the polarisation should be rotated* ($\sigma \rightarrow \pi$))

$La_{0.5}Sr_{1.5}MnO_4$ with fields up to 40 Tesla. The *raison d'être* of their research was the significantly higher temperature of $T_{co/oo}$ than T_N. This suggested a more dominant role of the charge and orbital degrees of freedom than in the spin degree of freedom in producing the CO state. Also the significant interest caused by the discovery of colossal magnetoresistance (CMR) in the bilayer systems inspired interest in the single layered samples. They observed a melting of charge order with an applied magnetic field. This was temperature dependent, although fairly constant between 50 K and 150 K, where a 25 T field was required to quench the ordering. At low temperatures (< 100 K) there is a large region displaying hysteresis, which at very low temperatures (4 K), extends from 10 T to 35 T. The CMR effect was always observed to be strongest at the transition temperature.

The effect of replacing the trivalent La with Nd has been studied in more detail by Park *et al.* [12]. They observed a difference between the pure La and the mixed LaNd compounds below 50 K. With a 50% replacement of La with Nd, the ac susceptibility shows a distinct peak at ~ 30 K that is not present in $La_{0.5}Sr_{1.5}MnO_4$. Park and co-workers attributed this to the spin-glass transition of the Nd moments. This can be compared to the manganite $Nd_{0.7}Sr_{0.3}MnO_3$ which shows ferromagnetic ordering at low temperatures [13].

Extending to the full substitution of La for Nd, Hong *et al.* [14] conducted a thorough

study of $Nd_{0.5}Sr_{1.5}MnO_4$ using neutron diffraction and magnetisation measurements. The main conclusion from their work, was the observation of magnetic superlattice peaks, as observed by Sternlieb [7] in $La_{0.5}Sr_{1.5}MnO_4$, together with an abrupt change in the magnetisation at 21 K, more evidence of the ordering of the Nd moments below this temperature. A small structural distortion was also observed, which appeared to persevere above T_N, however they observed no signals relating to a charge ordered state. High resolution structural data were also collected, which found that $Nd_{0.5}Sr_{1.5}MnO_4$ was isostructural with $La_{0.5}Sr_{1.5}MnO_4$.

By this time the experimental results had fuelled the interest of theorists, who proposed theoretical models for the data. Mahadevan *et al.* [15] used first principles band structure calculations to analyse the experimental evidence of charge and orbital ordering. Their study indicates the presence of two distinct Mn species with very different environments in the crystal. One of these (the 3+ ion) has a Jahn-Teller distortion of the oxygens surrounding the Mn. They also suggest that the resonant observations of the orbital order peak by Murakami is actually driven by this Jahn-Teller distortion. This is in contrast to Ishihara and Maekawa [16]. Their argument is based on the Coulomb interactions between the Mn $3d$ and $4p$ electrons. This suggests that when one of the e_g orbitals in the $3d$ band is occupied, the electron-electron interaction in the orbital ordered state breaks the cubic symmetry and thus lifts the degeneracy of the Mn $4p$ orbitals. This results in the anisotropy of the scattering factor.

Although the majority of the papers report results from the half doped $La_{0.5}Sr_{1.5}MnO_4$, there are a few papers that investigated different doping levels. Larochelle *et al.* [17] proposed the existence of three distinct regions; a disordered phase ($x < 0.4$), a charge-ordered phase ($x \geq 0.5$), and a mixed phase ($0.4 \leq x < 0.5$). This was discovered through low temperature non-resonant x-ray scattering. This study confirmed the presence of superlattice peaks at both $(\frac{1}{2},\frac{1}{2},0)$ type positions and $(\frac{1}{4},\frac{1}{4},0)$ positions. They also conclude that the low-temperature structural symmetry is orthorhombic rather than tetragonal. By changing the doping level Larochelle and co-workers observed a change in the superlattice modulation wavevector. For $x > 0.5$ the vector changes linearly with the doping level. For the $x = 0.65$ sample second and third harmonics were observed, although these are extremely weak, indicating that essentially the modulations are sinusoidal. For the samples with $x < 0.4$, no superstructure was observed, and only very weak diffuse scattering could be detected.

Within the doping regime ($0.4 < x < 0.5$) the width and intensity of the peaks decreased dramatically from a highly ordered $x = 0.5$ state to a almost disordered $x = 0.4$ system.

Larochelle *et al.* [18] then published a second paper, expanding their study to incorporate the doping range from $0 \leq x < 0.7$. As well as non resonant x-ray scattering, this article also included neutron diffraction. Using this data and their previous data they were able to construct a phase diagram, shown in Figure 1.7. This phase diagram displays a single charge ordered phase in the range $0.45 \leq x < 0.7$. This charge ordered phase is accompanied at low temperature by a CE-type magnetic phase. Given that this magnetic phase occurs in the cubic, single layered, and bilayer phases, it appears to depend only weakly on the dimensionality of the system. High resolution x-ray powder diffraction studies of the $x = 0.5$ doped manganite suggests a splitting of the (220) Bragg peak below T_{co}, but the (200) peak remains unchanged. This, Larochelle argues, is indicative of the lattice becoming orthorhombic with a 45° rotation of the axis in the $a - b$ plane. This reduction in symmetry is effectively a structural distortion, and has been observed previously through electron diffraction [5]. Superlattice peaks were observable throughout the entire $0.4 \leq x < 0.7$ range (the highest doping of the samples grown). This range showed a marked change in the superlattice wavevector, suggesting that the ordering is strongly doping dependant. The relationship between the electron density, n_e, and superlattice modulation wavevector, ϵ, was linear, such that at $x = 0.5$ the superlattice modulation doubles the high temperature structure, and at $x = 0.67$ it is three times larger. This is similar to that observed in the cubic manganites [19].

Below the charge order regime, Larochelle describes an intermediate region where $0.15 < x < 0.45$ and a third phase where $0 \leq x < 0.15$. In the intermediate phase there is very little long range order. Diffuse scattering can be seen around the principal Bragg peaks suggesting small or poorly correlated distortions. The magnetic order in this range is also weak. Through neutron scattering, very weak two-dimensional scattering rods were observed at low temperature, suggesting a spin-glass phase. The third region below $x = 0.15$ is by contrast a magnetically well ordered phase. The sample orders antiferromagnetically with a T_N between 120 K and 130 K. There are no observations of any structural distortions and charge disproportionation is unlikely at this doping level.

Kimura *et al.* [22] studied the overdoped $Nd_{1-x}Sr_{1+x}MnO_4$ with $0.67 < x < 1.0$. Electrical resistivity measurements showed a change in gradient at $\sim$ 250 K, obvious in the

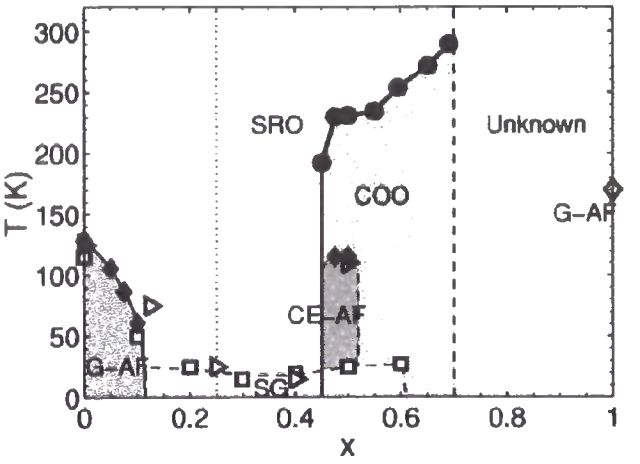

Figure 1.7: Magnetic and structural phase diagram of $La_{1-x}Sr_{1+x}MnO_4$. The data come from x-ray structural scattering (• [18]), neutron scattering (♦ [18] and ◊ [20]), magnetometry (□ [5]) and muon spin rotation (▷ [21]) measurements. The abbreviations are $G-$AF, G-type antiferromagnet (*composed of spins aligned antiferromagnetically with respect to their neighbours*); CE-AF, CE-type antiferromagnet (*ferromagentic zig-zag chains coupled antiferromagnetically*); SG, spin glass; COO, charge/orbital order phase; SRO, short-range charge and orbital order. The dotted vertical line at $x = 0.25$ indicates the extent to which the SRO is visible. *Figure from Larochelle et al.* [18].

$x = 0.67$ and $x = 0.75$, but less distinct in the samples with $x \geq 0.78$. More interestingly in the samples with $x = 0.78$ and $x = 0.8$, there is a drop in the resistivity near 150 K, which also shows a considerable thermal hysteresis. In order to resolve the origins of these anomalies, electron and x-ray diffraction was performed (Fig. 1.8). The electron diffraction patterns of the $x = 0.67$ and $x = 0.75$ samples show distinct superlattice peaks at $(\frac{1}{6}, \frac{1}{6}, 0)$ and $(\frac{1}{8}, \frac{1}{8}, 0)$ respectively. These can be supposed to originate from the same phenomena as the $(\frac{1}{4},\frac{1}{4},0)$ and $(\frac{1}{2},\frac{1}{2},0)$ peaks observed in $La_{0.5}Sr_{1.5}MnO_4$. Meanwhile, the x-ray diffraction shows a splitting of the major Bragg peaks in the ($x > 0.67$) samples at low temperature (< 40 K). This appears to be a structural phase transition from a high temperature tetragonal phase to a low temperature orthorhombic phase. This study was extended by Nagai *et al.* [23] who looked in detail at the electron diffraction patterns of $Nd_{1-x}Sr_{1+x}MnO_4$ with $0.67 < x < 1.0$. They observed a sinusoidal transverse modulation over a long period (≈ 8 unit cells). This they used to support their model of a Wigner-crystal like model for the orbital arrangement in the high doped manganite. This model incorporated a long range sinusoidal structural distortion, observed via the electron diffraction pattern.

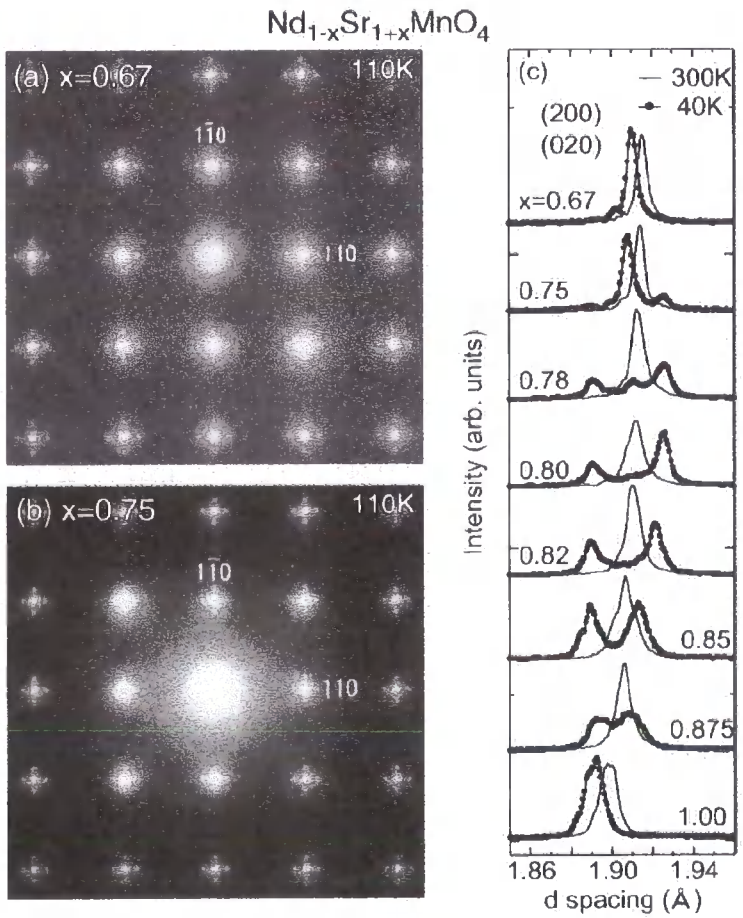

Figure 1.8: [001] zone-axis electron diffraction patterns of (a) $x = 0.67$ and (b) $x = 0.75$ crystals at 110 K. The superlattice reflections with modulation wave vector $(\delta, \pm\delta, 0)$ ($\delta \approx \frac{1}{6}$ and $\frac{1}{8}$ for $x = 0.67$ and $x = 0.75$ crystals, respectively) are evident. (c) X-ray powder diffraction patterns around the (200) and (020) Bragg peaks in $Nd_{1-x}Sr_{1+x}MnO_4$ ($0.67 \leq x \leq 1.0$) at 300 K and 40 K. *Figure from Kimura et al.* [22].

1.2.2 The Bilayer Manganites

There have been a large number of papers published on the bilayer series in the last decade. In order to try and present these to the reader in a logical fashion, they will be divided into sections. First the papers that describe the mid doped $x = 0.5$ bilayer sample will be presented, alongside those papers that attempt to explain the whole doping series. Secondly the papers describing the underdoped, and more specifically the $x = 0.4$ bilayer will be introduced, which will be expanded in Chapter 4. Lastly, there will be a brief summary on the few papers describing the overdoped bilayers. A detailed explanation of these papers will be given in Chapter 3.

The interest in the bilayer manganites was initiated by the groundbreaking paper of Moritomo *et al.* [2] in 1997 describing the discovery of colossal magnetoresistance in the manganite $La_{1.2}Sr_{1.8}Mn_2O_7$ ($x = 0.4$). A reduction in the resistivity of up to 20,000% (with 7 T applied field) was reported, and a decrease of ~3,000% with a 1 T applied field (Fig. 1.9), compared to just 110% seen in the cubic manganites. This huge magnetoresistant effect was observed just above T_C, in the paramagnetic phase. Two possible origins of this effect were postulated in the paper, both highlighting the influence of the reduced dimensionality. The first suggestion was that due to the high anisotropy of the exchange interaction (the inter-layer interaction being much weaker than intra-layer interaction), the spin correlations are maintained within the layer above T_C within the paramagnetic phase. Applying a magnetic field then increases the magnetisation and reduces the spin scattering of the charge carriers. The second postulate is that the reduced dimensionality and lifting of the degeneracy of the e_g electron state reduces the transfer interaction of these electrons. Just above T_C the compound is subject to instabilities, such as antiferromagnetic super-exchange, Jahn-Teller distortions, and charge ordering. The phenomena can then be interpreted as an induced metal-insulator transition, caused by the applied magnetic field.

Following the publication by Moritomo describing the discovery of colossal magnetoresistance in $La_{1.2}Sr_{1.8}Mn_2O_7$ [2], many other groups conducted research on this system. One of the first groups to publish studied the crystal using neutron and synchrotron x-ray diffraction was that of Battle *et al.* [24]. This study was based on the half doped ($x = 0.5$) bilayer manganite. Their results suggested a bi-phasic sample, the majority of which was antiferromagnetic, with a minority ferromagnetic phase. The majority phase adopted the magnetic structure below $\sim$ 210 K, with the minor ferromagnetic phase occurring below

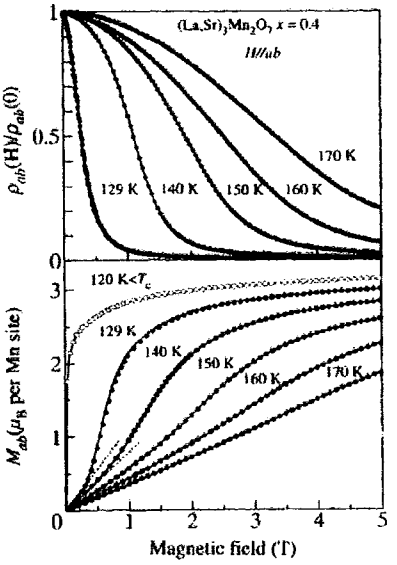

Figure 1.9: Top panel, change of the in-plane component of resistivity with increasing magnetic field for a single crystal of $(La_{0.4}Sr_{0.6})_3Mn_2O_7$. Bottom panel, field induced magnetization. Open and filled circles are the data in the ferromagnetic and paramagnetic phases. Dotted lines represent the initial slopes of the $M - H$ curves. *Figure from Moritomo et al.* [2].

~125 K. Battle *et al.* question their results with regard to the simultaneous existence of two phases, but view their successful synthesis of monophasic $Sr_2LnMn_2O_7$ where Ln = Tb, Dy, Ho, Er and Y as an endorsement of their preparative technique. Despite this, they later raised the suggestion that their samples in fact have a mixed elemental composition. Later phase diagrams confirmed this suggestion that perhaps their composition was a mix of a lower doped concentration ferromagnetic sample and the mid doped antiferromagnetic sample. In addition to the magnetic characterisation, Battle *et al.* also accurately measured the structural parameters of the system.

In addition to the early x-ray and neutron diffraction work, Li and co-workers [25] observe a charge ordered state in the bilayer sample through transmission election microscopy. Further electron diffraction revealed superlattice spots in the *ab* plane corresponding to a fourfold (strong) and twofold (weak) periodicity which were found at low temperature. A model of such possible charge and orbital ordering was produced based on Goodenough's [4] earlier work. In addition to Li *et al.*, Kimura and co-workers [26] used electron and x-ray diffraction to study the superlattice modulations. This paper reported only superlattice peaks corresponding to a fourfold periodicity, however they did study their temperature de-

pendence. They found that the modulations were only observable in a narrow temperature range between $\sim$ 210 K and $\sim$ 100 K. This was also reflected in resistivity measurements that displayed distinct gradient changes at these temperatures. It was speculated that this melting of the charge order state may be due to a changed magnetic order, as the lower doped ($x = 0.4$) samples were ferromagnetic below 120 K.

With the rise of interest by experimentalists in the bilayer system, a number of theorists began to undertake calculations in order to explain the experimental evidence. Among these Maezono and Nagaosa [27] examined the change of magnetic phase from ferromagnetic in the $x = 0.4$ doping level to antiferromagnetic in the half doped sample. Their paper considered two possibilities, firstly a phase diagram without canting, where there is a discontinuity between the two phases, and secondly where there is a spin canting that provides a gradual transition between the two states. Their final explanation was a combination of the two. Maezono and Nagaosa theorise an orbital transition at around $x = 0.125$ with a spin canting over the transition between the two magnetic states.

Following the discovery of charge and possibly orbital ordering in the bilayers, Chatterji *et al.* [28] investigated these phenomena using high energy x-ray diffraction, resonant x-ray diffraction and neutron diffraction. Their results were limited to the half doped $LaSr_2Mn_2O_7$. Satellite peaks were detected at $(h \pm \frac{1}{4}, k \pm \frac{1}{4}, l)$ using both high energy and resonant x-ray diffraction. No mention in the paper was made of satellite peaks at $(h \pm \frac{1}{2}, k \pm \frac{1}{2}, l)$ like positions. Compared to the single layered manganites a strange temperature dependence was recorded for the aforementioned peaks. This strange temperature dependance had previously been indicated by Kimura *et al.* [26]. They were first detected at 220 K, and increased in intensity as the temperature was reduced, reaching a maximum of intensity at 180 K. The intensity then *decreased* again, becoming very weak at $\sim$100 K. Then at very low temperatures below 40 K, there appeared to be a re-entrant phase, where the intensity increased again, albeit to a much lesser degree than found at higher temperatures. This was observed on all of the satellite peaks. In addition Chatterji and co-workers studied the magnetic structure using neutron diffraction. They observed the (001) antiferromagnetic peak; a normally structurally forbidden reflection due to the symmetry of the $I4/mmm$ space group. The appearance of the (001) magnetic peak occurs at $T_N \approx 170\ K$, which is noted to be the same temperature that the intensity of the satellite peaks in the *ab* plane reduce in intensity. By refining the magnetic structure from a large number of nuclear and

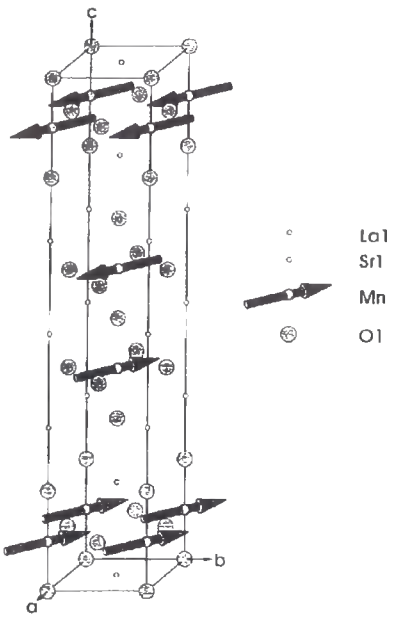

Figure 1.10: Schematic representation of the antiferromagnetic structure of $LaSr_2Mn_2O_7$. *Figure from Chatterji et al.* [28].

magnetic peaks, Chatterji *et al.* were able to come up with a magnetic structure comprising of ferromagnetic planes aligned antiferromagnetically (A-Type AFM) (Fig. 1.10). Following on shortly from Chatterji *et al.*, Andreica and co-workers [29] published the first muon spectroscopy (μSR) results from $LaSr_2Mn_2O_7$. These results found a strange behaviour between the charge order transition temperature and T_N. This was difficult to interpret, but was thought to be a consequence of residual magnetic correlations above T_N.

Argyriou *et al.* [30] combined Raman spectroscopy with transport measurements, neutron diffraction and high resolution x-ray diffraction to try and explain the behaviour in $LaSr_2Mn_2O_7$. Through the use of Raman scattering they were able to detect charge fluctuations well above the charge ordering temperature, up to $\sim$ 340 K. These fluctuations, termed polarons, were considered to be a precursor to the stable ordering.

With the arrival of experimental data the first phase diagrams across the doping range began to appear. These were produced by Ling *et al.* [31] (which was then modified slightly and republished [32] (Fig. 1.11)), and Dho *et al.* [33] (Fig. 1.12). The work of Ling *et al* [31] was mostly through neutron powder diffraction, and so concentrated on the magnetic structure. This revealed four distinct magnetic phases, one ferromagnetic and three different antiferromagnetic, and canted 'mixed' phases between. In addition there appears according

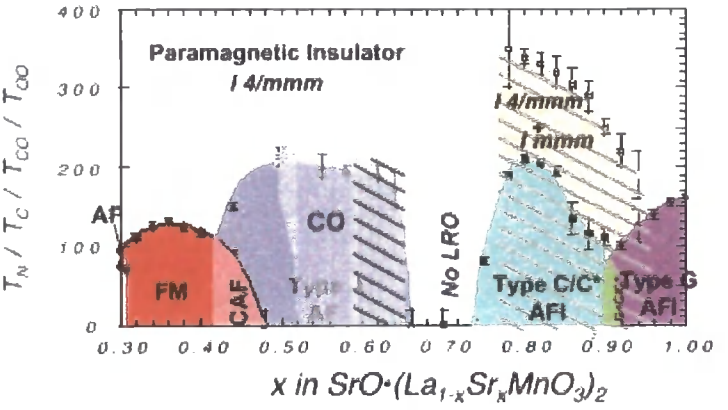

Figure 1.11: Structural and magnetic phase diagram of the bilayer manganite $La_{2-2x}Sr_{1+2x}Mn_2O_7$ in the range $0.3 \leq x \leq 1.0$ determined by neutron powder diffraction. Solid markers represent the magnetic transition temperature (T_C or T_N); open squares delineate the tetragonal to orthorhombic transition. Several magnetic phases are identified: ferromagnetic metal (FM), canted antiferromagnetic (CAF), and A-, C- and G-type antiferromagnetic insulators (AFI). The region marked 'No LRO' has no magnetic diffraction peaks at T≥5 K. Samples in the reqion marked 'CO' exhibit long-range charge ordering reflections in X-ray and/or election diffraction. *Figure from Qui et al.* [32].

to Ling *et al.* [31] a long range order hole, between the doping levels of $x = 0.66$ and $x = 0.74$ where no long range order exists. The phase diagram of Dho *et al.* [33] is somewhat different. Their paper was based on transport and magnetisation measurements, and concentrated on the area of charge ordering in the phase diagram. Figure 1.12 shows a large area of charge ordering extending as far as $x = 0.75$ and possibly further. There appears no gap in the long range order as shown by Ling *et al.*. There does appear to be a collapse in the charge ordering around $x = 0.5$ in the temperature region $\sim 50 - 150$ K. This is in agreement with previous results reported by Chatterji *et al.* [28].

A second muon spectroscopy study was conducted on $La_{2-2x}Sr_{1+2x}Mn_2O_7$ with $0.4 \leq x < 1$ by Coldea *et al.* [34]. Muon spectroscopy is a local probe of the magnetism in the sample, and is therefore effective in detecting short range magnetic correlations that may be undetected by other techniques. Coldea *et al.* [34] detected a slowing in the magnetic fluctuations, corresponding to a spin-freezing below ~ 60 K. This was found over a large doping range from $x = 0.5$ to $x = 0.75$, including within the previously suggested area of no long range order. The effective range probed by muons is in the order of 20 Å, perhaps suggesting that the correlations in the range $0.5 < x < 0.75$ are so short as to be undetected by neutron scattering. It is interesting to note that this area of spin freezing corresponds to

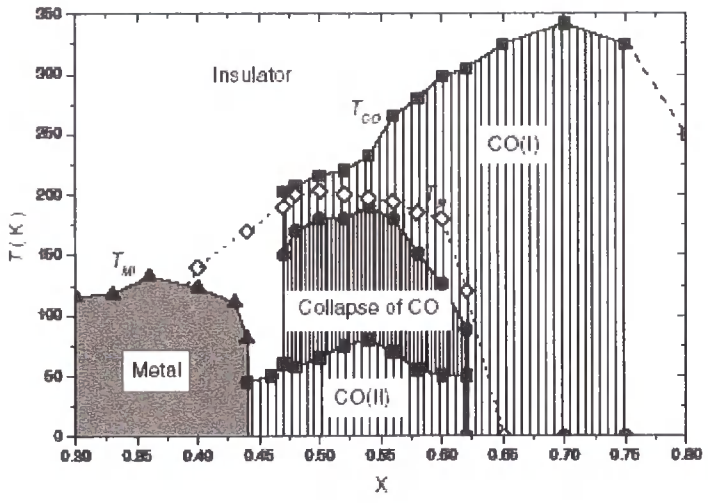

Figure 1.12: The phase diagram of $La_{2-2x}Sr_{1+2x}Mn_2O_7$ as a function of T and x. Filled symbols are obtained from the transport data shown in figure 2 (*in ref* [33]) and open ones are taken from the reported values. Filled squares and triangles represent T_{CO} and T_{MI}, respectively. The 'Collapse of CO' (densely hatched region) are corresponds to the thermal hysteresis region observed in the $\rho-T$ and $M-T$ curves. The sparsely hatched are represents the charge-ordered insulating state which is divided into two regions, CO(I) and CO(II). The type-A AFM transition temperature (open diamonds) taken from reference [31] is also shown schematically. *Figure from Dho et al* [33].

the re-entrant charge order temperature according to Dho *et al.* [33].

Further x-ray scattering was undertaken by Wilkins *et al.* [35]. High energy and resonant x-ray diffraction was conducted on $La_{2-2x}Sr_{1+2x}Mn_2O_7$ with $x = 0.475$ and $x = 0.5$. In addition to superlattice peaks appearing at $(h \pm \frac{1}{4}, k \pm \frac{1}{4}, l)$, they were also detected at $(h \pm \frac{1}{2}, k \pm \frac{1}{2}, l)$ type positions. This was direct evidence that both a structural 'Jahn-Teller' like distortion and a charge ordered phase were coexistent. In addition both peaks were detected at low temperatures in the region of charge order melting, albeit very weakly. A large increase in the inverse correlation length of the ordering, indicated by a broadening of the superlattice reflection accompanied the decrease of intensity. This suggests that the ordering is not entirely disrupted by the antiferromagnetic order, but persists even at low temperature, however the correlation length of this ordering was very much reduced. A small increase was detected in the intensity of these reflections at the proposed reentrant temperature. Resonant scattering at the Mn K edge showed distinctly different behaviours of the two peaks. The structural distortion appeared very similar to a weak Bragg peak, whereas the charge order peak resonated at the absorption edge. All the superlattice peaks were found to be highly correlated in the ab plane, and very weakly correlated out of the

plane. This confirms the two dimensional nature of the material, as anticipated from the crystal structure. A second paper by Wilkins *et al.* [36] used resonant soft x-ray diffraction at the Mn L edge to detect the (001) antiferromagnetic peak. This in itself added relatively little understanding to the bilayer system, however the huge resonances observed at the absorption edge promised further more interesting work in this energy regime. This technique will be elaborated on further in Part II.

The realisation that both Jahn-Teller distortions and the more interesting orbital ordering would produce superlattice reflections at the same wavevector stimulated heated discussions as to which phenomena had been experimentally detected. Di Matteo *et al.* [37] performed resonant x-ray scattering at the Mn K edge, and in addition calculated the expected resonance. Their conclusion was that the scattering is almost entirely originating from the structural distortion, with the orbital ordering signal an order of magnitude weaker. They did not exclude the possibility that orbital ordering may be observable at other absorption edges, such as the Mn L edge.

The Underdoped Bilayer ($x < 0.5$)

The discovery of colossal magnetoresistance in $La_{1.2}Sr_{1.8}Mn_2O_7$ stimulated significant interest in this underdoped region. In addition to this discovery, the paper by Moritomo *et al.* [2] established the magnetic state of the material to be paramagnetic at room temperature and ferromagnetic below $T_C = 126$ K.

One of the most prolific groups studying this sample was at Argonne National Laboratory led by J. Mitchell [38, 39, 40, 41, 42, 43, 44, 45, 46]. This extended research commenced in 1997 with a neutron diffraction study of the compound [38]. The main argument in this paper is the substantial lattice parameter change at T_C. The structural change occurs almost entirely within the *ab* crystal plane, where the lattice parameter deviates from a constant contraction upon cooling, to a slow down in the contraction as T_C is approached, followed by a sudden fall in the lattice parameter (by 0.004 Å) as the temperature cools through T_C. It was suggested that such a change in the structure was linked to the ferromagnetic ordering and charge delocalisation. Evidently this effect occurs within the *ab* plane, as there was relatively little change in the *c* lattice parameter.

A second paper [39] following this research line looked at the perovskite under pressures up to 6 kbar, using neutron powder diffraction. They observed that the sign of the compression of the apical Mn-O bonds (those out of the *ab* plane) reversed after cooling through T_C.

That is to say, at 300 K (above T_N) applied pressure on the sample resulted in the Mn ions in neighbouring sheets moving closer together. At 100 K (below T_N), the same applied pressure resulted in the Mn-O bonds between neighbouring sheets increasing, moving the Mn ions apart, with the compression reducing the distance between the pairs of MnO planes. This unusual behaviour is explained by magnetic striction. The absence of magnetic superlattice peaks suggests that the sample is indeed a ferromagnet, however a canted-spin ferromagnetic phase was proposed. A further communication [40] examined the crystal structure with an applied magnetic field, again using neutron powder diffraction. They detected a significant magnetostriction at T_C, with the a axis contracting and c axis expanding. In addition the magnetisation data suggested the presence of short range magnetic order in the region above T_C up to room temperature. Virtually simultaneously, Perring *et al.* [47] published date from single crystal neutron diffraction looking at the magnetic behaviour of $La_{1.2}Sr_{1.8}Mn_2O_7$. This paper shows the coexistence of ferromagnetic critical scattering as well as *antiferromagnetic* short range order above T_C (Fig. 1.13). This discovery was proclaimed to be vitally important to the understanding of colossal magnetoresistance in the material. As far as calculations are concerned, the existence of antiferromagnetic clusters coexisting with short range spin correlations removes the validity of the mean field approach. It also implies that the charge carriers in the paramagnetic phase are progressing through a medium of mixed ferro- and antiferromagnetic bonds. Traditionally such electron hopping would be easy across ferromagnetic bonds, but suppressed over antiferromagnetic bonds, and as such the antiferromagnetic clusters could be visualised as mobile 'walls' through the material. Obviously this has significant effects for the understanding of colossal magnetoresistance.

With the discovery of charge and orbital ordering in $LaSr_2Mn_2O_7$ it was obvious to search for such correlations in the paramagnetic phase of $La_{1.2}Sr_{1.8}Mn_2O_7$. Yamamoto *et al.* [48] used Raman spectroscopy to search for signature phonon peaks. Their study comprised looking at both $x = 0.5$ and $x = 0.4$ doping levels, by comparing the two spectrum, they are able to suggest that short range charge and orbital ordering occur in the paramagnetic phase above T_C in the $x = 0.4$ sample as well as in the $x = 0.5$ sample. The correlations in the $x = 0.4$ sample are then strongly suppressed in the ferromagnetic phase.

Vasiliu-Doloc *et al.* [46] first introduced the idea of polaron formation in $La_{1.2}Sr_{1.8}Mn_2O_7$. In this paper, polarons are described as a localised charge with an associated lattice distortion field, which give rise to diffuse scattering around the Bragg peaks. Scattering ascribed

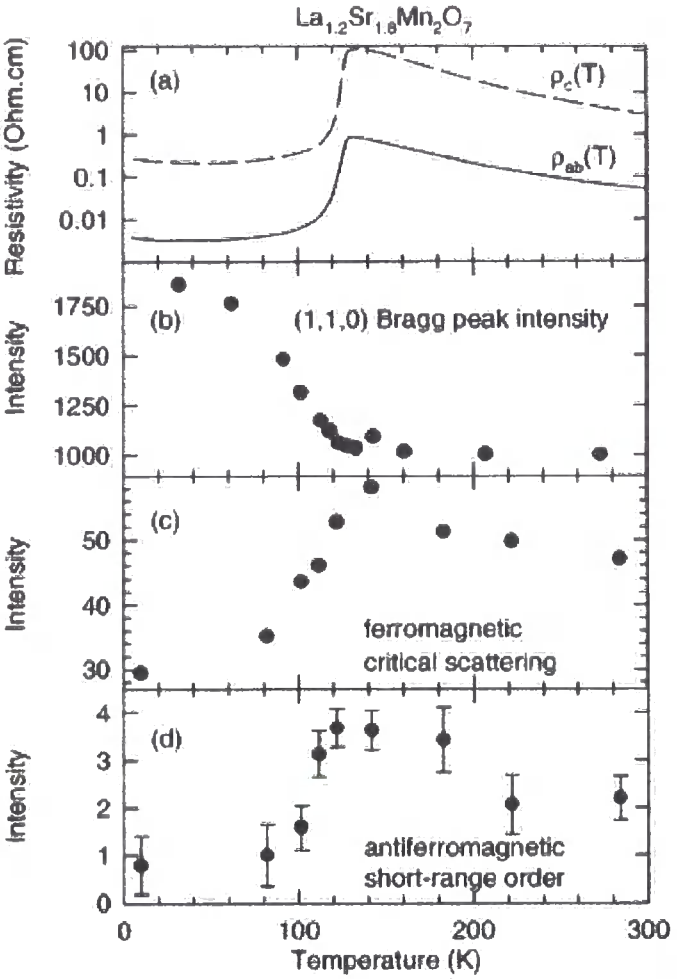

Figure 1.13: Temperature dependence of (a) resistivity in basal plane ρ_{ab} (solid line), and along the c axis ρ_c (dashed line), (b) integrated intensity of the (1,1,0) Bragg peak, (c) ferromagnetic critical scattering and (d) antiferromagnetic cluster scattering. Scattering intensities shown in (b)-(d) are integrals (measured by monitor) over the relevant solid angles and energy transfers, and as such can be compared to one another. *Figure from Perring et al.* [47].

to the presence of polarons was observed using x-ray and neutron scattering, at two different wavevectors, the first around the Bragg peak, and the second at 0.3 reciprocal lattice units from the Bragg peak in the *ab* plane. Details of these polarons will be elaborated on in Chapter 4. The polarons were observed above T_C in the paramagnetic phase, reducing in intensity as the temperature increased, but still present at 300 K. In addition to the $x = 0.4$ doped bilayer, various other underdoped regions have been studied, in particular the $x = 0.3$ has stimulated considerable interest. This was prompted by Kimura *et al.* [49] finding evidence of CMR in this doping level. Analogous to the $x = 0.4$ doping level, $La_{1.4}Sr_{1.6}Mn_2O_7$ shows a magnetoresistance of up to $10,000\%$ above $T_C \approx 90$ K with a field of 5 T. Perring *et al.* [50] studied the magnetisation state of the $x = 0.3$ compound. This was proposed to consist of ferromagnetic sheets stacked antiferromagnetically. The ferromagnetic sheets have the spins aligned along the *c* axis rather than in the *ab* plane. This is remarkably different to the observation of the spins aligned fully ferromagnetically within the *ab* planes in the $x = 0.4$ bilayer. However with an applied field of 1.5 T, the antiferromagnetic stacking in the $x = 0.3$ sample was observed to switch to a fully ferromagnetic state. This occurred with the field perpendicular to the spin direction, and the resulting ferromagnetic order is magnetically isostructural to that in $La_{1.2}Sr_{1.8}Mn_2O_7$.

Kubota *et al.* [51] coalesced this magnetic information, and with the use of neutron powder diffraction and Reitveld refinement, produced a magnetic phase diagram for the doping levels $0.3 \leq x \leq 0.5$ (Fig. 1.14). Even within this small doping range there exists five different magnetic structures, reflecting the complexity of this compound. In addition, further evidence of a canted spin structure in the $x = 0.45$ doping level is provided by a second paper by Kubota *et al.* [52] through neutron scattering.

The Overdoped Bilayer ($x > 0.5$)

The bilayer series with $x > 0.5$ has not been studied nearly so much as the half doped and underdoped samples. Chapter 3 presents results from $x = 0.55, 0.6$ and $x = 0.7$ and the details of previous publications will be expanded at that point. Initial results from polycrystalline samples were obtained by Dho [33] and Ling [31], as outlined above and in Figure 1.12. An early publication concentrating on the overdoped samples by Mitchell *et al.* [53] used x-ray and neutron diffraction to examine the structural and magnetic order. A gap in the long range ordering was confirmed between $0.66 < x < 0.72$. In addition charge ordering was observed up to $x = 0.6$.

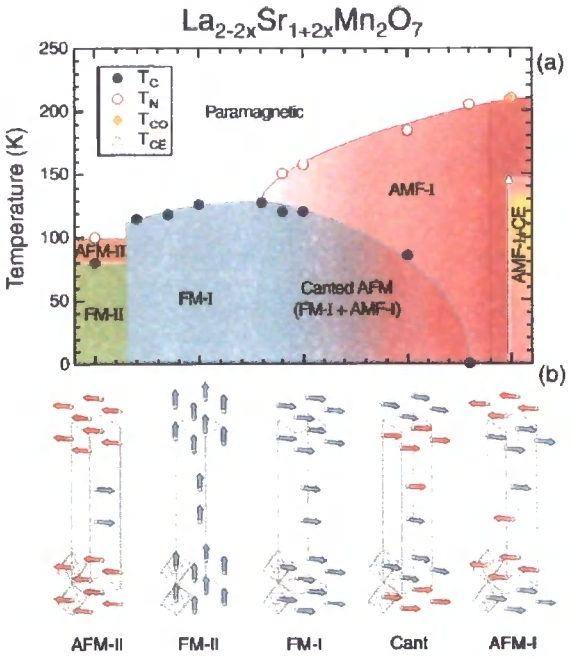

Figure 1.14: (a) Magnetic phase diagram of $La_{2-2x}Sr_{1+2x}Mn_2O_7$ ($0.3 \leq x \leq 0.5$). (b) Several different magnetic structures appearing in the phase diagram are schematically drawn. *Figure from Kubota et al.* [51].

A theoretical paper suggesting an explanation for the ordering in the overdoped samples was recently published by Maitra and Taraphder [54]. This suggests that the magnetic ordering is itself driven by orbital ordering, while the orbital arrangement is determined by the underlying structure. Further single crystal neutron diffraction and resistivity data was provided by Cambell *et al.* [55]. Here a region of enhanced charge order stability was found in the vicinity of $x = 0.62$. The evidence for this is an increased $T_{CO} = 230$ K, and an incomplete conversion to a purely magnetic ordered state at low temperature. The charge order structure was then expanded on by Luo *et al.* [56] and Beale *et al.* [57], who through electron microscopy and x-ray diffraction respectively, observed a bi-stripe phase.

1.3 Charge ordering

One of Goodenough's initial requirements of his long range ordering, is a spontaneous charge disproportion of the transition metal ions below a certain transition temperature T_{CO}. In the simplest format this can be imagined as an alternating pattern of Mn^{3+} and Mn^{4+} (Fig. 1.15). Of course the idea of a single electron as a point charge in the crystal lattice

is rather simplistic. One can in fact imagine that the charge probability wave over the whole MnO octahedra varies within the *ab* plane depending on the doping of the crystal. This charge disproportionation may not even be integer charge disproportion. It has been suggested that it is $Mn^{+3-\delta}$ and $Mn^{+4-\delta}$ where $\delta \ll 0.5$. One can argue that as the samples go through a metal / insulator transition as they enter the charge ordered phase, that there must be some electron band gap. However this does not have to be located entirely on the Mn ions, it could very easily be spread over the MnO_6 octahedra. Because of this, experiments such as XANES (X-ray Absorption Near Edge Structure) which could possibly detect the Mn valency may well not be conclusive. Despite all of this, it is easy to talk about Mn^{3+} and Mn^{4+} as a model, however it is should be remembered that this is merely a convenient representation and method for describing the charge ordering phenomena.

As the charge ordering distinguishes the two Mn sites, the normal chemical unit cell is not valid in this regime. As such, we can describe the extended superstructure encompassing the charge order as the charge order unit cell (Fig. 1.15), where $a_{CO} = b_{CO} = 2a = 2b$. Bearing these points in mind we can describe the charge ordering in the manganites. The parent compound, $LaSrMnO_4$ displays no charge ordering, as all of the Mn have an average +2 charge associated with them. Similarly if we were to completely replace the La by a group 2 metal, such as Sr all the Mn ions would be entirely Mn^{4+}. Continuing this rationale, doping half of the La with Sr, such that $x = 0.5$ produces an average valency of +3.5. It has been shown, both experimentally, and also justified theoretically, that below T_{CO} this produces a charge disproportionation, and the crystal falls into an energetically favourable state of charge ordering. This minimises the Coloumb repulsion between the electrons in the lattice. The charge ordering takes the form of a real space ordering of the e_g electron in the MnO octahedra.

As the doping of the Sr ions is altered away from $x = 0.5$ there are two possibilities in order to produce charge neutrality. Either the valence on the manganese changes to $Mn^{(3+x)+\delta}$ and $Mn^{(3+x)-\delta}$, where, and the doping pattern remains the same, or the valencies continue to be $Mn^{+3+\delta}$ and $Mn^{+4-\delta}$, and the pattern of the charge density changes. It appears that it is mostly the latter, although there a number of more stable charge patterns which the ordering 'locks' to. These more stable ordering patterns are those which tie in with the crystal lattice. It is especially evident in the bilayer crystals and is described further in chapter 3.

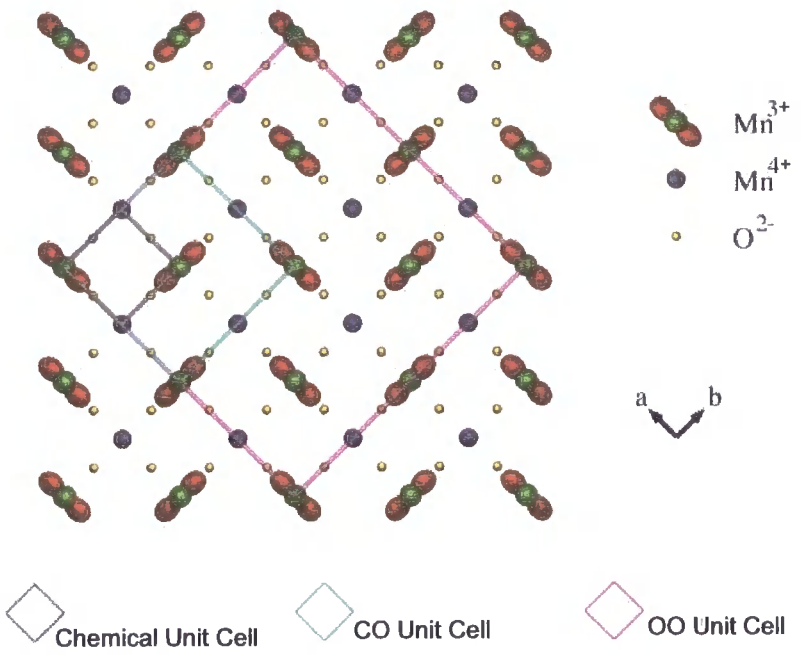

Figure 1.15: Schematic of the charge and orbital ordering in $La_{0.5}Sr_{1.5}MnO_4$ showing the unit cells for the chemical, charge, and orbital order. This diagram represents the $x = 0.5$ sample. Other doping patterns will have a different order pattern.

1.4 Jahn-Teller Distortions and Orbital Ordering

An effect of the charge ordering is to position in real space a single e_g electron on each Mn^{3+}. This electron sits in a degenerate electron band (Fig. 1.16). The two possible orbital occupancies are the $3_{x^2-y^2}$ and $3_{z^2-r^2}$ (Fig. 1.17). Concomitant to the onset of charge ordering, the extra electron on the Mn^{3+} falls into the lower of these two electron orbitals. Unfortunately calculating which of these orbitals has a lower energy is not trivial, and there has been intense discussion as to which it is. Similarly, experimental determination of the correct orbital is difficult, although recent experiments using x-ray magnetic circular dichroism appears to able to detect the orbital occupancy.

An electron preferentially occupying a particular orbital will shorten the bond length in that direction between the Mn and O ions. The degeneracy of the cation can then be stabilised by a distortion of the octahedra to a lower symmetry. Since a bulk crystal distortion requires spontaneous electron ordering in order to create a low-temperature, low symmetry structure, this can only occur if the concentration of the Jahn-Teller active ions is greater than a critical fraction. If this is the case, below a transition temperature, the octahedra

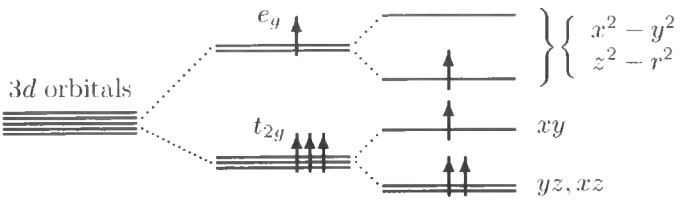

Figure 1.16: The degenerate $3d$ energy levels for a lone Mn ion. The orbital ordering and associated Jahn-Teller distortion is caused by the e_g electron occupying the lower of the two degenerate states

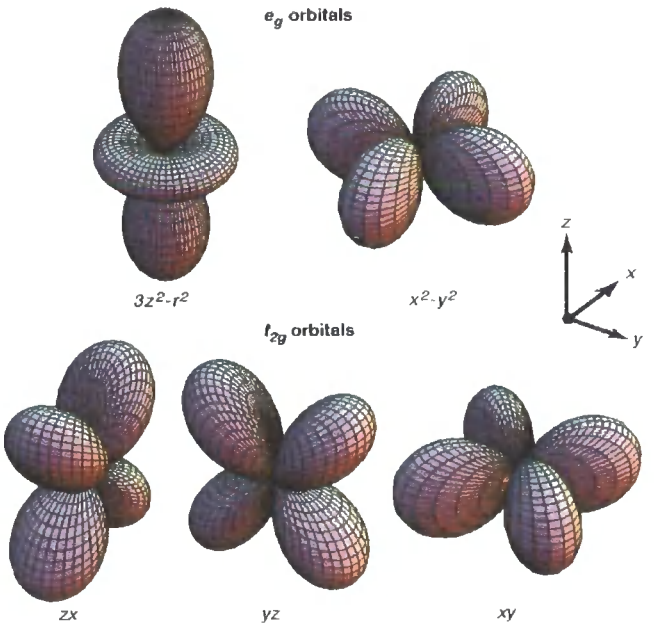

Figure 1.17: The shapes of the $3d$ orbitals. The fivefold degeneracy is lifted in the presence of the crystal field. Taken from Tokura and Nagaosa [58]

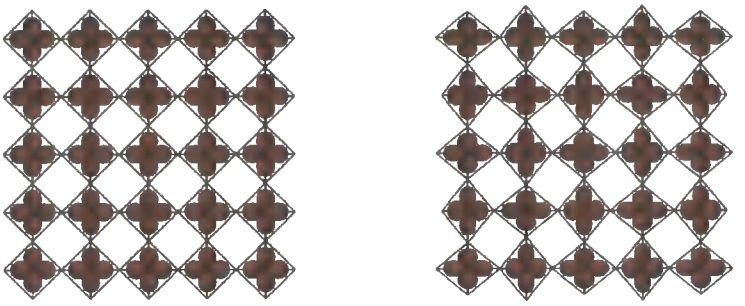

Figure 1.18: A representation of a Jahn-Teller undistorted crystal (left) and a crystal with a cooperative Jahn-Teller distortion (right). The Jahn-Teller effect causes a distortion of the MnO octahedra.

organise to form a co-operative Jahn-Teller distortion (Fig. 1.18)[59].

This effectively means that the orbitals are also ordered. It will be discussed chapters 6 and 7 whether the orbitals are initially ordered which causes a Jahn-Teller distortion, or the ordering of the distortions produces and orbital ordered state. This is a subtle difference, which will be elaborated on in Part II. Whichever is the underlying mechanism, orbital ordering and Jahn-Teller distortions occur simultaneously in space and temperature.

1.5 Magnetic X-ray Diffraction

The following section briefly outlines the process of Magnetic X-ray scattering. This section is strongly based on the work by Blume [60], Blume and Gibbs [61], Hannon and Trammel [62], and Hill and McMorrow [63]. The reader is advised to consult these texts and references therein for further details.

This section highlights the results that are important to this work from the mentioned papers, in particular the emphasis is placed on the resonant dipole transition and its subsequent polarisation dependence. Before we get to resonant diffraction, we start with the Hamiltonian of an electron in an electromagnetic field which is composed of the momentum of the electron in the field; the electromagnetic field; the interaction of the spin of the electron and the magnetic field from the photon; the interaction of the spin of the electron and the magnetic field caused by the Ampere induction of the movement of the electron in a magnetic field and the annihilation and creation of a photon.

It can be written as

$$\begin{aligned}\mathscr{H} &= \sum_j \frac{1}{2m}\left(\mathbf{P}_j - \frac{e}{c}\mathbf{A}(\mathbf{r}_j)\right)^2 + \sum_{ij} V(\mathbf{r}_{ij}) - \frac{e\hbar}{2mc}\sum_j \mathbf{s}_j \cdot \nabla \times \mathbf{A}(\mathbf{r}_j) \\ &\quad - \frac{e\hbar}{2(mc)^2}\sum_j \mathbf{s}_j \cdot \mathbf{E}(\mathbf{r}_j) \times \left(\mathbf{P}_j - \frac{e}{c}\mathbf{A}(\mathbf{r}_j)\right) + \sum_{\mathbf{k}\lambda} \hbar\omega_k (C^+(k\lambda)C(k\lambda) + \frac{1}{2}) \quad (1.1)\end{aligned}$$

where $\mathbf{P}$ is the momentum of the electron, $\mathbf{A}$ is the vector potential of the photon, V is the potential of each electron from the remaining electrons, $\mathbf{E} = -\Delta\phi - \frac{1}{c}\dot{A}$, where ϕ is the Coulomb potential. $\mathbf{s}$ is the spin of the electron, ω_k ($\omega_{k'}$) is the angular frequency of the incident (scattered) wave, and C^+ and C are the creation and annihilation operators.

The terms relevant to scattering are those containing the photon vector potential, $\mathbf{A}$, thus the scattering Hamiltonian can be rewritten

$$\begin{aligned}\mathscr{H}' &= \frac{e^2}{2mc^2}\sum_j \mathbf{A}^2(\mathbf{r}_j) - \frac{e}{mc}\sum_j \mathbf{A}(\mathbf{r}_j)\cdot\mathbf{P}_j - \frac{e\hbar}{mc}\sum_j \mathbf{s}_j \cdot [\nabla \times \mathbf{A}(\mathbf{r}_j)] \\ &\quad - \frac{e\hbar}{2(mc)^2}\frac{e^2}{c^2}\sum_j \mathbf{s}_j \cdot [\dot{\mathbf{A}}(\mathbf{r}_j) \times \mathbf{A}(\mathbf{r}_j)] \quad (1.2) \\ &\equiv \mathscr{H}'_1 + \mathscr{H}'_2 + \mathscr{H}'_3 + \mathscr{H}'_4 \quad (1.3)\end{aligned}$$

It is noted that $\mathscr{H}'_1$ and $\mathscr{H}'_4$ are quadratic in $\mathbf{A}$, whereas $\mathscr{H}'_2$ and $\mathscr{H}'_3$ are linear in $\mathbf{A}$.

The scattering process involves a change of state of an electron. This can either be a single stage process, whereby the electron in incident quantum state $|a\rangle$ with energy E_a transfers to a final quantum state $|b\rangle$ with energy E_b, or can involve intermediate quantum states. The probability for these transitions is found in Fermi's 'Golden Rule', which when written to second order is:

$$w = \frac{2\pi}{\hbar}\left|\langle f|\mathscr{H}'|i\rangle + \sum_n \frac{\langle f|\mathscr{H}'|n\rangle\langle n|\mathscr{H}'|i\rangle}{E_i - E_f}\right|^2 \times \delta(E_i - E_f) \quad (1.4)$$

In our case the initial quantum state i is state a with photon $\mathbf{k}\lambda$ and final state f is quantum state b with photon $\mathbf{k}'\lambda'$. Similarly $E_i = E_a + \hbar\omega_k$ and $E_f = E_b + \hbar\omega_{k'}$. Given the order of $\mathbf{A}$ in the terms of equation 1.2, $\mathscr{H}'_1$ and $\mathscr{H}'_4$ contribute to the first term in the Golden Rule, whereas $\mathscr{H}'_2$ and $\mathscr{H}'_3$ contribute to the second. As such we then have:

$$w = \frac{2\pi}{\hbar}\left|\langle b;\mathbf{k}'\lambda'|\mathscr{H}_1' + \mathscr{H}_4'|a;\mathbf{k}\lambda\rangle + \sum_n \frac{\langle b;\mathbf{k}'\lambda'|\mathscr{H}_2' + \mathscr{H}_3'|n\rangle\langle n|\mathscr{H}_2' + \mathscr{H}_3'|a;\mathbf{k}\lambda\rangle}{E_a + \hbar\omega_k - E_n}\right|^2$$

$$\times\, \delta(E_a - E_b + \hbar\omega_k - \hbar\omega_{k'}) \tag{1.5}$$

By combining equations 1.5 and 1.2 and multiplying the result by the density of final states and dividing by the incident flux, we conclude with the scattering cross section:

$$\left(\frac{d^2\sigma}{d\Omega' dE'}\right)_{\substack{a\to b\\ \lambda\to\lambda'}} = \left(\frac{e^2}{mc^2}\right)^2 \left|\left\langle b\left|\sum_j e^{i\mathbf{K}\cdot\mathbf{r}_j}\right|a\right\rangle \epsilon'\cdot\epsilon - i\frac{\hbar\omega}{mc^2}\left\langle b\left|\sum_j e^{i\mathbf{K}\cdot\mathbf{r}_j}\mathbf{s}_j\right|a\right\rangle\cdot\epsilon'\times\epsilon\right.$$

$$+\frac{\hbar^2k^2}{m}\sum_{ij}\sum_c\left(\frac{\left\langle b\left|\left(\frac{\epsilon'\cdot\mathbf{P}_i}{\hbar} - i(\mathbf{k}'\times\epsilon')\cdot\mathbf{s}_j\right)e^{-i\mathbf{k}'\cdot\mathbf{r}_i}\right|c\right\rangle\left\langle c\left|\left(\frac{\epsilon'\cdot\mathbf{P}_j}{\hbar} - i\,(\mathbf{k}\times\epsilon)\cdot\mathbf{s}_j\right)e^{i\mathbf{k}\cdot\mathbf{r}_j}\right|a\right\rangle}{E_a - E_c + \hbar\omega_k - i\frac{\Gamma_c}{2}}\right.$$

$$\left.\left.+\frac{\left\langle b\left|\left(\frac{\epsilon\cdot\mathbf{P}_j}{\hbar} + i(\mathbf{k}\times\epsilon)\cdot\mathbf{s}_j\right)e^{i\mathbf{k}\cdot\mathbf{r}_j}\right|c\right\rangle\left\langle c\left|\left(\frac{\epsilon'\cdot\mathbf{P}_j}{\hbar} - i\mathbf{k}'\times\epsilon'\cdot\mathbf{s}_j\right)e^{-i\mathbf{k}'\cdot\mathbf{r}_j}\right|a\right\rangle}{E_a - E_c - \hbar\omega_{k'}}\right)\right|^2$$

$$\times\, \delta(E_a - E_b + \hbar\omega_k - \hbar\omega_{k'}) \tag{1.6}$$

where $\mathbf{K} = \mathbf{k} - \mathbf{k}'$ and ϵ (ϵ') is the polarisation state of the incident (scattered) photon. The first term of the equation is the non-resonant charge scattering. This is the source of charge scattering from structural Bragg peaks. This term involves a single transition, and in the usual case of elastic scattering $|b\rangle \equiv |a\rangle$.

The second term of equation 1.6 concerns the non-resonant magnetic scattering. The pre-factor to this term explains the extremely small intensity of this scattering contribution.

The third and forth terms in the scattering cross section are the anomalous scattering terms, commonly denominated at f' and f''. These terms explain resonant scattering, which arises when the incident photon energy is close to the difference in energy between quantum states a and c. The additional term $i\frac{\Gamma_c}{2}$ on the denominator of these terms accounts for the width of the energy band. Again, in the case of elastic scattering $|b\rangle \equiv |a\rangle$.

It is the resonant scattering terms that are of interest in this thesis. Part I contains data from Mn K edge resonant diffraction, where the incident energy is tuned to the energy difference between the $1s$ and $4p$. Here a core electron from the $1s$ band is promoted to the

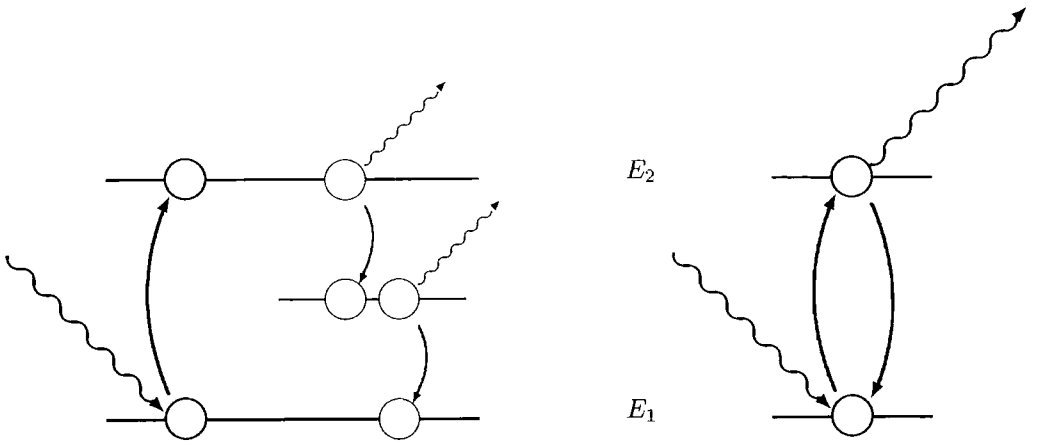

Figure 1.19: Schematic of photon absorption and subsequent emission (left) and resonant scattering (right). The resonant scattering process is a single process; this is easily seen in equation 1.5. By contrast absorption and emission are two separate processes.

unoccupied $4p$ electron band, and then relaxes back to the $1s$ band. Part II contains studies of resonant diffraction at the Mn L edge. This time electrons are promoted from the $2p$ electron band to the partially filled $3d$ electron band. Both of these transitions are dipole transitions, involving the change in m of 1. Higher order (quadrupole etc.) do occur, but are significantly weaker. Although resonant scattering is a two stage process (promotion and relaxation), these transitions should really be thought of as a single action, indeed a quick glance at equation 1.6 reveals these process as inextricably linked. Figure 1.19 displays the difference between a distinct absorption and emission process, and the resonant scattering process.

Equation 1.6 can therefore be summarised by the equation:

$$f = f_0 + f' + f'' + f_{spin} \tag{1.7}$$

The equation 1.6 describes the entire scattering, however in this thesis the results will exclusively be generated from electric dipole transitions. This is entirely due to the strengths of the transitions, due to the quadrupole and higher order transitions being increasingly weaker. Magnetic multipole transitions are a factor of $\frac{\hbar\omega}{mc^2}$ of the intensity of the respective electric transitions [62]. Concentrating entirely on the 2^L (dipole) transition, we can rewrite the resonant scattering amplitude (from Hannon *et al.* [62]) in terms of spherical harmonics,

$$f_{EL}(w) = \left(\frac{4\pi}{|k|}\right) f_D \sum_{M=-L}^{L} [\hat{\epsilon}'^* \cdot \mathbf{Y}^{(e)}_{LM}(\hat{\mathbf{k}}')\mathbf{Y}^{(e)*}_{LM}(\hat{\mathbf{k}}) \cdot \hat{\epsilon}] F^{(e)}_{LM}(\omega). \tag{1.8}$$

The first part of the summation (in the square brackets), concerns the polarisation of the incoming ϵ and outgoing ϵ' beams, and will be developed shortly. The final factor F_{LM} gives the strength of the resonance, and is determined by the overlap integrals of the electron bands by the following equation:

$$F^{e}_{EL}(\omega) = \sum_{\alpha,\eta} \frac{P_\alpha P_\alpha(\eta)\Gamma_x(\alpha M\eta; \mathrm{EL})/\Gamma(\eta)}{x(\alpha,\eta) - i} \tag{1.9}$$

where P_α is the probability of the ion exisiting in the initial state α and $P_\alpha(\eta)$ is the probability of the transition from initial state α to final state η. $\Gamma_x(\alpha M\eta; \mathrm{EL})$ gives the partial width for the EL radiative decay from $|\eta) \rightarrow |a)$, and $\Gamma(\eta)$ is the lifetime of the excited state; typically $\approx 1 - 10$ eV so that the scattering is fast $\approx 10^{-16}$ s.

One of the major advantages in resonant x-ray scattering is the ability to use the polarisation states (ϵ,ϵ') of the incoming (k) and scattered (k') beam (Fig. 1.20), to determine the origin of the resonant scattering. This is due to the term in square brackets in equation 1.8. For a dipole transition the change in the quantum number l is 1, and as such, we know that m_l can be either -1, 0 or 1. For $l = 1$ and $m_l = 1, -1$ the vector spherical harmonics can be written;

$$[\hat{\epsilon}' \cdot \mathbf{Y}_{1\pm1}(\hat{\mathbf{k}}')\mathbf{Y}^{*}_{1\pm1}(\hat{\mathbf{k}}) \cdot \hat{\epsilon}] = \frac{3}{16\pi}[\hat{\epsilon}' \cdot \hat{\epsilon} \mp i(\hat{\epsilon}' \times \hat{\epsilon}) \cdot \hat{\mathbf{z}}_n - (\hat{\epsilon}' \cdot \hat{\mathbf{z}}_n)(\hat{\epsilon} \cdot \hat{\mathbf{z}}_n)] \tag{1.10}$$

where $\hat{\mathbf{z}}_n$ is a unit vector in the direction of the magnetic moment of the n^{th} ion. For $l = 1$ and $m_l = 0$;

$$[\hat{\epsilon}' \cdot \mathbf{Y}_{10}(\hat{\mathbf{k}}')\mathbf{Y}^{*}_{10}(\hat{\mathbf{k}}) \cdot \hat{\epsilon}] = (\frac{3}{8\pi})[(\hat{\epsilon} \cdot \hat{\mathbf{z}}_n)]. \tag{1.11}$$

Through this equation the equation for the resonant scattering can be written directly displaying the dependence of the polarisation states of the incoming and emitted wave;

$$f^{XRES}_{nE1} = [(\hat{\epsilon}' \cdot \hat{\epsilon})F^{(0)} - i(\hat{\epsilon}' \times \hat{\epsilon}) \cdot \hat{\mathbf{z}}_n F^{(1)} + (\hat{\epsilon}' \cdot \hat{\mathbf{z}}_n)(\hat{\epsilon} \cdot \hat{\mathbf{z}}_n)F^{(2)}] \tag{1.12}$$

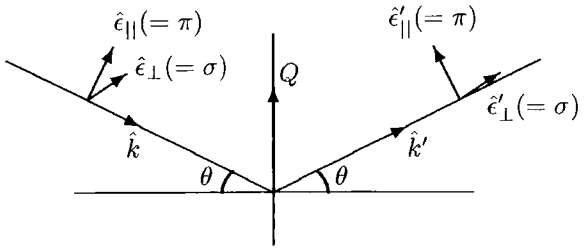

Figure 1.20: Conventional directions for describing the polarisation vectors. Incoming beam $\hat{k}$ has polarisation vector either parallel ($\hat{\epsilon}_{||}$) or perpendicular ($\hat{\epsilon}_{\perp}$) to the scattering plane. The scattered wavevector k' has a similar convention.

where

$$F^{(0)} = (\frac{3}{4k}[F_{11} + F_{1-1}]) \tag{1.13}$$

$$F^{(1)} = (\frac{3}{4k}[F_{11} - F_{1-1}]) \tag{1.14}$$

$$F^{(2)} = (\frac{3}{4k}[2F_{10} - F_{11} - F_{1-1}]) \tag{1.15}$$

It is immediately obvious that the terms in equation 1.12 each have a different polarisation dependence. The first term, which consists of entirely charge scattering, has an $(\hat{\epsilon}' \cdot \hat{\epsilon})$ dependence. Therefore the intensity of the scattered beam is unity with the polarisation vectors of the incident and scattered beam parallel, and zero when they are perpendicular. As the σ channel is defined as being perpendicular to the scattering plane, the σ channels of the incident and scattered beam are always parallel. Thus the scattering is present in the $\sigma \rightarrow \sigma$ channel, and there is no 2θ dependence. Likewise the σ channel of the incident (and scattered) beam is always perpendicular to the π channel. Therefore the $\sigma \leftrightarrow \pi$ terms in the polarisation matrix are zero. The $\pi \rightarrow \pi$ channel is slightly more complicated. If the incoming and scattered beams are parallel, then the $\hat{\epsilon}$ and $\hat{\epsilon}'$ are parallel, however if they are perpendicular (i.e. $2\theta = 90°$) then $\hat{\epsilon}$ and $\hat{\epsilon}'$ and there is no scattering in the $\pi \rightarrow \pi$ channel. As such the $\pi \rightarrow \pi$ polarisation matrix element is $\cos 2\theta = \hat{\mathbf{k}}' \cdot \hat{\mathbf{k}}$. Putting these four matrix elements together gives the polarisation dependence for the charge scattering contribution of the resonant scattering term;

$$\hat{\epsilon}' \cdot \hat{\epsilon} = \begin{pmatrix} 1 & 0 \\ 0 & \hat{\mathbf{k}}' \cdot \hat{\mathbf{k}} \end{pmatrix} \tag{1.16}$$

The second resonant scattering term $F^{(0)}$ has a $(\hat{\epsilon}' \times \hat{\epsilon})$ dependence. This precludes any scattering in the $\sigma \rightarrow \sigma$ channel, however scattering in the $\pi \rightarrow \pi$ channel is allowed, again with a 2θ dependence, this time $\sin 2\theta$. Scattering would be unity in the $\sigma \leftrightarrow \pi$ channels, however there is an additional interaction with the magnetic moment (as this term describes magnetic resonant scattering). As such the polarisation matrix for the $F^{(1)}$ term in a dipole transition is

$$\hat{\epsilon}' \cdot \hat{\epsilon} = \begin{pmatrix} 0 & \hat{\mathbf{k}} \\ -\hat{\mathbf{k}}' & \hat{\mathbf{k}}' \times \hat{\mathbf{k}} \end{pmatrix} \tag{1.17}$$

The third matrix for the f'' term can be calculated in the same way from the $(\hat{\epsilon}' \cdot \hat{\mathbf{z}}_n)(\hat{\epsilon} \cdot \hat{\mathbf{z}}_n)$ polarisation dependence of the $F^{(2)}$. By using geometric identities, these terms can be fully written in terms of θ to give

$$f_{nE1}^{XRES} = F^{(}0) \begin{pmatrix} 1 & 0 \\ 0 & \cos 2\theta \end{pmatrix} - iF^{(1)} \begin{pmatrix} 0 & z_1 \cos\theta + z_3 \sin\theta \\ z_3 \sin\theta - z_1 \cos\theta & -z_2 \sin 2\theta \end{pmatrix}$$
$$+F^{(2)} \begin{pmatrix} z_2^2 & -z_2(z_1 \sin\theta - z_3 \cos\theta) \\ z_2(z_1 \sin\theta + z_3 \cos\theta) & -cos^2\theta(z_1^2 \tan^2\theta + z_3^2) \end{pmatrix} \tag{1.18}$$

From an experimental point of view, equation 1.18 displays some important results. At a synchrotron, the light is highly polarised, and usually the diffractometer is orientated such that the incident light is in the σ channel. If the σ and π components of the scattered beam can be separated then it is possible to discover the origin of the scattered beam, in terms of f, f' and f''. Furthermore if the spin or orbital density is non-isotropic ($z_1 \neq z \neq z_3$), then as the sample is rotated around the scattering vector (and therefore $\hat{\mathrm{k}}$ and $\hat{\mathrm{k}}'$ are rotated around $\hat{\mathrm{z}}$) then the relative intensities in the different channels will change for f' and f''. Both polarisation analysis, and the azimuthal variation are explored through the experimental results in Part I.

Part I

High Energy and Resonant K edge X-ray Diffraction

Chapter 2

Long Range Order in $La_{1-x}Sr_{1+x}MnO_4$ and $Nd_{1-x}Sr_{1+x}MnO_4$

This chapter presents results from single layered manganites using high energy x-ray diffraction and resonant x-ray diffraction at the Mn K edge. This manganite series has been introduced in Chapter 1, and the structure is shown in figure 1.1. This chapter shows results from $(LaNd)_{1-x}Sr_{1+x}MnO_4$ with $0.5 < x < 0.8$, describing how the long range order changes throughout the stoichiometric range. It begins with a brief description of the experimental methods used, including polarisation analysis. The attribution of the superlattice peaks to structural distortions and charge and orbital ordering is then outlined; together with a description of the half doped samples. Comparisons are then made with those samples with higher doping levels. The purpose of this chapter is to introduce the reader to the general experiments that have been conducted on these crystals. These initial results will be developed in the following chapters.

2.1 Experimental Technique

The samples were studied using single crystal x-ray diffraction. This part of the thesis reports experimental data taken on resonant x-ray beamlines with an incident energy near the Mn K edge (such as BM28 at the ESRF), and non-resonant high energy x-ray beamlines (such as BW5 at HASYLAB). The following subsections will outline the procedure at the beamlines, and also the initial sample preparation required.

2.1.1 Sample Preparation

The samples were grown using the floating zone method, at the University of Oxford. The growth recipe was initially developed for the half doped sample $La_{0.5}Sr_{1.5}MnO_4$. Once high quality single crystal growth had been achieved, this is modified in order to grow higher doped samples. The floating zone method is preferable to growing crystals in a crucible as it minimises contamination, and therefore enables higher quality crystals to be grown. There is however an inherent difficulty with the growth of $La_{1-x}Sr_{1+x}MnO_4$ when $x > 0.5$ because phase segregation starts to occur within the sample. As such, it is extremely difficult to grow homogeneous samples. As an alternative, Nd has been substituted for the La, which due to the slightly different ionic radius, allows non-phase segregated single crystals of adequate size and quality to be grown.

The crystals are checked and pre-aligned using a rotating anode laboratory source, before commencing a synchrotron radiation experiment. This x-ray source uses a water cooled copper rotating anode, the x-ray beam from which is focussed by a pair of graded d-spacing parabolic mirrors. These mirrors produce a parallel beam of approximately 1×1 mm [64], which is incident on the sample. The scattered x-rays diffract off an analyser crystal to improve the instrumental resolution.

X-ray resonant diffraction has been undertaken in reflection geometry and as such it is only possible to reach certain areas of reciprocal space from each sample face. By cutting or grinding the crystal, such that the required scattering vector is surface normal, required reflections can be reached. The ground face can then be polished with alumina paste down to 0.25 μm, which removes any surface blemishes and any damage caused by grinding. The layered manganites have strong cleavage planes perpendicular to the c axis. If the experiment can be designed so that x-rays are diffracted from this cleaved surface, then no further preparation after cleaving is necessary. After preparation the samples are attached onto the diffractometer mount. The sample is normally secured to the mount using a heat conductive glue, either a silver epoxy, or a silver conductive paint. The latter is preferential as it can be dissolved in acetone for safe sample removal, as the use of stronger solvents can cause fracture in the crystals.

At an experimental beamline, the mount with sample attached is then fixed to the end of a cold finger of a closed cycle helium cryostat. These cryostats are capable of temperatures as low as 6 K without further modification. Because of the relatively low x-ray energies used

in resonant x-ray diffraction, the heat shrouds of the cryostat are machined from beryllium to reduce their x-ray absorption. When using high energy x-rays, the absorption from a few mm of aluminium is negligible, simplifying the design and use of the heat shrouds.

2.1.2 High Energy X-ray Diffraction

The benefits of high energy diffraction can be summarised by the large attenuation length, which is typically in the order of centimetres. As such, x-rays pass right through the sample, which is aligned in Laue geometry. This gives an extremely high scattering volume, which can be used to observe phenomena that have a small scattering cross section. The technique is a pure bulk measurement, as the scattering from the surface layers corresponds to a negligible proportion of the entire scattered signal.

The disadvantage with high energy x-ray diffraction, is that the x-ray energy is far from any absorption edges, and as such the scattering is purely non-resonant. This severely limits the technique, and so control of environmental parameters such as temperature and magnetic field is often used to study phases in the material. The most successful studies have been where high energy diffraction is combined with a second technique providing additional information on the nature of the x-ray scattering in the sample. Other complementary techniques often include magnetism and transport measurements, and also resonant x-ray scattering.

Despite the absence of absorption edges at high energies, magnetic scattering has been conducted with high energy x-ray diffraction. The total scattering factor (Eqn. 1.6) has a very small contribution from non-resonant magnetic scattering. Strempfer *et al.* [65] detected the magnetic peak in MnF_2 using high energy diffraction, however it must be emphasised that this model system was used because of the availability of large, and extremely high quality samples, which have a large magnetic moment. In general this is currently not a feasible technique to study magnetic scattering.

The high energy x-ray diffraction results were collected using the BW5 beamline at HASYLAB, Hamburg [66], and beamline ID15 at the ESRF [67]. These experiments were typically conducted with an incident energy of 100 keV, and the beamlines were equipped with Huber cradles, closed cycle cryostats and solid state detectors. Single channel analysers were used at both beamlines to filter out higher harmonics from the scattered x-ray beam.

2.1.3 Resonant K edge Diffraction

K edge resonant diffraction involves tuning the energy of the incident x-ray beam, so that it is equal to that of the excitation energies from the 1s level. This can be in the form of a quadrupole (E2) transition from the $1s \rightarrow 3d$, but is more usually a dipole transition (E1) from the $1s \rightarrow 4p$ electron levels. The quadropole transition occurs at a slightly lower energy than the dipole, and is significantly weaker. In spite of the weak intensity, the $1s \rightarrow 4p$ quadrupole transition has been observed in a range of materials including CoO [68] and NiO [69], and also $KCuF_3$ [70] and V_2O_3 [71]. Because of the multi-electron transitions involved in the quadrupole transitions, the energy dependences are more difficult to fit. The very nature of a resonant signal provides information on the electron transition, and therefore the technique is element and electron band specific. This selectivity is unavailable using standard neutron diffraction, and is one of the major advantages of resonant x-ray diffraction.

Polarisation Analysis

In addition to element selectivity, the scattered beam can be studied using polarisation analysis. The theoretical explanation of this technique has been outlined in section 1.5. It has been established that different scattering processes rotate the polarisation vector in different ways. With a detector positioned directly in the scattered beam, all the x-rays, regardless of their polarisation state are counted. In order to separate the polarisation states a second scattering process is used after the beam is scattered by the sample. An analyser crystal is placed in the scattered beam. This analyser crystal is selected such that the 2θ angle for a Bragg reflection from the analyser crystal is as close as possible to 90°. As Bragg peaks are normally composed entirely of charge scattering the only scattered channel is $\sigma \rightarrow \sigma$. Thus the crystal can be aligned either with the scattering vector of the analyser crystal within the scattering plane of the diffractometer (allowing through only the σ component of the scattered beam) or perpendicular to the scattering plane of the diffractometer (allowing through only the π component, as the π polarisation state of the scattered beam from the crystal is now the σ component of the incoming beam of the analyser crystal).

This is an elegant solution as the polarisation analyser both increases the resolution of the system and separates the polarisation components of the beam. Unfortunately, however it is limited to the number of crystals suitable as an analyser, and selecting a crystal with

$2\theta \approx 90°$ at the required energy is not always possible. The manganese resonance at the K edge in the layered manganites lies at approximately 6.555 keV. The closest match to this energy is the (220) Bragg peak of Cu, which at this energy has $2\theta = 95°$ This gives approximately 3% leakthrough, between the σ and π channels.

2.2 Experimental Method and Results

The section is organised by sample stoichiometry, with increasing Sr doping, from $x = 0.5$ to $x = 0.8$. Data are presented from both high energy x-ray diffraction and resonant energy diffraction.

2.2.1 $La_{0.5}Sr_{1.5}MnO_4$ and $Nd_{0.5}Sr_{1.5}MnO_4$

Figure 2.1 shows a set of four Jahn-Teller distortion satellites around the (0,2,0) Bragg peak in $Nd_{0.5}Sr_{1.5}MnO_4$. In this image the central Bragg peak has been removed, although the edge of it can still be seen. According to the pattern of the charge ordering (Fig. 1.15), the superlattice peaks should occur in pairs oppositely arranged around a Bragg peak, rather than in set of four. However x-ray diffraction is a bulk sensitive probe, and is sensitive to an average ordering pattern. Despite being a single crystal, the long range order in the crystal occurs in multiple domains, and some which order at 90° to one another. On an x-ray diffraction pattern this appears as four superlattice peaks around the Bragg peak. The data was taken with a 2D Mar^{TM} detector with a 200 s exposure, on beamline ID15, with the sample at 10 K.

In the layered manganites the scattering from the Jahn-Teller distortion appears significantly stronger than the charge ordering. This is not necessarily because the charge order effect is very small, but more likely because the Jahn-Teller distortion involves a movement of the Mn ion and the O octahedra, which together produce a large scattering cross-section. The 2D detector on the high energy beamline was unable to observe the charge order signal above the background noise. One of the major disadvantages of 2D detectors is that there is no analyser, and the experiment is limited to double axis geometry. Thus there is no reduction in the background scatter, which leads to and extremely high background signal in comparison with a triple axis geometry. The resolution of the 2D detector is physically fixed (as an xy grid), but can effectively be changed in reciprocal space by altering the distance between the detector and the sample; thereby changing the angular acceptance of each pixel.

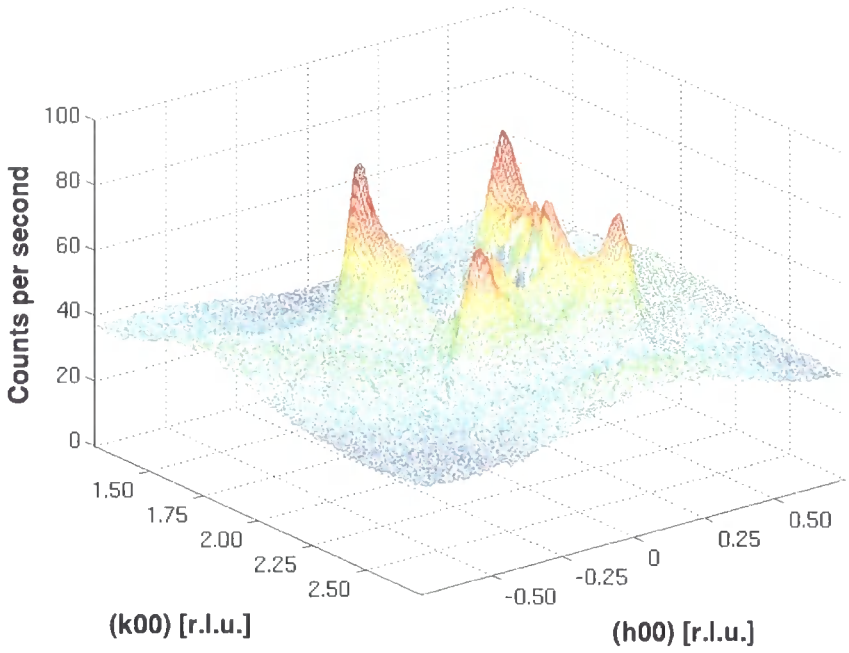

Figure 2.1: The four Jahn-Teller peaks in $Nd_{0.5}Sr_{1.5}MnO_4$ around the (020) Bragg peak (blanked out), these peaks exist at $(\pm 0.25, 2 \pm 0.25, 0)$ positions. Data taken with a 2D detector with a 200 s exposure, at 10 K, using x-rays with an incident energy of 100 keV.

However in this experiment, the detector position was kept constant, and so there was no change in the area of reciprocal space sampled.

The Jahn-Teller distortion peaks appear strong at 10 K, and upon warming they gradually get weaker. Figure 2.2 shows the evolution of the Jahn-Teller distortions in $Nd_{0.5}Sr_{1.5}MnO_4$ as a function of temperature. The intensity of the satellite peaks gradually gets weaker, until they are virtually non-existent at room temperature. Although the 2D scans give a good overall picture of the ordering, it is difficult to extract quantitative results. It is possible to analyse cross sections of the data, however the background noise is very high, and for these results a triple axis system is more efficient. A point detector with an analyser crystal vastly reduces the background noise, with little effect on the strength of the scattered signal, providing a significantly higher signal / noise ratio, and in addition has a much higher spatial resolution.

The left panels in figure 2.3 show the superstructure peaks corresponding to the charge and orbital ordering and the Jahn-Teller distortions in $La_{0.5}Sr_{1.5}MnO_4$. In comparison to the previous data this was taken with a point detector, with an analyser crystal. The results were taken on BM28 (XMaS) at the ESRF, with an incident energy of 6.55 keV, which

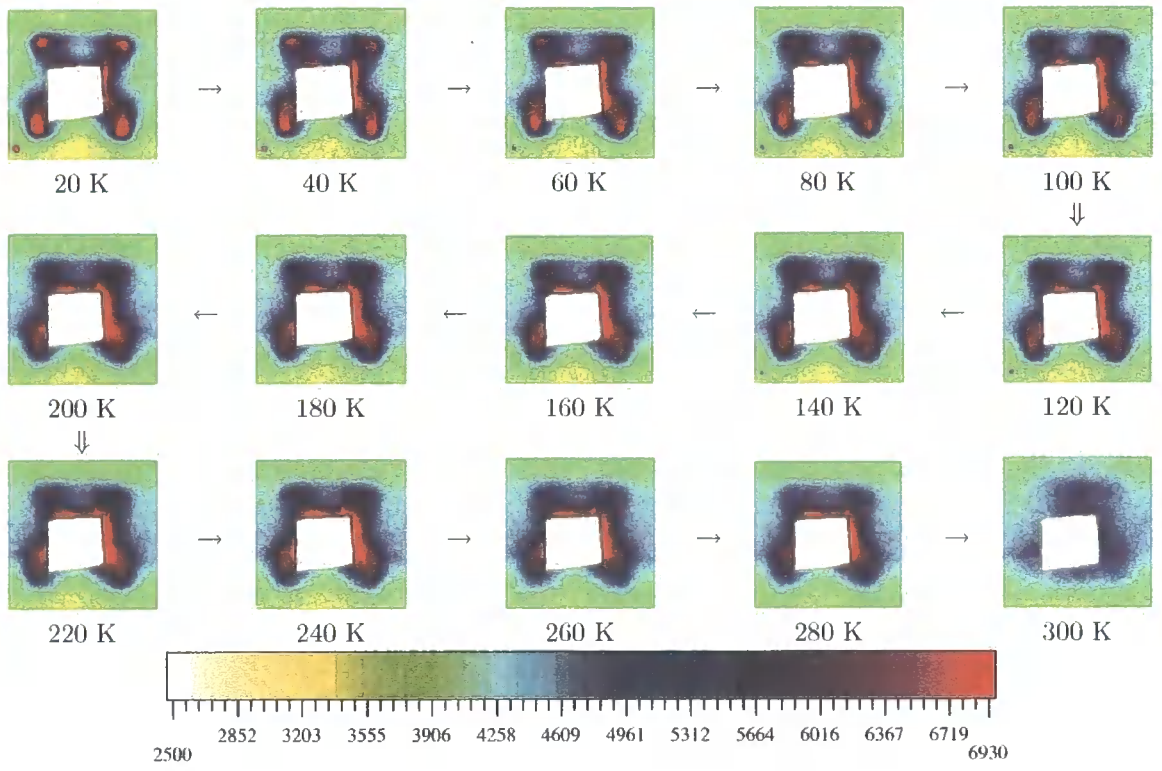

Figure 2.2: Evolution of Jahn-Teller distortions in $Nd_{0.5}Sr_{1.5}MnO_4$ with increasing temperature. Each image was collected with a 100 s exposure on the high energy ID15 beamline, with 100 keV incident x-ray energy.

corresponds to the Mn K edge.

Although a quantitative measurement of the intensity of the signal originating from each phenomena can be given, directly comparing these intensities is rather difficult. Different samples are of different sizes, and are of different qualities, so comparing absolute measurements of intensity between different samples is liable to error. Even comparing the intensity of different peaks in the same sample is not entirely straightforward. The manganese K edge is relatively low in energy, and so moving between peaks significantly changes the orientation of the sample in the beam. As such, even if the beam is coincident with the centre of rotation, the beam footprint will change. In addition the form factor of x-ray scattering will reduce the intensity of peaks further from the origin in reciprocal space. In conclusion, the intensity of a peak can only really be compared to the intensity of the same peak when changing an environmental condition such as temperature or external magnetic field. Despite this, a rough comparison of the intensity of the peaks gives an idea of the signal strength, and the quality of the data.

Each of the superlattice peaks in the left panels of figure 2.3 has been fitted with a Lorentzian squared lineshape. This lineshape is typical of the resolution function of a triple axis diffractometer where the resolution of the instrument and the rocking curve width of the sample are matched. If the peak is a different shape, typically Gaussian, then it normally indicates that the instrumental resolution is substantially lower than that of the rocking curve width of the sample. In the case of a Gaussian fit meaningful data from the width of the peak cannot be extracted as this is heavily convoluted with the instrument resolution. This is normally the case with Bragg peaks.

Resonant scattering has the ability to firstly detect and secondly separate each of these three superlattice peaks. The peak displayed in the upper panel of Figure 2.3 occurs at (1.75,0.25,0). This would immediately suggest that it is related to a fourfold increase in the unit cell. Looking at the ordering schematic (Fig. 1.15), it seems likely that it is either due to the orbital ordering or the concomitant co-operative Jahn-Teller distortion. The peak occurs in the $\sigma \rightarrow \sigma$ channel and did not appear in the $\sigma \rightarrow \pi$ channel, suggesting it is charge based scattering. The right hand panel shows an energy scan of the intensity through the Mn K edge. The intensity of the scattered signal was measured as a function of the incident x-rays energy, as it was scanned through the manganese absorption edge. Because the diffraction angles are determined by the energy of the x-ray beam as well as

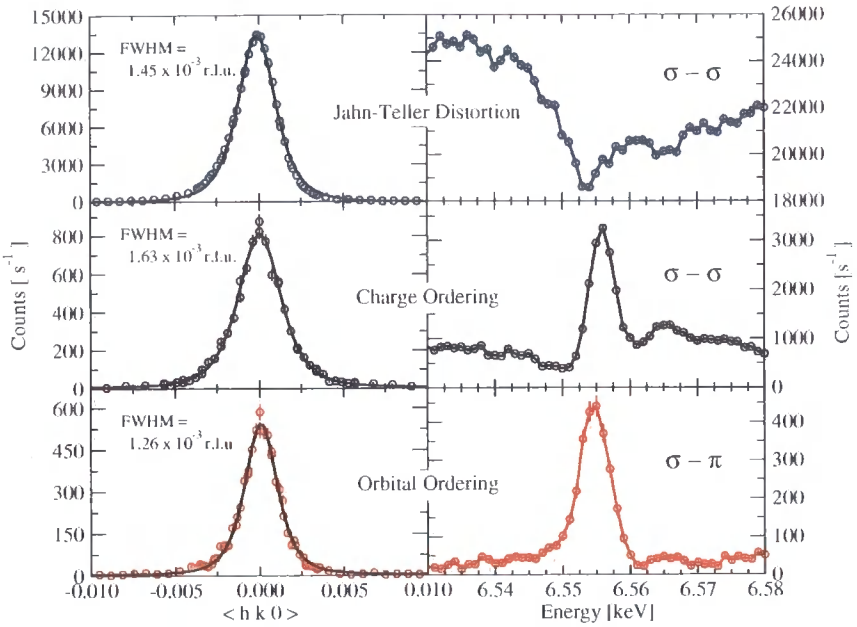

Figure 2.3: Scans through the Jahn-Teller distortion ($\frac{1}{4}$,$\frac{1}{4}$,0) , charge ordering ($\frac{1}{2}$,$\frac{1}{2}$,0), and orbital order ($\frac{1}{4}$,$\frac{1}{4}$,0) reflections in $La_{0.5}Sr_{1.5}MnO_4$ in reciprocal space at constant energy (left), and energy scans at constant Q vector. The Jahn-Teller and charge ordering signal was measured in the $\sigma \rightarrow \sigma$ channel, and the orbital ordering in the $\sigma \rightarrow \pi$ channel. Data normalised to a ring current of 100 mA.

the crystal lattice parameters, corrections in the positions of the motors, and in turn the diffraction angles, took place each time the incident energy changed, in order to stay at a constant wavevector. This ensures that there is no movement in reciprocal space and that the incident energy of the x-ray beam is the only scattering parameter that is altered. This absorption edge in the energy scan is similar to that observed on the Bragg peaks. It occurs because the absorption of the material increases as the energy of the incident x-rays corresponds to an absorption edge in the sample. The higher absorption reduces the intensity of the scattered beam. Taking these factors into account, it seems likely that this peak is due to a structural distortion, as this would appear identical to a weak Bragg peak. This type of structural distortion in the perovskite series is commonly called a Jahn-Teller distortion.

The peak in the middle panels occurs at (1.5,0.5,0), and again occurs only in the $\sigma - \sigma$ channel. The intensity of this superlattice reflection is significantly lower than the Jahn-Teller peak, however the width is slightly narrower, possibly indicating a longer correlation length. This peak, as well as existing at a different wavevector, shows a very different energy dependence. There is a slight dip, followed by a strong resonant peak, followed at slightly higher energy by a second small peak. This complex energy dependence indicates an

interference term. If, as might be expected from the order schematic (Fig. 1.15), the peak is due to some kind of charge modulation or charge ordering, then it will be composed of a contribution from the Mn^{3+} and the Mn^{4+} ions. The resonance occurs due to a preferential scattering from the $1s \rightarrow 2p$ electron transition, from the resonant addition to the $f^{(0)}$ term (Eqn. 1.12).

Finally the third peak in Figure 2.3 occurs with the same wavevector as the Jahn-Teller distortion, at (1.75,0.25,0). Unlike the Jahn-Teller distortion this peak occurs in the $\sigma - \pi$ channel. Although it occurs at the same wavevector as the Jahn-Teller peak, it is not simply caused by the leakthrough in the polarisation channels from the Jahn-Teller signal, as the energy dependences of the peaks are totally different. Instead of showing an absorption edge at the Mn K edge, there is a strong resonance to the extent that the signal could not be seen away from the resonant energy. It is not clear whether the scattering that is responsible for this peak, also exists in the $\sigma - \sigma$ channel, as assuming that the intensity in the $\sigma - \sigma$ channel would be similar to that in the $\sigma - \pi$, it would be negligible compared to the signal from the Jahn-Teller distortion. The existence of scattering in the $\sigma - \pi$ channel discounts normal charge scattering. As such, the scattering must originate from either the f' or f'' anomalous scattering terms. The presence of the Jahn-Teller distortion prevents confirmation of the existence of scattering in the $\sigma \rightarrow \sigma$ channel, as this would distinguish between f' and f''. However we do know that this is a resonant scattering process, from the dipole transition $1s \rightarrow 4p$. The orbital ordering that is thought to occur at the same wavevector as the Jahn-Teller could be the origin of the scattering, however the ordered orbitals are in the $3d$ electron band, and this dipole transition is not directly sensitive to this energy level. As such, the scattering must be sensitive to an ordering on the $4p$ electrons that is induced by the ordering of the $3d$ electrons. This explains the very weak signal.

In conclusion, it appears likely that in the half doped manganites, the signal that occurs at $(h \pm \frac{1}{2}, k \pm \frac{1}{2}, l)$, and resonates in the $\sigma \rightarrow \sigma$ channel is caused by ordering of the Mn^{3+} and Mn^{4+} ions. The signal at $(h \pm \frac{1}{4}, k \pm \frac{1}{4}, l)$ with an absorption edge in the $\sigma \rightarrow \sigma$ channel is caused by a co-operative Jahn-Teller distortion, and the signal with the same wavevector that resonates in the $\sigma \rightarrow \pi$ channel is from an induced ordering of the $4p$ electron orbitals.

Figure 2.4 shows the temperature dependence of the three superlattice satellites. All three peaks have a similar temperature dependence and disappear at 200 K, corresponding to the simultaneous transition temperature of the charge ordering, orbital ordering and

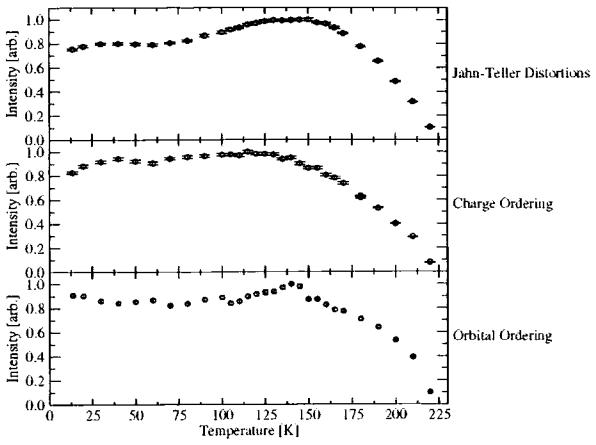

Figure 2.4: Integrated intensity of the Jahn Teller and charge order superlattice reflections in $La_{0.5}Sr_{1.5}MnO_4$, measured in the σ-σ channel and the orbital order superlattice reflection, measured in the σ-π channel. The charge and orbital order reflections were measured at 6.555 keV, and the Jahn-Teller at 6.530 keV.

Jahn-Teller distortion ($T_{CO/OO/JT}$). There is however a slight difference in the shape of the temperature dependences. The charge order and orbital order reflection are observed to have a constant intensity at temperatures below 120 K, above this temperature they begin to reduce in intensity until the transition temperature. The Jahn-Teller peak appears to increase slightly at 100 K, reaching a maximum at 140 K, before reducing in intensity. The increase in intensity is only of the region of 20%, however that may signify that the Jahn-Teller and orbital order peaks are not due to entirely the same underlying mechanism. The position of all of the peaks did not alter as a function of temperature. The width of the peaks was constant, until the scattering became very weak, and then the signal degraded and the width increased, indicative of critical fluctuations. This suggests that the ordering quickly becomes long range correlated, and the increase in scattering intensity is due to an increase in the valence difference, or increase in singular orbital occupation, rather than an increase in ordering throughout the crystal.

If the composition of the sample, (x), is changed and more strontium is added, the Sr^{2+} ions randomly replace the La^{3+} ions. This increases the number of mobile holes throughout the crystal lattice. Thus increasing the Sr doping in $La_{1-x}Sr_{1+x}MnO_4$ or $Nd_{1-x}Sr_{1+x}MnO_4$ changes the average valency of the Mn ions. Intuitively one would expect this to change the low temperature long range ordering as this is due initially to a charge segregation. There are two possible scenarios. Either the ordering pattern changes, such that there are nominally Mn^{3+} and Mn^{4+} in non-equal numbers, or the ordering pattern remains and the valency on

the Mn ions becomes $Mn^{3+\delta}$ and Mn^{4+}. We can discriminate between these two different scenarios by studying the x-ray scattering from different crystals with different stoichiometry. The distinction should be obvious from the wavevector of the superlattice peaks.

2.2.2 $Nd_{0.33}Sr_{1.67}MnO_4$

In $Nd_{0.33}Sr_{1.67}MnO_4$ very weak and broad superstructure peaks at $(\frac{1}{6}, \frac{1}{6}, 0)$ in the $\sigma - \sigma$ channel could be observed corresponding to the Jahn-Teller distortions. No superstructure peaks at $(\frac{1}{3}, \frac{1}{3}, 0)$ could be seen, or any peaks in the $\sigma - \pi$ channel. Figure 2.5 shows the evolution of the Jahn-Teller signal as a function of temperature. The wavevector of these peaks was not exactly $\frac{1}{6}$ (0.167), but appears to be slightly larger, further from the Bragg peak. This is interesting as it would normally be assumed that the position of the peak would 'lock' into the commensurate position, even if the stoichiometry was slightly incorrect. This intermediate phase of the layered maganites corresponding to $x = \frac{2}{3}$ appears to only have weak long range ordering. Although it is difficult to directly compare the intensities of the superlattice peaks between samples, the superstructure in this doping has particularly weak and broad peaks compared to the crystallographic Bragg peaks. This suggests that in this system the cooperative Jahn-Teller distortions are small (as evidenced by the small intensity) and poorly correlated (as evidenced by the increased width). There was no significant change in peak width with temperature and hence the inverse correlation length is constant. The significant increase in the error on the wavevector (position) of the superlattice distortions as the temperature is increased in Figure 2.5 is due to the difficulty in fitting to the very weak peak.

2.2.3 $Nd_{0.25}Sr_{1.75}MnO_4$

The $Nd_{0.25}Sr_{1.75}MnO_4$ manganites, ($x = 0.75$), have a much higher correlation length of charge order and Jahn-Teller distortion than was observed in the $x = 0.6$ doped sample. Figure 2.6 shows the superlattice peaks in the $\sigma - \sigma$ channel either side of the (0 0 6) Bragg peak. The position of the peaks is slightly further out than expected, similar to that observed in $Nd_{0.33}Sr_{1.67}MnO_4$. With this doping level it would be expected that the peaks would occur at 0.125 and 0.25 reciprocal lattice units from the Bragg reflection.

These peaks were measured in the *ab* plane around the (006) Bragg peak and not in the *hk*0 plane. This was designed so that the scattering occurred from a cleaved surface.

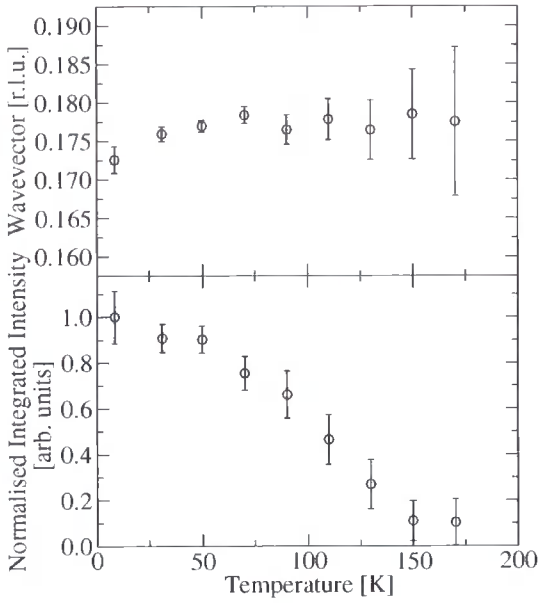

Figure 2.5: Wavevector and normalised integrated intensity of the Jahn-Teller superlattice peak in $Nd_{0.33}Sr_{1.67}MnO_4$ measured in the $\sigma - \sigma$ channel. The charge and orbital order peaks were not detected.

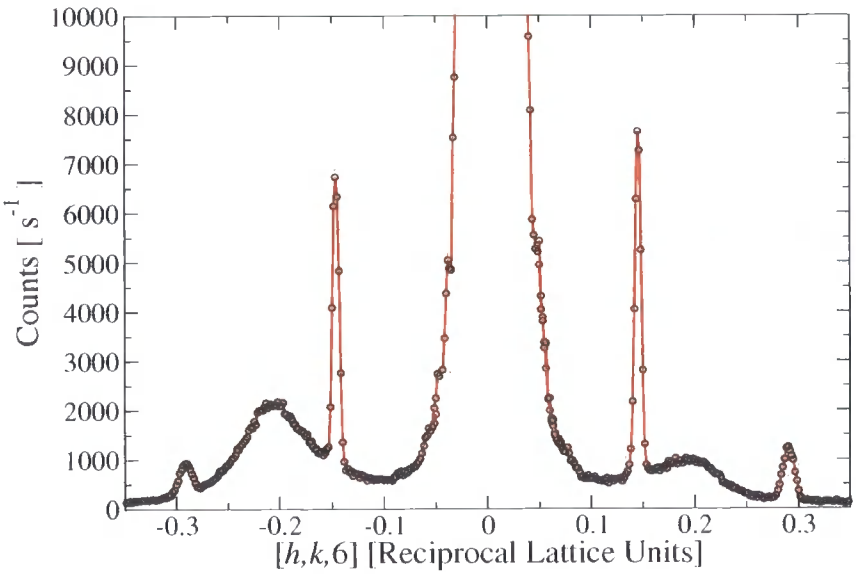

Figure 2.6: Charge order and Jahn-Teller distortions are shown either side of the (006) Bragg peak in $Nd_{0.25}Sr_{1.75}MnO_4$. The scan was taken in the $[hk0]$ direction, in the $\sigma - \sigma$ channel at 10 K, data normalised to a beam current of 200 mA.

Because of the layered nature of the crystal (Fig. 1.1) the crystals cleavage planes, correspond to the crystallographic *ab* plane, with [001] surface normal. As the crystals were small, it was difficult to prepare a face perpendicular to the *c* axis, as this dimension tended to be very thin (typically $<$ 1mm). Although conventionally it would be assumed that to access superlattice peaks at $(\frac{1}{4},\frac{1}{4},0)$ and $(\frac{1}{2},\frac{1}{2},0)$ like positions, a crystal cut with [110] surface normal would be ideal this is not always the case. Due to the macroscopic layered nature of the crystals, cutting a face parallel to the *c* axis requires cutting though the layers of the crystal. Even with a small x-ray beam a number of these layers are illuminated. These layers are not necessarily well correlated, and so even the Bragg peaks can be very weak with a large crystal mosaic, and finding superlattice peaks can be impossible. A superlattice peak that is easy to find when scattering from the cleaved *c* axis surface normal, can be impossible to find when scattering from a [110] surface normal face *in the same crystal.*

Careful observation of Figure 2.6 reveals broad peaks at $(\pm 0.2, \pm 0.2, 6)$, superimposed on the charge order and Jahn-Teller superlattice peaks. This diffuse scatter suggests a periodic modulation on a completely different length scale. The correlation length of these modulations is very short, and no resonant enhancement was observed suggesting some kind of structural distortion. The signal could originate from a Sr deficient area of the crystal, and represent a weak Jahn-Teller distortion in this area. These weak superlattice reflections are observed as single peaks, and appear at consistent wavevectors. As such they are unlikely to originate from different crystallites.

In addition to the charge order and Jahn-Teller superlattice peaks, weak peaks which resonated in both channels were found at the same wavevector as the Jahn-Teller distortion. It has been noticed in many samples that the Jahn-Teller distortion peaks were only present around specific Bragg peaks (this is also evident in the bilayer series). As such, around Bragg peaks where the Jahn-Teller peaks were not present (because of systematic absences), it was possible to observe the orbital induced ordering in both polarisation channels. Figure 2.7 shows the evolution of the intensity of these superlattice peaks with temperature. The charge order and structural distortions show a gradual decrease of intensity upon increasing temperature towards $T_{CO/JT}$, similar to that seen in $Nd_{0.33}Sr_{1.67}MnO_4$. The orbital order peak appears to show a difference in the intensities in the two channels. This is rather unexpected. What is interesting is that the divergence of these intensities occurs at T_N. It is not unreasonable that the breakdown in magnetic order effects the orbital ordering

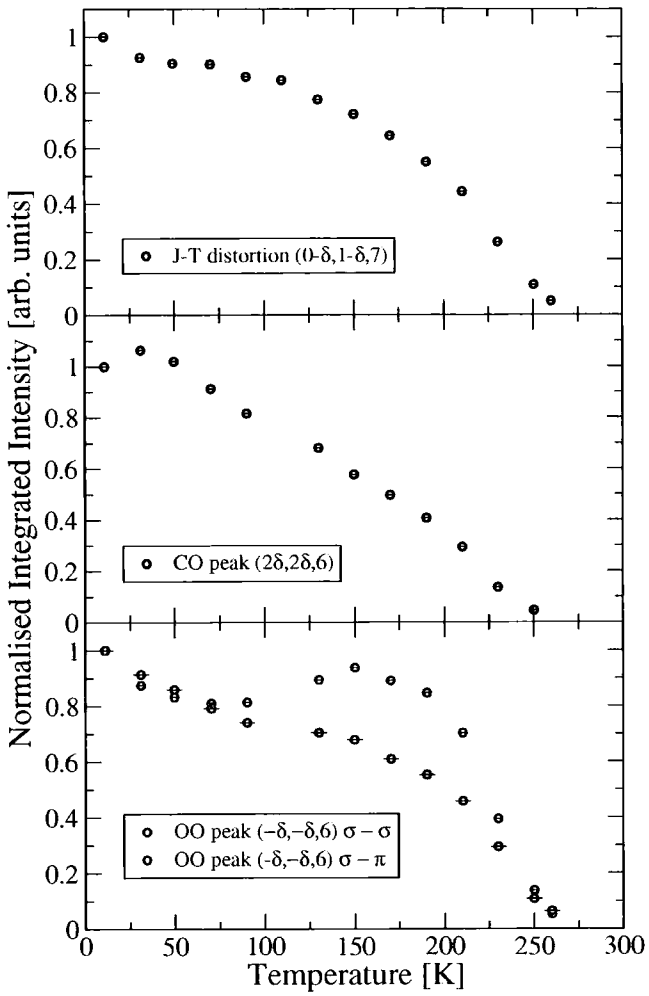

Figure 2.7: Intensity of the Jahn-Teller, charge order, and orbital order signals in $Nd_{0.25}Sr_{1.75}MnO_4$as a function of temperature. The charge and orbital order signals were measured on the Mn K edge (6.555 keV), the Jahn-Teller distortion was measured at 6.530 keV, just below the edge.

parameters. This is an indication that the orbital ordering is more fundamental than just being a by-product of the structural distortion and of strong magnetic orbital correlations.

Figure 2.8 shows the wavevector of the superlattice peaks with respect to temperature. As can be seen there is very little deviation until 220 K where critical fluctuations are observed. The sharp fall in the wavevector suggest that initially the critical fluctuations have a greater periodicity (although their correlation lengths would be less), and as they evolve into distinct ordering they reduce their incommensurate wavevector values. Similar to the $Nd_{0.33}Sr_{1.67}MnO_4$ sample the superlattice peaks do not seem to be commensurate. This suggests that the doping is not precisely 0.75, and the long range order is only weakly

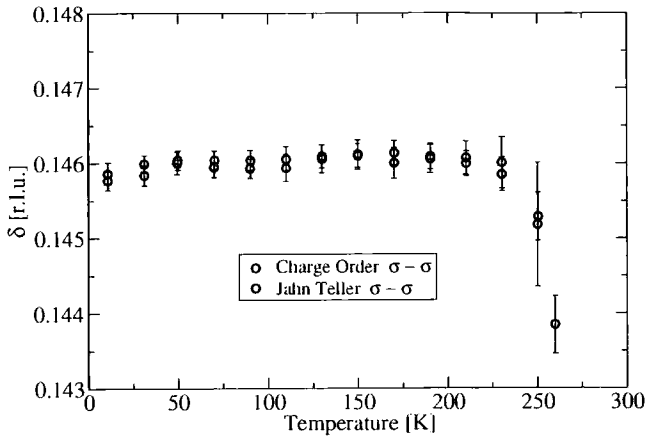

Figure 2.8: δ for the Jahn-Teller and charge order signals in $Nd_{0.25}Sr_{1.75}MnO_4$. The charge order signal was measured at 6.555 keV, the Jahn-Teller at an energy of 6.530 keV.

linked to the crystal lattice.

2.2.4 $Nd_{0.2}Sr_{1.8}MnO_4$

The $Nd_{0.2}Sr_{1.8}MnO_4$ sample appears markedly different from those with $x \leq 0.7$. Below 150 K the sample undergoes a structural phase transition, with an orthorhombic phase appearing in the sample. This is evident by a splitting in the principal Bragg peaks below this temperature (Fig. 2.9). Despite the orthorhombic phase becoming the dominant phase below 150 K, a small tetragonal component exists in the Bragg peak down to 10 K (Fig. 2.10). This is most likely in the form of small crystallographic domains that remain tetragonal in the majority orthorhombic phase.

Superlattice peaks were observed near to the expected Jahn-Teller and charge order wavevectors at low temperatures. These superlattice peaks were not split below the structural phase transition, suggesting that the long range ordering only exists in the tetragonal phase. As such, figure 2.10 shows the intensity of the superlattice peaks originating from the Jahn-Teller distortions and charge order *normalised to the tetragonal phase of the Bragg peak.* The absence of any significant change in intensity of either the charge order superlattice peak, or the Jahn-Teller distortion superlattice peak, around the structural phase transition, demonstrates the intensity of the superstructure ordering follows the intensity of the tetragonal phase. It seems indisputable therefore that these are co-existant.

A small proportion of the crystal remains tetragonal down to 10K, and is accompanied by the long range ordering. Figure 2.11 shows the charge order and Jahn-Teller distortion

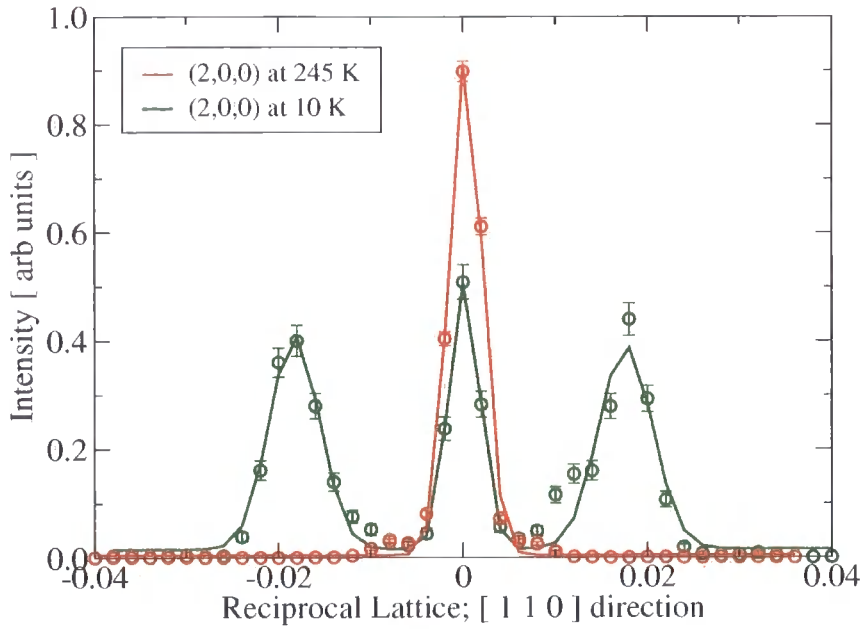

Figure 2.9: The (200) Bragg peak in $Nd_{0.2}Sr_{1.8}MnO_4$ at 10 K and 245 K. At 10 K the Bragg peak is split by an orthorhombic phase coexisting with the tetragonal phase. At 245 K the crystal is virtually entirely tetragonal. The solid lines correspond to a Gaussian fit.

superlattice peaks at 10K, both of which are fitted well with Lorentzian squared lineshapes. The position of these peaks indicates that the doping level is very close to $x = 0.8$. However the slight incommensurability suggests that at these doping levels the ordering is unbound to the crystal lattice.

Unlike the temperature dependences observed in the previous manganites, the charge ordering and structural distortion do not appear to decrease simultaneously. It appear that the intensity of the Jahn-Teller distortion remains high, whilst the charge order decreases. This result must be taken with some care, as these intensities have been calculated by normalising to the Bragg Peak. In addition T_{CO} and T_{JT} are concurrent.

2.3 Discussion

Moritomo *et al* [5] made resistivity and magnetic susceptibility measurements on single crystals of $La_{1-x}Sr_{1+x}MnO_4$ with $0.0 \leq x \leq 0.7$, and also perfomed electron diffraction on $La_{0.5}Sr_{1.5}MnO_4$. The resistivity measurements of $La_{0.5}Sr_{1.5}MnO_4$ and $La_{0.4}Sr_{1.4}MnO_4$ displayed a kink at ~ 230 K and ~ 250 K respectively, indicating a change in the electronic structure. This was the first indication that there might be some periodic arrangement

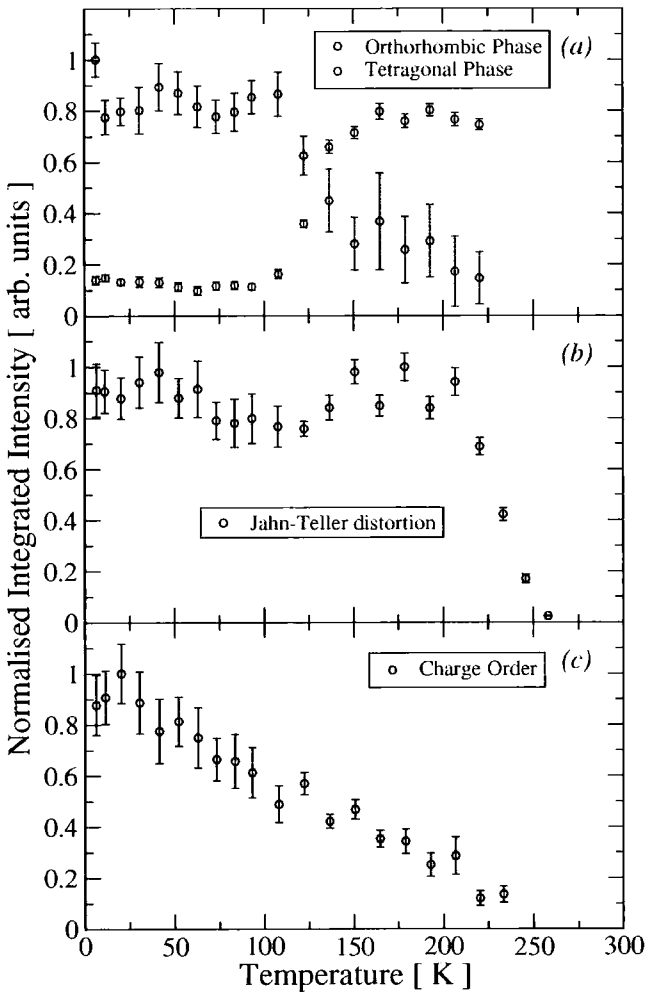

Figure 2.10: (*a*) The relative intensities of the Bragg peaks of the tetragonal and orthorhombic phases in $Nd_{0.2}Sr_{1.8}MnO_4$. (*b*) The integrated intensity of the $(2.125, -0.125, 0)$ Jahn-Teller satellite peak, and (*c*) the $(1.75, 0.25, 0)$ charge order peak, normalised to the intensity of the tetragonal phase Bragg peak.

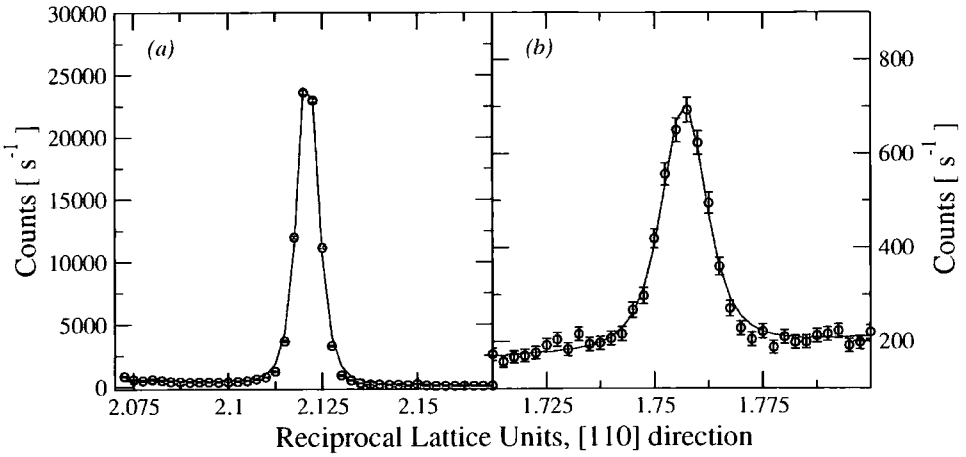

Figure 2.11: (*a*) The $(2.125, -0.125, 0)$ Jahn-Teller and (*b*)$(1.75, 0.25, 0)$ charge order superlattice peak, as measured in the [110] direction in $Nd_{0.2}Sr_{1.8}MnO_4$. The red lines are Lorentzian squared lineshapes fitted to the data which is normalised to a ring current of 200 mA.

of holes in the MnO_2 sheets. This was accompanied by a suppression of the Curie-Weiss like increase in the magnetic susceptibility of the samples at these doping levels at these temperatures. In addition electron diffraction revealed a fourfold modulation parallel to the [110] direction. Sternlieb *et al.* [7] followed Moritomo [5] with a elastic neutron diffraction study of $La_{0.5}Sr_{1.5}MnO_4$. Again superlattice reflections were observed with wavevector $\mathbf{q}_{co} = (\frac{1}{2}, \frac{1}{2}, 0)$ below $T_{CO} = 217$ K. The neutron diffraction was also able to observe the magnetic moments below $T_N = 110$ K.

Murakami *el al.*[9] then published details of an experiment at the Mn K edge looking at charge and orbital ordering from $La_{0.5}Sr_{1.5}MnO_4$. They observed superlattice peaks originating from charge ordering, and an anisotropy of the $4p$ electrons caused by underlying orbital ordering of the $3d$ electrons. The azimuthal dependence of the orbital order peak was measured, giving an indication of the anisotropy. There was no mention by Murakami of any structural distortions, nor any superlattice peaks at $(\frac{1}{4}, \frac{1}{4}, 0)$ that do not resonate. Their model of the charge order energy resonance was compiled from a room temperature absorption measurements of the spectra of Mn^{3+} (from $LaSrMnO_4$) and Mn^{4+}. The energy difference of 4 eV between the absorption spectra accurately modelled their observations. This requires a near integer difference in the charge disproportionation.

These papers, although not solely studying the half doped sample, tend to concentrate on the mid-doping level. There have been relatively few papers concentrating on the higher dopings. Nagai *et al.*[23] used electron diffraction to look at superlattice spots on the $x = 2/3$

and $x = 3/4$ doping levels. Only superlattice peaks at the Jahn-Teller type positions were observed, although they also observed a sinusoidal type modulation in the [110] direction with a periodicity of ~ 8 unit cells. This they attribute to a long range crystal distortion.

Nakao *et al.*[72] used resonant x-ray diffraction at the Mn K edge to look at the $x = 2/3$ and $x = 3/4$ doped samples, in which they observed resonant peaks both at the charge order and orbital order positions. Again there is no mention of any structural distortion accompanying the orbital ordering.

Very recently Larochelle *et al*[18] conducted a thorough study of $La_{1-x}Sr_{1+x}MnO_4$ with $0 \leq x < 0.7$. Their study revealed three separate phases, low ($x < 0.12$), intermediate ($0.12 \leq x < 0.45$) and high ($x \geq 0.45$). In the high phase they observe charge and orbital ordering and also observe that above $x = 0.5$ the superlattice becomes incommensurate.

It is clear from the results in this chapter that the situation is rather more complicated than suggested in the previous literature. Throughout the doping range studied there exists three distinct ordering phenomena. The first and possible the easiest to comprehend is the charge order. This has been observed in all samples except the $Nd_{0.33}Sr_{1.67}MnO_4$. There are still questions about the degree of real space ordering of the Mn ions. It was suggested by Murakami[9] that the resonances observed at $(\frac{1}{2},\frac{1}{2},0)$ positions could only be created by full integer ordering. However there have been theoretical studies [73] that claim that charge ordering cannot be integer ordering, by looking at the relative displacements of the Mn ions. This may be complicated by the fact that the charge ordering occurs on the entire MnO_6 octahedra, rather than entirely on the Mn ion. It is required that the charge ordering occurs in some form or another, in order to facilitate the orbital ordering. This orbital ordering appears to be accompanied by a structural distortion, namely a cooperative Jahn-Teller distortion. It appears obvious from the results in this chapter that both of these phenomena exist. They are observed to form entirely different signals. It is impossible that a pure orbital order signal would be observed with such intensity using high energy diffraction, and electron diffraction as seen by Nagai [23] and Moritomo [5]. Possibly the strongest indication is that the dual signals are seen with resonant diffraction. The structural distortion can be observed as a weak Bragg peak with an absorption edge, whereas the orbital induced signal can be seen resonating in both polarisation channels.

One of the major implications brought to light by the results in this chapter is the de-coupling of the long range order and the structural lattice. It was generally assumed that

the ordering would occur at commensurate wavevectors that would 'lock' into the crystal structure. Therefore, all the doped crystals near to the $x = 0.5$ doping level would arrange themselves as shown in Fig. 1.15. These results, especially from the higher doped $Nd_{0.2}Sr_{1.8}MnO_4$ suggest that this is not true. By contrast, it seems that the wavevector is probably almost entirely governed by the exact doping of the crystal rather than the crystal lattice.

2.4 Conclusions

A study of the effects of doping has been made of the single layered manganite series. Long range ordering has been observed throughout the doping range of $0.5 < x < 0.8$. These results have outlined the experiments that have been conducted on this series, and provide an introduction to the detection of long range order using x-ray diffraction.

There is a strong connection between the doping level and the wavevector of the superlattice peaks. In all of the samples the position of the Jahn-Teller and charge order peaks were $(h \pm \delta, k \pm \delta, l)$ and $(h \pm 2\delta, k \pm 2\delta, l)$ respectively, where $\delta = \frac{1-x}{2}$. This is strong evidence that the pattern of the long range order changes with doping level. As such the Mn in the MnO octahedra appear to remain nominally Mn^{3+} and Mn^{4+}. High energy diffraction proved an excellent tool for observing the Jahn-Teller distortions. A resonant enhancement of the charge ordering and induced orbital ordering improved the ability to observe these peaks at the Mn K edge. Resonant enhancements coupled with polarisation analysis are capable of probing the origins of the superlattice signals.

A complete understanding of the orbital and charge ordering is not possible at this absorption edge. Although it gives us some indication as to the processes happening in these materials, it is looking indirectly at the effects of the $3d$ electron band. What exactly is the connection between orbital ordering and Jahn-Teller distortions, and how integer-like is the charge ordering? We can only hope to answer by looking directly at the $3d$ electrons. We can do this by undertaking resonant scattering at the L edges. This will be investigated in Part II.

Chapter 3

Wigner, Stripe and Bi-Stripe Lattices in $La_{2-2x}Sr_{1+2x}Mn_2O_7$

This chapter describes a study of $La_{2-2x}Sr_{1+2x}Mn_2O_7$ in the stoichiometry range $0.55 < x < 0.7$ using high energy x-ray diffraction and resonant x-ray diffraction at the Mn K edge. As the Sr doping is varied the long range ordering changes from a checkerboard pattern Wigner lattice into a quasi bistripe and finally develops into a complete bistripe phase. Despite a proliferation of studies performed on the half doped bilayer, there have been relatively few papers written on samples with $x > 0.5$. This may be partially due to the difficulties in growing such crystals.

The same arguments that Goodenough [4] applied to $La_{0.5}Sr_{1.5}MnO_4$ can also be applied to the bilayer series. According to his theories it would be expected that in the $LaSr_2Mn_2O_7$ doped bilayer, charge and orbital ordering would occur, together with magnetic ordering. Indeed charge ordering has been observed in the half doped bilayer manganites, both using resonant and high energy diffraction. As will been shown in chapter 7, the AFM ordering of these crystals has been observed not only using neutron diffraction, but also using soft x-ray resonant diffraction. Despite a large number of studies using a variety of techniques the complicated phase diagram of the bilayer manganite series is still under review. Initially Dho *et al.* [33] produced a phase diagram (Fig. 1.12) that had a charge ordered phase over a large area of the doping range, from $x = 0.475$ up to at least $x = 0.75$. Dho *et al.* [33] also suggested a collapse of the charge ordering below T_N followed by a re-entrant effect at ~50 K. A later phase diagram proposed by Qui *et al.* [32] (Fig. 1.11) shows a breakdown in both the charge and magnetic long range order, which appears to be unique to the bilayer crystals in the phase diagrams of the manganites. This chapter provides evidence of the existence of charge ordering persisting at least up to $x = 0.7$, with no evidence of a breakdown in

electron long range correlations.

The $x = 0.475$ and 0.5 samples have already been studied by the Wilkins *et al* [35]. Charge ordering in the half doped bilayer was observed at $(\frac{1}{2},\frac{1}{2},0)$, and cooperative Jahn-Teller distortions at $(\frac{1}{4},\frac{1}{4},0)$. These distortion and charge order signals have unusual temperature dependences compared to the $La_{1-x}Sr_{1+x}MnO_4$ series. Instead of the superlattice peaks appearing at $T_{CO/JT}$ and remaining at a roughly constant intensity to low temperatures, they appear at $T_{CO/JT}$ and then *decrease* in intensity again at T_N. It appears that the onset of the antiferromagnetic ordering between the *ab* planes has the effect of quenching the long range order within the *ab* plane.

As will be shown, different behaviour is observed as the doping of Sr is increased. Although the temperature dependence is similar in the $x = 0.6$ to the half doped samples, the wavevector at which the superlattice peaks appear is significantly different, and indeed shows a striking variation around T_N. The $x = 0.7$ bilayer has no AFM phase, and as such there are significant differences in the temperature dependence of the electron ordering. A non Wigner-lattice bistripe phase is proposed in the $x = 0.6$ samples which takes into account the wavevector of these superlattice peaks and the azimuthal dependence of the JT/OO ordering. Very recently there has been similar work published by Luo *et al.* [56]. They have undertaken electron microscopy studies, showing a pattern of superlattice reflections due to the crystal distortion, and used the position of the superlattice reflections to produce an orbital lattice for the $x = 0.6$ identical to that suggested in this chapter.

Further resonant scattering experimental results suggest that a full bistripe phase is developed for samples with $x = 0.7$. The absence of an AFM phase produces a temperature dependence of the superlattice order peaks that is similar to that observed in the $La_{1-x}Sr_{1+x}MnO_4$ series.

3.1 Experimental Methods and Results

High quality single crystals of $La_{2-2x}Sr_{1+2x}Mn_2O_7$ were grown using the floating zone method at the University of Oxford [74]. These crystals were pre-aligned using an in-house Cu rotating anode x-ray generator [64]. Synchrotron experiments were performed using high energy (100 keV) x-ray diffraction and resonant x-ray scattering at the Mn K edge. High energy single crystal x-ray diffraction was performed at the BW5 beamline at HASYLAB, Hamburg [66]. The beamline is equipped with a wiggler insertion device, and a water cooled

Cu filter to produce x-rays in the spectral range 60-150 keV. The analyser and monochromator were matched SiGe graded crystals to provide a resolution matched to the sample rocking curve width. In this experiment, the incident x-ray beam had a beamsize of 1×1 mm, and an energy of 100 keV. Photon detection was provided by a solid state detector, energy gated through a single channel analyser in order to remove higher harmonics. The samples were mounted on a the cold finger on an APD displex cryofurnace capable of a temperature in the range 10 K$< T <$ 400 K. The orientation of the sample was such that the c axis was parallel to the incident beam, and the ab plane perpendicular.

Resonant x-ray diffraction was undertaken at the UK CRG beamline, BM28 at the ESRF [75]. An incident beam energy in the region of 6.555 keV (Mn K edge) was provided by a double bounce Si(111) water cooled monochromator, with harmonic rejection mirrors. Crystals pre-cleaved with the c axis surface normal were mounted with the c axis along the scattering vector, allowing access to the $(00l)$ type reflections. The sample environment was similar to that at BW5 with a closed cycle cryostat held in a Eulerian cradle. A Cu (220) single crystal was used for polarisation analysis which at 6.555 keV has a scattering vector 47° from the incident beam. This allows a leak-through of $\sim 3.5\%$ between the two polarisation channels.

The results in the following three sections are organised by doping stoichiometry, starting with $x = 0.55$, and increasing through the chapter to $x = 0.7$.

3.1.1 $x = 0.55$

The sample was mounted on the high energy beamline. Upon cooling the sample below the charge ordering temperature (T_{CO}) superlattice peaks appeared at wavevectors $(\frac{1}{4},\frac{1}{4},0)$ and $(\frac{1}{2},\frac{1}{2},0)$. These superlattice peaks, arise from Jahn-Teller (JT) structural distortions and real space charge ordering (CO). They were found regularly throughout reciprocal space with the JT peaks of intensity ~15000 counts per second, and the CO peaks were in the region of ten times weaker than the JT peaks. In this chapter, a nomenclature will be adopted whereby the JT peak occurs at $(h \pm \delta, k \pm \delta, l)$ positions and the CO peak at $(h \pm 2\delta, k \pm 2\delta, l)$. In this case with $x = 0.55$ and $\delta = 0.25$.

The peak shapes from both the JT and CO signals displayed a Gaussian lineshape (Fig. 3.1). This suggests that the experimental resolution was limited by the instrument, and not giving a true indication of the sample. Indeed a measurement of the $(2,0,0)$ Bragg peak

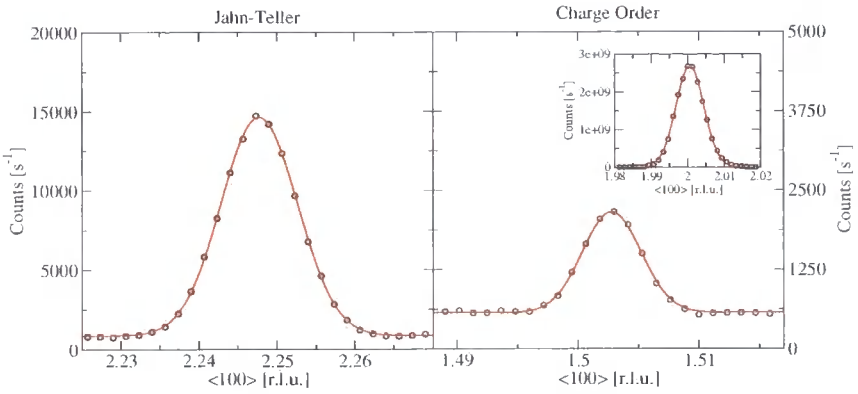

Figure 3.1: The line shapes of (left) the Jahn-Teller $(2-\delta, -\delta, 0)$ and (right) the charge order $(2-2\delta, -2\delta, 0)$ peaks taken at 170 K measured from the $x = 0.55$ sample in the [100] direction in $La_{0.9}Sr_{2.1}Mn_2O_7$ ($x = 0.55$). The inset shows the (2,0,0) Bragg peak. The solid lines show Gaussian fits to the data. Errors are within the size of the symbols.

shows a similar width and shape. The peaks had a far greater width in the [00l] direction. This is attributed to the two-dimensional nature of the crystal structure.

The $x = 0.55$ sample was cooled to the base temperature of 12 K, and measurements were taken on the JT and CO peaks throughout a warming cycle. At each temperature thermal equilibrium was achieved before the intensity and the width were measured. In order to accurately measure the commensurate wavevector, the position of two satellite peaks opposite each other with respect to a Bragg peak was determined. No significant change of the position (Fig. 3.2*a*) or peak width was detected throughout the temperature range. The measured integrated intensity displayed a significant increase at ~120 K and then reached a maximum at T_N (180 K) (Fig. 3.2*b*). The intensity of the peaks then fell sharply with increasing temperature, until reaching background at 220 K. This behaviour is extremely similar to that observed in the $x = 0.475$ and 0.5 compounds [35]. A slight increase in the transition temperatures (T_N, T_{CO}) of about 10 K was observed compared to that found in the $x = 0.5$ sample [35].

3.1.2 $x = 0.575$

The only satellite peaks detected by high energy x-ray diffraction in $La_{0.85}Sr_{2.15}Mn_2O_7$ were located at $(h \pm \delta, k \pm \delta, l)$ positions. These peaks, associated with JT distortions, were significantly weaker than those found in the $x = 0.55$ sample. Comparing the relative intensities of the peak strength at $\pm 2\delta$ with that at $\pm\delta$ in the $x = 0.55$ system, a signal of similar proportions in the $x = 0.575$ sample would not have been detected. As such it is

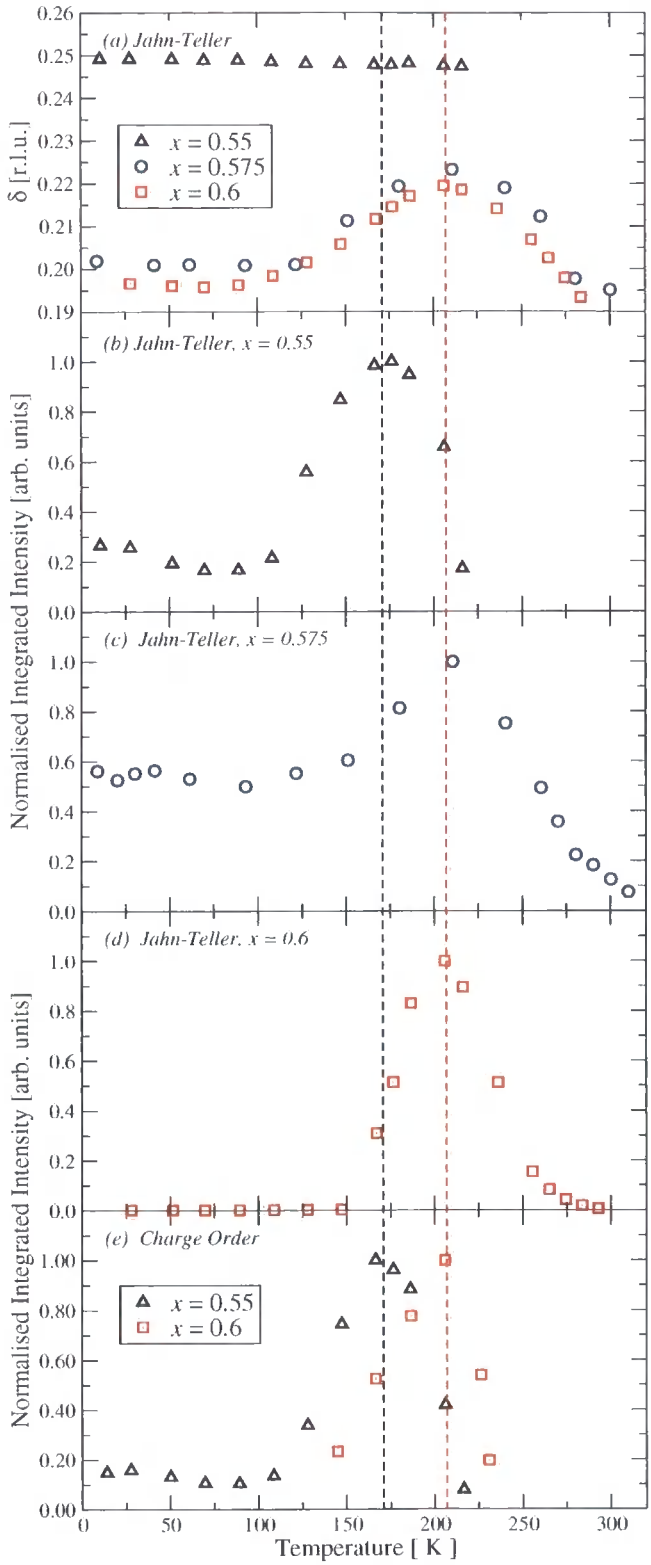

Figure 3.2: *Top panel:* Measurement of the wavevector of the Jahn-Teller distortion peak at $(h \pm \delta, k \pm \delta, l)$ for the doping levels $x = 0.55$ (black triangles), $x = 0.575$ (blue circles), and $x = 0.6$ (red squares) as a function of temperature upon warming from base temperature. *Middle panels:* Integrated intensity of the Jahn-Teller peak for the $x = 0.55, 0.575, 0.6$ (as above). *Lower panel:* Intensity of the charge order in the $x = 0.55$ (black triangles) and $x = 0.6$ (red squares) doping levels. The maximum intensity of the superlattice peaks corresponding to T_N in the samples is shown by the vertical dashed lines.

likely that charge ordering does exist, but it is too weak to detect. The peak at $(2-\delta, -\delta, 0)$ was much broader in the $x = 0.575$ sample than in the $x = 0.55$ sample, and as such, the measurements were not limited by the instrumental resolution. The shape of the peak was Lorentzian squared in the high resolution [100] direction. This suggests that the resolution effects are negligible to the width of the peak, despite this we observed no significant variation of the peak width with temperature. Unlike the $x = 0.55$ sample the Jahn-Teller signal in the $x = 0.575$ sample does display a significant variation in the wavevector, δ (Fig. 3.2*a*). This variation follows a strikingly similar pattern to the variation of the intensity of the JT distortion as a function of temperature. Initially at low temperature $\delta \approx 0.202 \pm 0.002$, however on warming, and with increasing intensity, this value reaches $\delta = 0.222 \pm 0.002$. As the temperature is further increased above T_N towards T_{CO}, δ reduces back to below $\delta = 0.200$.

3.1.3 $x = 0.60$

Satellite peaks were found using high energy x-ray diffraction at both $(h \pm \delta, k \pm \delta, l)$ and $(h \pm 2\delta, k \pm 2\delta, l)$ in the $x = 0.60$ sample (Fig. 3.3). The Jahn-Teller peak is significantly stronger than that occurring in either the $x = 0.55$ or $x = 0.575$ doped samples. The charge order peak however, was some 40 times lower in intensity than the Jahn-Teller peak, compared to only 10 times lower in the $x = 0.55$ sample. As with the $x = 0.575$ sample the peaks are not resolution limited and they can be fitted accurately with a Lorentzian squared lineshape. Similar to the $x = 0.575$ sample there is a significant variation of the incommensurate wavevector, δ, with the intensity (Fig. 3.2*a*, *b*), and this is present also in the charge order peaks.

Resonant diffraction at the Mn K edge of the $x = 0.6$ bilayer sample was performed specifically to look at the anisotropy of the structural distortion and concomitant orbital order. These results rely on the $3d$ electron orbitals inducing an anisotropic effect to the $4p$ electron orbitals. The resonant signal of the $(\delta, \delta, 10)$ was collected, which was found to resonate in both the $\sigma - \sigma$ and $\sigma - \pi$ channels (Fig. 3.4). These resonances occurred at the same energy as the absorption edge measured at the (0,0,10) Bragg peak, and display a Lorentzian lineshape.

As expected these resonances can be fitted with a Lorentzian lineshape, typical of a dipole transition [76]. This resonant energy is identical to that seen in $La_{1-x}Ca_xMnO_3$ by XANES

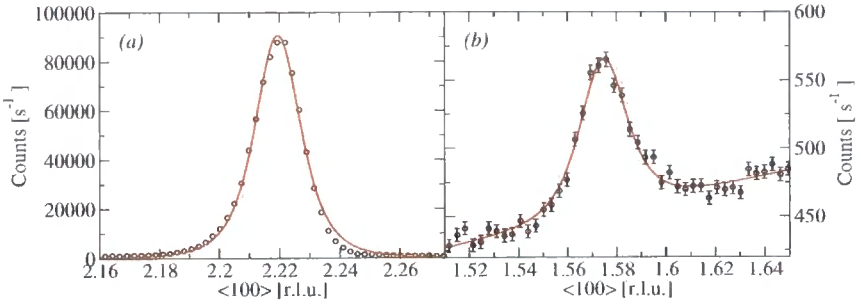

Figure 3.3: Scans of the (a) $(2+\delta, 0-\delta, 0)$ Jahn-Teller superlattice peak, and (b) the $(2-2\delta, -2\delta, 0)$ charge order superlattice peak, in $La_{0.8}Sr_{2.2}Mn_2O_7$ ($x = 0.6$) sample at 210 K measured in the [h00] direction. Solid lines are fits to the data using Lorentzian squared lineshapes and a linear background. Data normalised to a ring current of 120 mA.

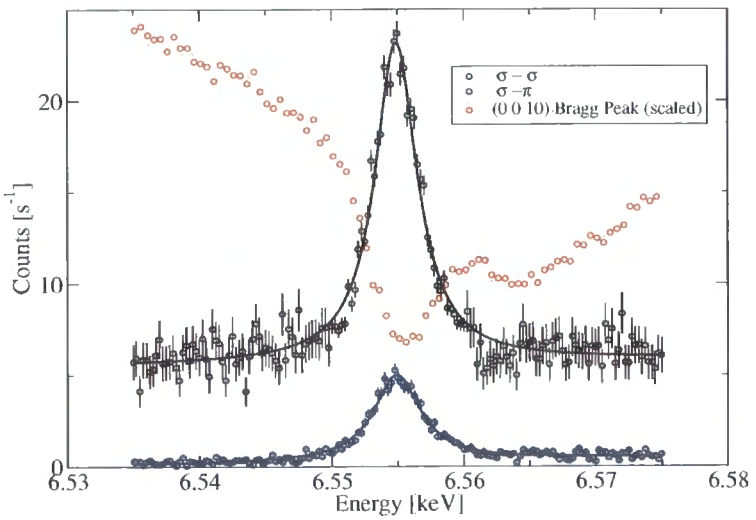

Figure 3.4: Energy dependence at fixed Q of $(\delta, \delta, 10)$ in the $\sigma - \pi$ channel (blue), $\sigma - \sigma$ channel (black) in $La_{0.8}Sr_{2.2}Mn_2O_7$ ($x = 0.6$). The energy dependence of the (0,0,10) Bragg peak is shown for comparison.

by Bridges *et al.* [77], who attribute this main peak to a dipole transition. Bridges *et al.* also observed weak pre-edge features $\sim$ 15 eV below this which could be due either to forbidden quadrupole transition or hybridisation of the $4p$ level. We did not observe these peaks by diffraction in any of the bilayer samples.

Azimuthal Dependence

Due to the anisotropy of the shape of the probability density of the electron orbitals, it is expected that the scattering from the orbital ordering will vary as the sample is rotated around the scattering vector. This is known as an azimuthal dependence. By modelling the expected variation and then making a comparison with experimental data, it is possible to get an idea of the nature and origin of the orbital ordering pattern.

The azimuthal angle dependence was collected by measuring the integrated intensity of the superlattice peak in each polarisation channel for a regular set of azimuthal angles. Due to the simultaneous presence of a signal in both polarisation channels we have calculated the Stokes parameter of the scattered x-ray beam; defined by

$$P_1 \text{ (Stokes parameter)} = \frac{I_{\sigma-\sigma} - I_{\sigma-\pi}}{I_{\sigma-\sigma} + I_{\sigma-\pi}} \tag{3.1}$$

This has the effect of self-normalisation and removes any effect of angular changes in the size of the geometric beam footprint. The integrated intensity of the signal in either channel was measured through a scan in θ of the polarisation analyser crystal. It should be noted that the Jahn-Teller structural distortion and the orbital ordering have the same symmetry around the Mn^{3+} ion. As such this azimuthal dependence is valid for both phenomena, independent of any sensitivity arguments.

A model of the charge and orbital order was constructed for the high doped phase (Fig. 3.5). This model was made in such a way to agree with the fivefold periodicity. Using this model the azimuthal dependence has been calculated by using the Anisotropy of the Tensor of Susceptibility (ATS). The calculations for performing this simulation are outlined in the Appendix.

The azimuthal dependence of the $(\delta,\delta,10)$ superlattice peak is displayed in Figure 3.6, together with the simulation. The experimentally determined Stokes parameter does not fall to -1 as predicted by the ATS simulation. This is due to the $\sigma - \sigma$ signal being much larger than the $\sigma - \pi$ and so even a relatively small $\sigma - \sigma$ signal dramatically increases the

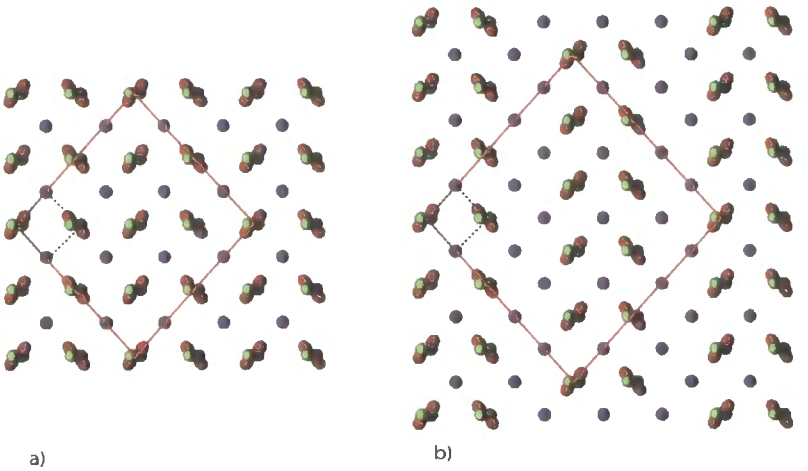

Figure 3.5: The accepted orbital pattering in the $x = 0.5$ doped bilayer (left), compared to the proposed orbital pattering in the higher doped $x = 0.6$ bilayer (right). This orbital pattern has a fivefold increase in the chemical unit cell in the [110] direction compared to the fourfold increase found in the $x = 0.5$ sample.

parameter value. This small $\sigma - \sigma$ signal is probably due to small amount of background scatter present in this channel. Overall though, there is a general agreement between the fit and the data, suggesting a correct model of the orbital anisotropy has been used. The total angular range of ϕ was limited by a restriction of the movement of the motor.

3.1.4 $x = 0.7$

$La_{0.6}Sr_{2.4}Mn_2O_7$ lies in a different part of the phase diagram than the mid doped bilayer crystals. Although there is some question about the presence of long range electron ordering, it has been shown to have no low temperature AFM magnetic phase. As such, if any long range electron ordering does exist, it would not be expected to decrease in intensity at low temperature as has been seen in the previous sections.

The sample of $La_{0.6}Sr_{2.4}Mn_2O_7$was grown using the same method as the lower doped crystals. Experiments were performed solely at the resonant scattering beamline BM28. The sample was mounted with the *c* axis vertical, and the *ab* plane horizontal. The scattering geometry was vertical, however a rotation of the sample out of the scattering plane allowed sufficient access to superlattice peaks near the (001) axis. The sample was mounted in this geometry as it was formed as a very thin plate.

Following previous experience of the bilayer samples, superlattice peaks were searched for around the (0,0,10) and (1,0,5) superlattice peaks. Figure 3.7 shows a [110] scan out

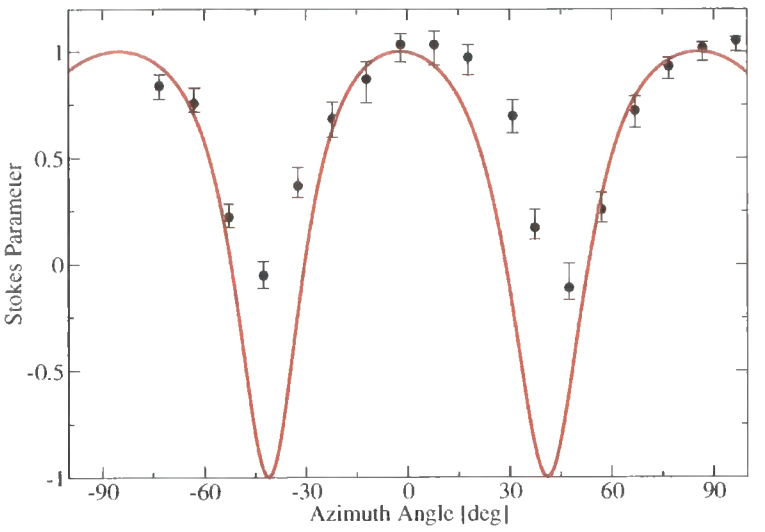

Figure 3.6: The azimuthal dependence of the Stokes parameter (equation 3.1), calculated using the structure proposed in Figure 3.5 (solid red line), with the experimentally determined intensity of orbital order signal measured in the $\sigma - \sigma$ and $\sigma - \pi$ channels (black dots).

from the (0,0,10) Bragg peak at 10 K. This clearly shows a peak at both (0.18,0.18,0) and (0.36,0.36,0), near where the orbital and charge order peaks would be expected. The lower axes on this figure show the energy dependences of these peaks in the $\sigma \rightarrow \sigma$ and $\sigma \rightarrow \pi$ channels. As has been observed in the $x = 0.6$ samples, the orbital order signal is seen to resonate in both channels, and the charge order signal is only seen in the $\sigma \rightarrow \sigma$ channel, where it too resonates at the Mn K edge.

By comparison, Figure 3.8 shows an identical scan in the [110] direction through the (1,0,5) Bragg peak. In this scan there is a very sharp feature at (1.18,0.18,5), and interestingly no signal at the charge order position. Again, as previously observed, the Jahn-Teller signal shows an absorption edge at the Mn K edge. The JT peak is also considerably weaker than observed in previous samples, indeed it is weaker than the measured orbital order signal. This may not be a true measurement, as the considerable geometrical change necessary to access this reflection will mean a different part of the crystal is illuminated. This very low intensity could explain the apparent absence of the charge order peak around the (1,0,5) Bragg peak.

The magnetic phase boundary between $La_{0.8}Sr_{2.2}Mn_2O_7$ and $La_{0.6}Sr_{2.4}Mn_2O_7$ samples raises the possibility of the intensity of the superlattice peaks showing a completely different temperature dependence than that seen in samples where $x \leq 0.6$. Figure 3.9 shows that there is no reduction in the intensity of either the charge or orbital order signals at any point

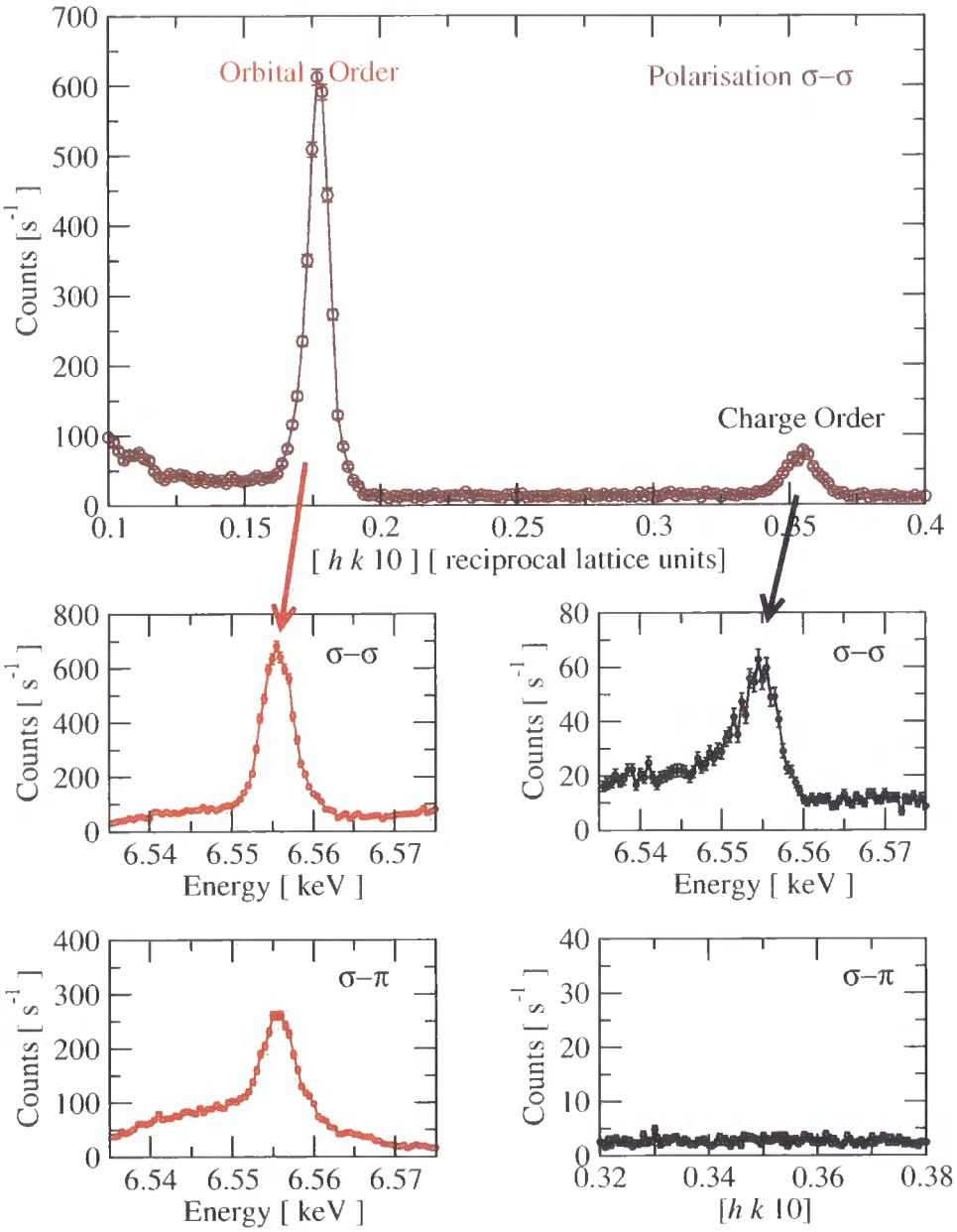

Figure 3.7: (top) A scan in the [110] direction from the (0 0 10) Bragg peak in $La_{0.6}Sr_{2.4}Mn_2O_7$ at 10 K showing the orbital order and charge order superlattice peaks. (lower) The energy dependence of these peaks in each polarisation channel is shown. Note there is no charge order peak in the $\sigma - \pi$ channel. All data normalised to a ring current of 200 mA.

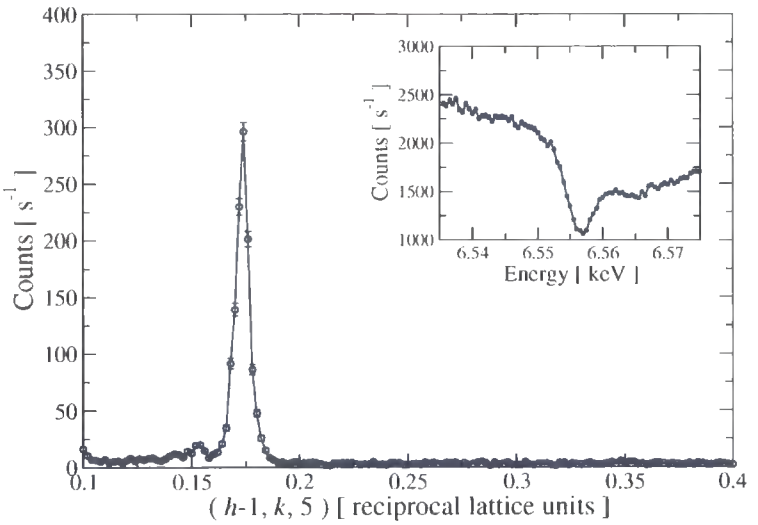

Figure 3.8: A scan in the [110] direction from the (1,0,5) Bragg peak showing the Jahn-Teller superlattice peak. The energy dependence of this peak is shown in the inset. The data is normalised to a ring current of 200 mA.

during cooling. The Jahn-Teller signal shows a strange hybrid dependence, where there is a very small reduction of intensity below 250 K, but only by 20%. These results are normalised with respect to the nearest Bragg peak (for the CO and OO peaks, this is the (0,0,10), and for the JT peak the (1,0,5)).

The temperature dependence of the charge and orbital order show very similar characteristics. The intensity increases steadily upon cooling from appearing at 320 K until 50 K, where the intensity remains constant as the temperature is lowered further. By comparison the temperature dependence of the Jahn-Teller peak increases rapidly from 330 K until 250 K, where the intensity then decreases slowly until it is 80% of the peak value at 150 K, it then increases in intensity slowly as the temperature is reduced further.

The existence of these superlattice peaks demonstrates unequivocally that there exists long range electronic order in the $x = 0.70$ sample. The absence of a quenching effect on the charge and orbital order signals reinforce the evidence that there is no AFM phase. The wavevectors of these peaks reflect the absence of any change in magnetic state, as they stay constant throughout the temperature region (Fig. 3.10). There is a small decrease in the wavevectors as the temperature approaches $T_{CO/OO/JT}$, however this is much smaller than the observed change in the $x = 0.6$ and $x = 0.575$ samples. There is also no change in the wavevector of the Jahn-Teller peak corresponding to the slight reduction in intensity.

The increase in the doping level changes the ordering pattern, both of the charge and

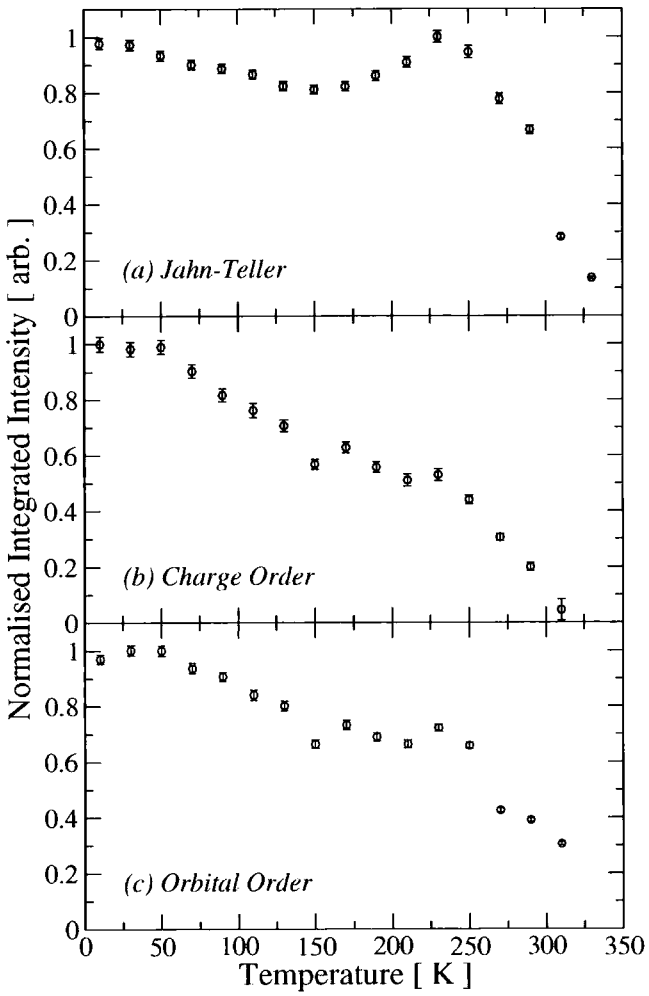

Figure 3.9: Temperature dependence of the intensity of the Jahn-Teller, charge order and orbital order superlattice peaks in $La_{0.6}Sr_{2.4}Mn_2O_7$.

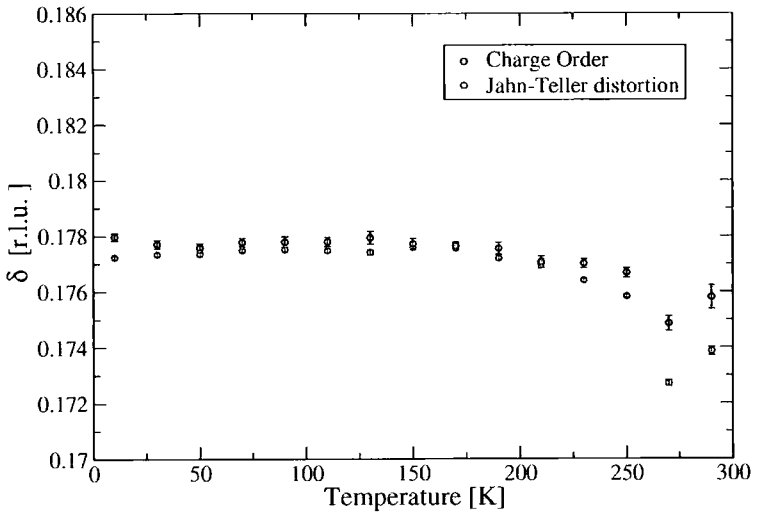

Figure 3.10: Variation of the wavevector δ, for the charge order and Jahn-Teller distortion peaks in $La_{0.6}Sr_{2.4}Mn_2O_7$as a function of temperature.

of the orbitals. The doping of $La_{0.6}Sr_{2.4}Mn_2O_7$ is close to a 2/3 Sr doped material, which one may expect to be particularly stable. If the quasi-bistripe orbital model predicted for the $x = 0.6$ is extended, then the orbital pattern will develop into either a full bistripe or Wigner lattice model. These models are both shown in Figure 3.11.

These two order models can be differentiated between by studying the azimuthal dependences of the orbital order peak. As in the $x = 0.6$ the Stokes parameter of the peak is used as this removes any influence of beam footprint and scattering geometry. Figure 3.11 shows azimuthal simulations for both of these models for the $(\delta, \delta, 10)$ orbital peak in $La_{0.6}Sr_{2.4}Mn_2O_7$. It is evident that at this wavevector the peaks have a very similar azimuthal dependence. Ideally a superlattice peak further from the [001] would have been used, as this would have a greater variation in the two azimuth dependences, however the experiment was restricted by geometric limitations. Figure 3.13 shows the data mapped onto the bistripe simulation. This simulation fits the data significantly better at the two minima at 90° and 270° than the Wigner lattice model. The azimuthal data was taken in much smaller steps than the $x = 0.6$ sample, and in addition the diffractometer was re-orientated in order to collect data over the full 360° without the removal of the sample or the cryostat. The absence of data points at certain parts of the rotation is due to signal contamination by multiple scattering. This is most unfortunate around 180°, as this area shows the greatest difference between the two simulations.

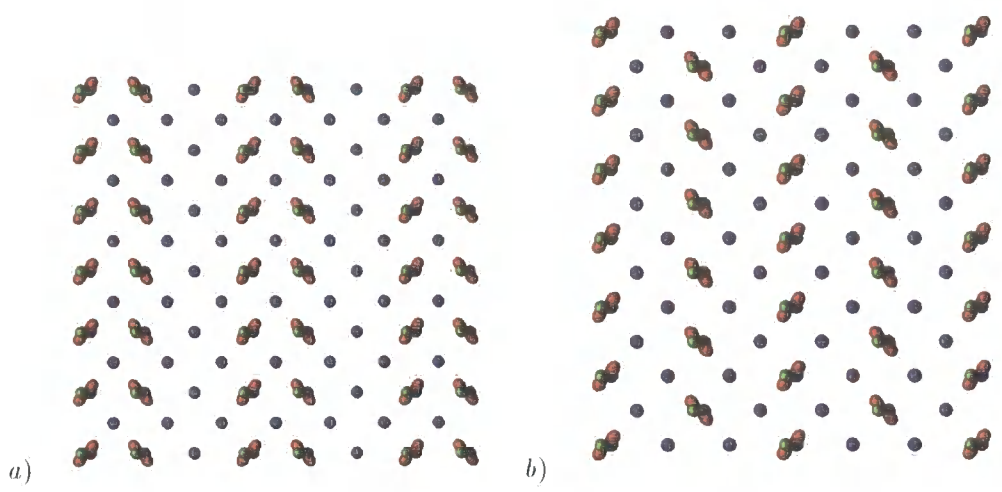

Figure 3.11: Two possible ordering patterns for $La_{0.6}Sr_{2.4}Mn_2O_7$. *a*) The bistripe model and *b*) the Wigner lattice model. Blue spheres represent the Mn^{4+} and red and green lobes represent the Mn^{3+} ions.

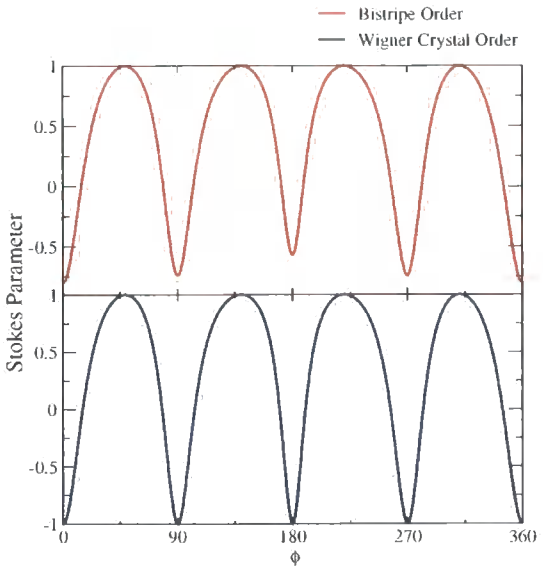

Figure 3.12: Modelled Stokes parameter for the two possible orderings for $La_{0.6}Sr_{2.4}Mn_2O_7$. The upper panel shows the predicted azimuthal dependence for bistripe model, and the lower panel shows the same for the Wigner lattice model (Fig. 3.11)

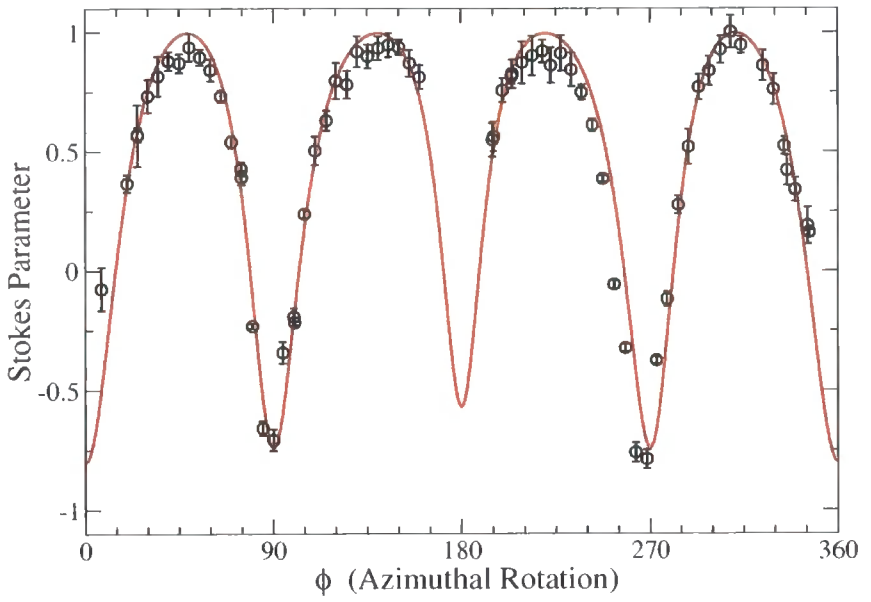

Figure 3.13: Azimuthal dependence of the induced orbital order signal in $La_{0.6}Sr_{2.4}Mn_2O_7$ with the projected azimuthal dependence for the bistripe order model (Fig. 3.11)

3.2 Discussion

The distinct change in the behaviour of the bilayer suggests that there are a number of 'sub' phases that exists at different doping regions in the material, similar to that observed for $Nd_{1-x}Sr_{1+x}MnO_4$. There is the previously described checkerboard phase, encompassing the range ($0.475 \leq x \leq 0.55$), then the quasi-bistripe phase ($0.575 \leq x \lesssim 0.65$). Finally there is the fully bistripe phase where $x \gtrsim 0.65$. These three different phases display considerably different behaviour. The most obvious change is the magnetic phase boundary between the AFM quasi-bistripe phase and the paramagnetic bistripe phase.

Substantial discussion was generated after the original discovery of the charge ordered systems in the $ABMnO_3$ compounds, as to the relative merits of the bistripe [78] and Wigner [19] lattice models [79, 80, 81]. These models provide solutions to the orbital ordering of compounds where the ratio of nominally Mn^{3+} and Mn^{4+} is not 1:1. The lowest stable bistripe and Wigner lattice models have $x = 0.66$, with an orbital order propagation vector of $(\frac{1}{3}, 0, 0)$. The samples studied show two separate higher doping phases, the higher of these two phases corresponds to this stable order pattern. The lower phase lies midway between the stable checkerboard and this second phase. A possible model for this mid phase has been outlined (Fig. 3.5), which offers similarities to both the bistripe and Wigner crystal model. The unusual aspect of this model is the uneven pattern of the Mn^{4+} stripes. This asymmetric

aspect is necessary to generate the five-fold increase in the chemical unit cell required by the position of the satellite peaks. This quasi-bistripe order has also been proposed by Luo *et al.* [56], who looked at the same stoichiometry using electron diffraction. They created a model in response to the position of the superlattice peaks observed in the diffraction pattern. In addition they proposed the existence of a bistripe system for higher doped bilayers, however do not report any experimental studies on these systems. It should be remembered at this point that these models are all over-simplistic. As described in Chapter 2, it is not expected that the valence electrons on the Mn reside entirely on the Mn ion, but rather are spread over the MnO_6 octahedra.

The behaviour of the $x = 0.55$ sample is very similar to that of the lower doping levels. This can be seen by comparing the results for the $x = 0.55$ sample with those reported by Wilkins *et al.* [35]. The interaction between the AFM order below T_N and the orbital and charge ordering appears to be unique to the bilayer manganites. The onset of the ferromagnetic planes ordered antiferromagnetically simultaneously reduces the intensity of the in-plane ordering. It was originally thought that the CO completely collapsed [33] and then was re-entrant again at lower temperatures. This collapse now appears to be incomplete and any increase at low temperatures is very small. Similar behaviour was also seen in $x = 0.475$ and 0.5 [35]. It has been suggested that a spin freezing occurs below 100 K [34], which corresponds to the minimum in the charge order reflection intensity. This suggests that there are spin fluctuations occurring below T_N which gradually slow to form a spin-frozen state at 100 K.

The maximum value of the JT superlattice peaks corresponding to T_N changes discretely as the Sr doping increases. Figure 3.2 shows vertical lines displaying an increase of 30 K of T_N in the checkerboard and quasi-bistripe phases. Concomitant to this increase in T_N, T_{CO} is also seen to increase as the doping increases. Wilkins *et al.* [35] measured T_{CO} of $LaSr_2Mn_2O_7$ to be 220 K, whereas Figure 3.2 shows T_{CO} of $La_{0.8}Sr_{2.2}Mn_2O_7$ is 310 K, and Figure 3.9 shows $La_{0.6}Sr_{2.4}Mn_2O_7$ to have a T_{CO} of 330 K. The value of T_{CO} does not seem to be related to the correlation length of the ordering that is formed below T_{CO}, but rather to be more directly related to the La,Sr ratio. The confirmation of this effect in the AFM phase on the long range electron order is provided by the temperature dependence of the electron order in the $La_{0.6}Sr_{2.4}Mn_2O_7$ sample. This shows no decrease in intensity, unlike that observed in the checkerboard and quasi-bistripe phases.

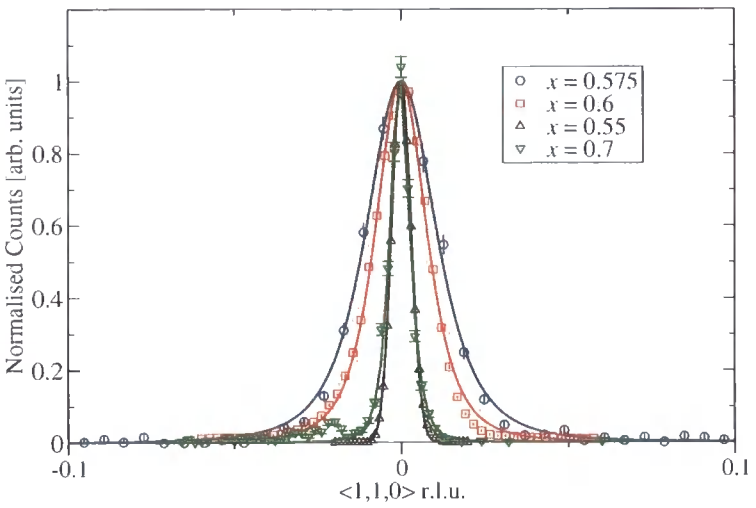

Figure 3.14: Comparison of the Jahn-Teller superlattice peaks in the $x = 0.55, 0.575, 0.60, 0.7$ samples. The solid line shows a Lorentzian squared fit for the $x = 0.575$ and 0.60 samples, and a Gaussian fit for the $x = 0.55$ sample (Section 3.1.1). The intensities of the peaks have been normalised, and the centre of the fits set to zero. All the linear backgrounds have been removed after fitting the data.

The enhanced stability of the JT distorted phase was shown before by Campbell *et al.* [55], however no explanation was given for this. Possible schematics of the orbital and charge ordering in the higher doped bilayer manganites were shown, but this does not explain why $T_{CO(=JT=OO)}$ increases as the Sr level increases. It would perhaps be more easily explained if the half doped manganite had the highest T_{CO} as this could be explained by the stable checkerboard ordering. The correlation lengths of the ordering appear to be unrelated to the value of T_{CO}. The correlation lengths of the ordering, calculated from the width of the JT superlattice peak, show a high correlation length for the half doped checkerboard and the bistripe phase, and a much lower correlation length for the quasi-bistripe phase (Tab. 3.1 and Fig. 3.14). This suggests that the ordering temperature is unrelated to the form that the ordering takes.

Unlike previous reports [82, 17] a smooth transition of the wavevector with doping level is not observed. It has been suggested that δ follows the trend $\delta = \frac{(1-x)}{2}$, however discrete changes in the wavevector is seen, shown graphically in Figure 3.15. It appears more likely that the value of δ varies such that is in the nearest stable commensurate position. This is contrary to that observed in the $La_{1-x}Sr_{1+x}MnO_4$ manganites, where the commensurability seemed entirely determined by the the dopant stoichiometry. In addition the wavevector is not stable throughout the temperature range of the charge ordered regime in the case of the

x	Position at 10 K (δ)	Correlation Length (10^{-2} Å^{-1})
0.475[1]	0.250 ± 0.002	3300±50
0.5[1]	0.250 ± 0.002	3300 ± 50
0.55	0.250 ± 0.002	$\leq 1000 \pm 20$
0.575	0.202 ± 0.002	270 ± 10
0.6	0.197 ± 0.002	450 ± 10
0.7	0.175 ± 0.002	1000 ± 20

Table 3.1: Position and correlation lengths of the Jahn-Teller superlattice peaks with respect to the doping of the sample. Correlation lengths were measured at peak intensity and the wavevector, δ was taken at base temperature.

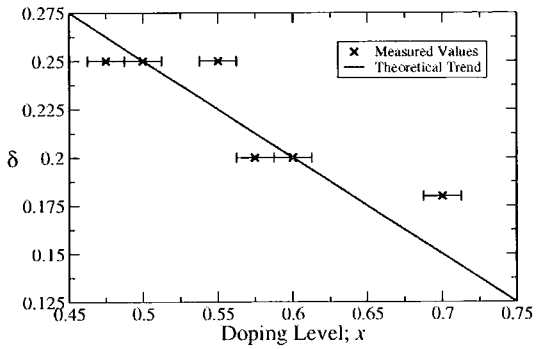

Figure 3.15: A comparison between the measured value of the wavevector, δ for each doping level with the theoretical trend generated through the equation $\delta = \frac{1-x}{2}$.

$x = 0.575$ and $x = 0.6$ samples.

The wavevector of the superlattice peaks in the quasi-bilayer phase is particularly interesting, as it varies significantly with a change of temperature. This variation appears to be directly linked to the intensity of the superlattice reflections. The change in wavevector suggests that the ordering changes within a particular crystal.

From base temperature, increasing the temperature of the sample alters both the intensity and the incommensurate wavevector of the charge ordered peaks of the high doped phase. The wavevector, δ, increases, however it does not reach the stable checkerboard value of $\delta = 0.25$. As δ increases we can imagine the 2-1 (3+; 4+; 3+; 4+; 4+; 3+) stripe model gradually turning into the mid-doped stripe phase (4+; 3+; 4+; 3+) by losing double stripes. The incommensurability reaches a point of maximum intensity where every other double stripe is now a single stripe and so instead of a double stripe and then a single stripe repeated, there is now a double stripe and then two single stripes before a second double stripe (3+; 4+; 3+; 4+; 3+; 4+; 4+; 3+). It would be expected that this model would not

[1] Data taken from Wilkins *et al.* [35]

be as well correlated as there are not sufficient Mn^{3+} ions. This explains the lack of increase in correlation length often seen as the intensity of the signal increases. As the temperature increases further, and the intensity decreases, δ reverts back to the $\delta = 0.2$ observed in the high doped samples.

Azimuthal analysis is becoming an increasingly important technique for resonant x-ray scattering. By rotating the sample it is possible to get an idea for the anisotropy of the electron orbits in the sample. In the manganites, the quadrupole orbitals on the Mn^{3+} ion are the source of this anisotropy. Comparing azimuthal simulations with experimental data provides reinforcement of the predicted orbital ordering in the higher doped manganites. In the case of the quasi-bistripe phase, the azimuth measurements agree reasonably with the simulation. Two distinct models were presented for the fully bistripe $x = 0.7$ phase. Although the two simulations show common features, the experimental data agrees more closely to the simulation for the bistripe phase.

Other publications have used azimuthal simulations to confirm asymmetric ion ordering, in particular, a similar study has been reported by Di Matteo *et al.* [37], on the $x = 0.5$ doped bilayer. In this paper, Di Matteo *et al.* simulated the traditional Jahn-Teller distorted checkerboard pattern and found an excellent agreement with their experimental resonant scattering data.

3.3 Conclusions

X-ray diffraction experiments have been undertaken on the higher doped bilayer crystals; $La_{2-2x}Sr_{1+2x}Mn_2O_7$, where $0.5 < x < 0.7$. Three distinct phases are observed within this doping range. The first phase up with $x < 0.55$ shows similar characteristics to the half doped samples, with a commensurate wavevector of 0.25 for the orbital and Jahn-Teller distortions. The second phase where ($0.575 < x \lesssim 0.65$) forms a quasi-bistripe phase, with a wavevector varying throughout the temperature range below T_{CO}. The wavevector increases with increasing intensity, and it is speculated that this approaches a more stable condition as $\delta \rightarrow 0.25$. Finally where $x \gtrsim 0.65$, the system enters a full bistripe phase. The wavevector is stable, and the correlation length increases significantly from the quasi-bistripe phase approaching that observed in the half doped checkerboard pattern.

Chapter 4

Magnetic field effects in $La_{2-2x}Sr_{1+2x}Mn_2O_7$, $x = 0.4, 0.5$

The data in this chapter investigates the effects of an external magnetic field on the long range order in the bilayer manganites. The effects are studied on charge disproportionation and Jahn-Teller distortions, and also on polarons that occur just above T_N in the underdoped bilayers.

Although there have been significant investigations into the presence of long range ordering in the manganites, relatively little work involving high magnetic fields has been reported. This is partly due to the availability of experimental resources. Resonant x-ray scattering is now a standard tool, however high magnetic fields are difficult to use because of the need for non-magnetic diffractometers, combined with a high acceptance angle needed with the magnet. High energy x-ray diffraction dispenses with the latter of these problems, as the angular deviation of the x-rays from the incident to exit beam is typically less than 10°. The number of experimental groups conducting single crystal high energy diffraction is fairly limited, and the simultaneous use of high field magnets is rare.

The existence of Jahn-Teller structural distortions in the bilayer manganites has been discussed in Chapter 3. The first half of this chapter investigates the effect of an applied magnetic field on the strength of the distortions on the $x = 0.5$ bilayer, $LaSr_2Mn_2O_7$. These results form a preliminary study, and more data is needed, possibly from resonant diffraction in order to gain a more complete understanding of these effects. The drive behind this research is based on the idea that as the onset of antiferromagnetic ordering causes a significant reduction of the structural distortions, an applied magnetic field may induce a change in the magnetic state, causing changes in the long range order.

By examining the phase diagrams of the bilayer manganite (Fig. 1.12 and Fig. 1.11), it

can be seen that charge ordering is only present in the AFM phase down to $x = 0.475$. The underdoped bilayers with $x = 0.4$ enter a ferromagnetic phase below 110 K. Just above T_C diffuse scattering around Bragg peaks, and weak addition incommensurate satellite peaks have been observed. The second half of the chapter will look at the existence of this diffuse scattering, and the behaviour of this scattering in an applied magnetic field.

4.1 Structural Distortions in $LaSr_2Mn_2O_7$

4.1.1 Experimental Method

The experiments were conducted on the BW5 beamline at HASYLAB, with a 10 T cryomagnet. The cryomagnet is a four-pole magnet providing a horizontal field, with the magnet poles positioned such that the field is either parallel or perpendicular to the incident beam. This design of magnet limits the angular acceptance, however this is not a problem when using high energy diffraction.

The sample of $LaSr_2Mn_2O_7$ was grown at Argonne National Laboratory using the floating zone method. The sample was cleaved with the c axis normal to the sample surface. This resulted in the thin plate-like sample with a depth of approximately 0.7 mm. The sample was mounted with the c axis vertical (perpendicular to the scattering plane), allowing access to the entire $a - b$ crystallographic plane. The cryomagnet restricts the movement in the χ and ϕ angles, and so the experiment was conducted within this plane. Because the sample was mounted on a cleaved surface, it was possible to keep χ and ϕ constant throughout the experiment.

The superconducting magnet is kept cool by liquid cryogens. The coils are in a bath of liquid helium, which is insulated from room temperature by a jacket of liquid nitrogen. The sample temperature can be varied from 4.2 K to 300 K, controlled by a small heater coil on the sample stick, which sits in a vacuum in the centre of the cryomagnet.

4.1.2 Results

Observations were made of superlattice peaks at $(h \pm 0.25, k \pm 0.25, l)$ and $(h \pm 0.5, k \pm 0.5, l)$ type positions. Without resonant diffraction, there are limited means of testing the origin of the superlattice peaks. They are at the expected wavevector, and so we assume these are due to Jahn-Teller distortions and charge ordering respectively, as described both by

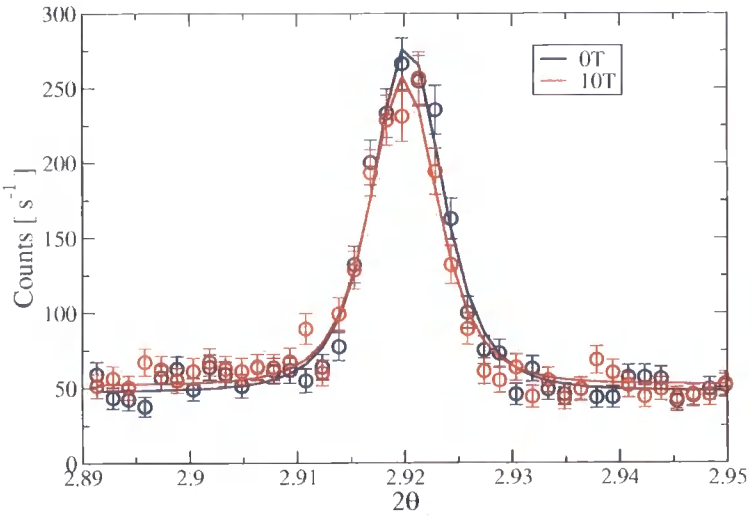

Figure 4.1: A $\theta - 2\theta$ scan through the $(1.5, 0.5, 0)$ charge order superlattice peak in $LaSr_2Mn_2O_7$ with 0 T and 10 T applied magnetic field. The data is normalised to a ring current of 120 mA.

Wilkins *et al.* [35] and in the previous chapter. In addition, upon warming the sample, the superlattice peaks disappeared at the previously observed transition temperature. Because of the limited time available for the experiments, all the measurements were taken at 4.2 K.

Figure 4.1 shows a superlattice peak at (1.5, 0.5, 0) showing the presence of charge ordering in the sample. The figure shows a $\theta - 2\theta$ scan through the peak, with applied magnetic fields of 0 T and 10 T. For this measurement the magnetic field was parallel to the incident beam. No obvious effect, on either the peak position, width of lineshape was found upon application of a 10T magnetic field. Many other charge order superlattice peaks were measured, none of which displayed any significant change in intensity upon applying a magnetic field, either parallel or perpendicular to the incident beam.

Figure 4.2 shows the Jahn-Teller superlattice peak at $(1.25, 0.25, 0)$. As the measurements are taken using high energy x-rays, this technique is not sensitive to orbital order, and so we are only observing the structural distortion of the crystal. Remarkably, this superlattice peak decreased significantly in intensity as the magnetic field was applied. The figure shows a $\theta, 2\theta$ scan through the peak with applied magnetic fields up to 10 T. It can be seen that the greatest change of intensity is between 2 and 4 T. There appears to be no reduction in the correlation length of the Jahn-Teller distortion as the magnetic field is applied. Figure 4.3 shows scans in the [110] direction through the charge order and Jahn-Teller superlattice peaks with an applied field of 5 T. This shows that the ordering is very highly correlated,

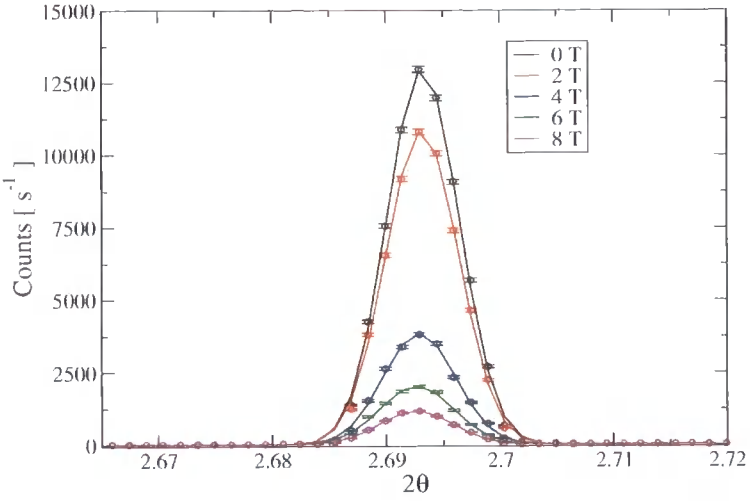

Figure 4.2: $\theta - 2\theta$ scans through the (1.25, 0.75, 0) Jahn-Teller superlattice peak in $LaSr_2Mn_2O_7$ with applied magnetic fields. The magnetic field direction was parallel to the incident beam. Data normalised to a ring current of 120 mA.

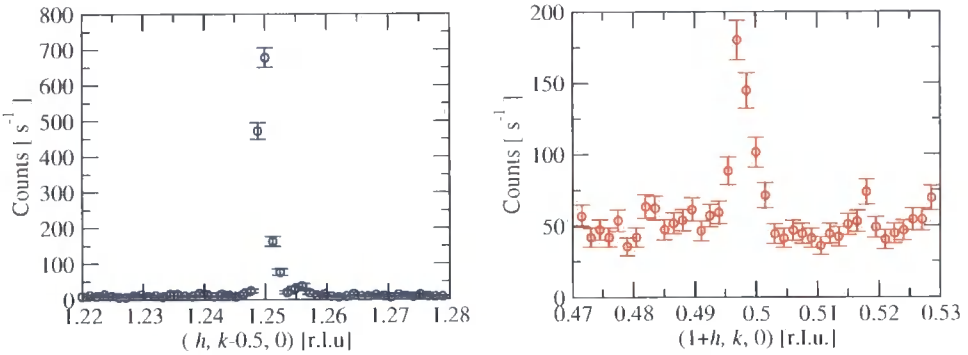

Figure 4.3: Scans in the [110] direction through reciprocal space of the Jahn-Teller distortions (left panel) and charge ordering (right panel) with an applied magnetic field of 5 Tesla. Data normalised to a ring current of 120 mA.

especially the structural distortion.

The response of the intensity of the Jahn-Teller signal to the applied magnetic field does not appear to be identical for each peak in reciprocal space. Figure 4.4 shows the intensity variation of three separate Jahn-Teller peaks. In all of these cases the magnetic field was parallel to the incident beam (roughly perpendicular to the scattering vector). As can be seen the response of the superlattice peak at (1.25, -0.75, 0) is much smaller that the response of the other two peaks. This peak is in a different quadrant of reciprocal space to the other peaks. This means that there is a significant rotation in the θ direction, turning the crystal with respect to the applied magnetic field. As such this may change the orientation of the

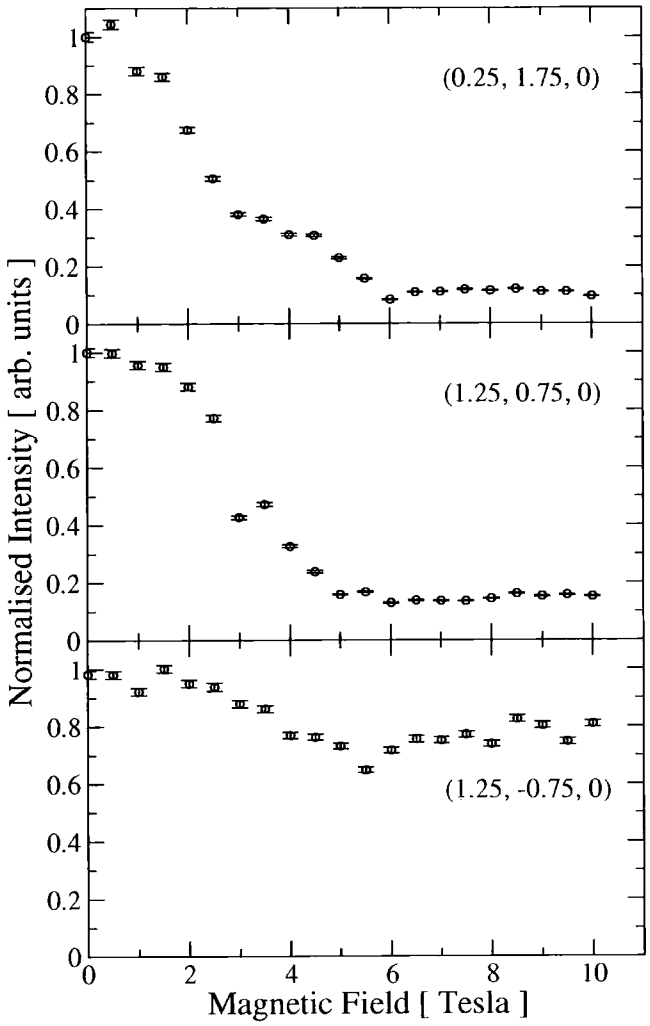

Figure 4.4: Intensity of different Jahn-Teller superlattice peak as a function of applied magnetic field. This intensities of the Jahn-Teller peak are divided by the intensity of the (2 0 0) Bragg peak for each magnetic field measurement. This removes any effect of sample movement. The results are then normalised to unity for a zero field.

major domain within the crystal with respect to the magnetic field.

4.1.3 Discussion

A response has been observed of the structural distortion upon application of an external magnetic field. It is, however, not entirely clear as to the extent of the effect of the magnetic field, especially regarding the relative orientation of the crystal in the field. It is unsurprising, however, that upon applying a vector field the response would be anisotropic. Possibly the most unexpected result is that there is a marked response by the Jahn-Teller distortions, and yet the charge ordering seems unaffected. As such, the quenching process is not identical to

that observed by the onset of AFM order at T_N where both ordering parameters are affected equally.

There have been relatively few published studies on high magnetic field effects on the bilayer manganites. Hayashi *et al* [83] looked at the magnetoresistance and magnetic properties under high magnetic fields, looking at fields up to 40 T. They found that the application of such a field gradually changed the magnetic state to a ferromagnet, and at the same time reduced the magnetoresistance. Chen *et al.* [84] studied the resistivity of $LaSr_2Mn_2O_7$ with respect to a magnetic field, however their publication concentrated on the temperature range 220 K to 300 K, above the charge order transition.

In comparison to other compounds, García-Landa *et al.* [85] looked at $Nd_{2-2x}Sr_{1+2x}Mn_2O_7$ single crystals under fields up to 30 T. They observed signs of spin-flipping, however this was induced in fields greater than 10 T, and was more pronounced in the lower doped samples ($x = 0.35 - 0.4$). Tomioka *et al.* looked at $Pr_{0.5}Ca_{0.5}MnO_3$ [86], and found that a metal-insulator transition (accompanied by a melting of the charge ordered state) could be induced by a field as low as 6 T.

No change in the intensity of the charge order reflection occurred in $LaSr_2Mn_2O_7$, as such it appears that 10 T is not sufficient to cause a metal-insulator transition. Indeed, if this was so, one would expect a complete reduction in the intensity of the Jahn-Teller distortions. It seems more likely that the magnetic field is affecting the splitting of the electronic bands in the Mn ions, which thereby causes a reduction in the Jahn-Teller distortion. The distortion and the splitting of the two e_g bands in this sample is very small (this will be discussed further in Chapter 7). It is possible that the application of a magnetic field is reducing the energy gap between these two bands even further. This reduction in the energy gap between the two levels, then decreases the dominant occupancy in the lower energy level, reducing the structural distortion.

4.2 Electric Polarons in $La_{1.2}Sr_{1.8}Mn_2O_7$

Diffuse scattering has been observed by Vasiliu-Doloc *et al.* [46] in the underdoped bilayer manganites around Bragg peaks above T_N. In addition weak diffuse peaks have also been observed to occur at incommensurate positions between the Bragg peaks. These two areas of diffuse scatter are shown in figure 4.6. This scattering is thought to originate from polaron formation. A polaron is a general term for a isolated charge or magnetic moment, coupled

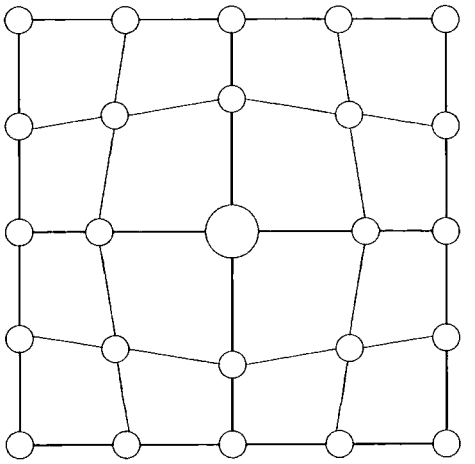

Figure 4.5: Schematic impression of a polaron. The inner large particle distorts the nearby crystal lattice. Regular positioned polarons throughout a lattice can be detected through diffraction.

with a strain field. This causes a perturbation in the crystal field (Fig. 4.5), thereby forming a scattering cross-section. The origin of these polarons can be as simple as the presence of impurities within a sample, or they can arise from an isolated charge or magnetic moment.

The appearance of the scattering in two distinct areas suggests two different arrangements of these polarons. Firstly the scattering around the Bragg peaks (figure 4.6*a*) is caused by a polaron lattice that is coupled with the crystal lattice. This coupling is relatively weak, as the broadness of the scattering (almost one-fifth of a Brillion zone in the a-b plane, and almost continuous along the c axis), suggests an extremely disordered system. By contrast the second type of polaron (Fig. 4.6*b*) observed, occurs at $(h \pm 0.3, k, l)$ and $(h, k \pm 0.3, l)$ positions. This suggests a distinct periodicity approximately three times that of the crystal lattice. Again the scattering is broad, however not to the extent of the scattering around the Bragg peaks. In many respects this appears at first glance like very weak disordered charge ordering.

4.2.1 Experimental Method

The experiment was also conducted on the BW5 beamline, with a helium cooled cryomagnet producing an applied field of up to 4 T. Due to the limited movement in χ and ϕ, the sample was orientated in order to maximise access of the a-c plane. The incident beam size at the sample was 1 mm × 1 mm, and the analyser and monochromator were both Si-Ge graded

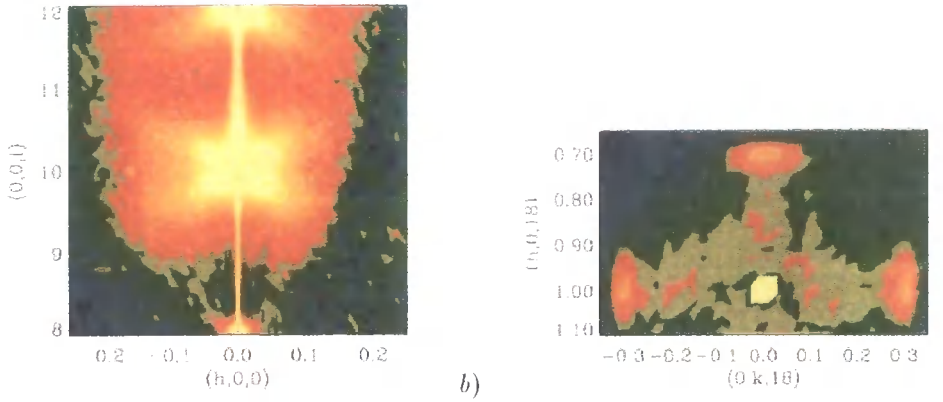

Figure 4.6: Polaron ordering in $La_{1.2}Sr_{1.8}Mn_2O_7$. (*a*) Contour plot showing the lobe-shaped pattern of diffuse x-ray scattering at $T = 300$ K around the (0,0,8), (0,0,10), and (0,0,12) reflections. (*b*) Contour plot of the x-ray intensity in the (hk) plane at $l = 18$, collected at $T = 125$ K. Three incommensurate peaks are observed, characterised by the wave vector $(\pm\epsilon, 0, l)$ or $(0, \pm\epsilon, l)$. The expected fourth peak was not accessible experimentally. *Figures from Vasiliu-Doloc et al.* [46].

crystals. Detection was provided by a solid state detector, with a single channel analyser providing an energy gate to remove higher harmonics.

The sample has a T_C of approximately 110 K, and previous publications have suggested that the polarons appear just above this phase transition. In order to detect these polarons the sample was cooled to 150 K. At this temperature diffuse scattering could be detected around the Bragg peaks, and at $(2.3, 0, 1)$.

4.2.2 Results

The shape of the diffuse signal from the polarons at (2.3,0,1) was anisotropic in reciprocal space (figure 4.7). In the out of plane direction in the c axis, the scattering encompasses almost an entire Brillion zone, while in the [100] direction the peak was confined to virtually one-tenth of that distance. This peak width in the [001] direction suggests a correlation length of 62.5 ± 1 Å. The shape and diffuse nature of the peak remained virtually constant throughout the temperature range. The small peak to the left of the main signal in the left graph of Figure 4.7 originates from multiple scattering.

As the sample was cooled, the temperature was held at regular intervals while $\theta/2\theta$ scans through the (2.3,0,1) peak measured the integrated intensity of the peak. This intensity, shown in Figure 4.8, was seen to drop dramatically at T_C. The sample was further cooled to 50 K, before the same procedure was conducted while warming. The measurements from

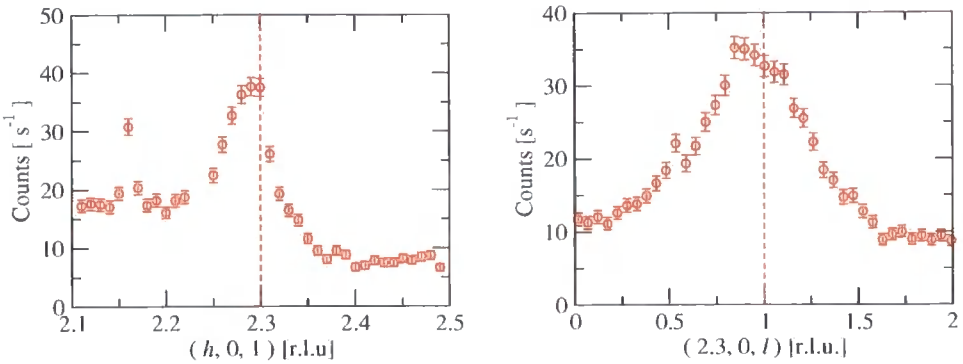

Figure 4.7: Scans in reciprocal space through the polaron signal observed at (2.3,0,1) in $La_{1.2}Sr_{1.8}Mn_2O_7$ at 130 K. Data normalised to a ring current of 120 mA.

cooling and warming are similar, suggesting that there is very little thermal hysteresis. The temperature dependence shows the polarons existing above T_C to ~240 K.

The diffuse distribution around the Bragg peaks could also be observed above T_C. In order to measure this intensity, it was impossible to scan through the (2,0,0) Bragg peak, as this would have saturated and damaged the detector. In addition, placing sufficient attenuation in the scattered beam path would have prevented the detection of the diffuse scatter. As such, scans were conducted in the [100] direction at $l = 0.5$, and in the [001] direction at $h = 2.06$, shown in figure 4.9. These scans are effectively horizontal and vertical slices through the colour map in figure 4.6*a*.

The scans confirm the unusual lobe shape seen by Vasiliu-Doloc, with scattering intensity appearing aligned approximately in the [100] direction. This scattering around the Bragg peaks was significantly more diffuse than that observed at (2.3,0,1), and due to their close proximity around the very strong Bragg peaks it was impossible to get a integrated intensity measurement of the diffuse scatter by going through the centre of the scattering. Instead, identical scans were taken along the [001] direction through (2.06,0,0) at specific temperatures, as the sample was warmed. These scans are shown in figure 4.10. The two images show the same data, the strong intensity in the middle of the scan is due to a scattering rod along the principal axis.

Compared to the polaron signal at (2.3,0,1), the increase of intensity above T_C is much more gradual. The intensity reaches a maximum at ~140 K, whereas the signal from the more correlated polarons had reached a maximum at 120 K. The full temperature range that the polarons exist in is similar in both cases, between ~100 K, and ~240 K.

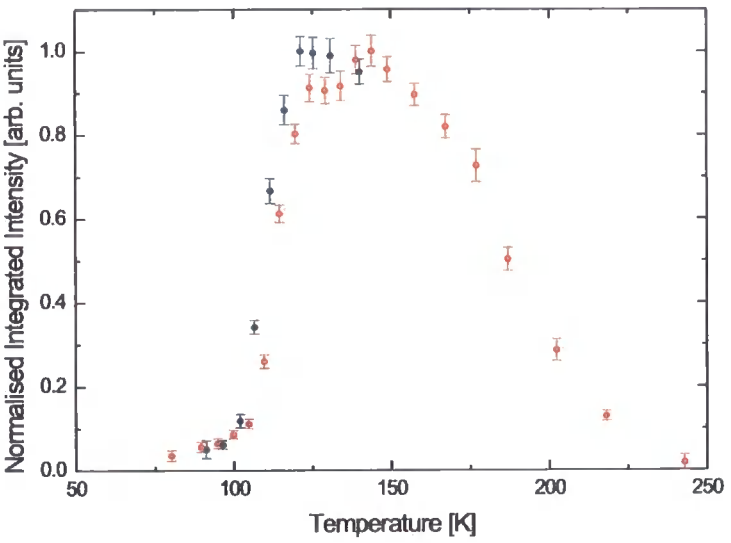

Figure 4.8: Temperature dependence upon cooling (blue, open circles), and warming (red, closed circles), of the correlated polarons centred at the wavevector (2.3, 0, 1). The sudden increase in the intensity of the polarons at 110 K is simultaneous to the reported transition between the ferromagnetic and paramagnetic phases. There is no evidence of significant thermal hysteresis.

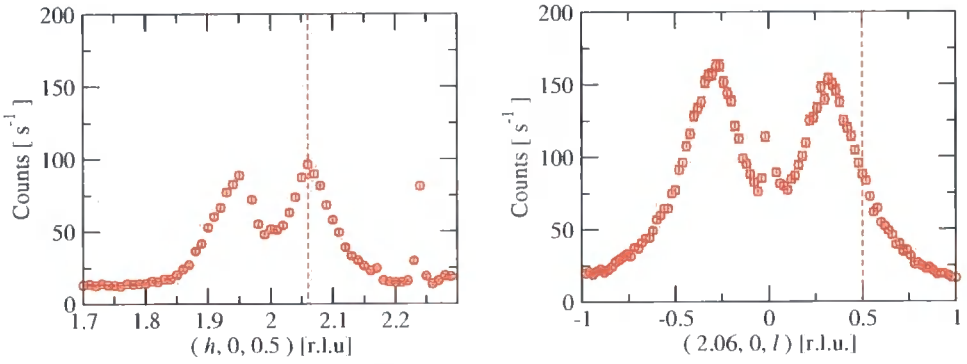

Figure 4.9: [100] (*left*) and [001] (*right*) scans through the diffuse polaron signal around the (2,0,0) Bragg peak in $La_{1.2}Sr_{1.8}Mn_2O_7$ at 130 K. The dashed lines show the position of the perpendicular scan in the opposite panel. Data normalised to a ring current of 120 mA.

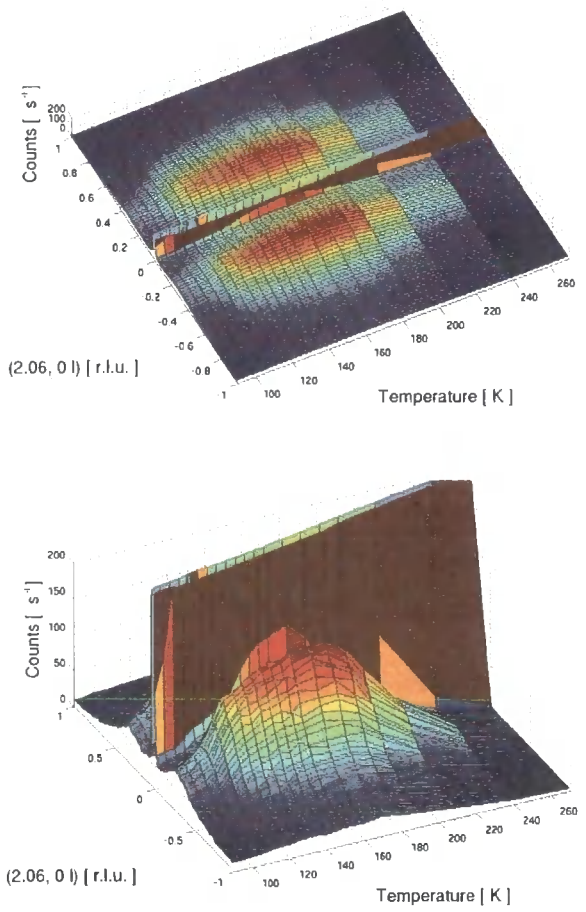

Figure 4.10: Temperature dependence of the diffuse scattering around the Bragg peaks. At each temperature a scan in the [001] direction through (2.06,0,0) is taken. The upper and lower axes show the same graph displayed from a different viewpoint. Data normalised to a ring current of 120 mA.

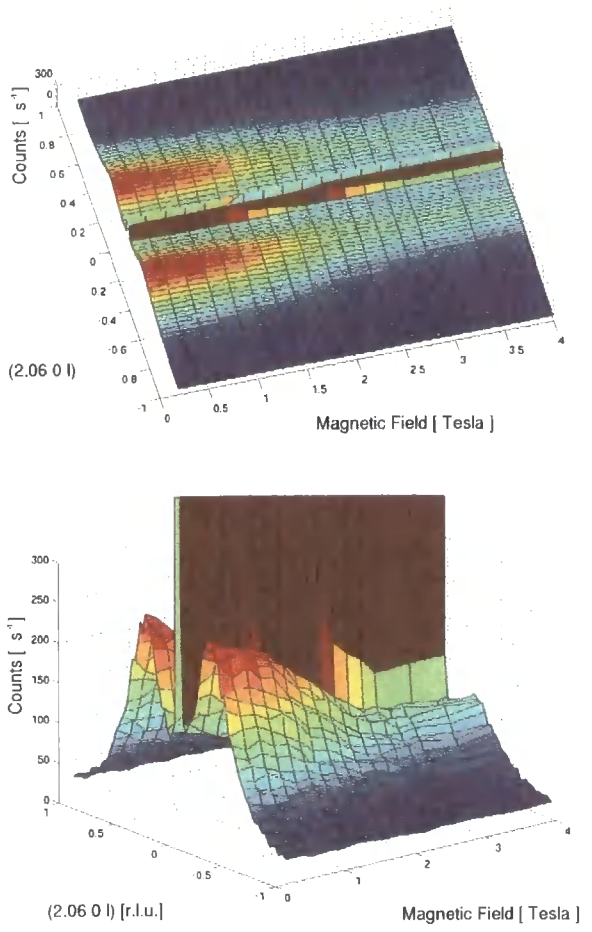

Figure 4.11: Applied magnetic field dependence of the uncorrelated diffuse polarons, measured at 130 K. The upper and lower axes show the same graph displayed from a different viewpoint. Data normalised to a ring current of 120 mA.

Measurements were taken of the dependence of the intensity of the polarons with respect to an applied magnetic field. Figure 4.11 shows the magnetic field dependence of the diffuse scattering around the (200) Bragg peak. The measurements were taken at 130 K, above T_C. With the application of 2 T, the intensity of the diffuse scatter reduces significantly. A further increase of the field strength up to 4 T appears to have little effect. A similar magnetic field dependence was also seen in the polaron signal at (2.3,0,1).

4.2.3 Discussion

The observation of polarons in $La_{1.2}Sr_{1.8}Mn_2O_7$ has been seen previously through neutron scattering. This work confirms the existence of these polarons, and also suggests that they

are not solely magnetic in nature. High energy x-ray scattering is generally insensitive to magnetic moments, and so it is highly likely that the polarons found here correspond to charge scattering. This, of course, does not mean that the polarons detected by neutron scattering are unrelated to those described here. Their respective properties are so similar, that it seems likely that the two techniques are sensitive to different faces of the same phenomenon.

In the higher doped bilayer manganites, it has been seen that the mixed valence state results in a low temperature real space ordering of the charges (Wilkins *et al.* [35] and Chapter 3). This sample lies below the charge ordered and magnetic phase in the stoichiometric scale, in fact entering a ferromagnetic state below T_C. Above this temperature the observation of polarons, both around the Bragg peaks, and also at specific sites in reciprocal space, suggest some kind of charge segregation. It seems possible that there is some form of charge disproportionation, even if this is very weakly, or not at all, ordered. As such, only diffuse scatter is seen around Bragg peaks, and very weak diffuse scatter at positions in reciprocal space. The observation of diffuse scatter at positions $(h + 0.3, k, l)$ suggest that there is a weak ordering of some of the polarons, with a periodicity of approximately 3 times the unit cell. This scattering is significantly weaker and more diffuse that observed in the charge order phase. The onset of ferromagnetism totally removes any polaron signal, either around Bragg peaks, or at $(h+0.3, k, l)$. In addition the application of a 3 T magnetic field severely reduces the signal strength. This suggests that the system may be aligned ferromagnetically slightly above T_C by the application of such a field. Osborn *et al.* [43], interpreted this scattering to be canted ferromagnetic scattering above T_C, and as such it is not surprising that the application of a magnetic field reduces this canting angle.

4.3 Conclusions

Magnetic field effects have been investigated in both $LaSr_2Mn_2O_7$ and $La_{1.2}Sr_{1.8}Mn_2O_7$. The strong Jahn-Teller distortion seen in the half doped manganites has been shown to vary under field, suggesting a change in the band structure. Interestingly, no evidence has been seen for an effect on the charge ordering. The experiments were conducted using high energy x-rays and so no direct observation of orbital ordering was possible. The effect on the Jahn-Teller distortion, although striking, has not been completely understood, especially regarding the effect of the different magnetic field directions.

Weak diffuse scattering has been seen above T_C in $La_{1.2}Sr_{1.8}Mn_2O_7$. This is attributed to unordered charge disproportionation. Further cooling of the sample below T_C quenches any diffuse scatter. In addition, the application of a 3 T magnetic field reduces the intensity of the polaron scattering significantly. The system is thought to exist in a canted ferromagnetic state above T_C, and such canting is reduced by the application of a field.

Part II

Soft X-ray Diffraction at the Mn L edges

Chapter 5

Soft X-ray Magnetic Scattering

Part I of this thesis investigated charge and orbital ordering phenomena with resonant diffraction at the manganese K edges. This generated interesting results, but it was limited by the indirect probe of the $3d$ electron band. Part II of the thesis reports on experiments looking directly at the $3d$ band through resonant scattering at the L edges. In particular, the L_{II} and L_{III} edges, corresponding to dipole transition from the $2p \rightarrow 3d$ electron bands.

The following two chapters investigate the single layer and bilayer manganites, respectively. This chapter describes the published literature of soft x-ray diffraction, and in addition describes the three soft x-ray chambers used to generate the results in this thesis. Chapter 6 builds on the work undertaken on $La_{0.5}Sr_{1.5}MnO_4$ and studies in detail at the temperature dependences and an azimuthal dependence. Chapter 7 investigates the orbital and magnetic ordering in $La_{2-2x}Sr_{1+2x}Mn_2O_7$. Both of these chapters display energy spectra fits calculated from theoretical models by the group at the *Abdus Salam International Centre for Theoretical Physics, Trieste*, led by M. Altarelli.

5.1 Soft X-ray Magnetic Scattering - A Review

Resonant x-ray magnetic scattering at the Mn L edge was predicted by Hannon *et al.* [62], long before any experiments were undertaken. Even using synchrotron radiation, resonant scattering has concentrated on the absorption edges that are available in the energy range 3-20 keV. Thus, direct scattering into magnetically active electron bands has been limited to the heavier elements, such as the actinides and the rare earths. More recently however, there has been a realisation that through using soft x-ray spectroscopy beamlines, it is possible to scatter at very low incident x-ray energies, directly accessing the magnetic properties of the $3d$ transition metals.

The results published to date from this 'new' technique fall neatly into four categories.

The first category encompasses the study of multilayers, which some may argue is reflectivity rather than diffraction. The second category covers the manganites, which is by far the most prolific area. This has been pursued by a number of groups, and covers the cubic, single layered, and bilayer manganites. The third category covers the cuprates. This is potentially one of the most interesting topics, due to its relevance to high T_C superconductors. The final category is that of the nickelates.

Although the most prominent results generated through soft x-ray diffraction has been with the transition metals, studies have been conducted on more exotic compounds. In particular, Spencer *et al.* [87] looked at the magnetic peak in holmium (at the M_V edge).

5.1.1 Soft Reflectivity from Multilayers

The first scattering experiment at a transition metal L edge was performed by Kao *et al.* [88]. In this paper they describe an experiment directly testing the prediction by Hannon of a resonant enhancement. The experiment was performed on a single crystal of Fe(110), 35Å thick. The experimental setup on the U-15 beamline on the uv ring at National Synchrotron Light Source (NSLS), had a fixed 2θ angle of 35.2°, and the iron clamped in the jaws of an electromagnet with a field of 400 G, orientated with the field perpendicular to the scattering plane. The experiment was not performed in vacuum, but in a 50% argon-ethane gas mixture at 28 torr. Figure 5.1 shows the results of the experiment, with an inset displaying the experimental setup. The experiment measured the asymmetry ratio of the Fe resonance, when the magnetic field direction was reversed. The solid lines show the measured data for each magnetic field direction. The results show an extremely large resonance at the Fe L edge, as predicted by Hannon *et al.*. By constructing a simple model of the reflectivity, they were able to demonstrate that these results were sensitive to the magnetic parameters calculated for iron. Although this was really a demonstration experiment, it has paved the way to further soft reflectivity experiments.

Kao *et al.* [89] later extended this experiment by looking at a Co thin film with circular polarised light. This experiment was performed on the AT&T Bell Laboratories Dragon beamline at the NSLS. By combining the dichroic effects of circular polarised light with magnetic reflectivity, asymmetry ratios are obtainable for weak magnetic moments, as a function of depth in the material. Figure 5.2 shows the resonances at the Co L edges for various 2θ angles. This figure shows the expected reflectivity curves, and is superimposed by

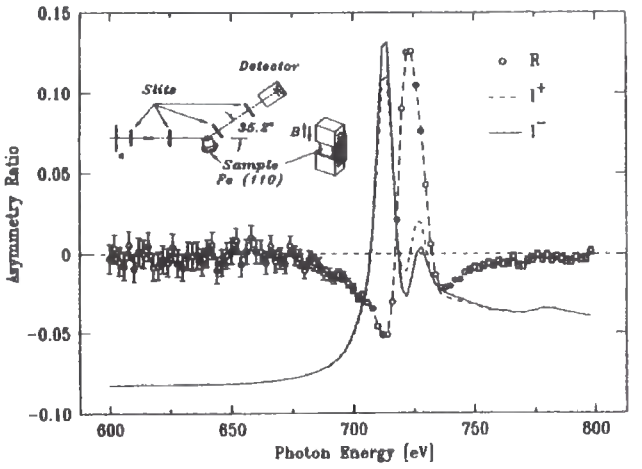

Figure 5.1: Specular reflectivity of p-polarized light I^+ and I^-, and asymmetry ratios R measured from a 35-Å Fe(110) crystal. The line through the asymmetry ratios is only to serve as a guide to the eye. Inset: Scattering geometry. The polarization of the radiation is in the scattering plane, the applied magnetic field is perpendicular to the scattering plane, and the scattering angle, 2θ, is 35.2°. *Figure from Kao et al.* [88].

the asymmetry ratio. This ratio appears to follow the reflectivity curves out of phase. The experiment helps to demonstrate that this technique could be used to separate the magnetic and structural roughness of thin films.

Nickel was the next transition metal to be studied, in the form of a Ni/Ag multilayer by Tonnerre *et al.* [90]. This experiment performed on station SB3 on Super ACO at LURE, observed the antiferromagnetic peak of the artificial layered structure. Figure 5.3 shows this peak at 14° at the Ni L_3 absorption edge. Again, as with the Co and Fe by Kao *et al.*, a huge resonant enhancement is seen at the L_3 edge, and as such it is possible to directly observe a magnetic peak in the multilayer. In addition to this experiment, similar studies were also made on Co/Cu [91], Fe/Mn [92], Fe/Co [93] and Gd/Fe [94].

The first true multilayer soft x-ray experiment was conducted by Hase *et al.* [95, 96] who looked at samples of Co/Cu multilayers with 25 and 50 repeats. The aim of this experiment was to question the relationship between the structural and magnetic roughness; which had previously been assumed to be directly related. Figure 5.4 shows the specular scatter around the structural Bragg peak, and the antiferromagnetic peak. This clearly shows significantly more scatter around the magnetic peak. By modelling the reflectivity curves, Hase *et al.* were able to show that the magnetic roughness was one or two orders of magnitude larger than the structural roughness.

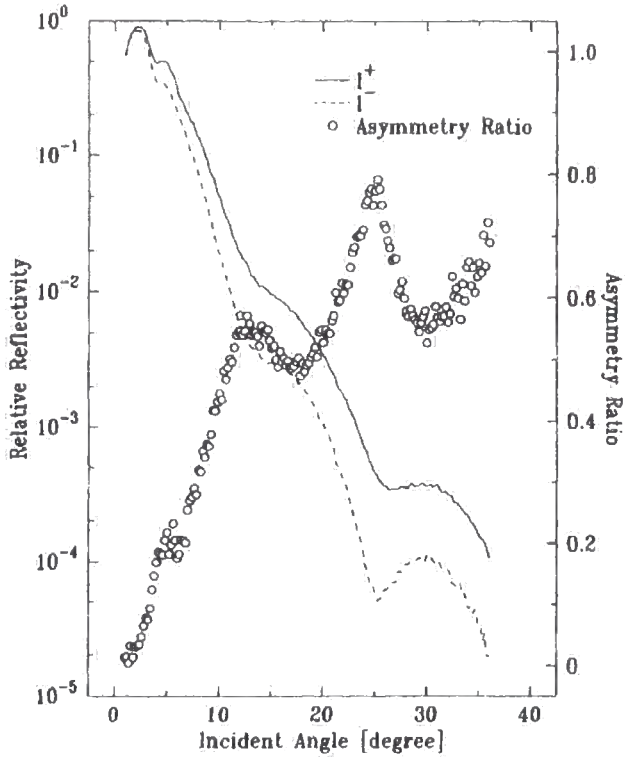

Figure 5.2: Reflectivity as a function of grazing angle measured at the peak of the Co L_3 edge (786.5 eV). The solid and broken lines denote the two opposite magnetization directions used in the measurements. Also included in the figure is the asymmetry ratio derived from the two reflectivity curves. *Figure from Kao et al.* [89] *describing a Co thin film.*

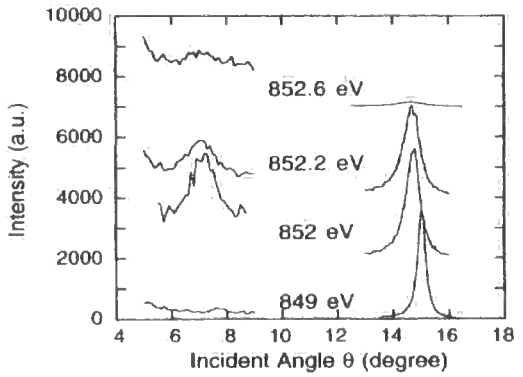

Figure 5.3: Diffraction patterns of a Ag/Ni multilayer for different energies around the Ni L_3 absorption edge using a linearly polarized beam. The intensity of the AF peak (see text) has been scaled by a factor of 50. The various curves have been vertically shifted by 2000, 4000, and 7000 respectively. *Figure from Tonnerre et al.* [90].

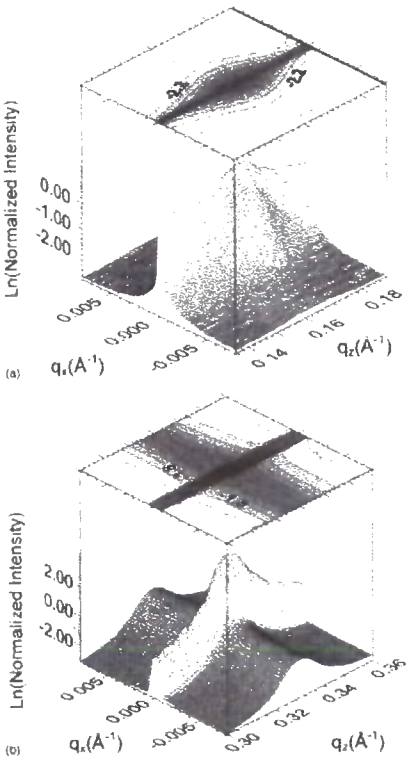

Figure 5.4: Full reciprocal space maps of the diffuse scatter around the magnetic (a) and structural (b) Bragg peaks. The contours are in increments of 0.4. The instrument resolved specular ridge is seen in the data as a streak at $q_x = 0$. *Figure from Hase et al.* [95] *describing a Co/Cu multilayer.*

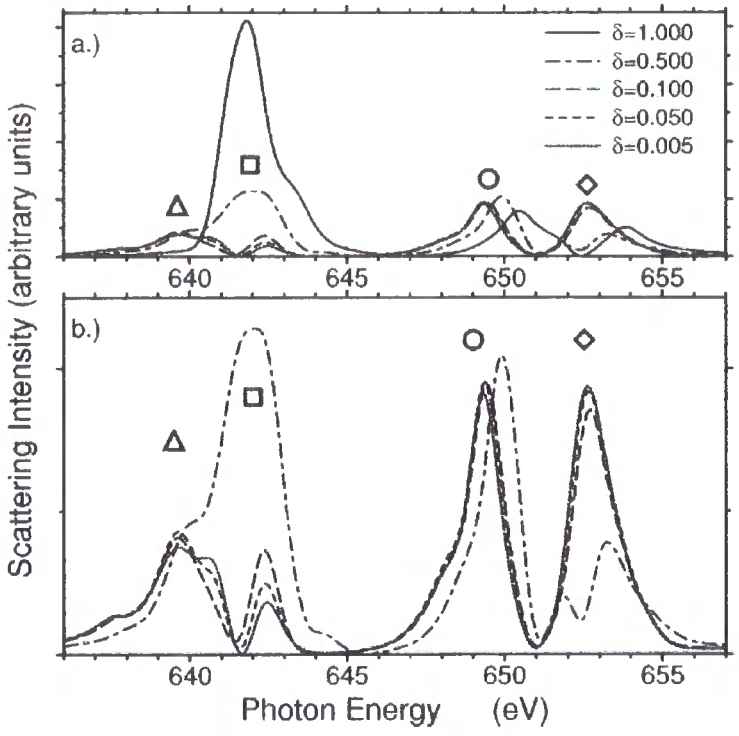

Figure 5.5: (a) Scattering with D_{4h} contributions reduced by δ. (b) Peak detail at lower δ values. *Figure from Castleton and Altarelli* [97] *describing the orbital order peak in* $La_{0.5}Sr_{1.5}MnO_4$. δ *indicates the size of the tetragonal crystal field. Other symbols relate to further figures in their paper.*

5.1.2 The Manganites

The interest in studying $La_{0.5}Sr_{1.5}MnO_4$ was sparked by a theoretical paper by Castleton and Altarelli [97], in which they calculated the possible differences in the resonant spectra between a strongly Jahn-Teller distorted system, and a weakly distorted one. Figure 5.5, shows the spectra of the orbital order peak, with various crystal field values (D_{4h}). Very simply, this suggests that the main peak at the L_3 edge (centred around 642 eV) was mainly due to the crystal field distortion, and decreases rapidly in intensity as the field is reduced. By contrast the L_2 edge (centred around 650 eV) appears relatively unchanged by the reduction in crystal field, suggesting that this peak is due far more to the Goodenough type orbital ordering. These calculations were based on atomic multiplet calculations, using the Cowan code [98] and Racah calculations [99].

It was some three years later before experimentalists managed to test the ideas of Castleton and Altarelli. In fact the first experimental study of a manganite looked at the (001) antiferromagnetic peak in $LaSr_2Mn_2O_7$. This precursor to the study of orbital ordering, was

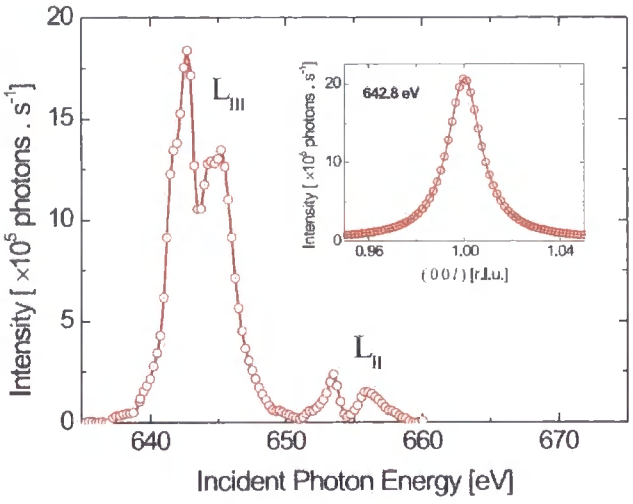

Figure 5.6: An energy scan at fixed wave vector through the (001) antiferromagnetic ordering reflection at 83 K. The inset shows a scan through the same peak in the (00l) direction, with the solid line being a Lorentzian fit to the experimental data (open circles). *Figure from Wilkins et al.* [36] *describing* $La_{0.5}Sr_{1.5}MnO_4$.

necessary to refine and prove the ability of the experimental technique. The publication by Wilkins *et al.* [36] simply showed the energy scans at fixed wavevector through the magnetic (001) (Fig. 5.6) and charge (002) Bragg peaks. Although there is a modest resonance on the charge peak, the magnetic peak shows a resonance far in excess of anything seen at the K edge. In addition a temperature dependence of the magnetic peak was measured, which was in agreement with previous neutron studies.

Shortly after this initial paper on the (001) peak in $La_{2-2x}Sr_{1+2x}Mn_2O_7$, Wilkins *et al.* [100] and Dhesi *et al.* [101] published the first results on $La_{0.5}Sr_{1.5}MnO_4$. Both papers display the similar energy resonances of the $(\frac{1}{4},\frac{1}{4},0)$ peak, that from Dhesi *et al.* is shown in Figure 5.7. In addition Dhesi *et al.* also shows a resonance at the Mn L_1 edge, that was not detected by Wilkins *et al.*. Regarding accurate fitting of the spectra, Wilkins *et al.* provided no direct fitting, other than comparing their results to the predictions from Castleton and Altarelli. From this paper, they deduced that co-operative Jahn-Teller distortions are the dominant form of orbital ordering in this material. In addition they suggest that the ordering type is $3d_{x^2-z^2}/3d_{z^2-y^2}$ rather than $3d_{3x^2-r^2}/3d_{3y^2-r^2}$ as previously thought; again this is predicted from the simulations of Castleton and Altarelli. Dhesi *et al.* by comparison included fitting of the spectrum (displayed in Fig. 5.7), calculated through ligand-field atomic multiplet calculations. These calculations provide a reasonable fit to the experimental data,

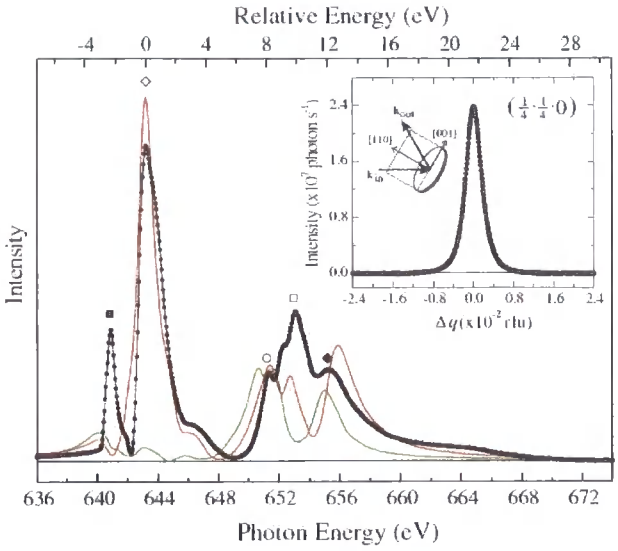

Figure 5.7: The energy dependence (solid circles with line) of the $(\frac{1}{4},\frac{1}{4},0)$ peak recorded over the Mn $L_{2,3}$ edges at 134 K and the calculated spectrum in D_{2h} symmetry for large (red line) and small (green line) JTD. The inset shows a $(\frac{1}{4}+\Delta q,\frac{1}{4}+\Delta q,0)$ scan of the forbidden reflection arising from OO at a photon energy of 643.8 eV and at $T = 134$ K (open circles). The solid line is a Lorentzian fit to the peak. The experimental geometry is also shown. *Figure from Dhesi et al.* [101] *describing* $La_{0.5}Sr_{1.5}MnO_4$

however there are certain parts of the spectrum that are not modelled at all, in particular the pre edge feature of the Mn L_3 edge at 642 eV. The analysis by Dhesi *et al.* agrees that the structure is strongly Jahn-Teller distorted, however they argued for an occupation of the $3d_{3x^2-r^2}/3d_{3y^2-r^2}$ type.

Both papers showed a temperature dependence of the orbital peak, seemingly disappearing at ~230 K, however the experimental chamber on ID08 used by Dhesi *et al.* at the time was only able to reach 134 K. Wilkins *et al.* measure the temperature dependence of the difference parts of the resonant spectrum, which they suggested split at T_N. Below this temperature the peaks in the L_3 part of the spectrum appear to increase in intensity more than those in the L_2 part. Directly relating this to Castleton and Altarelli, it was speculated that this means that the two causes of orbital ordering (that of Jahn-Teller and Goodenough) are separate, as they behave separately with regard to temperature.

These two papers on $La_{0.5}Sr_{1.5}MnO_4$ encouraged further study, both by Wilkins *et al.* [102] and Staub *et al.* [103], as well as more complete theoretical studies by Stojić *et al.* and various conference proceedings and invited publications [104, 105, 106, 107]. The paper by Wilkins *et al.* [102] described results that are presented in Chapter 6, and so a thorough

explanation will be given there. In essence this paper presents further more accurate studies of both the orbital order $(\frac{1}{4},\frac{1}{4},0)$ peak in $La_{0.5}Sr_{1.5}MnO_4$ and the magnetic $(\frac{1}{4},\frac{1}{4},\frac{1}{2})$ peak. The spectra of these are then directly modelled using multiplet calculations. In addition, further experimental work shows the azimuthal dependence of the magnetic peak, and the temperature dependences of both peaks. Staub *et al.* also showed detailed azimuthal dependences, however this time of the orbital peak at $(\frac{1}{4},\frac{1}{4},0)$. Interestingly they observed evidence of an additional component in there azimuth experimental data which is neither two-fold or four-fold. This is attributed to complex mixed phase where the $(\frac{1}{4},\frac{1}{4},0)$ peak is composed in the major part from orbital origin, but there is some contribution from a magnetic origin. This idea is undisputed by polarisation analyses of the orbital signal, however these results are very recent, and yet to be confirmed by another experimental group.

In addition to the single layered $La_{0.5}Sr_{1.5}MnO_4$, both the cubic and the bilayer systems have also been studied. The former was investigated by Thomas *et al.* [108] at NSLS, with $Pr_{0.6}Ca_{0.4}MnO_3$. This was reported shortly after the papers by Dhesi *et al.* and Wilkins *et al.* on $La_{0.5}Sr_{1.5}MnO_4$. Although in essence this material has similar properties to the layered sample, having both magnetic and orbital superlattices, the strong twinning of the sample means that these superlattice features are superimposed (Fig. 5.8). As such, it is only really possible to study the orbital contribution above T_N, as below the signal is swamped by the magnetic contribution. Uniquely, they observed a shifting of the energy spectra between the orbital and magnetic peaks, something that has not been observed in the layered sample by other groups.

Finally, the bilayer manganite $LaSr_2Mn_2O_7$ has been studied by Wilkins *et al.* [109]. The results in this study are presented in Chapter 7, and again show energy spectra of the orbital order, as well as the previously observed magnetic order peak. This sample is particularly interesting, as the Jahn-Teller contribution to the orbital ordering is seen to be very small indeed, and so the spectra show a much purer Goodenough orbital order type.

5.1.3 The Cuprates

Despite the vast interest in the cuprates, due to high T_C superconductivity, and the proliferation of papers utilising various experimental techniques, there is currently only one group that has published soft x-ray diffraction on the Cu compounds. Abbamonte *et al.* [110] started looking at the cuprates by studying thin films of $La_2CuO_{4+\delta}$, where they observed

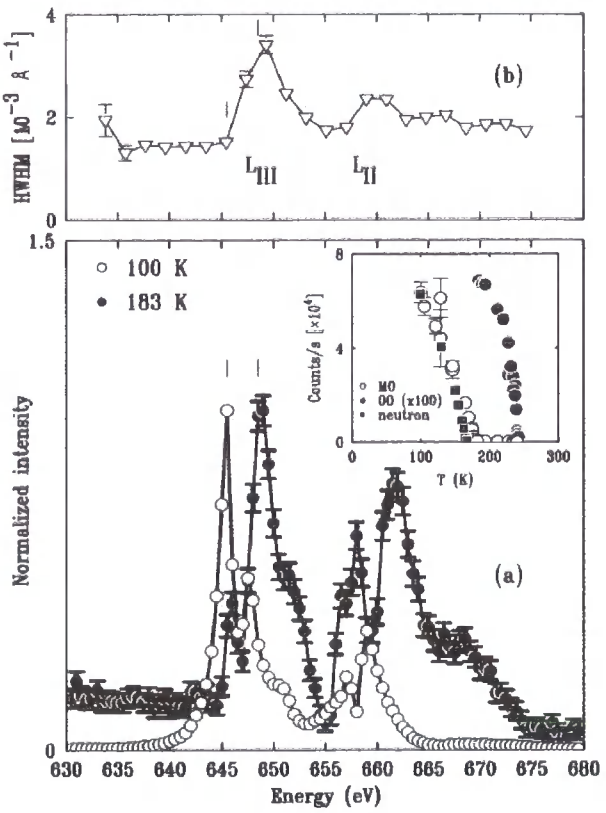

Figure 5.8: (a) Energy scans at a fixed wave vector at 100 K ($T < T_N$) and 183 K ($T_N < T < T_{OO}$). (Inset) Temperature dependence of the peaks in the magnetic (MO, open circles) and orbital (OO, closed circles) spectra and the $(\frac{3}{2}, 0, 0)$ magnetic reflection measured with neutrons (dark squares). (b) HWHM *Half-Width-Half-Maximum* of the $(\frac{1}{2}, 0, 0)$ magnetic peak verses energy, indicating the increase in absorption at the Mn L edges. The tick marks denote the peaks in the magnetic and orbital spectra. *Figure from Thomas et al.* [108] *describing* $Pr_{0.6}Ca_{0.4}MnO_3$

resonances in the fluorescence both at the Cu L edge, and also the O K edge. In fact these reflectivity studies concentrated more on a pre-peak at the O K edge, which they attributed to a "mobile carrier peak". The explanation of this peak is that the observation is sensitive to a regular distribution of holes through the sample (hole crystal), and is caused by the distribution of the carrier density. By studying the reflectivity fringes, Abbamonte *et al.* [110] attempt to interpret the carrier density in the region immediately above the substrate. An observation of damped fringes, leads to the explanation of either a carrier depletion region, oxygen interdiffusion at the substrate, or a structural reconstruction of the film near the substrate. Further modelling suggested a depletion zone around the substrate. Within the paper, there exists a scan through the energy of the fluorescence around the Cu edge, but relatively little discussion regarding it.

Following on from this initial thin film paper, Abbomonte *et al.* [111] looked at the spin ladder compound $Sr_{14}Cu_{24}O_{41}$. In a similar vein to the previous paper, this concentrated on the idea of a hole crystal. In this case a superlattice reflection was found at (0,0,0.2), the energy scans at fixed wavelength are shown in Figure 5.9. Note that in this figure the energy dependence in the region of 530 eV is well below the tabular value for the O K edge of 543 eV, and so Abbamonte *et al.* describe the resonance as a mobile carrier peak, rather than a structural distortion peak. In comparison the energy resonances on the Cu edge correspond well to the tabulated value of the L_3 (932 eV), and L_2 (952 eV), however again Abbamonte *et al.* argued that the small difference in the resonant edge between that from the fluorescence signal and the peak signal indicated that the peak arises from holes on neighbouring ligands. Very recently Rusydi *et al.* have measured further results from the Ca doped spin ladder, $Sr_{14-x}Ca_xCu_{24}O_{41}$ [112]. For the values $x = 10, 11, 12$, they report the observation of a superlattice peak, with a wavevector (0,0,1/3). With similar arguments to the previous paper, and observing a similar resonance at the pre- O K edge, they suggested a hole crystal. No observation was made of a superlattice peak at $(0, 0, 1/4)$ in other appropriately doped samples, suggesting that the lattice is only stable for odd periodicities.

In addition to the spin ladder compounds, Abbamonte *et al.*, published results on the single layered $La_{2-2x}Ba_xCuO_4$. Single crystals with $x = 1/8$ were grown, and superlattice reflections were observed at (1/4, 0, 3/2) below 60 K, corresponding to the expected static charge stripe correlations. In addition to resonating at the so-called mobile carrier hole

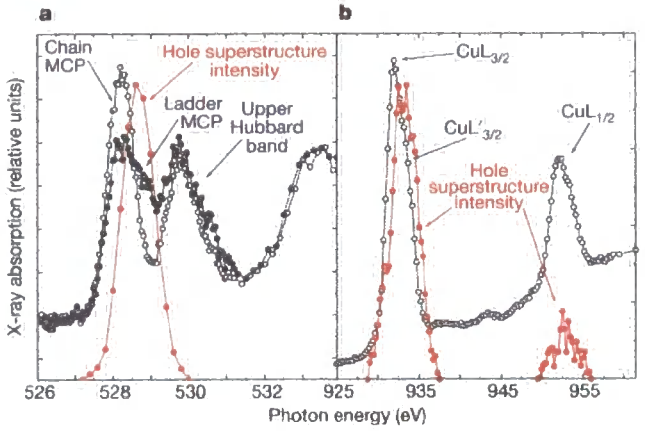

Figure 5.9: Energy dependence of the hole superstructure reflection compared to X-ray absorption spectra. Black symbols, absorption spectra of $Sr_{14}Cu_{24}O_{41}$, taken *in situ* in fluorescence-yield mode, in the vicinity of **a**, the oxygen K edge, which is a $1s \rightarrow 2p$ transition, and **b**, copper $L_{3/2,1/2}$ edges, which are $2p \rightarrow 3d$ transitions where the core hole is left with its spin either parallel ($j = 3/2$) or antiparallel ($j = 1/2$) to its orbital moment. Open circles, data taken with the photon polarization $\mathbf{E}||\mathbf{a}$; filled circles, data taken with $\mathbf{E}||\mathbf{c}$. The data are in good agreement with ref.13[*sic*][a]. "Chain MCP" and 'ladder MCP" indicate the respective oxygen mobile carrier prepeaks (MCP) where scattering from the holes is enhanced. Red symbols, integrated intensity of the hole superstructure reflection as a function of incident photon energy. The reflection is visible only when the X-ray energy is tuned to the ladder MCP or the copper $L_{3/2}$ ligand hole sideband, indicating the presence of a standing wave in the hole density in the ladder. *Figure from Abbamonte et al.* [111].

[a]Ref 13; N. Nücker *et al. Phys. Rev. B* **62** 14384 (2000)

energy below the O K edge, the peak also resonated a few eV higher than the carrier hole resonance, which was then interpreted to give an indication to the degree of the behaviour as a Mott insulator. Such a peak in reciprocal space, therefore requires both the Mott state and the carrier density to be modulated in real space. The sharp resonance at the Cu edge was stated as most likely being a distortion in the Cu lattice.

5.1.4 The Nickelates

In addition to the manganites and cuprates, Schüßler-Langeheine *et al.* [113] have reported a soft x-ray diffraction study of $La_{1.8}Sr_{0.2}NiO_4$. The nickelates show many similar properties to the manganites, and there have been detailed studies using both x-rays [114] [115] and neutrons [116] [117] [118]. This soft x-ray study observed both the charge and the magnetic order peak in $La_{1.8}Sr_{0.2}NiO_4$ (Fig. 5.10). The nickelate compounds have a distinct advantage due to the wavevector of the superlatttice peaks strongly dependent on the doping level. Thus it is possible to reach the charge order peaks in compounds with $x < 0.28$ and the magnetic order peaks when $x > 0.18$. Thus there are a range of doping levels where both the charge and magnetic peak are available in the same sample (albeit in different directions). In addition there have been theoretical predictions by Hotta and Dagotto [119] that there may be orbital ordering occurring in the $x = 0.5$ sample, although there have been no experimental reports so far. In comparison to the manganite and cuprate resonances, the energy spectra from the nickelates is relatively simple, however by modelling the resonance of the charge order peak, Schüßler-Langeheine *et al.* was able to confirm that the charge order as well as the magnetic order resides in the NiO_2 layers.

5.2 Technical Feasibility

The majority of the difficulties with soft x-ray diffraction can be summed up by one factor; the absorption length of the x-rays. Although x-rays at the Mn K edge suffer from air absorption, they have enough energy so that beryllium domes, and flight paths with mylar windows can all be used. At the L edges of the transition metals, the x-ray energies are typically below 1 keV. The absorption length in air falls to less than 1 cm. No beryllium shrouds can be made thin enough, and so the entire path of the x-rays from the synchrotron to the sample to the detector must be entirely under vacuum, and only very thin contamination windows can be used. In addition the small penetration depth of the x-rays mean that the

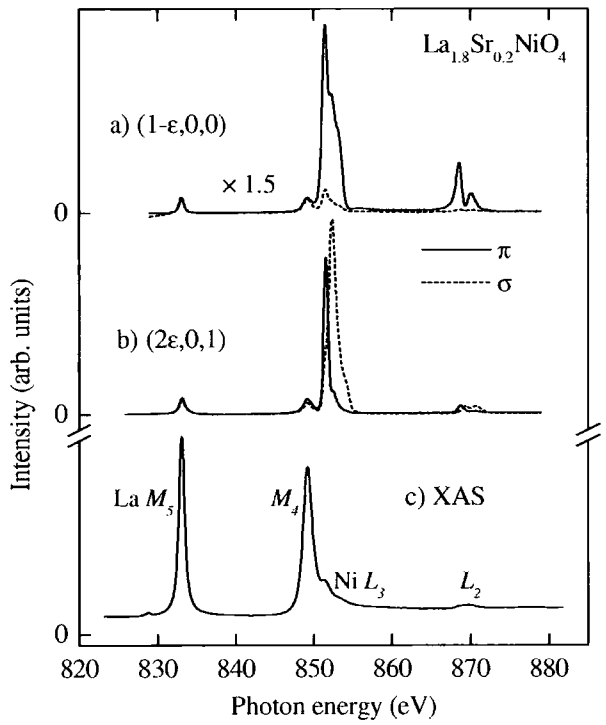

Figure 5.10: Intensities of the (a) $(1-\epsilon, 0, 0)$ spin-order and (b) $(2\epsilon, 0, 1)$ charge-order superstructure peaks as a function of photon energy at 60 K for π-polarized (dashed line) light. The insets show scans through the respective superstructure peaks on a linear scale recorded with π-polarized light along the [100] (H) and [001] (L) direction; (c) x-ray absorption signal. *Figure from Schüßler-langeheine et al.* [113] *describing* $La_{1.8}Sr_{0.2}NiO_4$.

samples must have a high quality surface, and the surface must be identical to the bulk.

The second, more fundamental problem, and ultimately the limit of the usefulness of soft x-ray diffraction, is the size of **Q** space. An x-ray with an energy of 642 eV (Mn L_3 edge), has a wavelength of 19.31 Å. Therefore in order for a peak to be in the Ewald Sphere at this energy, its period has to greater than 9.66 Å (half the wavelength) in real space. The first observation of a Bragg peak was by Wilkins *et al.* [36], who observed the (002) in the bilayer manganite $La_{1.05}Sr_{1.95}Mn_2O_7$. This was an ideal sample, not only was it available in high quality samples, it also cleaved along the required surface. It therefore required no additional surface preparation after cleaving, and is one of the few compounds from which a Bragg peak is visible at room temperature. Not only that, the study could be extended beyond looking at a simple Bragg peak by cooling the sample down and observing the (001) magnetic peak.

Unfortunately, things get a lot harder quickly. The next sample of interest $La_{0.5}Sr_{1.5}MnO_4$, was studied simultaneously by Wilkins *et al.* [35] and Dhesi *et al.* [101]. Not only did this sample have no Bragg peak in the Ewald sphere, the orbital order reflection at $(\frac{1}{4},\frac{1}{4},0)$ required cutting and polishing the sample, and then aligning without a Bragg peak for reference. As there is no Bragg peak, there is no reference apart from the surface of the crystal. Thus it is extremely important to accurately align and cut the sample so that the required reflection is surface normal, in order to find it.

5.3 Soft X-ray Chambers

This thesis describes results taken from three different beamlines, beamline 5U.1 at Daresbury Synchrotron, UK; beamline ID08 at the European Synchrotron Radiation Facility (ESRF), France; and beamline X1B at the National Synchrotron Light Source (NSLS), USA. All these beamlines serve a varied user community, and x-ray diffraction is only a small proportion of experiments scheduled. The end stations that are in use at each of these beamlines are different and are described below. These endstations could be described as first generation soft x-ray diffractometers. As such none are ideal, however modifications are continually made to improve their performance. It is hoped that the successes and difficulties discovered in running these endstations can be taken advantage of, if second generation chambers are designed and built. In the UK this may coincide with the construction of Phase II beamlines at DIAMOND light source.

5.3.1 5U.1, Daresbury, UK

This soft energy beamline is located on an undulator at the SRS. The storage ring is a 2 GeV machine, with an operating current of 200 mA. The undulator has recently been replaced in autumn 2004, however these results were taken on the previous insertion device, producing only linearly polarised light.

The Chamber

The diffraction chamber used on this beamline was originally designed for testing optics. It has subsequently been developed for diffraction and reflectometry. The chamber is cylindrical (Fig. 5.11), housing a θ stage and a 2θ arm. The θ sample stage has two translational movements, one horizontal, perpendicular to the beam, and the other vertical. These translations are rotated about the centre of rotation with θ. Further modification added a pseudo-χ movement, by adding a translation stage onto the 2θ arm to move the detector out of the scattering plane. The sample stage is cooled by passing liquid nitrogen through narrow bore tubes into the chamber and through the sample mount. A heater coil is also mounted on the sample stage to enable a stable controllable sample temperature. The base temperature is in the region of 83 K.

The chamber is evacuated by a large turbo pump located on the base of the unit. The chamber has a large door on the front, enabling easy access. This is invaluable for effectively mounting samples, and thus achieving good thermal contact between the sample, mount and cooling stage. This also means that modifications can be made to the chamber set-up during experimental time. The door is sealed by a rubber seal, despite this, vacuums exceeding 10^{-6} mbar are achieved within ~ 2 hrs of closing the chamber. A combination of simplification and access has made this the most reliable soft x-ray chamber. The limitation has always been the liquid nitrogen cooling, meaning a base temperature of 80 K. This chamber is currently being modified to enclose a closed cycle ^{4}He cryostat, initial reports indicate that the base temperature has been lowered to 40 K.

Beamline 1.1

A few results in Chapter 7 were taken on the 1.1 beamline at Daresbury. This was using the same experimental chamber as 5U.1. The beamline is based on a bending magnet, and as such the flux is significantly lower than that on 5U.1. The radiation used on the beamline

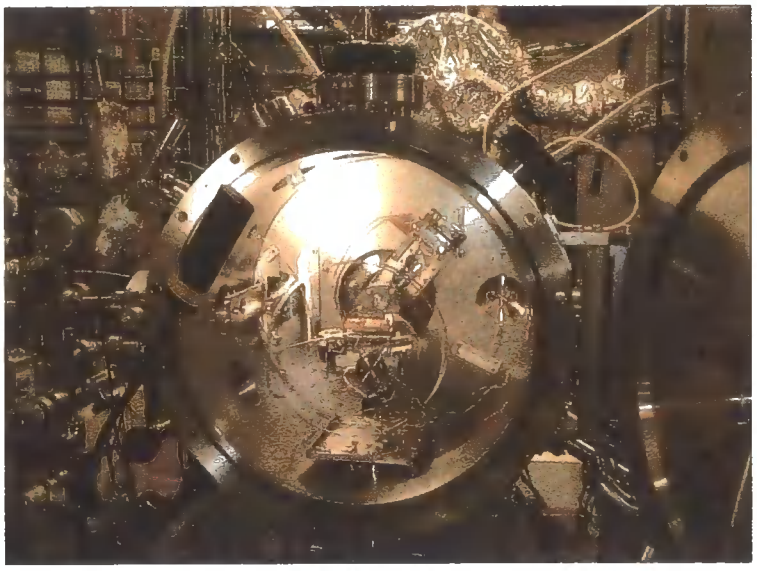

Figure 5.11: The diffractometer installed on the 5U.1 beamline, Daresbury, UK. X-rays enter from the left, and are scattering from the sample (shown here at $\theta = 0$) and detected by the photodiode mounted on the 2θ arm (here at approximately 60°).

was linearly polarised.

5.3.2 ID08, European Synchrotron Radiation Facility, France

The ID08 beamline is very successful for soft x-ray spectroscopy at the ESRF. The beamline has a number of endstations, and can also accommodate users' own endstations. The beamline photons are provided by two APPLE (Advanced Planar Polarised Light Emitter) type variable polarisation undulators, which are currently configured to provide linear polarised light, aligned vertically and horizontally, plus left and right circular polarised light.

The Chamber

The diffraction chamber is a hemispherical shape, with the flat edge vertical and parallel to the beam. Onto this flat face is mounted the θ and 2θ movements, and also the cooling, which is provided by a liquid helium cooled stage, with Cu braids to the sample mount. The strength of this chamber has always been the number of available motor movements, in particular the ability to perform azimuthal scans. There were initially problems with the cooling, especially when the load-lock sample transfer was in use. This suffered from poor thermal contact between the sample mount and the cold stage. A vast improvement has been made through a combination of dispensing with the sample transfer, and redesigning

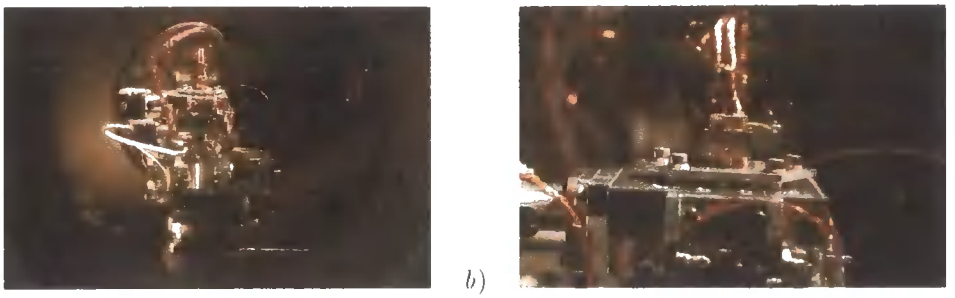

a) *b)*

Figure 5.12: Detail of the diffraction chamber on the ID08 beamline, ESRF. *a)* shows the main internal structure with the xyz movement mounted on the theta drive. *b)* shows the detail of the crystal mounting assembly with the liquid ^{4}He cooled braids attached to the rear of the mechanism.

the mount. The chamber is now capable of achieving a base sample temperature of 22 K.

5.3.3 X1B, National Synchrotron Light Source, USA

A small quantity of results have come from beamline X1B. The beamline has a number of end stations as well as the diffractometer. There are however severe limitations in the beamline. Firstly the energy is not calibrated, and so either fluorescence or a Bragg peak is necessary to initially calibrate the energy. In addition the chamber is not highly reliable, and the control system suffers from over complexity.

The Chamber

In contrast to ID08 and 5U1, the scattering plane of the diffractometer is horizontal (Fig. 5.13). This was designed in order to minimise charge background scatter. Unfortunately the incident beam is only $\sim 60\%$ horizontally polarised, and so is only partially effective, and the mixed incident polarisation makes theoretical modelling tricky. The chamber operates at a very low pressure (10^{-9} mbar), and sample mounting is through a load-lock. Despite this the base temperature is an impressive 20 K, which was until recently the lowest available. Temperature is the strength of this beamline as the intensity of the beam appears less than 5U.1, and the reliability of the chamber and the synchrotron is less than ideal.

5.4 Future Technical Advances

The soft x-ray diffraction chambers that have been described represent the first generation of soft diffractometers. Clearly the major drive for these chambers has been low temper-

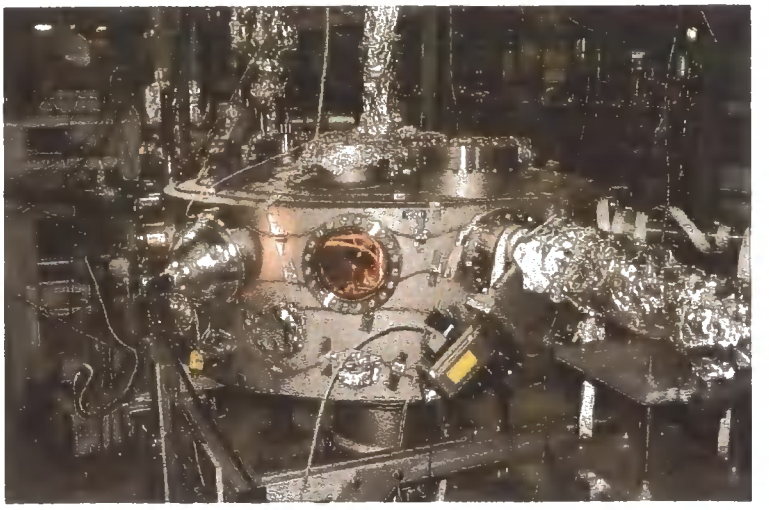

Figure 5.13: The soft x-ray chamber on X1B, NSLS. In contrast to 5U1 and ID08 the scattering is horizontal, in an attempt to minimise charge background. The sample transfer assembly can be seen in front of the computer rack in the left hand side of the photograph.

atures. This is probably the most important single function of a chamber. This has been relatively successful, and there are reports that other chambers (on BESSY, Germany, and SLS, Switzerland) can reach even lower temperatures (5 K is reported on the latter). This is likely to be near the limit of temperatures obtainable. The very nature of the technique requires the sample to have an entirely open view of the incident beam and the detector. This complicates and design of a radiation shield, which would normally encase a sample.

There are a number of other features of a diffractometer, along with temperature that would be very useful. Polarisation analysis is increasingly becoming an essential tool with transition metal K edge diffraction. Due to the very long wavelengths used, work is underway designing polarisation analysers using multilayers. Theoretically these could be designed specifically for each resonant edge.

In addition, and in parallel to polarisation analysis, azimuthal scans are a necessary aspect of magnetic scattering. This is already possible on the ID08 chamber, and the chamber on the Swiss Light Source, although only with a range of ϕ of 180°.

5.5 Future Soft X-ray Studies

The initial emphasis driving this new technique has been the desire to understand the nature of the ordering in the transition metal oxides. Unfortunately this is limited by samples. To date, cuprates, nickelates and manganites have been studied. The specific samples have been

limited by the requirement of a superlattice peak occurring within the Ewald sphere! This becomes even more difficult as one moves down the series. The vanadates and titanates would potentially reveal some very interesting results, however their absorption edges are so low in energy that finding suitable samples where the reflections fall inside the Ewald sphere is virtually impossible. It is the author's opinion that the future of transition metal studies lies in specifically grown thin film samples. Thin films and multilayers can be specifically grown in order that the magnetic order has a sufficiently long periodicity.

There may also be a future for something completely different. Biological samples typically have massive unit cells, and although are chiefly composed of carbon and oxygen, there may be instances where additional information can be gained from samples containing metals, such as haemoglobin.

Chapter 6

Orbital and Magnetic Order in $La_{0.5}Sr_{1.5}MnO_4$

This chapter reports studies on $La_{0.5}Sr_{1.5}MnO_4$ using soft x-ray diffraction which was introduced in the previous chapter. One of the major reasons for developing soft x-ray diffraction was in order to look at the orbital scattering from $La_{0.5}Sr_{1.5}MnO_4$ and to compare with the predictions by Castleton and Altarelli [97], as shown in Figure 5.5. The previous chapter has also listed some of the limitations of this technique, in particular the small region of reciprocal space accessible. Despite this, both the orbital order peak at $(\frac{1}{4},\frac{1}{4},0)$ and the magnetic order peak at $(\frac{1}{4},\frac{1}{4},\frac{1}{2})$ both lie within the Ewald sphere at the Mn L edges. Unfortunately the charge order peak at $(\frac{1}{2},\frac{1}{2},0)$ is outside the Ewald sphere. Attempts have been made to look at $La_{1-x}Sr_{1+x}MnO_4$ with a higher Sr doping, in which the charge order peak is accessible, however none have yet been successful due to the difficulty in growing high enough quality samples.

The main reason for looking at this compound, is to examine the long range ordering at low temperatures. It is well known that the material magnetically orders at $T_N \approx 120$ K, however is it unknown what effect this has on the possible orbital ordering and charge ordering. Indeed, the relationship between the orbital ordering and the structural Jahn-Teller distortion is a mystery. Are these two phenomena actually the same thing, or are they fundamentally different. If so, which drives what? Is the orbital order the more basic parameter, and does this then drive a structural distortion, or is it vice-versa? There are multiple possibilities for the orbital occupancy as shown in Figure 6.1, depending on the exact splitting of the e_g electron band determining whether the lower occupied orbital state is of the $d_{3x^2-y^2}$ type or the $d_{x^2-y^2}$ type.

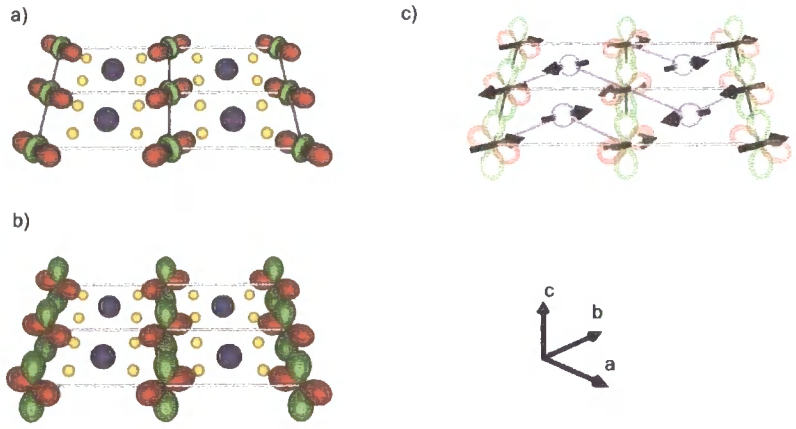

Figure 6.1: The structure of $La_{0.5}Sr_{1.5}MnO_4$. (a) and (b) show two different types of orbital ordering, $d_{3x^2-z^2}/d_{3y^2-r^2}$ type in (a) and $d_{x^2-z^2}d_{y^2-z^2}$ in (b). (c) shows that magnetic ordering with blue lines representing the ferromagnetic spin chains. The orbitals are drawn for the Mn^{3+} ions, while the small yellow spheres represent the oxygen atoms, and large blue spheres represent the Mn^{4+} ions.

6.1 Previous soft x-ray diffraction in $La_{0.5}Sr_{1.5}MnO_4$

Because of the interest in $La_{0.5}Sr_{1.5}MnO_4$ virtually every soft x-ray beamline has published results from this sample. Initially Wilkins *et al.* [100] published an energy scan of the orbital order peak, and a temperature dependence of various features in the energy scan at the Mn L_3 and L_2 edges. The energy scan is significantly more complex than that observed at the Mn K edge, appearing to have three distinct peaks at each edge. Unfortunately the energy resolution of the beamline 5U.1 where the data was collected is only 0.5 eV, and so fine structure is difficult to separate. The temperature dependence suggests that there is a deviation of the intensities of these points on the energy spectra at T_N, perhaps suggesting that the magnetic ordering affects the orbital ordering, or the crystal field. There was no theoretical fitting displayed with the data, although comparisons were made with Castleton and Altarelli [97].

Shortly after Wilkins *et al*, Dhesi *et al.* [101] published similar results collected from the ID08 beamline at the ESRF. This paper also concentrated entirely on the orbital order peak in $La_{0.5}Sr_{1.5}MnO_4$. The ID08 beamline does have a significantly higher energy resolution $\sim$ 100 meV), and so the three features at both the L_3 and L_2 edges are more distinct. Despite this, there are no obvious additional features that were not observed by Wilkins *et*

al. Interestingly Dhesi and co-workers observed a resonance at the L_1 edge of manganese, which Wilkins did not report (possibly this was unobservable due to the lower beamline intensity). This they compare to the Mn K edge resonance, as the L_1 involves mainly $s-p$ virtual transitions. A temperature dependence of the orbital reflection was also measured by Dhesi *et al.*, however the lowest temperature reported was 130 K, and so the interesting observations made by Wilkins *et al* at T_N are are not comparable.

Of more interest is the theoretical fits that Dhesi *et al.* published with the orbital spectra. These calculations were done using ligand field atomic-multiplet calculations, and the conclusion that was reached was that the electron occupancy was almost entirely on the $3z^2-r^2$ orbital (Fig. 1.16). Interestingly in the same month Huang *et al.* [120] published a study of $La_{0.5}Sr_{1.5}MnO_4$ using soft x-ray linear dichroism. This is a well developed technique that involves looking at the absorption spectra of the sample in different orientations. Thus there is no need to accurately align the sample in a specific orientation, as is the case with diffraction, rather a difference is observed in the spectra when the polarisation of the incident beam is perpendicular or parallel to the c axis of the sample (Fig. 6.2).

Huang and co-workers also presented a theoretical model, calculated through LDA+U band structure calculations. The LDA (Local Density Approximation) model is a first principal approach, that is there are no parameters that can be adjusted through empirical means. The straight LDA model is somewhat deficient for strongly correlated systems, as it is based on a many-body problem which is mapped onto a non-interacting system. The U represents the Coloumb repulsion, which modifies the system, and produces more realistic results. It has successfully been used to study perovskite materials such as $PrBa_2Cu_3O_7$ [121], and Jahn-Teller active materials such at $KCuF_3$ [122]. The LDA+U model by Huang *et al.* is shown in the bottom panel of Figure 6.2. They have modelled both the occupancy of the $d_{x^2-z^2}$ type orbitals and the $d_{3x^2-y^2}$ orbitals and shown that there exists a significant difference between the two. Perhaps the most striking difference is the sign of the L_2 part of the spectrum. The $d_{x^2-z^2}$ orbital shows a peak, while the $d_{3x^2-r^2}$ shows a trough. The experimental data show a peak for all doping levels. In addition there are differences in the L_3 part, and again the $d_{x^2-z^2}$ orbital type is a closer match. This suggests that in $La_{0.5}Sr_{1.5}MnO_4$ the orbital occupancy is dominated by the $d_{x^2-y^2}$ orbital. The principal difference between these two orbital types, as shown in Figures 1.17 and 6.1, is that the $3y^2-r^2$ (or $3z^2-r^2$) involves an elongation in a single direction (in the direction of the

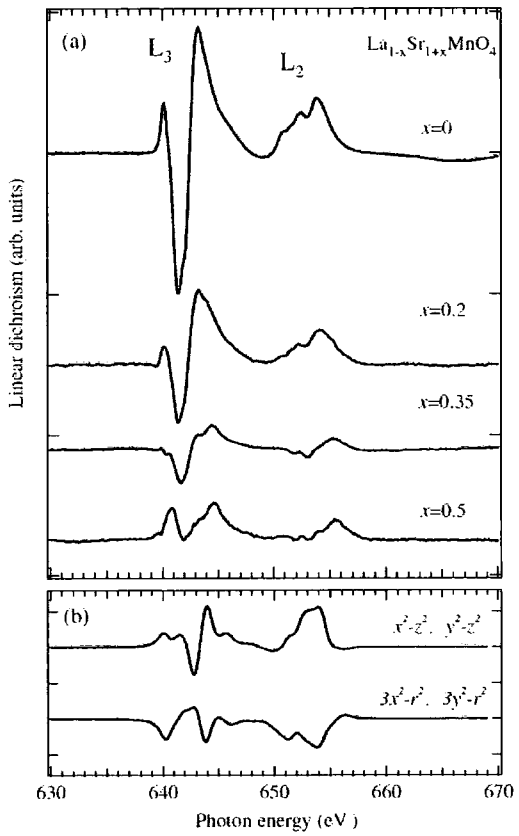

Figure 6.2: (a) LD in Mn $L_{2,3}$-edge XAS of $La_{1-x}Sr_{1+x}MnO_4$ with varied doping. Linear-dichroism spectra were derived from XAS normalised to the same peak intensity at Mn L_3 edge and measured at 300 K for $x \leq 0.35$ and 150 K for $x = 0.5$. (b) Calculated LD spectra of Mn^{3+} ions with $d_{x^2-z^2}/d_{y^2-z^2}$ and $d_{3x^2-r^2}/d_{3y^2-r^2}$ orbitals occupied. *Figure from Huang et al.* [120].

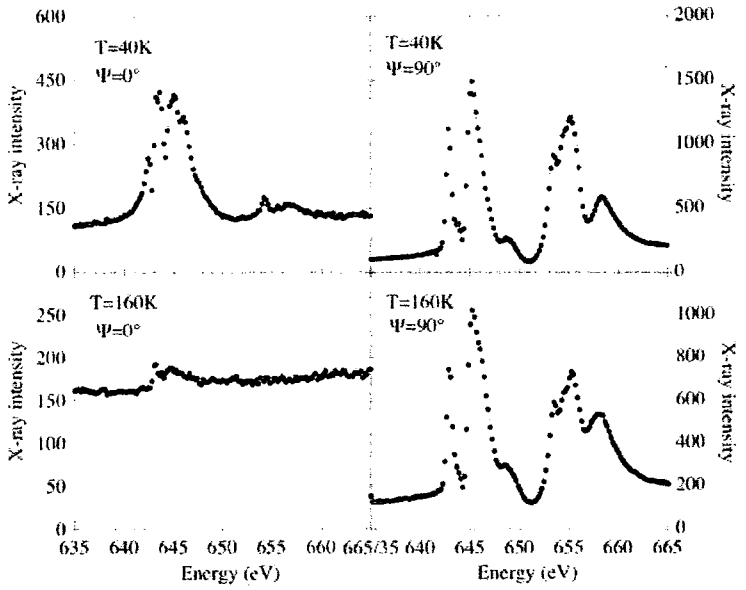

Figure 6.3: Photon energy dependencies of the intensity of the $(\frac{1}{4},\frac{1}{4},0)$ reflection in $La_{0.5}Sr_{1.5}MnO_4$ taken at $T < T_N$ (40 K) and $T_N < T < T_{CO}$ (160 K) are compared with two different azimuthal angles with incident π polarisation. *Figure from Staub et al.* [103].

orbital), whereas the $y^2 - z^2$ (or $x^2 - y^2$) orbitals effectively cause a contraction in a single direction (in the direction with no orbital).

Recently, Staub *et al.* [103] have published soft x-ray diffraction data from $La_{0.5}Sr_{1.5}MnO_4$. This was measured at the Swiss Light Source, on the SIM beamline. As with Wilkins *et al.* and Dhesi *et al.*, their measurements were confined to the $(\frac{1}{4},\frac{1}{4},0)$ orbital order peak. A temperature dependence of the peak was measured with an incident energy of 645.2 eV. There appears a jump in the intensity as the temperature is reduced below T_N, however no dependencies were measured at other energies for comparison. The temperature dependence was measured down to 30 K, lower than published by either Wilkins *et al.* or Dhesi *et al.*, however no major features appear below T_N. A big advantage in the end-station used by Staub *et al.*, is the ability to perform azimuthal scans.

The data from Staub and co-workers suggests that the nature of the orbital order peak changes at T_N. They display energy scans taken at $\phi = 90°$ and $\phi = 0°$, both between T_{OO} and T_N and below T_N (Fig. 6.3). For the scans taken at $\phi = 90°$ there appears no change between the two temperatures. The scan taken at $\phi = 0°$ shows very little scattering above T_N, and then shows a very different energy scan to those taken at $\phi = 90$ ° below T_N.

In addition, azimuthal scans of intensity at different energies were performed on the

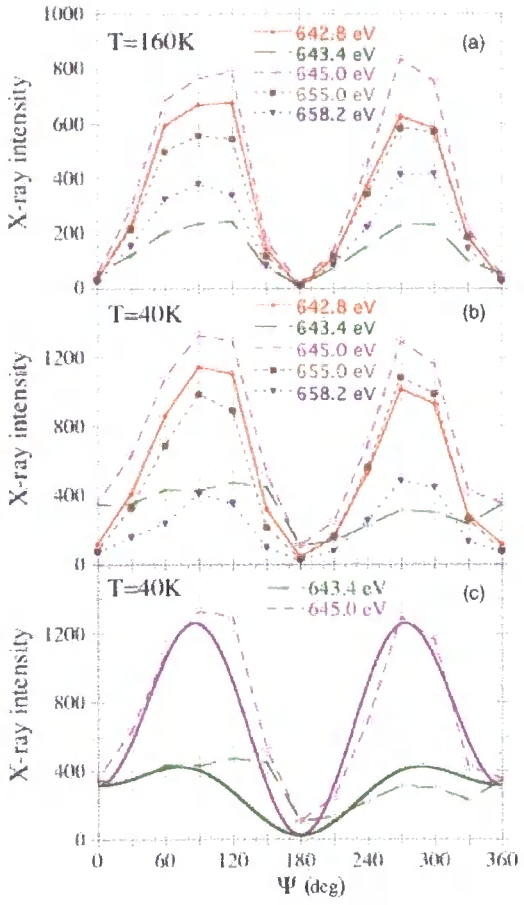

Figure 6.4: Azimuthal angle dependence of the intensity of $(\frac{1}{4},\frac{1}{4},0)$ reflection taken at various photon energies and π incident polarisation for (a) 160 K and (b) 40 K. (c) The azimuthal angle dependence of the two features at 40 K which no longer show two-fold symmetry, compared to calculations based on an orbital (or JT) and a magnetic contribution with $\alpha = 35°$. *Figure from Staub et al.* [103] $\alpha = 35°$ *corresponds to the magnetic moment aligned* 35° *from the* [110] *direction in the ab plane.*

orbital order peak (Fig. 6.4). This showed a general agreement with the majority of the azimuthal scans showing a twofold symmetry. The anomaly occurred with the low energy feature at 643.4 eV, which could be described as a pre-edge peak. This feature appears to show a different azimuthal dependence (fig 6.4c). This is the same feature that Dhesi *et al.* found difficult to predict theoretically. Polarisation analysis of the scattered beam was also shown by Staub and co-workers. This is a major achievement at soft energies. This showed that the entire spectrum existed purely in the $\pi \rightarrow \sigma$ channel and not in the $\sigma \rightarrow \sigma$ channel, suggesting that the peak is entirely magnetic, and not charge based. This included the pre-edge feature.

Finally, Wilkins *et al* [102] have published a second study looking at both the $(\frac{1}{4},\frac{1}{4},0)$ orbital order and $(\frac{1}{4},\frac{1}{4},\frac{1}{2})$ magnetic order peak, showing spectra of both peaks at the $L_{2,3}$ peaks together with a temperature dependence of these peaks, and an azimuthal dependence on the magnetic peak. This paper is based on the results presented in this chapter, together with theoretical fits, which will also be described.

6.2 Experimental Method

Unlike previously published results on $La_{0.5}Sr_{1.5}MnO_4$, this experiment looked at both the orbital order peak $(\frac{1}{4},\frac{1}{4},0)$, and the magnetic order peak at $(\frac{1}{4},\frac{1}{4},\frac{1}{2})$. This proved to be extremely useful for the multiplet calculations. An azimuthal scan was performed on the orbital order peak. No polarisation analysis was conducted, due to experimental limitations of the chamber.

The experiments were performed at beamlines 5U1 at Daresbury and ID08 at the European Synchrotron Radiation Facility (ESRF). Single crystals of $La_{0.5}Sr_{1.5}MnO_4$ with dimensions $10 \times 3 \times 3$ mm^3 were grown at the University of Oxford using the floating zone method. They were cut with either [110] or [1$\bar{1}$2] directions surface normal and polished with 0.25 μm diamond paste to a flat shiny surface.

The crystals were mounted in the ID08 four-circle diffractometer (see section 5.3.2) operating at a base pressure of 1×10^{-8} mbar, and equipped with a photodiode detector. The beamline x-rays are provided by an APPLE type undulator, configured for horizontal, vertical, left and right circularly polarised light. The x-ray beam has an incident flux of 10^{12} photons s^{-1} at 650 eV with an energy resolution of 200 meV. Sample cooling was achieved using a liquid ^{4}He cryostat attached to the sample stage by copper braids resulting in a base temperature of 63 K.

On the 5U1 beamline (see section 5.3.1), crystals were mounted on a two circle diffractometer enclosed in a high vacuum chamber with a base pressure of 1×10^{-8} mbar. The incident beam has a resolution of 500 meV, and a beamsize of 1×1 mm^2. The sample was mounted on a liquid nitrogen cooled copper block, with a small manual χ adjustment for initial orientation. The base temperature achieved was 83 K. Temperature stability between 83 K and 300 K was achieved with a heater element, and control thermometer mounted next to the sample.

At both beamlines the experimental procedure was identical. The incident energy was

set to the manganese L_3 edge, and superlattice peaks located at the $(\frac{1}{4},\frac{1}{4},0)$ and $(\frac{1}{4},\frac{1}{4},\frac{1}{2})$ positions. Each reflection was measured on a separate sample. Energy scans of the reflections were performed at fixed wavevector. The integrated intensity was measured by longitudinal scans through the peak at fixed energy.

The azimuthal dependence of the orbital order superlattice reflection was measured on the ID08 diffractometer by rotating the sample around the scattering vector, $\vec{Q}$. In the absence of an orientation matrix this was achieved by rotation of the ϕ axis in the diffractometer.

6.3 Results

6.3.1 Orbital Reflection

Figure 6.5 shows the energy dependence of the intensity of the scattered beam at fixed wavevector of $\vec{Q}_{OO} = (\frac{1}{4}, \frac{1}{4}, 0)$. This shows a strong resonance at the L_3 edge, and a weaker resonance at the L_2 edge. These energy resonances are not simple Lorentzian peaks, as has been seen previously at the Mn K edge, but contain some fine structure. Each peak appears to be comprised of three separate features, although these are not in the same ratio in each peak. Concentrating on the lower energy peak at the L_3 edge, there is an extremely sharp peak at 640.5 eV, approximately 2 eV below the main resonance. This peak has a small high energy shoulder to it. Then there is the main resonance at 642.5 eV. This is fairly symmetrical, with no obvious shoulders. Finally there is a very weak peak, some 4 eV above the main resonance.

The resonance at the L_2 edge is weaker by comparison to the L_3 edge and much broader. The definition between the peak features at the L_2 edge is less distinct, than those at the L_3. Again, however, there are three obvious peaks, and the separation of these peaks in energy from the main peak is similar to that observed at the L_3 edge. The high energy peak is far more distinct at the L_2 edge, having an intensity almost half that of the main resonance. In comparison the peak intensity of the L_2 edge is just over one half that at the L_3 edge.

6.3.2 Magnetic Reflection

In addition to measuring the orbital order peak in $La_{0.5}Sr_{1.5}MnO_4$ we were able to access the magnetic peak at $(\frac{1}{4},\frac{1}{4},\frac{1}{2})$. The magnetic peak in the bilayer material $LaSr_2Mn_2O_7$ has previously been measured through soft x-ray diffraction [36], and has been observed to be

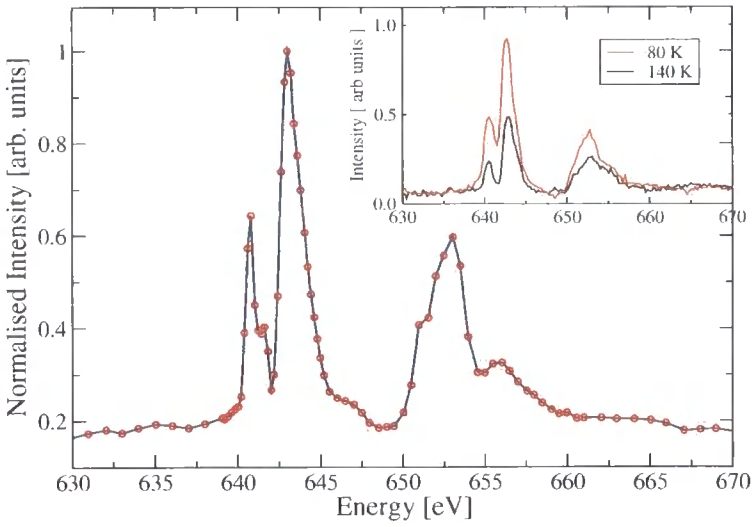

Figure 6.5: Energy scan at fixed Q of the $(\frac{1}{4},\frac{1}{4},0)$ orbital order reflection in $La_{0.5}Sr_{1.5}MnO_4$. Data taken at ID08, at 63 K. Inset shows the energy scan taken above and below T_N, data taken at 5U.1.

extremely strong. As such, it was no surprise that the the magnetic peak in $La_{0.5}Sr_{1.5}MnO_4$ was several orders of magnitude stronger than the orbital peak. Because the wavevectors of each peak lay in different directions, two separate samples were prepared with the required wavevector normal to the surface of the corresponding sample.

The energy spectrum of the magnetic peak, as shown in Figure 6.6, is significantly different to the spectrum of the orbital order peak. The resonance at the L_3 edge is a factor of 10 larger than that at the L_2 edge. The spectrum at the L_3 edge is also more complicated. There are two main resonances, the peak with the lower energy is split into two, and also has an additional small peak on the low energy shoulder. The higher energy peak in the L_3 edge also has a small higher energy peak. The L_3 peak is not so obviously split into two parts as was seen in the orbital order peak. The resonance at the L_2 edge is very weak, and also quite broad. Despite this, there is a small amount of structure to the peak with a noticeable 'pre' peak at 652 eV, before the main broad peak centred at 654 eV. There is no indication of a third peak at higher energies.

6.3.3 Azimuthal Dependence

The azimuthal dependence of the orbital order peak was measured using the diffractometer on the ID08 beamline. This end-station is capable of a 180° rotation in ϕ, allowing a reasonable azimuthal dependence to be measured. If necessary the sample could be removed, and

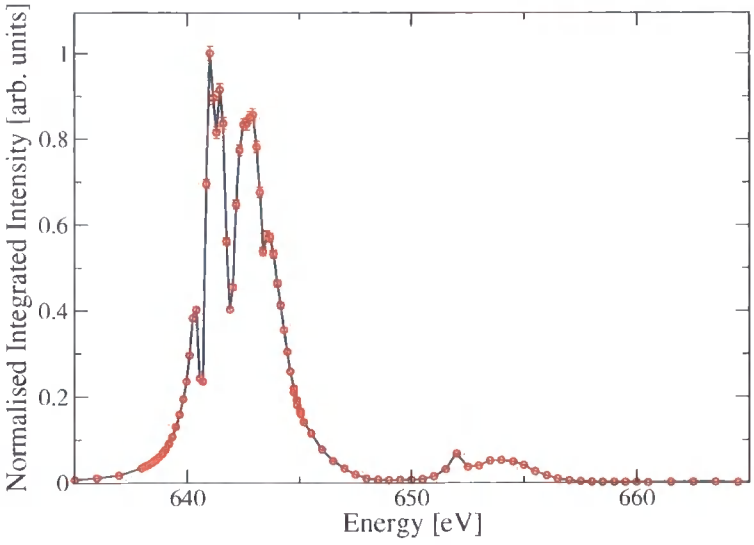

Figure 6.6: Energy scan at fixed Q of the $(\frac{1}{4},\frac{1}{4},\frac{1}{2})$ magnetic order reflection in $La_{0.5}Sr_{1.5}MnO_4$. Data taken at ID08 at 63 K.

remounted through 180° in order to collect the full rotation. Given the simple nature of this azimuth dependence, this was deemed to be unnecessary, and not an effective use of beamtime. The azimuthal dependence is shown in Figure 6.7. In addition the solid line shows a simulation of the azimuthal dependence of the orbital order peak. This has been calculated in the same way that was conducted in Chapter 3, outlined in the Appendix. Note that these calculations only take into account the symmetry of the orbitals (in the *ab* plane), and so there is no way to distinguish between the two orbital types as discussed earlier. This simulation does give information regarding the direction of the orbitals. As can be seen in Figure 6.7, there appears to be very good agreement between the simulation and the data, suggesting that the proposed ordering of the orbitals is correct.

It is noted that, as can be seen in Figure 6.7, the intensity of the $(\frac{1}{4},\frac{1}{4},0)$ peak *completely* disappears at a point on the azimuth. This is important, as there has been speculation on the twinning of these crystals, allowing the orbital order peak to be contaminated by the magnetic order peak, which could have explained the anomaly at T_N. This azimuthal dependence was taken at 63 K, below T_N. As the magnetic peak has no azimuthal dependence, if part of the resonance was due to the magnetic peak, one would not expect the intensity to go to zero, as there would be a constant peak intensity from the magnetic ordering. Interestingly, the different spectrum observed by Staub *et al.* [103] (Fig. 6.3) below T_N at an azimuthal angle of $\phi = 0°$ at the orbital order reflection appears very similar to the spectrum of the

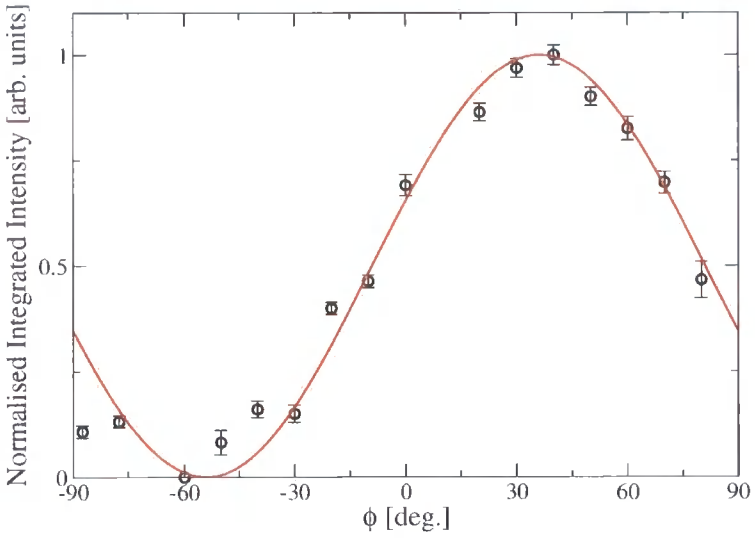

Figure 6.7: Azimuthal dependence of the intensity of the $(\frac{1}{4},\frac{1}{4},0)$ orbital order reflection in $La_{0.5}Sr_{1.5}MnO_4$. The position of ϕ corresponds to the motor position in the chamber, and is not aligned with respect to any crystallographic direction. Data taken at ID08 at 63 K.

magnetic order reflection (Fig. 6.6), suggesting that crystal twinning was apparent in his observations.

In addition to measuring the intensity of the main peak at the L_3 edge, as a function of ϕ, energy scans were measured at fixed wavevectors at regular intervals around the azimuth. Figure 6.8 shows there is very little change in the energy scan as the sample is rotated. This confirms the reasoning that the entire resonance is composed of the orbital signal.

6.3.4 Temperature Dependence

The intensity of the orbital and magnetic peaks were measured as a function of temperature (Fig. 6.9). These measurements were made on the 5U.1 diffractometer, where the temperature stability is better than on ID08. Consequentially, the base temperature achieved was only 80 K. Measurements as a function of temperature were made with a wide (300 μm) slit in the incident beam. This increases the intensity of the scattered beam, and also decreases the energy resolution (to $\sim$1 eV). This has the affect of broadening the peak, so ensuring that any slight variation of incident energy does not affect the results significantly.

The magnetic peak was measured solely at the L_3 edge. The intensity of the peak drops fast and disappears at T_N as expected. The intensity of the orbital peak show a rather more interesting behaviour. The orbital peak was measured at both the major resonance at the L_2

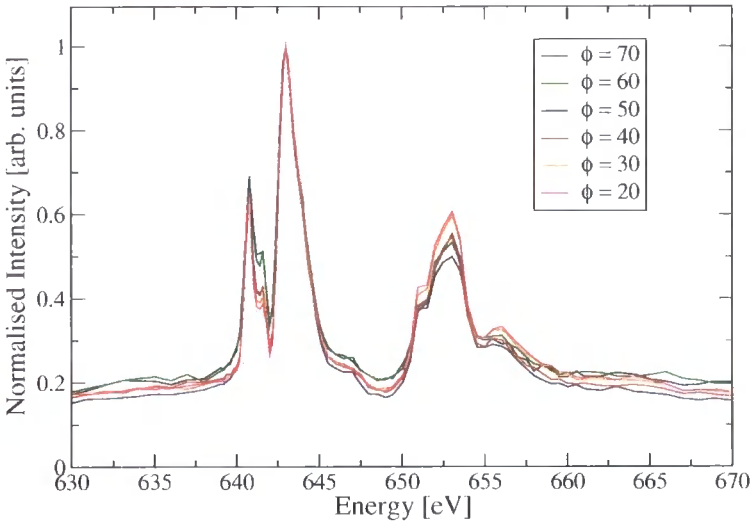

Figure 6.8: Energy scans of the orbital order peak in $La_{0.5}Sr_{1.5}MnO_4$ at various ϕ positions around the azimuth. This shows there is very little change in the shape of the energy spectrum as the intensity of the orbital order peak changes. Data taken at ID08 at 63 K.

edge and the L_3 edge. The intensity of both these resonances is fairly stable between 80 K and T_N. At the temperature is increased above T_N there is a significant drop in the intensity of both resonances. At a temperature 20 K above T_N, the intensity of the peaks steadily decreases, before dropping off at T_{OO}. The middle panel of Figure 6.9 shows the ratio of the intensity of the L_3 and L_2 peaks, which will be referred to as the branching ratio. This ratio is always above 1, even when both peaks are very weak. The interest of this branching ratio, originated from Castleton and Altarelli's paper [97] showing that the resonance at the L_3 edge was primarily due to the structural distortion, whereas that at the L_2 edge is due to the orbital ordering. Therefore a change in this branching ratio would represent a de-coupling of these two orderings. It is important not to emphasise this association of resonances with ordering types too strongly, as this is a rather simplistic view, and it would be incorrect to determine the strengths of these orderings directly from the strengths of each resonance. Despite this, the change in the ratio between the intensities of these two resonances, does appear to imply that there is a different behaviour with temperature between the orbital ordering and the Jahn-Teller distortions.

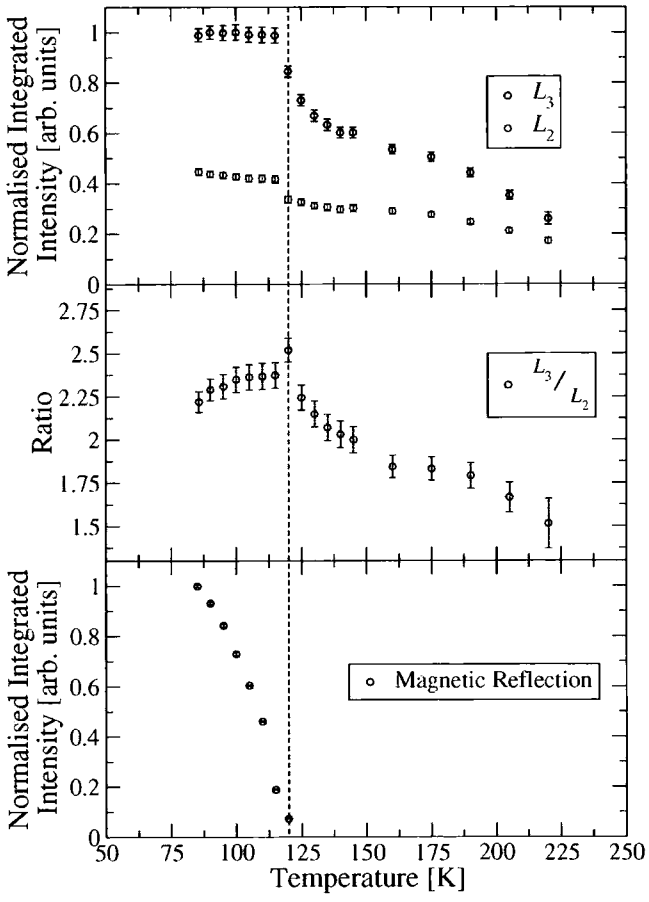

Figure 6.9: Temperature dependence of the main features at the L_3 and L_2 parts of the orbital order spectrum (*top*). The ratio of the intensity of these two features (branching ratio) (*middle*), and the temperature dependence of the $(\frac{1}{4},\frac{1}{4},\frac{1}{2})$ magnetic peak as a comparison (*lower*). The vertical line corresponds to T_N. Data taken at 5U.1, with 300 μm slits.

6.4 Theoretical Model

The theoretical fits shown with this data were calculated by N. Stojić and N. Binggeli led by M. Altarelli, at ICTP, Trieste. The model was developed with the data in this chapter, where the simulation parameters were adjusted in order to fit the experimental data. There is further information on the details of this model in the recent paper by Stojić *et al.* [123]. The model is based on atomic multiplet calculations in a crystal field. The calculations originate from the Hannon-Trammell formula (Eqn. 1.12) [62]. Cowan's atomic multiplet program [98] provided *ab-initio* values of the radial Coulomb integrals, and the spin-orbit interaction for an isolated Mn^{3+} ion. The core hole lifetime representation $\Gamma = 0.5$ eV, and the scattering intensity was convoluted with a 0.1 eV Gaussian to simulated the experimental resolution. The fitting procedure starts with adjusting the crystal field type and strength by modifying the cubic (X^{400}) and tetragonal (X^{220}) crystal field parameters.

The results turn out to be insensitive to small orthorhombic distortions. Orbital and magnetic spectra calculated using the atomic multiplet code and including the crystal field effects were then compared to the experimental spectra and the procedure is continued until the optimised set of crystal field parameters is found. In order to take into account the screening effects present in a real crystal with respect to the atomic picture, the Slater integrals were scaled to 75 % of their atomic values.

6.5 Discussion

The increase in complexity in the information from resonant scattering at the Mn L edge means that the results are almost meaningless without some form of theoretical calculation to interpret the results. The calculations that are presented here do not take into account temperature, and so are only valid for the low temperature phase. Figure 6.10 show calculated fits to the experimental data for the $(\frac{1}{4},\frac{1}{4},0)$ peak. The upper two panels show the two possible orbital orientations, the lower panel shows the $d_{x^2-z^2}$ orbitals with an orthorhombic addition to the crystal field. For this reflection there appears to be very little difference between the two orbital models, however examination of Figure 6.11 will reveal that this is not the case for the magnetic $(\frac{1}{4},\frac{1}{4},\frac{1}{2})$ peak. Here there is a very clear difference between the top two spectra. Although it appears that the $d_{3x^2-y^2}$ produces a better fit at the L_2 edge, the L_3 edge is completely missing the major peak in the resonance. As such, it would

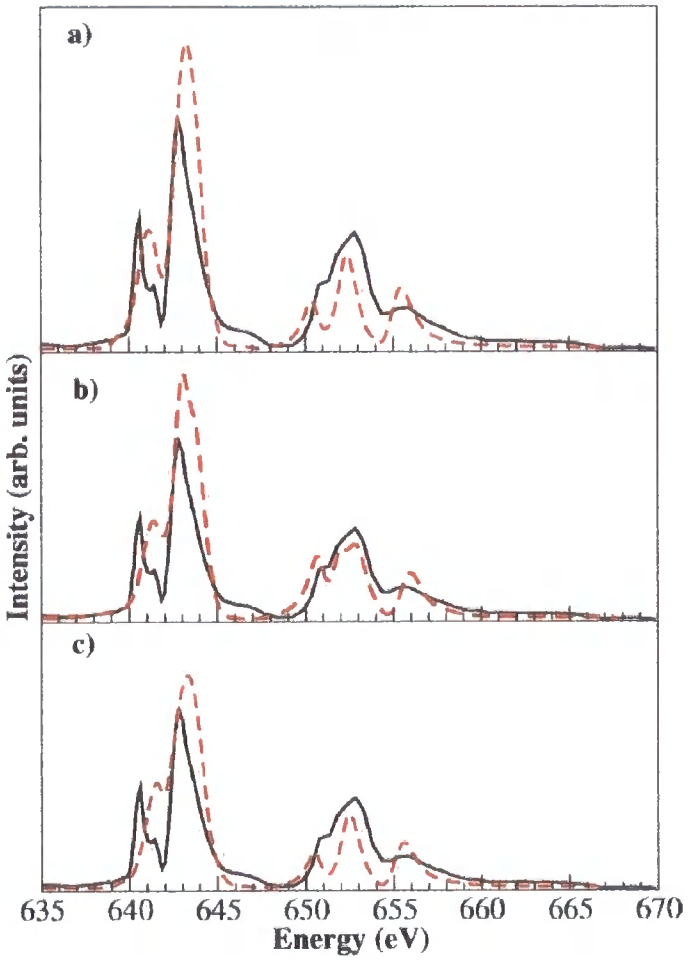

Figure 6.10: Theoretical fits to the experimental data of the orbital $(\frac{1}{4},\frac{1}{4},0)$ peak. The black line shows the experimental data, and dashed red lines the theoretical fits. The upper panel (a) shows the simulation from the $d_{x^2-z^2}$ model, (b) $d_{3x^2-y^2}$ model, and (c) shows the fit for the orthorhombic crystal field. Data taken on the ID08 beamline at 63 K.

seem more likely that the occupied orbital is in fact the $d_{x^2-z^2}$ orbital. This is in agreement with the XMCD data from Huang *et al.* [120].

Both the experimental spectra were fitted using the same optimised crystal field parameters: $X^{400} = 5.6$ eV, $X^{220} = 3.75$ eV. In addition, the panel (c) in Figures 6.10 and 6.11, had and additional orthorhombic crystal field: $X^{222} = -1.1$ eV. These can be expressed in terms of the energy of the crystal field distortions, and is shown schematically in Figure 6.12. This shows very clearly that there is a significant splitting of the e_g electron band, suggesting a large Jahn-Teller distortion. The effect of reducing the tetragonal crystal field can be seen in Figure 6.13, showing a massive reduction in the size of the L_3 peak, and relatively little change at the L_2 edge.

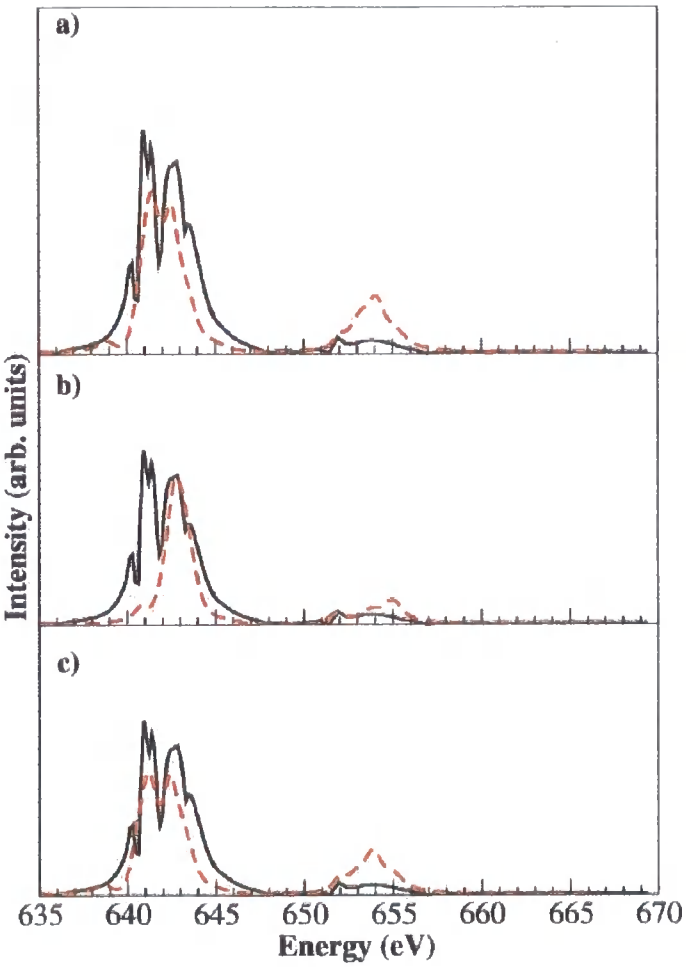

Figure 6.11: Theoretical fits to the experimental data of the magnetic $(\frac{1}{4},\frac{1}{4},\frac{1}{2})$ peak. The black line shows the experimental data, and dashed red lines the theoretical fits. The upper panel (a) shows the simulation from the $d_{x^2-z^2}$ model, (b) $d_{3x^2-y^2}$ model, and (c) shows the fit for the orthorhombic crystal field. Data taken on the ID08 beamline at 63 K.

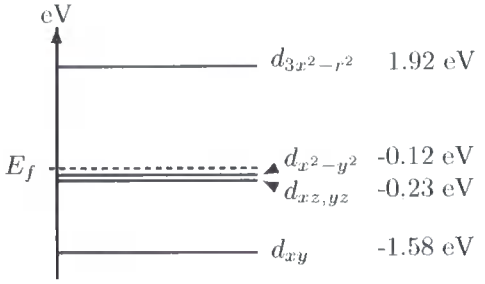

Figure 6.12: Representation of the relative energies of the $3d$ orbitals corresponding to the theoretical calculations shown in Figures 6.10(a) and 6.11(a).

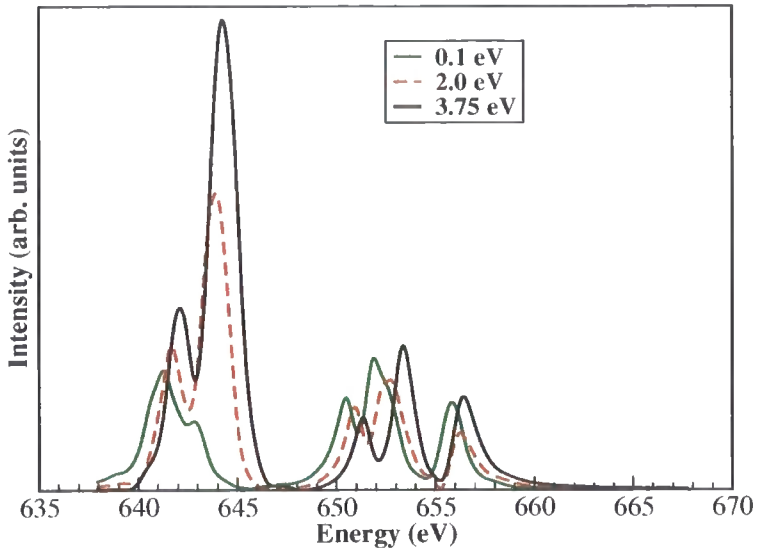

Figure 6.13: Variation of the Jahn-Teller effect through the reduction of the tetragonal crystal field: $X^{220} = 3.75$ eV (full black line), 2 eV (dashed red line) and 0.1 eV (full green line).

As mentioned previously, the temperature dependence is difficult to fit as the calculations are all performed at zero temperature. However, if the argument specifying the L_3 edge corresponding to the Jahn-Teller type distortion, and the L_2 edge corresponding to the Goodenough type orbital ordering is true, Figure 6.9 shows that the ratio of these peaks varies with temperature. Indeed at T_N there appears a change (possibly in the sign) of the gradient, suggesting that the onset of the magnetic ordering has a significant effect on the orbital order. The direction of the alignment of the spins can not be obtained from these results, however Stojić *et al.* [123] has used post-scattering polarisation analysis from Staub *et al.* [103] in order to make a prediction for the antiferromangetic spins to be lying in the [110] direction. The temperature dependence suggests that the Jahn-Teller distortions become more dominant as the temperature is lowered, at least down to T_N.

A similar effect has also been seen in other materials. In $KCuF_3$ a jump in intensity of the orbital order peak, by almost a factor of two, was seen just above the Neél temperature for the system [124, 70]. This was suggested by Binggeli and Altarelli [125] to be due to a small structural transition at T_N, however no such structural transition has been observed in $La_{0.5}Sr_{1.5}MnO_4$. Perhaps more related, Murakami *et al* [126] observed a smaller, but

significant increase in the orbital order reflection in $LaMnO_3$, however these results were collected at the Mn K edge, and so are more likely to be sensitive to the induced effect on the $4p$ electron orbitals. Ishihara and Maekawa [127] proposed that in the case of the manganites, such a change at T_N was due to a different orbital occupancy, however this would be indicated by a significant change in the shape of the peaks that is not observed. The most interesting factor of the temperature dependence is the de-coupling of the orbital ordering and Jahn-Teller distortions, something no other measurements are currently sensitive to. It remains to be seen whether this is unique to $La_{0.5}Sr_{1.5}MnO_4$, or whether other materials display similar behaviour.

6.6 Conclusion

Observations have been made of the orbital and magnetic signals at the Mn L edges in $La_{0.5}Sr_{1.5}MnO_4$. The use of this direct probe has allowed theoretical fitting with the intention of establishing the relative importance of Goodenough orbital ordering and Jahn-Teller distortions. It has been observed that the orbital order in $La_{0.5}Sr_{1.5}MnO_4$ is predominantly due to Jahn-Teller distortions. In addition, it seems likely that the orbitals occupied are of the $d_{x^2-z^2}$ type, in agreement with XMCD measurements by Huang *et al.* [120].

An azimuthal dependence of the orbital order peak has been established, confirming the expected anisotropic behaviour. In addition, there is a complete absence of intensity at the zero point in the azimuth, suggesting a lack of twinning in the crystal. A temperature dependence has been recorded of both the superlattice reflections, the orbital ordering showing a discontinuity at T_N. In addition there appears a change in the ratio of the main L_3 and L_2 resonances, suggesting a change in the relative dominance in the Jahn-Teller and Goodenough orbital order. This in turn suggests a de-coupling between the two contributions. Various ideas for the origin of the discontinuity have been reviewed, however none are remarkably satisfactory.

Chapter 7

Orbital and Magnetic Order in $La_{2-2x}Sr_{1+2x}Mn_2O_7$

The long range order in the bilayer manganites has been discussed at length in Part I of this thesis. The results presented in that section were collected through high energy x-ray diffraction and resonant diffraction at the Mn K edge. This chapter reports studies on $La_{2-2x}Sr_{1+2x}Mn_2O_7$ using soft x-ray diffraction at the Mn L edge. $LaSr_2Mn_2O_7$ has been studied by soft x-ray diffraction, although this was limited to the magnetic (001) peak. This chapter will describe results taken both on this peak, and on the orbital $(\frac{1}{4},\frac{1}{4},0)$ peak. In addition the results of theoretical calculations of these results will be displayed. The previous chapter described similar results from $La_{0.5}Sr_{1.5}MnO_4$ however $La_{0.5}Sr_{1.5}MnO_4$ is a strongly Jahn-Teller distorted material, where the orbital degree of freedom is strongly controlled by the crystal field. By contrast, $LaSr_2Mn_2O_7$ has a very small Jahn-Teller distortion, especially at low temperature [36, 30, 51], allowing a much greater orbital freedom. This is especially interesting, as it may help to understand whether orbital order is simply a bi-product of the crystal field, or alternatively the orbital ordering 'drives' the distortion. In addition the bilayer system, as previously described, shows an extremely large magneto-resistance, the understanding of which is intrinsically linked to the transport properties, and the ordering in the material.

As had been shown in previous chapters, the bilayer crystals are also charge ordered, concomitantly to the small Jahn-Teller distortion. The unusual temperature dependence of the charge order and Jahn-Teller distortion raises more interest in looking directly at the orbital order. Does this ordering follow the temperature dependence of the charge ordering and the Jahn-Teller ordering?

Figure 7.1 reminds the reader of the structure of $LaSr_2Mn_2O_7$, and in addition shows the

proposed orbital order. The magnetic ordering of the crystal is known to be A-Type antiferromagnetic, that is each layer is ferromagnetically ordered, and the ordering between the layers is antiferromagnetic. There does, however, appear to be little experimental evidence to suggest the orientation of the magnetic moments within the *ab* planes. In the absence of such evidence, the spins are assumed for the purposes of the theoretical calculations, to be aligned in the [110] direction.

7.1 Experimental Method

The majority of the data within this chapter were taken on the ID08 beamline at the ESRF, however a small amount was also measured using the X1B beamline, NSLS, and beamline 1.1 at the SRS. Very high quality single crystals were grown using the float-zone method at Argonne National Laboratory. The quality of the samples was of upmost importance for looking at the orbital $(\frac{1}{4},\frac{1}{4},0)$ peak, as the reflection is situated 90° from a strong cleavage plane. The samples were pre-aligned using a rotating anode diffractometer, and two selected to be suitable for observing the (001) and $(\frac{1}{4},\frac{1}{4},0)$ reflection. The former of these samples could be used from a cleaved surface, however the [110] aligned sample require cutting and then polishing with graded alumina paste of 1/4 μm diameter.

The three beamlines have been described in Chapter 5, and a relatively similar procedure was adopted at each beamline. The variation in the beamlines produced different appearances to the data, especially regarding the energy scans at fixed wavevector, where ID08 has a significantly higher energy resolution, and as such, more detail can be seen in the scans. The temperature dependences using soft x-ray diffraction are notoriously difficult to take. Because of the low energy x-rays, there is significant photon absorption by the sample, resulting in beam-heating. It is unknown the extent of this effect, although it could conceivably be in the region of $\sim$ 10 K. This of course is directly limited to the intensity of the beamline, and so beam heating at ID08 is likely to be greater than either X1B or 5U.1 and 1.1. In addition (with the exception of the Daresbury chamber) the cooling is provided by a liquid ^{4}He cold finger attached with a copper braid, and as such there is a temperature gradient from the end of the cold finger to the sample. Although the temperature sensors are placed close to the sample, there is a limit how close they can physically be placed. Further modification of the ID08 chamber, involving removal of the load transfer equipment, produced a base temperature of 25 K. Because the Daresbury chamber is cooled directly by liquid nitrogen,

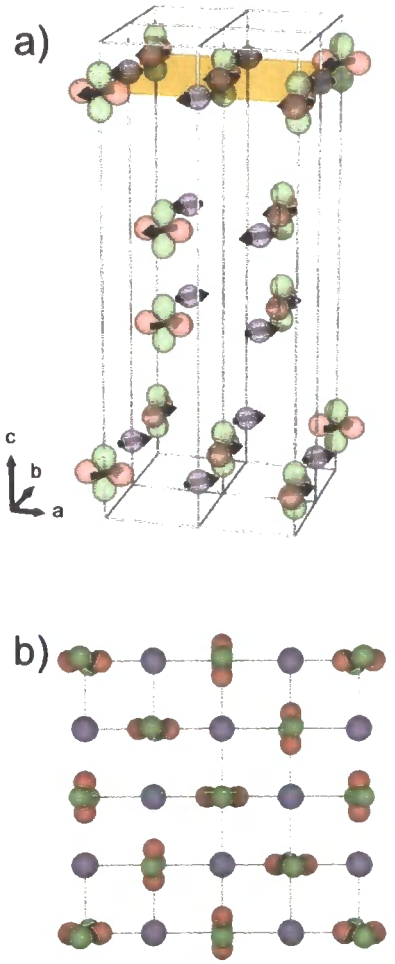

Figure 7.1: The crystal structure of the bilayer manganite $LaSr_2Mn_2O_7$ at low temperature. (a) the arrangement of the previously proposed Mn^{3+} and Mn^{4+} manganese ions are shown within the tetragonal unit cell. The spin and orbitals on the Mn^{3+} are shown schematically. A plan view of the orbitals within the *ab* plane shown in yellow, displaying orbital order of the $x^2 - z^2, y^2 - z^2$ type is given in (b). This is the dominant type of orbital ordering found in [128] for a doping of $x = 0.42$. The results suggest for the non Mn^{3+} sites a valence closer to Mn^{2+}, than to Mn^{4+}.

the massive cooling power and direct contact virtually eliminates any thermal problems. Unfortunately it also means the low temperature is limited to 80 K. Although this is not meant to totally remove any confidence in the temperature dependences, it is written as a warning for reading too much information into the precise values.

The detector counting provided by the ID08 and Daresbury chambers is through a photodiode. Rather than counting photons, this provides a current. This current is then amplified and converted into a voltage, which in itself is converted to 'counts'. As such the idea of counts is rather abstract, and as such all of the data from these beamlines are shown with arbitrary units. By contrast, the NSLS beamline uses a channeltron detector, and so photons are actually counted.

7.2 Results

Figure 7.2 displays the energy dependence of the scattered beam at a fixed wavevector $\vec{Q} = (001)$. This shows a huge resonance at the Mn L_3 edge, and a much smaller resonance at the L_2 edge. The data show a splitting of these resonances, as has previously been observed [36]. Both panel (*a*) and (*b*) show identical experimental data, panel (*c*) shows the absorption of the sample, measured through a contact attached to the surface of the sample. Black lines on the spectra show theoretical fits to the data. These theoretical fits originate from multiplet calculations, similar to those in the previous chapter, and were calculated by the N. Stojić and N. Binggeli, led by Massimo Altarelli at ITCP, Trieste. The Mn^{3+} site has a symmetry of D_{4h}, however the addition of the magnetic spins lowers the symmetry to C_i. The outcome of the calculations is the generation of two crystal field parameters, cubic (X^{400}) an tetragonal (X^{220}). In a similar method to the calculations for $La_{0.5}Sr_{1.5}MnO_4$, $\Gamma = 0.5$ eV was used for the core hole lifetime, and the scattering intensity was convoluted with a Gaussian of width 0.1 eV to simulate the experimental resolution.

It has always been assumed that the valence on the Mn are 3+ and 4+, however a theoretical fit with these values is shown in panel (*a*), and an obvious displacement in energy can be seen. The energy calibration on the beamline, is performed using known standards, and as such the absolute accuracy of the energy is within 0.2 eV. The displacement seen between the experimental and theoretical fits is in the order of 2 eV. This raises the possibility that the valence on the Mn is not correct. Panel (*b*) shows a theoretical model with Mn^{2+} and Mn^{3+}, and the fitting can be seen to be significantly better. Not only does the energy

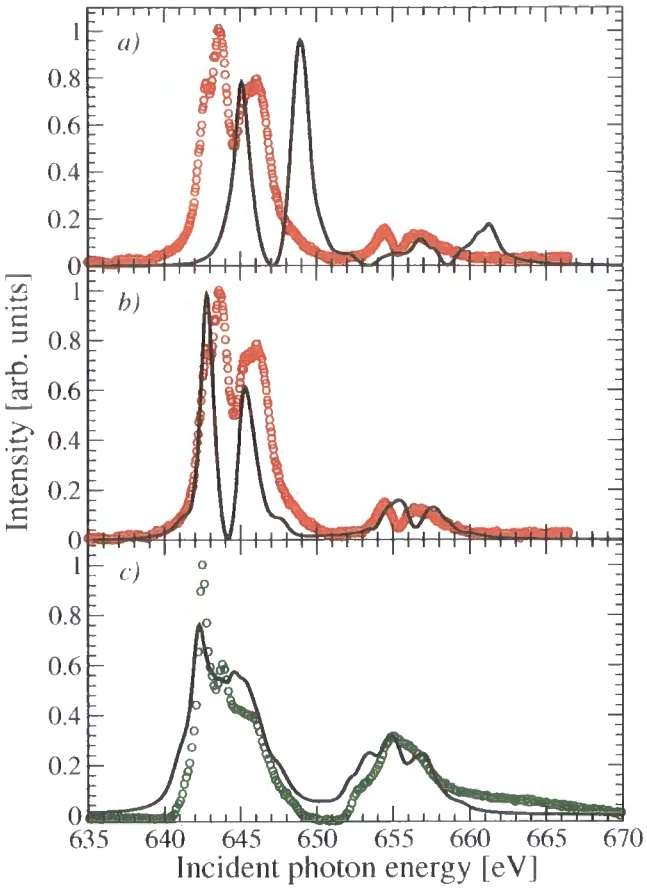

Figure 7.2: Energy scan at fixed Q through the (001) magnetic reflection in $LaSr_2Mn_2O_7$(red circles), with theoretical fits (black line). (*a*) shows the theoretical fit with a superposition of Mn^{3+} and Mn^{4+}, while (*b*) shows the superposition of Mn^{2+} and Mn^{3+}. The third panel (*c*) shows the absorption spectrum (green circles) with theoretical fit. Data taken at 63 K, on the ID08 beamline.

scale agree more, the relative intensities of each of the two peaks at the L_2 and L_3 edge agree much more closely to the experimental data. The origin of the Mn^{3+} and Mn^{4+} charges is the doping of the crystal. Obviously, by suggesting the valence to be more Mn^{2+} and Mn^{3+} the implication is not that the crystal is charged, rather that the a small proportion of the electron density is shifted from the oxygen ligands onto the manganese ions. The fit to the absorption spectra in panel (*c*) is modelled with Mn^{2+} and Mn^{3+} valencies.

Conveniently the association of Mn^{2+} and Mn^{3+} does not alter the ability of the sample to be Jahn-Teller active, as this is associated with the Mn^{3+} ion. In addition the Mn^{2+} ion has a full e_g electron level, and so is not Jahn-Teller active, and behaves like the Mn^{4+} ion.

Figure 7.3 displays the temperature dependence of the magnetic (001) peak. This data was taken at X1B, NSLS, which at the time had the a much lower base temperature than

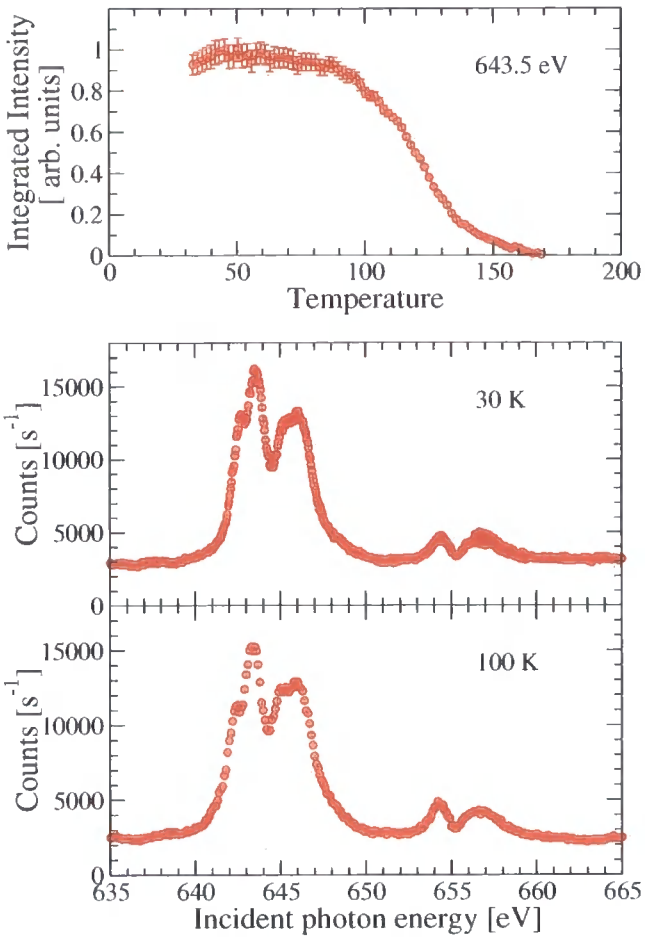

Figure 7.3: (*upper panel*) Temperature dependence of the intensity of the (001) magnetic signal in $LaSr_2Mn_2O_7$ measured at 643.5 eV. The lower two panels compare the scattered x-ray intensity at fixed Q, at 20 K and 100 K (data taken at X1B, NSLS).

ID08. The temperature dependence shows a T_N of 160 K, and the intensity of the magnetic reflection increasing to 100 K, where the intensity stabilises. The bottom two panels show a energy scans at fixed wavevector at 30 K and 100 K, showing little change in the spectra.

Figure 7.4 shows an energy scan a fixed wavevector through the $(\frac{1}{4},\frac{1}{4},0)$ peak. This peak shows and extremely complex spectra. In addition to the two peaks seen on the L_2 and L_3 edges, there is in addition an extremely sharp and strong pre-peak at each edge. Comparing this energy scan with the (001) magnetic peak it is immediately obvious that the L_2 edge is far more pronounced. In the magnetic spectrum the two peaks at each edge are of comparable intensity, whereas the orbital spectrum shows the lower energy peak with much higher intensity. The spectrum of the orbital order peak was taken at 63 K, significantly below T_N.

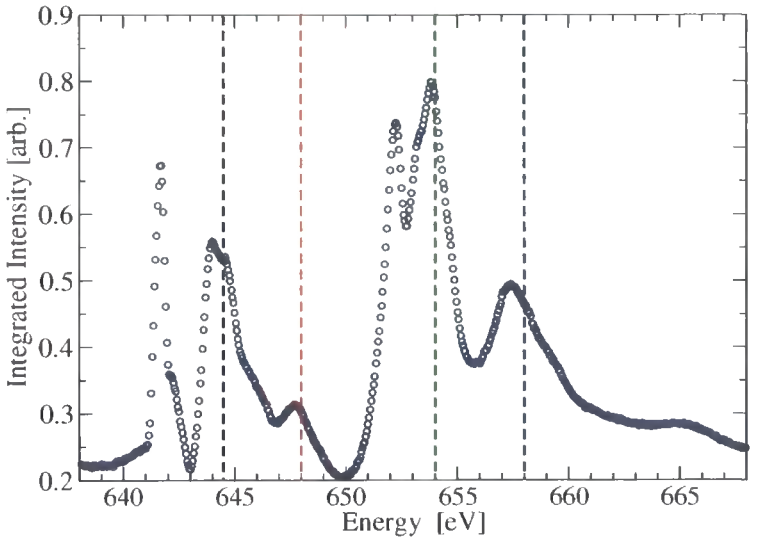

Figure 7.4: Energy scan at fixed Q through the $(\frac{1}{4},\frac{1}{4},0)$ orbital order reflection in $LaSr_2Mn_2O_7$. Data taken at 63 K, on the ID08 beamline. The vertical lines correspond to the energies where a temperature dependence was measure (Fig. 7.6).

Figure 7.5 displays this complex orbital spectrum, with a theoretical fit. As can be seen the fit is far from ideal, in particular the pre-peak of the L_3 edge is completely absent. In addition the high energy peak a the L_2 edge is poorly reproduced. Despite this the relative intensities of the edges and overall shape of the spectrum is reproduced reasonably well, giving us some confidence in the theoretical simulations. As has been stated, the $LaSr_2Mn_2O_7$ system has a very small Jahn-Teller distortion. The model is able to make specific predictions as to the size of the crystal field, and an upper limit of 0.4 eV can be given. This is significantly lower than the $X^{220} = 3.75$ eV seen in $La_{0.5}Sr_{1.5}MnO_4$. The lower panel of this Figure 7.5 shows the effect on the spectrum that a larger tetragonal crystal field would give, the purple line represents a model with a distortion a factor of eight times larger. This gives a massive L_3 peak, something that is not observed in the experimental data, strong evidence from the theoretical calculations that the L_3 edge is very sensitive to the size of the tetragonal crystal field.

Due to the spectrum of the orbital peak being so complex, and the system undergoing a magnetic phase transition within the orbitally ordered phase, it was important to take detailed measurements of the temperature dependence. Ideally, the entire spectrum would be measured at each temperature, however this is unfeasible, due to the length of time required. Instead, four different energies were chosen to measure the intensity with respect to temperature, and these energies are shown by vertical lines on Figure 7.4. The temperature

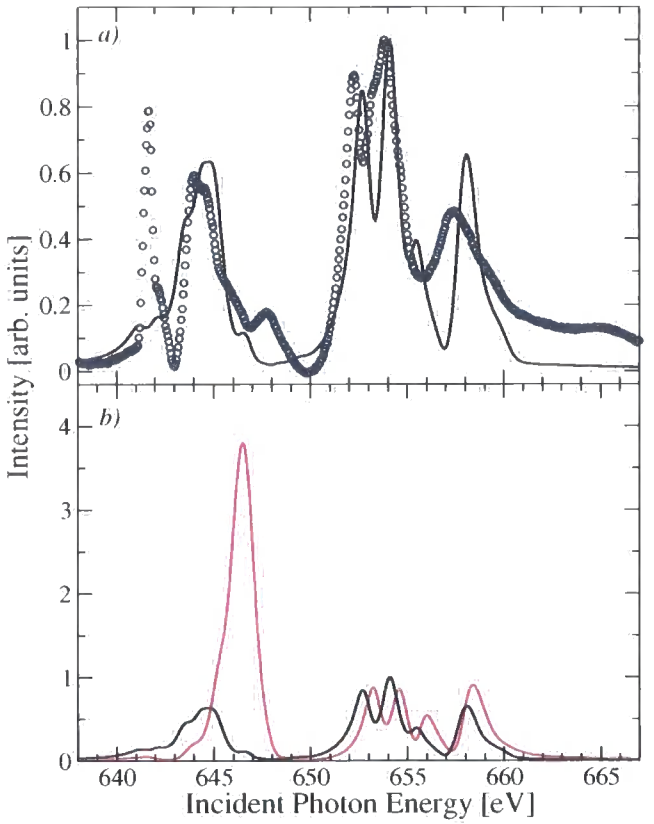

Figure 7.5: *a*) Energy scan at fixed Q through the $(\frac{1}{4},\frac{1}{4},0)$ orbital order reflection in $LaSr_2Mn_2O_7$(blue circles). Black line shows the theoretical fit using identical parameters to the fit in Figure 7.2*b*. *b*) Shows the effect of increasing the tetragonal field by a factor of 8 (purple line), representing an increased Jahn-Teller distortion. Black line identical to that in *a*) for comparison. Data taken at 63 K, on the ID08 beamline.

depedencies of these points in the energy scan are shown in Figure 7.6, the top panel showing the absolute values, and the middle panel showing all the curves normalised at 120 K. The lower panel shows the the ratio of the intensities of the peaks at 654 eV and 644.5 eV as a function of temperatures. For the duration of the temperature measurements, the slits on the beamline pre- and post- grating, which define the energy resolution were opened, in order to integrate over a larger area of the energy scan for each temperature measurement. As such, the energy integration for each curve was approximately 1 eV. The consequence of this was a significantly larger signal / noise ratio, and also reduced the effect of any possible small energy drift during the measurements.

In addition to the temperature curves, low resolution energy scans at fixed wavevector were taken of the orbital peak at 25 K, 100 K, and 200 K (Fig. 7.7). These show only small differences in the spectrum taken at different temperatures. In particular the high energy peak on each of the resonant edges appears less dependent on temperature, and so are significantly more prominent in the higher temperature scans.

The temperature dependance of the orbital and magnetic reflections can be combined, and together with previous data of the structural distortion can be combined in order to give an overall picture (Fig 7.8). This shows, as expected, an identical temperature of T_{OO} and T_{JT}. Somewhat more surprising is the difference between the temperature dependences of these two phenomena. The crystal distortion decreases immediately at T_N, whereas the orbital reflection appears to increase further, until the magnetic reflection has got much stronger, before decreasing. This difference suggests a decoupling between the two phenomena. In addition the decrease in the intensity of the structural distortion is more pronounced than the orbital reflection.

In addition to the studies on the $x = 0.5$ bilayer sample, an energy scan at fixed wavevector at the (001) orbital peak was measured on samples with $x = 0.55$ and $x = 0.6$ (Fig. 7.9). These results were taken on beamline 1.1, which situated on a bending magnet at the SRS. Consequentially, the intensity is rather low, and so magnetic reflections are the only viable reflections to study. In addition the measurements were taken on the large *ab* cleaved face, the only faces large enough for the higher doped samples. The energy scans show relatively little difference as the doping is increased. As shown in previous chapters, these samples are also charge ordering and Jahn-Teller active / orbitally ordered.

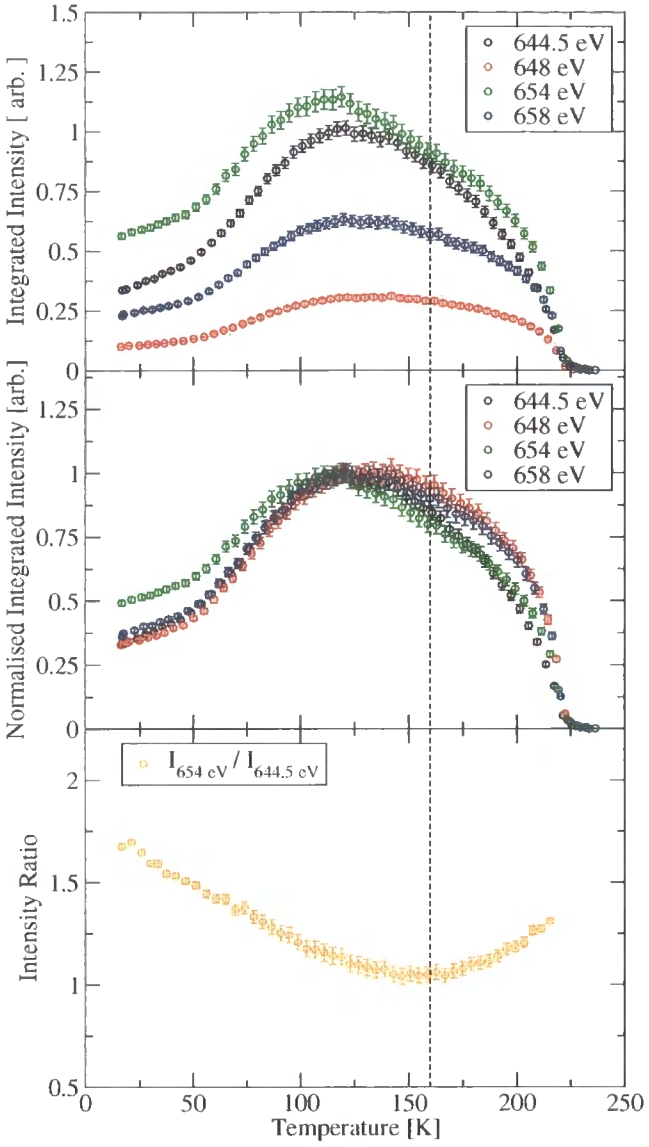

Figure 7.6: Temperature dependence of the four main features on the orbital order energy scan (Fig. 7.4) at 644 eV, 648 eV, 654 eV and 658 eV. (top panel) Data representing the relative intensities of each part of the spectrum. (middle panel) Each curve is normalised at 120 K. (lower panel) The ratio of the main peaks in the L_2 and L_3 edges. The dashed line marks T_N. Data taken at ID08.

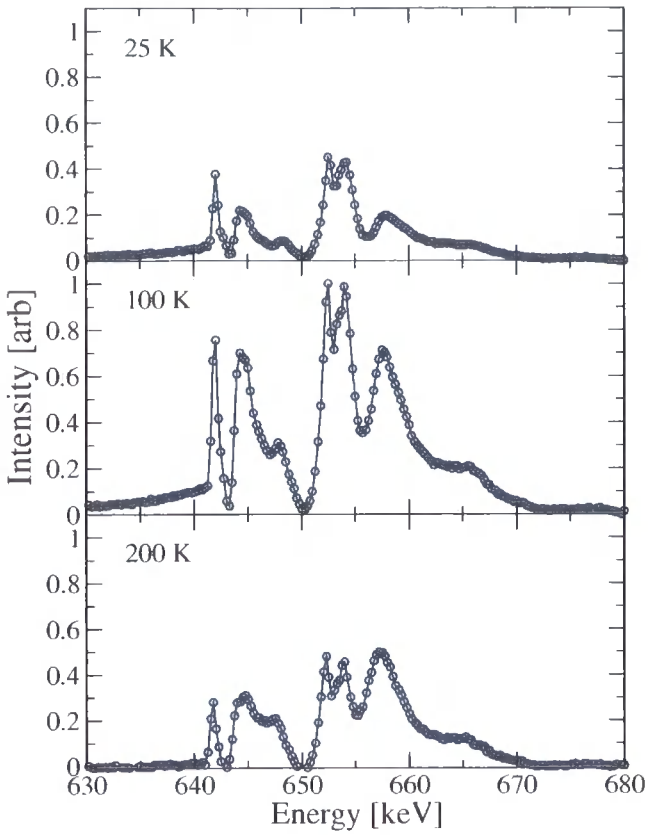

Figure 7.7: Energy scan at fixed Q through the $(\frac{1}{4},\frac{1}{4},0)$ orbital order reflection in $LaSr_2Mn_2O_7$, at different temperatures. The relative intensities of the spectra are maintained. Data taken at 63 K, on the ID08 beamline.

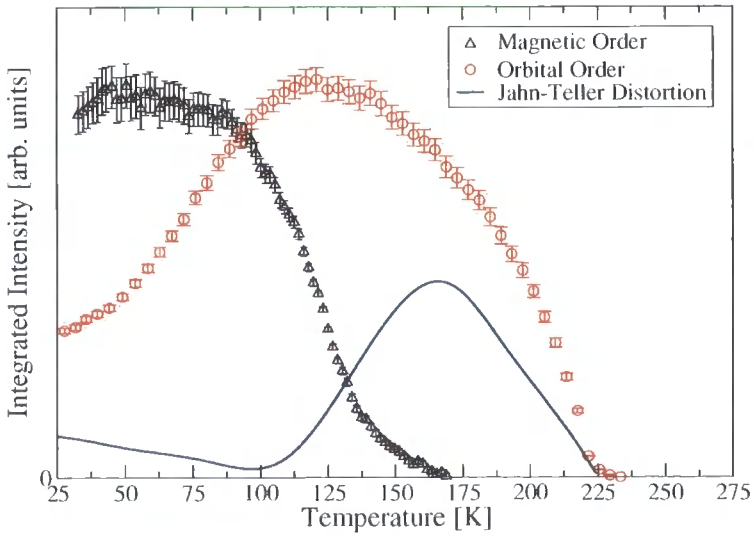

Figure 7.8: The temperature dependence of the intensity of the orbital order and magnetic signals. These are compared to the intensity of the Jahn-Teller distortion measured by high energy x-ray diffraction by Wilkins *et al.* [35]

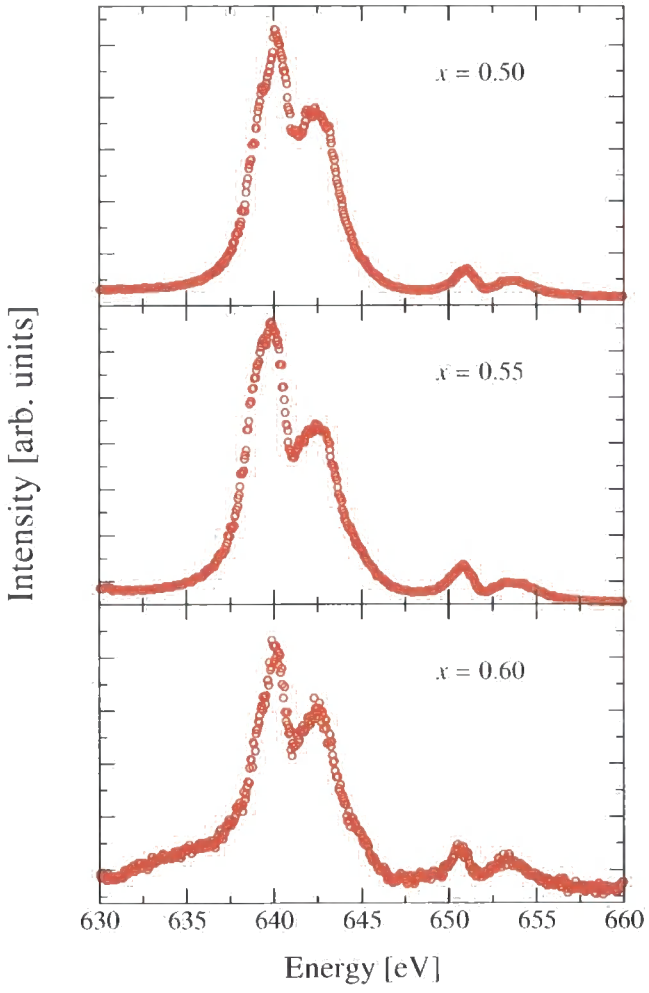

Figure 7.9: Energy scans at fixed Q through the (001) magnetic peak of $La_{2-2x}Sr_{1+2x}Mn_2O_7$ with $x = 0.5, 0.55$ and 0.6. Data taken on the 1.1 beamline at Daresbury at 83K.

7.3 Discussion

The inability of the spectrum of the magnetic (001) to be fitted with a model containing only Mn^{3+} ions is a strong indication of charge ordering. The capacity to only handle integer valencies is an inherent limit to multiplet calculations, however an accurate representation of the energy gap between the two peaks at each edge is found. More surprising is the significantly better fit for Mn^{2+} / Mn^{3+} than Mn^{3+} / Mn^{4+}, however as described earlier this would not effect the orbital occupancy of the Mn^{3+} ion. Although unexpected, these low valencies have been observed before, especially in the cubic manganites. Ju *et al.* [129] studied the cubic manganite thin films using K edge electron-energy-loss spectra, and observed a pre-peak at the Fermi level, corresponding to transitions into empty oxygen states. Therefore they interpret the materials to be charge-transfer type materials, with the carriers having significant oxygen behaviour. This shift of the holes onto the oxygen is equivalent to a lowering of the valence on the Mn ion. Coming to a similar conclusion, Subías *et al.* [130] used soft x-ray spectroscopy to understand the electron structure of various cubic manganites, and again interpreted pre-peaks in the spectrum to originate from a charge transfer from the Mn to the oxygen site. In addition to these experimental works, Ferrari *et al.* [131] and Zheng *et al.* [132] performed Hartree-Fock calculations on $La_{0.5}Ca_{0.5}MnO_4$, both finding the resulting calculations better described with a degree of charge transfer, in the case of Ferrari *et al.*, even describing the results as a charge-density wave of oxygen holes.

The orbital order peak was fitted using the same crystal field parameters as the magnetic peak. Although the fitting is good, and reproduces the major peaks, the strong pre-peak feature is not fitted. Observing the magnetic peak carefully, it is possible to determine a slight splitting of the two major peaks at the L_3 edge, which is absent in the theoretical fits. In addition the magnetic peak in $La_{0.5}Sr_{1.5}MnO_4$ (see previous chapter) also showed a pre-peak, which was absent in the theoretical calculations. Despite this limitation, the size of the tetragonal field is seen to make a huge difference to the fitting of the orbital peak in $LaSr_2Mn_2O_7$. Similar to $La_{0.5}Sr_{1.5}MnO_4$, it is possible to generalise the fitting by describing the L_3 edge strongly Jahn-Teller dependent, whereas the L_2 edge is relatively independent of any change in the tetragonal crystal field. The experimental observation of the L_3 edge having a lower intensity than the L_2 edge confirms a very small tetragonal crystal field.

Observing the temperature dependences of the orbital peak, it is immediately obvious that this is different to the temperature dependence of the Jahn-Teller distortion in the man-

ganites, seen in the previous chapter. Despite the magnetic phase transition there appears to be relatively few changes in the orbital order spectrum. The most obvious change, is that at high temperatures, just below T_N, the high energy shoulders on the two edges appear significantly more pronounced. This is verified by the temperature dependence, where the energies of 648 eV and 658 eV appear stronger at these temperatures. Unfortunately, it is difficult from the theoretical calculations to extract exactly what this means, and further analysis of the data is needed. What perhaps we are more interested in is the relative intensity of the peaks at 654 eV and 644.5 eV, as this would give us an idea of the change of Goodenough orbital order and Jahn-Teller distortion. The lower panel in Figure 7.6 shows this ratio. Interestingly the minimum of the ratio curve occurs at T_N. Thus this is the point where the Jahn-Teller distortion is most dominant. This concurs with the graph in Figure 7.8 where the Jahn-Teller distortion is strongest at T_N, and the variation in the distortion appears to be much more than in the orbital order. The lower panel of Figure 7.6 further suggests that the orbital order is most dominant to the spectrum of the orbital peak at low temperatures. The small increase seen in the intensity of the Jahn-Teller reflections at high energy, does not appear to be reflected in the ratio of the two edges. This interpretation is rather simplistic, and further theoretical studies should be conducted in order to develop a more sophisticated analysis.

The similarity of the spectra for the magnetic reflection in different doping levels is not entirely unexpected, due to the similarity of the charge and orbital ordering seen using other techniques. A further study which would be of far greater interest would be looking at the orbital order peak using soft x-rays, especially as x is increased such that there is no magnetic phase. The temperature dependence of the spectrum could then be compared to that observed in the half doped bilayer. Unfortunately at present, the only crystals of significant quality to study on a cut face are of the half doped bilayer.

7.4 Conclusions

The orbital and magnet superlattice reflections of $LaSr_2Mn_2O_7$ has been observed using soft x-ray diffraction, and the results fitted by multiplet calculations. The fitting of the magnetic spectrum is not possible with a single valence on the Mn, and requires a mixed valence. In addition, the energy of the strong resonant peaks suggests a valency of 2+ and 3+ on the Mn ion, requiring a charge transfer to the oxygen ions. The tetragonal crystal

field distortion obtained by the fitting is in the order of 0.4 eV, and is thus much smaller than that observed in $La_{0.5}Sr_{1.5}MnO_4$, suggesting an extremely small Jahn-Teller distortion. Temperature dependences of features in the orbital spectrum suggest that the Jahn-Teller distortions (always very weak) contribute most to the spectrum at T_N. The presence of orbital order with such a weak tetragonal crystal field suggests that the ordering of the e_g electrons is not solely a bi-product of a reduction in the orbital degree of freedom generated by a strong tetragonal crystal field. Rather, these results suggest that the orbital order plays an important role in the transport properties of the system.

Chapter 8

Conclusion

The aim of this thesis was to investigate the long range order in the layered manganites, and in particular to study the ordering of the electron orbitals. Chapter 2 began this investigation by looking at the single layer manganites with x-ray diffraction. Three distinct ordering phenomena were considered; charge ordering, Jahn-Teller structural distortions, and orbital ordering. The latter of these three was only observed using resonant scattering, whereas the charge order and Jahn-Teller distortions were also measured using high energy x-ray diffraction. There was some uncertainty reported regarding the orbital order observations due to the dipole transition probing the $4p$ rather than $3d$ electron shell of the Mn ion. As such, it was assumed that this scattering was in fact sensitive to the induced ordering of the $4p$ electrons, giving an indication to the orbital characteristics, but could not as such be described as a direct probe. Despite this shortfall, resonant scattering at the Mn K edge proved to be a very effective technique for studying a large stoichiometric range of the single manganite series. In particular, multiple ordering phenomena could be studied, and the varied size and orientation of the samples could be accommodated. High energy scattering was found to be useful, especially to detect the weak structural distortions, where the massive scattering volume increased the scattered signal. Trials were performed with an area detector, vastly increasing the speed of the result collection, however the high background and relatively low resolution limited its effectiveness for these experiments.

The research into the ordering of the higher doped bilayer system further utilised the aforementioned techniques. The long range order of the half doped bilayer manganite had already been published, however questions remained as to the ordering of the orbitals with a change of stoichiometry, and how the absence of the antiferromagnetic order would affect the results. A detailed study into the position of the orbital induced superlattice peaks in the higher doped bilayer, $La_{0.8}Sr_{2.2}Mn_2O_7$, pointed to a reorientation of the manganese orbitals. A proposed orbital pattern was predicted, which extended the Wigner lattice

model towards a bistripe model. The azimuthal dependence of the manganese orbitals gave an indication to their ordering, and appeared to agree with the simulation for the model. Taking this a further stage, the bilayer sample, $La_{0.6}Sr_{2.4}Mn_2O_7$, had a sufficient doping to form a completely new ordering formation. At this doping level, there was a choice of orbital orientations, either a fully bistripe model could be formed, or a Wigner lattice. Analysis of a detailed azimuth suggested that the bistripe model was more likely. In addition to a new orbital order orientation, this bilayer sample with $x = 0.7$, did not have a low temperature antiferromagnetic phase. As a consequence the charge and orbital ordering behave completely differently as a function of temperature. This is conclusive proof of the complex interaction between the magnetic ordering parameters and the charge and orbital ordering. With these measurements however, the observation of the orbital ordering was taken at the Mn K edge and as such is an indirect measurement.

One of the main benefits of high energy x-ray diffraction is the ability to observe extremely weak phenomena. This was apparent when looking at polaron formation in the underdoped bilayers in Chapter 4. This underdoped region is particularly interesting, as these are the samples that have displayed colossal magnetoresistance. Thus, the observation of polarons just above the Curie temperature was compelling. These polarons appeared in two formations, at different length scales. They were studied with both temperature, and an applied magnetic field. Polarons have been described in terms of a very weak, disordered charge ordering, however they were destroyed with the application of a magnetic field of 3 T, which has not been observed in true charge ordering. They do occur over a similar temperature range to the charge ordering, but are completely eradicated by the well aligned paramagnetism.

In addition to scrutinising polaron formation with an applied magnetic field, Chapter 4 was also briefly concerned with the field effect on the structural distortions and charge ordering in $LaSr_2Mn_2O_7$. Interestingly in this bilayer an applied magnetic field appeared to affect the Jahn-Teller distortions, but not the charge ordering. As the two phenomena have previously been observed to behave virtually identically, this was something of a revelation. Maybe the magnetic field directly affects the Jahn-Teller distortion, rather than affecting an underlying order and thus the charge ordering as well. It was speculated that the magnetic field altered the splitting of the e_g electron levels, and thereby altered the tetragonal crystal field, however this was very much an initial experiment, and further work is necessary to

establish exactly what effect is caused by an applied magnetic field.

Soft x-ray magnetic scattering was developed in Part II of the thesis. The technique is relatively new, with only a handful of papers reporting results. Despite this, the results have had a high impact, in particular amongst the existing magnetic scattering community. Soft x-ray diffraction begins to bridge the gap between diffractionists, and surface scientists, in particular those using magnetic dichroism. The results, although looking at diffracted reflections, contain so much information in the energy spectra, that they can be compared more closely to x-ray magnetic dichroism than resonant scattering at traditional energies. Given the complex spectra that are observed, there is an increasing need for experimentalists to seek the capability of theoreticians, as only the simplest of conclusions can be derived without complex models.

Chapters 6 and 7 described the use of soft x-rays to look at orbital ordering in two samples showing very different characteristics. Although both are layered manganites, Chapter 6 was concerned with the single layered $La_{0.5}Sr_{1.5}MnO_4$, which has a large tetragonal crystal field, and Chapter 7 with the bilayer $LaSr_2Mn_2O_7$, with a virtually non-existent tetragonal component. Both these samples displayed well established orbital ordering. The combination of experimental results and theoretical calculations was essential. The agreement between the experimental results and the theoretical calculations of the orbital and magnetic peak, was good. In particular the simulated magnetic spectra for the two orbital occupancies were different, and matching this simulation to the experimental data verified the occupancy of the $d_{x^2-y^2}$ orbital, in agreement with x-ray magnetic circular dichroism data. A significant shortfall of the theoretical calculations is the inability to model temperature. Some intriguing results were shown, concerning the behaviour of the orbital peak in the region of T_N, suggesting a change in the relative domination of the orbital order and Jahn-Teller distortion, and only very general conclusions were able to be made. By comparison to $La_{0.5}Sr_{1.5}MnO_4$, the theoretical fits to the $La_{2-2x}Sr_{1+2x}Mn_2O_7$ experimental data were not as good. Despite this, a number of important conclusions could be made. Primarily, this concerned the extremely small tetragonal crystal field in the sample. This small crystal field places a much smaller restriction on the orbital degree of freedom in the system, and yet despite this, the orbital ordering was still observed. In spite of this weak tetragonal field, the orbital ordering and Jahn-Teller distortions have identical transition temperatures, and as such it seems likely that the orbital ordering requires a small tetragonal component. It is still not clear

whether this small distortion is a direct result of the orbital ordering. What is evident, is that the strong change in the intensity of the Jahn-Teller distortion with regard to temperature, measured though high energy x-ray diffraction, is not mirrored by the orbital ordering superlattice peak, measured though soft x-ray diffraction. However, neither does this large change in the Jahn-Teller distortion become apparent in the spectrum of the orbit order peak measured with soft energy x-rays, despite the simulations suggesting a strong sensitivity to the size of the tetragonal crystal field. It is clear that the orbital order and Jahn-Teller distortions are not simply two sides of the same coin. They are different phenomena, and although they appear to always occur simultaneously, their intensity is not strongly coupled. Because the intensity of the orbital ordering measured at the Mn K edge does mirror the intensity of the Jahn-Teller distortion, it seems likely that the affect on the $4p$ orbitals is caused by the tetragonal crystal field distortion rather than the ordering of the $3d$ orbitals.

The aim has been stated to investigate the long range correlations in the manganites, however the ultimate goal for the research is understand their effects, and how they relate to real world problems, such as colossal magnetoresistance. This is often quoted as a driving force behind manganite research, in particular that of the bilayers. The soft x-ray diffraction data go some way to completing this goal, however there is a long way to go. In the near future, there is a lot of work to be undertaken looking at the different doping levels of the manganites using soft x-ray diffraction, in particular studying a sample with a high doping in order to look at the charge ordering. Although the manganites series is a productive area of soft x-ray diffraction, there are also other materials that have been studied, and others that show possibility for the future. Similar to the manganites, the magnetic and charge reflections in the nickelates have been observed. This has produced limited interest though, possibly because of the simple resonances and limited additional information gained above that previously found through neutron and K edge x-ray diffraction. By comparison the cuprates have always had a high profile. Although the work to date has been looking at hole lattices, there is the possibility for an extremely fascinating study looking at the proposed vortices in the high temperature superconducting systems. Another interesting possibility is the idea of speckle imaging. Here the idea is to look with very high resolution at the reflection in a time resolved manner, with the intention of observing the fluctuating signals from individual domains, and measuring a timescale for the fluctuations of the ordering. Success of this very technically challenging experiment has yet to be reported.

In addition to the manganites, cuprates, and nickelates, there are many other samples that may be studied using soft x-ray diffraction. Also a transition metal, the iron oxide Fe_3O_4 has an extremely complex structure, undergoing a structural phase transition at the Verwey transition while magnetically ordered. Although it may be optimistic to expect soft x-ray diffraction to solve the long-term conundrum of this system, it may well be able to shed new light on the problem. Although the transition metals lighter than Mn have been studied at the K edges, their extremely soft edges may well prevent access to the majority required reflections. Another group of systems of particular interest at the moment are the multiferroics, materials that are simultaneously ferromagnetic and ferroelectric. Soft x-ray diffraction may be able to provide useful information - in particular regarding their magnetic structure. If further developments can be made on the low temperature capabilities of the chambers, this will promote the possibility of many more samples, such as the boro-carbides that have magnetic transitions in the range 5-15 K.

So far only single crystals have been discussed. Soft x-ray diffraction was originally pioneered by the multilayer community, and this may ultimately be where they are of most use. Artificial structures have variable lattice parameters, and these tend to be much larger than single crystal systems, avoiding the restriction of a small reciprocal space. Such multilayers can be designed so as to study a particular phenomena, and the ability to adjust specific parameters make them ideal model systems.

Despite the interest that soft x-ray diffraction has generated, the community is still reliant on first generation chambers. Although these chambers have been optimised, they all have in built limitations. For fruitful progress of this area of physics, there needs to be a concerted effort to improve the experimental facilities. The regular tools of resonant x-ray diffraction, such as polarisation analysis and the ability to perform azimuthal scans needs to be a regular resource at soft x-ray energies. Increasing the range of sample environments is always an issue, the sample temperature is particularly important. Chambers capable of a sample temperatures of less than 10 K are essential, and temperatures down as low as 4.2 K should be achievable. The majority of x-ray beamtime while on soft x-ray experiments is consumed in aligning the sample and finding the (often single) peak. A huge benefit to this would be an alliance between the soft x-ray beamline and a higher energy x-ray source. With this ability the sample could be aligned using the high energy x-rays before finding the peak with soft x-rays. This source could be as simple as a small x-ray source mounted on the soft

x-ray chamber.

In summary, soft x-ray diffraction has been well received, with a number of high impact publications. Despite this, there are severe limitations, partly from physical limits and partly from limitations of current equipment. Even by resolving the experimental limitations the technique will always be limited by the sample availability and the access to reciprocal space. This thesis has reported some new results using soft x-ray diffraction, however these results have been supported by K edge diffraction results, which continue to produce data unavailable at low energies.

Appendix: Azimuthal Simulations

The magnetic scattering from an anisotropic ion can be seen to vary as the sample is rotated around the scattering vector. This rotation, denominated ϕ, is shown in Figure 8.1.

This anisotropy can be simply modelled through geometric considerations. Initially it is necessary to find the tensor that represents the crystal model. This thesis has concentrated on manganese ions. The Mn^{4+} ions are spherical, and so these do not contribute to the anisotropic tensor. The Mn^{3+} ions are quadrupoles, having one long axis and an two short axes.

As such they can be represented by the 3×3 tensor matrix

$$\widetilde{T}_{quad} = \begin{pmatrix} -\frac{1}{3} & 0 & 0 \\ 0 & -\frac{1}{3} & 0 \\ 0 & 0 & \frac{2}{3} \end{pmatrix} \tag{8.1}$$

where here the long axis is pointing along the z axis. The tensor is traceless, and anti-symmetric. By convention the values of $\frac{1}{3}$ and $\frac{2}{3}$ are used.

In order to build up a tensor of the entire crystal model, the tensor for each anistotropic ion (n), must be combined, together with the position of each ion. The general structure

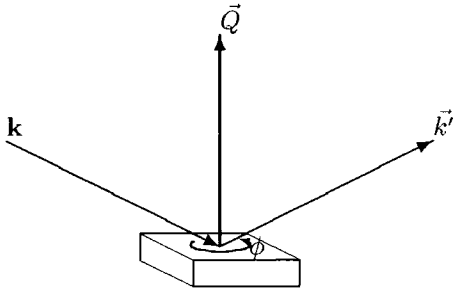

Figure 8.1: The azimuthal rotation ϕ is a rotation of the sample around the scattering vector $\vec{Q}$.

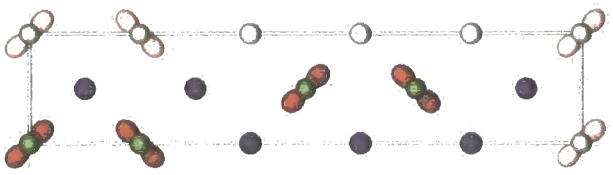

Figure 8.2: Unit cell used for calculating the azimuthal dependence of the $(\delta, \delta, 10)$ peak using ATS. The solid orbitals show those used in the calculation.

factor for the crystal is then

$$\widetilde{F} = \sum_{n} \widetilde{T}_n e^{2\pi i \mathbf{q}\cdot\vec{r}} \tag{8.2}$$

If as an example we look at the structure of the $La_{0.8}Sr_{2.2}Mn_2O_7$ (Fig. 8.2), we see that there are four contributing Mn^{3+} ions.

The first of these is at (0,0,0) and so the exponent expression is 1. The orbitals are directed in the [100] direction, and so the tensor is

$$\widetilde{T}_{(0,0,0)} = \begin{pmatrix} -\frac{1}{3} & 0 & 0 \\ 0 & \frac{2}{3} & 0 \\ 0 & 0 & -\frac{1}{3} \end{pmatrix} \tag{8.3}$$

The second Mn^{3+} ion is positioned at (1,1,0), orientated in the [100] direction. Thus the dot product between the position $\vec{r}$ and the scattering vector $\mathbf{q}(= (\frac{1}{6}, \frac{1}{6}, 0))$ is $\frac{1}{3}$. The tensor for this second ion is then

$$\widetilde{T}_{(\frac{1}{6},\frac{1}{6},0)} = \begin{pmatrix} \frac{2}{3}e^{\frac{2}{3}i\pi} & 0 & 0 \\ 0 & -\frac{1}{3}e^{\frac{2}{3}i\pi} & 0 \\ 0 & 0 & -\frac{1}{3}e^{\frac{2}{3}i\pi} \end{pmatrix} \tag{8.4}$$

In the same way the tensors for the final two ions at (2,3,0) and (3,4,0), these are then summed to give the tensor for the crystal

$$\widetilde{F}_{total} = \begin{pmatrix} -\frac{1}{3} + \frac{2}{3}e^{\frac{2}{3}i\pi} - \frac{1}{3}e^{\frac{5}{3}i\pi} + \frac{2}{3}e^{\frac{7}{3}i\pi} & 0 & 0 \\ 0 & \frac{2}{3} - \frac{1}{3}e^{\frac{2}{3}i\pi} + \frac{2}{3}e^{\frac{5}{3}i\pi} - \frac{1}{3}e^{\frac{7}{3}i\pi} & 0 \\ 0 & 0 & -\frac{1}{3} - \frac{1}{3}e^{\frac{2}{3}i\pi} - \frac{1}{3}e^{\frac{5}{3}i\pi} - \frac{1}{3}e^{\frac{7}{3}i\pi} \end{pmatrix} \tag{8.5}$$

This tensor can then be evaluated with the incoming and outgoing polarisation vectors to give a total structure factor

$$\mathbf{F} = \epsilon' \cdot \widetilde{F} \cdot \epsilon \tag{8.6}$$

In order to compute this equation the tensor and the polarisation vectors must be in the same coordinate system. This is where the angle ϕ is incorporated into the equation. There are two approaches to this rotation. Either the crystal tensor can be rotated, or the polarisation vectors can be rotated. Obviously experimentally, it is easier to rotate the sample rather than the synchrotron; however in order to simplify the calculation we will do the opposite.

Initially we create a coordinate system for the crystal. Rather than using the unit vectors of the crystal, we define a coordinate system based on the scattering vector and the azimuth reference vector (in this case (001)). These are then defined as

$$\begin{aligned}
\hat{\mathbf{c}}_3 &= -\tfrac{\mathbf{q}}{|\mathbf{q}|} &&\approx \begin{pmatrix} 0.0167 \\ 0.0167 \\ 0.997 \end{pmatrix} \\
\hat{\mathbf{c}}_2 &= \hat{\mathbf{c}}_3 \times \left(\tfrac{\mathbf{k}_{azref}}{|\mathbf{k}_{azref}|}\right) &&\approx \begin{pmatrix} 0.0167 \\ -0.0167 \\ 0 \end{pmatrix} \\
\hat{\mathbf{c}}_1 &= \hat{\mathbf{c}}_2 \times \hat{\mathbf{c}}_3 &&\approx \begin{pmatrix} 0.0167 \\ 0.0167 \\ -0.006 \end{pmatrix}
\end{aligned} \tag{8.7}$$

At this point the rotation ϕ is taken into account. These vectors are rotated around $\hat{\mathbf{c}}_3$ into a the coordinate system

$$\begin{aligned}
\hat{\mathbf{u}}_3 &= \hat{\mathbf{c}}_3 \\
\hat{\mathbf{u}}_2 &= \hat{\mathbf{c}}_1 \sin\phi + \hat{\mathbf{c}}_2 \cos\phi \\
\hat{\mathbf{u}}_1 &= \hat{\mathbf{c}}_1 \cos\phi - \hat{\mathbf{c}}_2 \sin\phi
\end{aligned} \tag{8.8}$$

Finally the polarisation vectors can be defined using this coordinate system. As the σ polarisation vector is normal to the scattering plane, it is dependent only on $\hat{\mathbf{u}}_2$, whereas the π polarisation vector is dependent on θ in addition to $\hat{\mathbf{u}}_3$ and $\hat{\mathbf{u}}_1$.

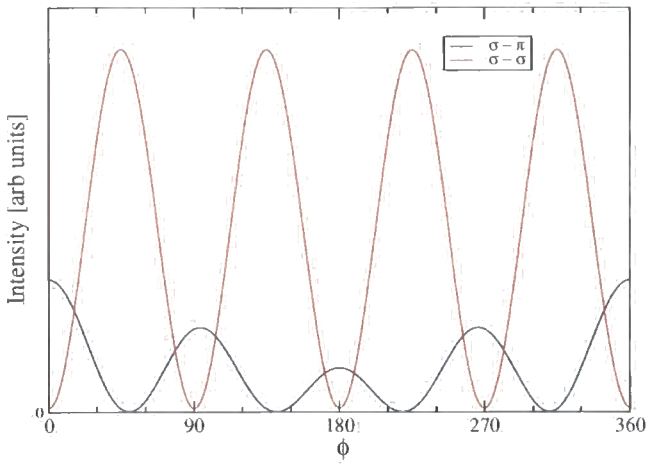

Figure 8.3: Simulation of the scattered intensity in the $\sigma \rightarrow \sigma$ and $\sigma \rightarrow \pi$ channels in $La_{0.8}Sr_{2.2}Mn_2O_7$ at (0.2,0.2,10) according the the model shown in Figure 8.2.

$$\begin{aligned} \hat{\epsilon}_\sigma &= \hat{\mathbf{u}}_2 \\ \hat{\epsilon}'_\sigma &= \hat{\mathbf{u}}_2 \\ \hat{\epsilon}_\pi &= \hat{\mathbf{u}}_1 \sin\theta - \hat{\mathbf{u}}_3 \cos\theta \\ \hat{\epsilon}'_\pi &= -\hat{\mathbf{u}}_1 \sin\theta - \hat{\mathbf{u}}_3 \cos\theta \end{aligned} \tag{8.9}$$

These polarisation vectors can now be fed back into equation 8.6, to give the expected amplitude in the $\sigma \rightarrow \pi$ and $\sigma \rightarrow \sigma$ channels, for each value of ϕ. The intensity in each channel is then found by multiplying the amplitude by its complex conjugate. The results for this crystal structure are calculated for each polarisation channel and shown in Figure 8.3. These can then be combined into the single Stokes parameter

$$P_1 \text{ (Stokes Parameter)} = \frac{I_{\sigma-\sigma} - I_{\sigma-\pi}}{I_{\sigma-\sigma} + I_{\sigma-\pi}} \tag{8.10}$$

yielding the results shown in Figure 8.4.

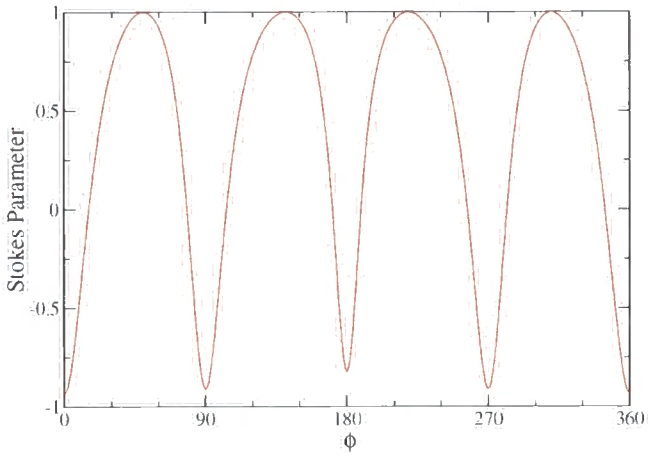

Figure 8.4: The Stokes parameter (equation 8.10) of the (0.2,0.2,10) signal in $La_{0.8}Sr_{2.2}Mn_2O_7$ as predicted by the model shown in Figure 8.2.

References

[1] J. Bednorz and K. A. Müller. *Possible High T_c Superconductivity in the Ba-La-Cu-O System.* Zeitschrift für Physik B, **vol. 64**; page 189, 1986.

[2] Y. Moritomo, A. Asamitsu, H. Kuwaha, and Y. Tokura. *Giant Magnetoresistance of Manganese Oxides with a Layered Perovskite Structure.* Nature, **vol. 380**; page 141, 1996.

[3] E. Wollan and W. Koehler. *Neutron Diffraction Study of the Magnetic Properties of the Series of Perovskite-Type Compounds $La_{(1-x)},Ca_xMnO_3$.* Physical Review, **vol. 100**; page 545, 1955.

[4] J. B. Goodenough. *Theory of the Role of Covalence in the Perovskite-Type Manganites $[La,M(II)]MnO_3$.* Physical Review, **vol. 100**; page 564, 1955.

[5] Y. Moritomo, Y. Tomioka, A. Asamitsu, Y. Tokura, and Y. Matsui. *Magnetic and Electronic Properties in Hole-Doped Manganese Oxides with Layered Structures: $La_{1-x}Sr_{1+x}MnO_4$.* Physical Review B (Condensed Matter), **vol. 51**; page 3297, 1995.

[6] C. N. R. Rao, P. Ganguly, K. K. Singh, and R. A. M. Ram. *A Comparative Study of the Magnetic and Electrical Properties of Perovskite Oxides and the Corresponding Two-Dimensional Oxides of K_2NiF_4 Structure.* Journal of Solid State Chemistry, **vol. 72**; page 12, 1988.

[7] B. J. Sternlieb, J. P. Hill, U. C. Wildgruber, G. M. Luke, B. Nachumi, Y. Moritomo, and Y. Tokura. *Charge and Magnetic Order in $La_{0.5}Sr_{1.5}MnO_4$.* Physical Review Letters, **vol. 76**; page 2169, 1996.

[8] Y. Moritomo, A. Nakamura, S. Mori, N. Yamamoto, K. Ohoyama, and M. Ohashi. *Lattice Effects on the Charge-Ordering Transition in $R_{0.5}Sr_{1.5}MnO_4$.* Physical Review B (Condensed Matter and Materials Physics), **vol. 56**; page 14879, 1997.

[9] Y. Murakami, H. Kawada, H. Kawata, M. Tanaka, T. Arima, Y. Moritomo, and Y. Tokura. *Direct Observation of Charge and Orbital Ordering in* $La_{0.5}Sr_{1.5}MnO_4$. Physical Review Letters, **vol. 80**; page 1932, 1998.

[10] T. Ishikawa, K. Ookura, and Y. Tokura. *Optical Response to Orbital and Charge Ordering in a Layered Manganite:* $La_{1/2}Sr_{3/2}MnO_4$. Physical Review B (Condensed Matter and Materials Physics), **vol. 59**; page 8367, 1999.

[11] M. Tokunaga, N. Miura, Y., and Y. Tokura. *High-Field Magnetization and Magnetoresistance of* $La_{0.5}Sr_{1.5}MnO_4$. Physical Review B (Condensed Matter and Materials Physics), **vol. 59**; page 11151, 1999.

[12] J. Park, S. Lee, J.-G. Park, I. P. Swainson, Y. Moritomo, and H.-C. Ri. *Spin-Glass State of* $(Nd,La)_{0.5}Sr_{1.5}MnO_4$. Physical Review B (Condensed Matter and Materials Physics), **vol. 62**; page 13848, 2000.

[13] J.-G. Park, M. Kim, H.-C. Ri, K. Kim, T. W. Noh, and S.-W. Cheong. *Magnetic Properties of* $Pr_{0.63}Sr_{0.37}MnO_3$ *and* $Nd_{0.7}Sr_{0.3}MnO_3$ *Single Crystals.* Physical Review B (Condensed Matter and Materials Physics), **vol. 60**; page 14804, 1999.

[14] C. Hong, E. O. Chi, W. S. Kim, N. H. Hur, K. W. Lee, and C. Lee. *Magnetic Properties and Structural Evolution in* $Nd_{0.5}Sr_{1.5}MnO_4$. Chemistry of Materials, **vol. 13**; page 945, 2001.

[15] P. Mahadevan, K. Terakura, and D. D. Sarma. *Spin, Charge, and Orbital Ordering in* $La_{0.5}Sr_{1.5}MnO_4$. Physical Review Letters, **vol. 87**; 066404, 2001.

[16] S. Ishihara and S. Maekawa. *Theory of Anomalous X-Ray Scattering in Orbital-Ordered Manganites.* Physical Review Letters, **vol. 80**(17); page 3799, 1998.

[17] S. Larochelle, A. Mehta, N. Kaneko, P. K. Mang, A. F. Panchula, L. Zhou, J. Arthur, and M. Greven. *Nature of* e_g *Electron Order in* $La_{1-x}Sr_{1+x}MnO_4$. Physical Review Letters, **vol. 87**(9); 095502, 2001.

[18] S. Larochelle, A. Mehta, L. Lu, P. K. Mang, O. P. Vajk, N. Kaneko, J. W. Lynn, L. Zhou, and M. Greven. *Structural and Magnetic Properties of the Single-Layer Manganese Oxide* $La_{1-x}Sr_{1+x}MnO_4$. Physical Review B (Condensed Matter and Materials Physics), **vol. 71**(2); 024435, 2005.

[19] P. G. Radaelli, D. E. Cox, L. Capogna, S.-W. Cheong, and M. Marezio. *Wigner-Crystal and Bi-Stripe Models for the Magnetic and Crystallographic Superstructures of* $La_{0.333}Ca_{0.667}MnO_3$. Physical Review B (Condensed Matter and Materials Physics), **vol. 59**(22); page 14440, 1999.

[20] J.-C. Bouloux, J.-L. Soubeyroux, G. L. Flem, and P. Hagenguller. *Bidimensional Magnetic Properties of b-Strontium Manganate(VI).* Journal of Solid State Chemistry, **vol. 38**; page 34, 1981.

[21] C. Baumann, G. Allodi, B. Büchner, R. D. Renzi, P. Reutler, and A. Revcolevschi. *Magnetism of* $La_{1-x}Sr_{1+x}MnO_4$ *as Revealed by* μSR. Physica B: Condensed Matter, **vol. 326**; page 505, 2003.

[22] T. Kimura, K. Hatsuda, Y. Ueno, R. Kajimoto, H. Mochizuki, H. Yoshizawa, T. Nagai, Y. Matsui, A. Yamazaki, and Y. Tokura. *Charge-Orbital Ordering and Ferromagnetic Chains in Single-Layered Manganite Crystals.* Physical Review B (Condensed Matter and Materials Physics), **vol. 65**(2); 020407, 2002.

[23] T. Nagai, T. Kimura, A. Yamazaki, T. Asaka, K. Kimoto, Y. Tokura, and Y. Matsui. *Transversely Modulated Crystal Structure of Charge-Orbital Ordered Manganites* $Nd_{1-x}Sr_{1+x}MnO_4$ $(x = 2/3, 3/4)$. Physical Review B (Condensed Matter and Materials Physics), **vol. 65**(6); 060405, 2002.

[24] P. Battle, D. E. Cox, M. A. Green, J. E. Millburn, L. E. Sping, P. G. Radaelli, M. J. Rosseinsky, and J. F. Vente. *Antiferromagnetism, Ferromagnetism and Phase Separation in the GMR System* $Sr_{2-x}La_{1+x}Mn_2O_7$. Chemistry of Materials, **vol. 9**; page 1042, 1997.

[25] J. Q. Li, Y. Matsui, T. Kimura, and Y. Tokura. *Structural Properties and Charge-Ordering Transition in* $LaSr_2Mn_2O_7$. Physical Review B (Condensed Matter and Materials Physics), **vol. 57**; page R3205, 1998.

[26] T. Kimura, R. Kumai, Y. Tokura, J. Q. Li, and Y. Matsui. *Successive Structural Transitions Coupled with Magnetotransport Properties in* $LaSr_2Mn_2O_7$. Physical Review B (Condensed Matter and Materials Physics), **vol. 58**; page 11081, 1998.

[27] R. Maezono and N. Nagaosa. *Spin and Orbital Ordering in Double-Layered Manganites.* Physical Review B (Condensed Matter and Materials Physics), **vol. 61**; page 1825, 2000.

[28] T. Chatterji, G. McIntyre, W. Caliebe, R. Suryanarayanan, G. Dhalenne, and A. Revcolevschi. *Reentrant Behavior of the Charge and Orbital Ordering and Antiferromagnetism in* $LaSr_2Mn_2O_7$. Physical Review B (Condensed Matter and Materials Physics), **vol. 61**; page 570, 2000.

[29] D. Andreica, F. Gygax, M. Pinkpank, A. Schenck, T. Chatterji, R. Suryanarayanan, G. Dhalenne, and A. Revcolevschi. *Charge/Orbital and Antiferromagnetic Ordering in* $LaSr_2Mn_2O_7$. Physica B, **vol. 289-290**; page 65, 2000.

[30] D. N. Argyriou, H. N. Bordallo, B. J. Campbell, A. K. Cheetham, D. E. Cox, J. S. Gardner, K. Hanif, A. dos Santos, and G. F. Strouse. *Charge Ordering and Phase Competition in the Layered Perovskite* $LaSr_2Mn_2O_7$. Physical Review B (Condensed Matter and Materials Physics), **vol. 61**(22); page 15269, 2000.

[31] C. D. Ling, J. E. Millburn, J. F. Mitchell, D. N. Argyriou, J. Linton, and H. N. Bordallo. *Interplay of Spin and Orbital Ordering in the Layered Colossal Magnetoresistance Manganite* $La_{2-2x}Sr_{1+2x}Mn_2O_7$ $(0.5 \leq x \leq 1.0)$. Physical Review B (Condensed Matter and Materials Physics), **vol. 62**(22); page 15096, 2000.

[32] X. Qui, S. Billinge, C. Kmety, and J. Mitchell. *Evidence for Nano-Scale Inhomogeneities in Bilayer Manganites in the* Mn^{4+} *Rich Region:* $0.54 \leq x \leq 0.80$. Journal of Physics and Chemistry of Solids, **vol. 65**; page 1423, 2004.

[33] J. Dho, W. S. Kim, H. S. Choi, E. O. Chi, and N. H. Hur. *Re-Entrant Charge-Ordering Behavoir in the Layered Manganites* $La_{2-2x}Sr_{1+2x}Mn_2O_7$. J. Phys.: Condens. Matter, **vol. 13**; page 3655, 2001.

[34] A. I. Coldea, S. J. Blundell, C. A. Steer, J. F. Mitchell, and F. L. Pratt. *Spin Freezing and Magnetic Inhomogeneities in Bilayer Manganites.* Physical Review Letters, **vol. 89**(27); 277601, 2002.

[35] S. B. Wilkins, P. D. Spencer, T. A. W. Beale, P. D. Hatton, M. v. Zimmermann, S. D. Brown, D. Prabhakaran, and A. T. Boothroyd. *Charge Ordering and Structural*

Distortions at Low Temperature in $La_{2-2x}Sr_{1+2x}Mn_2O_7$ ($x = 0.475$ *and* 0.5). Physical Review B (Condensed Matter and Materials Physics), **vol. 67**(20); 205110, 2003.

[36] S. B. Wilkins, P. D. Hatton, M. D. Roper, D. Prabhakaran, and A. T. Boothroyd. *Soft X-Ray Resonant Magnetic Diffraction.* Physical Review Letters, **vol. 90**; 187201, 2003.

[37] S. D. Matteo, T. Chatterji, Y. Joly, A. Stunault, J. A. Paixao, R. Suryanarayanan, G. Dhalenne, and A. Revcolevschi. *Resonant X-ray Scattering from* $LaSr_2Mn_2O_7$ *at the Mn K Edge.* Physical Review B (Condensed Matter and Materials Physics), **vol. 68**(2); 024414, 2003.

[38] J. F. Mitchell, D. N. Argyriou, J. D. Jorgensen, D. G. Hinks, C. D. Potter, and S. D. Bader. *Charge Delocalization and Structural Response in Layered* $La_{1.2}Sr_{1.8}Mn_2O_7$*: Enhanced Distortion in the Metallic Regime.* Physical Review B (Condensed Matter and Materials Physics), **vol. 55**; page 63, 1997.

[39] D. N. Argyriou, J. F. Mitchell, J. B. Goodenough, O. Chmaissem, S. Short, and J. D. Jorgensen. *Sign Reversal of the Mn-O Bond Compressibility in* $La_{1.2}Sr_{1.8}Mn_2O_7$ *below* T_C*: Exchange Striction in the Ferromagnetic State.* Physical Review Letters, **vol. 78**; page 1568, 1997.

[40] D. N. Argyriou, J. F. Mitchell, C. D. Potter, S. D. Bader, R. Kleb, and J. D. Jorgensen. *Unconventional Magnetostriction in Layered* $La_{1.2}Sr_{1.8}Mn_2O_7$*: Evidence for Spin-Lattice Coupling Above* T_C. Physical Review B (Condensed Matter and Materials Physics), **vol. 55**; page R11965, 1997.

[41] C. D. Potter, M. Swiatek, S. D. Bader, D. N. Argyriou, J. F. Mitchell, D. J. Miller, D. G. Hinks, and J. D. Jorgensen. *Two-Dimensional Intrinsic and Extrinsic Ferromagnetic Behavior of Layered* $La_{1.2}Sr_{1.8}Mn_2O_7$ *Single Crystals.* Physical Review B (Condensed Matter and Materials Physics), **vol. 57**; page 72, 1998.

[42] T. Kelley, D. Argyriou, R. Robinson, H. Nakotte, J. Mitchel, R. Osborn, and J. Jorgensen. *Short-Range Spin Correlations in the CMR Material* $La_{1.4}Sr_{1.6}Mn_2O_7$. Physica B, **vol. 241-243**; page 429, 1998.

[43] R. Osborn, S. Rosenkranz, D. N. Argyriou, L. Vasiliu-Doloc, J. W. Lynn, S. K. Sinha, J. F. Mitchell, K. E. Gray, and S. D. Bader. *Neutron Scattering Investigation of*

Magnetic Bilayer Correlations in $La_{1.2}Sr_{1.8}Mn_2O_7$: Evidence of Canting above T_C. Physical Review Letters, **vol. 81**; page 3964, 1998.

[44] M. Medarde, J. F. Mitchell, J. E. Millburn, S. Short, and J. D. Jorgensen. *Optimal T_C in Layered Manganites: Different Roles of Coherent and Incoherent Lattice Distortions.* Physical Review Letters, **vol. 83**; page 1223, 1999.

[45] J. E. Gordon, S. D. Bader, J. F. Mitchell, R. Osborn, , and S. Rosenkranz. *Specific Heat of $La_{1.2}Sr_{1.8}Mn_2O_7$.* Physical Review B (Condensed Matter and Materials Physics), **vol. 60**; page 6258, 1999.

[46] L. Vasiliu-Doloc, S. Rosenkranz, R. Osborn, S. K. Sinha, J. W. Lynn, J. Mesot, O. H. Seeck, G. Preosti, A. J. Fedro, and J. F. Mitchell. *Charge Melting and Polaron Collapse in $La_{1.2}Sr_{1.8}Mn_2O_7$.* Physical Review Letters, **vol. 83**; page 4393, 1999.

[47] T. Perring, G. Aeppli, Y. Moritomo, and Y. Tokura. *Antiferromagnetic Short Range Order in a Two-Dimensional Manganite Exhibiting Giant Magnetoresistance.* Physical Review Letters, **vol. 78**; page 3197, 1997.

[48] K. Yamamoto, T. Kimura, T. Ishikawa, T. Katsufuji, and Y. Tokura. *Probing Charge/Orbital Correlation in $La_{1.2}Sr_{1.8}Mn_2O_7$.* Journal of the Physical Society of Japan, **vol. 68**; page 2538, 1999.

[49] T. Kimura, Y. Tomioka, H. Kuwahara, A. Asamitsu, M. Tamura, and Y. Tokura. *Interplane Tunneling and Magnetoresistance in a Layered Manganite Crystal.* Science, **vol. 274**; page 1698, 1996.

[50] T. Perring, G. Aeppli, T. Kimura, Y. Tokura, and M. Adams. *Ordered Stack of Spin Valves in a Layered Magnetoresistive Perovskite.* Physical Review B (Condensed Matter and Materials Physics), **vol. 58**; page R14693, 1998.

[51] M. Kubota, H. Fujioka, K. Hirota, K. Ohoyama, Y. Moritomo, H. Yoshizawa, and Y. Endoh. *Relation Between Crystal and Magnetic Structures of Layered Manganite $La_{2-2x}Sr_{1+2x}Mn_2O_7$ ($0.3 \leq x \leq 0.50$).* Journal of the Physical Society of Japan, **vol. 69**; page 1606, 2000.

[52] M. Kubota, Y. Oohara, H. Yoshizawa, H. Fujioka, K. Hirota, Y. Moritomo, and Y. Endoh. *Highly Degenerate Canted Spin Structure in Bilayer Manganite $La_{1.1}Sr_{1.9}Mn_2O_7$.* Physical Review Letters, **vol. 91**; page 047201, 2003.

[53] J. Mitchell, C. Ling, J. Millburn, D. Argyriou, A. Berger, M. Medarde, D. Miller, and Z. Luo. *Heavily Doped Bilayer Manganites: Links Among Structure, Charge, and Spin.* Applied Physics A, **vol. 74**; page S1776, 2002.

[54] T. Maitra and A. Taraphder. *Magnetic and Orbital Order in Overdoped Bilayer Manganites.* Europhysics Letters, **vol. 65**; page 262, 2004.

[55] B. J. Campbell, D. N. Argyriou, J. F. Mitchell, R. Osborn, B. Ouladdiaf, and C. D. Ling. *Enhanced Stability of Charge and Orbital Order in* $La_{0.78}Sr_{2.22}Mn_2O_7$. Physical Review B (Condensed Matter and Materials Physics), **vol. 69**(10); 104403, 2004.

[56] Z. P. Luo, D. J. Miller, and J. F. Mitchell. *Electron Microscopic Evidence of Charge-Ordered Bi-Stripe Structures in the Bilayered Colossal Magnetoresistive Manganite* $La_{2-2x}Sr_{1+2x}Mn_2O_7$. Physical Review B (Condensed Matter and Materials Physics), **vol. 71**(1); 014418, 2005.

[57] T. A. W. Beale, P. D. Spencer, P. D. Hatton, S. B. Wilkins, M. v. Zimmermann, S. Brown, D. Prabhakaran, and A. T. Boothroyd. *Orbital Bi-Stripes in the Highly Doped Bilayer Manganites.* Physical Review B (Condensed Matter and Materials Physics), **vol. 72**; page 064432, 2005.

[58] Y. Tokura and N. Nagaosa. *Orbital Physics in Transition-Metal Oxides.* Science, **vol. 288**; page 462, 2000.

[59] J. B. Goodenough. *Magnetism and the Chemical Bond.* Interscience Publishers, 1963.

[60] M. Blume. *Magnetic Scattering of X-rays (invited).* Journal of Applied Physics, **vol. 57**; page 3615, 1985.

[61] M. Blume and D. Gibbs. *Polarization Dependence of Magnetic X-ray Scattering.* Physical Review B (Condensed Matter), **vol. 37**; page 1779, 1988.

[62] J. Hannon, G. Trammel, M. Blume, and D. Gibbs. *X-Ray Resonance Exchange Scattering.* Physical Review Letters, **vol. 61**; page 1245, 1988.

[63] J. P. Hill and D. F. McMorrow. *X-ray Resonant Exchange Scattering: Polarization Dependence and Correlation Functions.* Acta Crystallographica Sect. A, **vol. 52**; page 236, 1996.

[64] S. B. Wilkins, P. D. Spencer, P. D. Hatton, B. K. Tanner, T. A. Lafford, J. Spence, and N. Loxley. *Novel Diffractometer Optimized for the Study of Weak Superlattice Reflections Using Crossed Parabolic Mirrors.* Review of Scientific Instruments, **vol. 73**(7); page 2666, 2002.

[65] J. Strempfer, T. Brückel, U. Rütt, J. R. Schneider, K. D. Liss, and T. Tschentscher. *The Non-Resonant Magnetic X-ray Scattering Cross Section of MnF_2.2. High-Energy X-ray Diffraction at 80keV.* Acta Crystallographica A, **vol. A52**; page 438, 1996.

[66] R. Bouchard, D. Hupfeld, T. Lippmann, J. Neuefeind, H.-B. Neumann, H. F. Poulsen, U. Rütt, T. Schmidt, J. R. Scneider, J. Süssenbach, and M. von Zimmermann. *A Triple-Crystal Diffractometer for High-Energy Synchrotron Radiation at the HASYLAB High-Field Wiggler Beamline BW5.* Journal of Synchrotron Radiation, **vol. 5**; page 90, 1998.

[67] P. Suortti and T. Tschentscher. *High Energy Scattering Beamlines at European Synchrotron Radiation Facility.* Review of Scientific Instruments, **vol. 66**; page 1798, 1995.

[68] W. Neubeck, C. Vettier, K. B. Lee, and F. de Bergevin. *K-edge Resonant X-ray Magnetic Scattering from CoO.* Physical Review B (Condensed Matter and Materials Physics), **vol. 60**; page R9912, 1999.

[69] W. Neubeck, C. Vettier, F. de Bergevin, F. Yakhou, D. Mannix, O. Bengone, M. Alouani, and A. Barbier. *Probing the 4p Electron-Spin Polarization in NiO.* Physical Review B (Condensed Matter and Materials Physics), **vol. 63**; page 134430, 2001.

[70] R. Caciuffo, L. Paolasini, A. Sollier, P. Ghigna, E. Pavarini, J. van den Brink, and M. Altarelli. *Resonant X-ray Scattering Study of Magnetic and Orbital Order in $KCuF_3$.* Physical Review B (Condensed Matter and Materials Physics), **vol. 65**(17); 174425, 2002.

[71] L. Paolasini, C. Vettier, F. de Bergevin, F. Yakhou, D. Mannix, A. Stunault, W. Neubeck, M. Altarelli, M. Fabrizio, P. A. Metcalf, and J. M. Honig. *Orbital Occupancy Order in V_2O_3: Resonant X-Ray Scattering Results.* Physical Review Letters, **vol. 82**(23); page 4719, 1999.

[72] H. Nakao, T. Satoh, J. Satoh, Y. Murakami, M. Kubota, Y. Wakabayashi, H. Sawa, T. Kimura, and Y. Tokura. *Charge and Orbital Ordered States in* $Nd_{1-x}Sr_{1+x}MnO_4$ $(x = 0.67, 0.75)$. Physica B, **vol. 329**; page 809, 2003.

[73] A. Daoud-Aladine, J. Rodriguez-Carvajal, L. Pinsard-Gaudart, M. T. Fernandez-Diaz, and A. Revcolevschi. *Zener Polaron Ordering in Half-Doped Manganites.* Physical Review Letters, **vol. 89**; 097205, 2002.

[74] D. Prabhakaran and A. T. Boothroyd. *Single-Crystal Growth of* $La_{2-2x}Sr_{1+2x}Mn_2O_7$ *Under Pressure.* Journal of Material Science: Materials in Electronics, **vol. 14**; page 587, 2003.

[75] S. Brown, A. M. Beesley, A. Herring, D. Mannix, M. F. Thomas, P. Thompson, L. Bouchenoir, S. Langridge, G. H. Lander, W. G. Stirling, A. Mirone, R. Ward, M. Wells, and S. Zochowski. *The XMaS Beamline at ESRF: Instrument Developments and High Resolution Diffraction Studies.* Journal of Synchrotron Radiation, **vol. 8**; page 1172, 2001.

[76] P. Carra and B. T. Thole. *Anisotropic X-ray Anomalous Diffraction and Forbidden Reflections.* Review of Modern Physics, **vol. 66**; page 1509, 1994.

[77] F. Bridges, C. H. Booth, G. H. Kwei, J. J. Neumeier, and G. A. Sawatzky. *Temperature Dependent Changes of the Mn 3d and 4p Bands Near* T_c *in Colossal Magnetoresistance Systems: XANES Study of* $La_{1-x}Ca_xMnO_3$. Physical Review B (Condensed Matter and Materials Physics), **vol. 61**(14); page R9237, 2000.

[78] S. Mori, C. Chen, and S.-W. Cheong. *Pairing of Charge-Ordered Stripes in* $(La,Ca)MnO_3$. Nature, **vol. 392**; page 473, 1998.

[79] D. I. Khomskii and K. I. Kugel. *Elastic Interactions and Superstructures in Manganites and Other Jahn-Teller Systems.* Physical Review B (Condensed Matter and Materials Physics), **vol. 67**(13); 134401, 2003.

[80] T. Hotta, A. Feiguin, and E. Dagotto. *Stripes Induced by Orbital Ordering in Layered Manganites.* Physical Review Letters, **vol. 86**(21); page 4922, 2001.

[81] L. Brey. *Continuous Charge Modulated Diagonal Phase in Manganites.* Physical Review Letters, **vol. 92**(12); 127202, 2004.

[82] J. Q. Li, C. Dong, L. H. Liu, and Y. M. Ni. *Reentrant Charge-Ordering Transition and Phase Separation in the Layered Perovskite* $La_{2-2x}Sr_{1+2x}Mn_2O_7$. Physical Review B (Condensed Matter and Materials Physics), **vol. 64**(17); 174413, 2001.

[83] T. Hayashi, N. Miura, M. Tokunaga, T. Kimura, and Y. Tokura. *Magnetic Properties and CMR Effect in Layer Type Manganite* $LaSr_2Mn_2O_7$ *Under High Magnetic Fields.* Journal of Physics: Condensed Matter, **vol. 10**; page 11525, 1998.

[84] X. J. Chen, C. L. Zhang, J. S. Gardner, J. L. Sarrao, and C. C. Almasan. *Variable-Range-Hopping Conductivity of the Half-Doped Bilayer Manganite* $LaSr_2Mn_2O_7$. Physical Review B (Condensed Matter and Materials Physics), **vol. 68**(6); 064405, 2003.

[85] B. García-Landa, C. Marquina, M. Hilbers, M. Ibarra, P. Algarabel, A. del Moral, G. Balakrishnan, M. Lees, and D. M. Paul. *High Magnetic-Field Study of the Magnetization of Layered Manganite* $Nd_{2-2x}Sr_{1+2x}Mn_2O_7$ *single crystals.* Physica B, **vol. 294-295**; page 107, 2001.

[86] Y. Tomioka, A. Asamitsu, H. Kuwahara, Y. Moritomo, and Y. Tokura. *Magnetic-Field-Induced Metal-Insulator Phenomena in* $Pr_{1-x}Ca_xMnO_3$ *with Controlled Charge-Ordering Instability.* Physical Review B (Condensed Matter), **vol. 53**(4); page R1689, 1996.

[87] P. Spencer, S. Wilkins, P. Hatton, S. Brown, T. Hase, J. Purton, and D. Fort. *Soft X-ray Diffraction Study of Magnetic Ordering in Holmium.* Journal of Physics: Condensed Matter, **vol. 17**; page 1725, 2005.

[88] C. Kao, J. Hastings, E. Johnson, D. Siddons, G. Smith, and G. Prinz. *Magnetic-Resonance Exchange Scattering at the Iron* L_{II} *and* L_{III} *Edges.* Physical Review Letters, **vol. 65**; page 373, 1990.

[89] C.-C. Kao, C. Chen, E. Johnson, J. Hasting, H. Lin, G. Ho, G. Meigs, J.-M. Brot, S. Hulbert, Y. Idzerda, and C. Vettier. *Dichroic Interference Effects in Circularly Polarized Soft X-ray Resonant Magnetic Scattering.* Physical Review B (Condensed Matter and Materials Physics), **vol. 50**; page 9599, 1994.

[90] J. M. Tonnerre, L. Sève, D. Raoux, G. S. amd B. Rodmacq, and P. Wolfers. *Soft X-Ray Resonant Magnetic Scattering from a Magnetically Coupled Ag /Ni Multilayer.* Physical Review Letters, **vol. 75**; page 740, 1995.

[91] L. Sève, J. M. Tonnerre, D. Raoux, J. F. Bobo, M. Piecuch, M. D. Santis, P. Troussel, J. M. Brot, V. Chakarian, C. C. Kao, and C. T. Chen. *Resonant Magnetic Scattering in Soft X-ray Range Using Multilayers.* Journal of Magnetism and Magnetic Materials, **vol. 148**; page 68, 1995.

[92] J. M. Tonnerre, L. Seve, A. Barbara-Dechelette, F. Bartolome, D. Raoux, V. Chakarian, C. C. Kao, H. Fischer, S. Andrieu, and O. Fruchart. *Soft X-ray Resonant Magnetic Reflectivity Study of Thin Films and Multilayers.* Journal of Applied Physics, **vol. 83**; page 6293, 1998.

[93] M. Sacchi, C. Hague, E. Gullikson, and J. Underwood. *Resonant Magnetic Scattering of Polarized Soft X-rays: Specular Reflectivity and Bragg Diffraction from Multilayers.* Physical Review B (Condensed Matter and Materials Physics), **vol. 57**; page 108, 1998.

[94] H. Hashizume, N. Ishimatsu, O. Sakata, T. Iizuka, N. Hosoito, K. Namikawa, T. Iwazumi, G. Srajer, C. T. Venkataraman, J. C. Lang, C. Nelson, and L. Berman. *Resonant X-ray Magnetic Scattering from the Twisted States of an Fe/Gd Multilayer.* Physica B: Condensed Matter, **vol. 248**; page 133, 1998.

[95] T. P. A. Hase, I. Pape, B. K. Tanner, H. Dürr, E. Dudzik, G. van der Laan, C. H. Marrows, and B. J. Hickey. *Soft X-ray Resonant Magnetic Diffuse Scattering from Strongly Coupled Cu/Co Multilayers.* Physical Review B (Condensed Matter and Materials Physics), **vol. 61**; page R372, 2000.

[96] T. Hase, I. Pape, D. Read, B. Tanner, H. Dürr, E. Dudzik, G. van der Laan, C. Marrows, and B. Hickey. *Soft X-ray Magnetic Scattering Evidence for Biquadratic Coupling in Co/Cu Multilayers.* Physical Review B (Condensed Matter and Materials Physics), **vol. 61**; page 15331, 2000.

[97] C. W. M. Castleton and M. Altarelli. *Orbital Ordering in the Manganites: Resonant X-ray Scattering Predictions at the Manganese L_{II} and L_{III} edge.* Physical Review B (Condensed Matter and Materials Physics), **vol. 62**; page 1033, 2000.

[98] R. Cowan. *Theoretical Calculation of Atomic Spectra Using Digital Computers.* Journal of the Optical Society of America, **vol. 58**; page 808, 1968.

[99] G. Racah. *Theory of Complex Spectra. IV.* Physical Review, **vol. 76**; page 1352, 1949.

[100] S. B. Wilkins, P. D. Spencer, P. D. Hatton, S. P. Collins, M. D. Roper, D. Prabhakaran, and A. T. Boothroyd. *Direct Observation of Orbital Ordering in $La_{0.5}Sr_{1.5}MnO_4$ Using Soft X-ray Diffraction.* Physical Review Letters, **vol. 91**; 167205, 2003.

[101] S. S. Dhesi, A. Mirone, C. D. Nadai, P. Ohresser, P. Bencok, N. B. Brookes, P. Reutler, A. Revcolevschi, A. Tagliaferri, O. Toulemonde, and G. van der Laan. *Unraveling Orbital Ordering in $La_{0.5}Sr_{1.5}MnO_4$.* Physical Review Letters, **vol. 92**; 056403, 2004.

[102] S. B. Wilkins, N. Stojić, T. A. W. Beale, N. Binggeli, C. W. M. Castleton, P. Bencok, D. Prabhakaran, A. T. Boothroyd, P. D. Hatton, and M. Altarelli. *Resonant Soft X-ray Scattering Investigation of Orbital and Magnetic Ordering in $La_{0.5}Sr_{1.5}MnO_4$.* Physical Review B (Condensed Matter and Materials Physics), **vol. 71**(24); 245102, 2005.

[103] U. Staub, V. Scagnoli, A. M. Mulders, K. Katsumata, Z. Honda, H. Grimmer, M. Horisberger, and J. M. Tonnerre. *Orbital and Magnetic Ordering in $La_{0.5}Sr_{1.5}MnO_4$ Studied by Soft X-ray Resonant Scattering.* Physical Review B (Condensed Matter and Materials Physics), **vol. 71**(21); 214421, 2005.

[104] S. Wilkins, T. Beale, P. Hatton, J. Purton, P. Bencok, D. Prabhakaran, and A. Boothroyd. *Probing Orbital Order with Soft X-rays: The Case of the Manganites.* New Journal of Physics, **vol. 7**; page 80, 2005.

[105] P. Hatton, S. Wilkins, T. Beale, T. Johal, D. Prabhakaran, and A. Boothroyd. *Resonant Soft X-ray Scattering - A New Probe of Charge, Spin, and Orbital Ordering in the Manganites.* Journal of Magnetism and Magnetic Materials, **vol. 290**; page 891, 2005.

[106] P. D. Hatton, S. B. Wilkins, T. A. W. Beale, J. A. Purton, D. Prabhakaran, and A. T. Boothroyd. *Soft X-ray Diffraction - In Extremis.* Journal of Synchrotron Radiation, **vol. 12**; page 434, 2005.

[107] N. Binggeli and M. Altarelli. *Strain Effects and Anomalous X-ray Scattering in Tetragonal Manganites.* New Journal of Physics, **vol. 6**; page 165, 2004.

[108] K. J. Thomas, J. P. Hill, S. Grenier, Y.-J. Kim, P. Abbamonte, L. Venema, A. Rusydi, Y. Tomioka, Y. Tokura, D. F. McMorrow, G. Sawatzky, and M. van Veenendaal.

Soft X-Ray Resonant Diffraction Study of Magnetic and Orbital Correlations in a Manganite Near Half Doping. Physical Review Letters, **vol. 92**(23); 237204, 2004.

[109] S. B. Wilkins, N. Stojic, T. A. W. Beale, N. Binggeli, P. Bencok, S. Stanescu, J. F. Mitchell, P. Abbamonte, P. D. Hatton, and M. Altarelli. *Evidence of Orbital Ordering in Jahn-Teller Undistorted* $LaSr_2Mn_2O_7$. Condensed Matter e-Print archive, page 0412445, 2005.

[110] P. Abbamonte, L. Venema, A. Rusydi, G. A. Sawatzky, G. Logvenov, and I. Bozovic. *A Structural Probe of the Doped Holes in Cuprate Superconductors.* Science, **vol. 297**; page 578, 2002.

[111] P. Abbamonte, G. Blumberg, A. Rusydi, A. Gozar, P. Evans, T. Siegrist, L. Venema, H. Eisaki, E. Isaacs, and G. Sawatzky. *Crystallization of Charge Holes in the Spin Ladder of* $Sr_{14}Cu_{24}O_{41}$. Nature, **vol. 431**; page 1078, 2004.

[112] A. Rusydi, P. Abbamonte, H. Eisaki, Y. Fujimaki, G. Blumberg, S. Uchida, and G. Sawatzky. *Quantum Melting of the Hole Crystal in the Spin Ladder of* $Sr_{14-x}Ca_xCu_{24}O_{41}$. Condensed Matter e-Print archive, page 0511524, 2005.

[113] C. Schüßler-Langeheine, J. Schlappa, A. Tanaka, Z. Hu, C. F. Chang, E. Schierle, M. Benomar, H. Ott, E. Weschke, G. Kaindl, O. Friedt, G. A. Sawatzky, H.-J. Lin, C. T. Chen, M. Braden, and L. H. Tjeng. *Spectroscopy of Stripe Order in* $La_{1.8}Sr_{0.2}NiO_4$ *Using Resonant Soft X-ray Diffraction.* Physical Review Letters, **vol. 95**; page 156402, 2005.

[114] M. E. Ghazi, P. D. Spencer, S. B. Wilkins, P. D. Hatton, D. Mannix, D. Prabhakaran, A. T. Boothroyd, and S.-W. Cheong. *Incommensurate Charge Stripe Ordering in* $La_{1-x}Sr_xNiO_4$ *for* $x = (0.33, 0.30, 0.275)$. Physical Review B (Condensed Matter and Materials Physics), **vol. 70**(14); 144507, 2004.

[115] C.-H. Du, M. E. Ghazi, Y. Su, I. Pape, , P. D. Hatton, S. D. Brown, W. G. Stirling, and M. J. Cooper. *Critical Fluctuations and Quenched Disordered Two-Dimensional Charge Stripes in* $La_{5/3}Sr_{1/3}NiO_4$. Physical Review Letters, **vol. 84**; page 3911, 2000.

[116] P. G. Freeman, A. T. Boothroyd, D. Prabhakaran, C. D. Frost, M. Enderle, and A. Hiess. *Spin Dynamics of Half-Doped* $La_{3/2}Sr_{1/2}NiO_4$. Physical Review B (Condensed Matter and Materials Physics), **vol. 71**(17); 174412, 2005.

[117] P. G. Freeman, A. T. Boothroyd, D. Prabhakaran, D. Gonzalez, and M. Enderle. *Spin Reorientation Transition in the Incommensurate Stripe-Ordered Phase of* $La_{3/2}Sr_{1/2}NiO_4$. Physical Review B (Condensed Matter and Materials Physics), **vol. 66**(21); 212405, 2002.

[118] A. T. Boothroyd, P. G. Freeman, D. Prabhakaran, A. Hiess, M. Enderle, J. Kulda, and F. Altorfer. *Spin Correlations among the Charge Carriers in an Ordered Stripe Phase.* Physical Review Letters, **vol. 91**(25); 257201, 2003.

[119] T. Hotta and E. Dagotto. *Orbital Ordering, New Phases, and Stripe Formation in Doped Layered Nickelates.* Physical Review Letters, **vol. 92**(22); 227201, 2004.

[120] D. J. Huang, W. B. Wu, G. Y. Guo, H.-J. Lin, T. Y. Hou, C. F. Chang, C. T. Chen, A. Fujimori, T. Kimura, H. B. Huang, A. Tanaka, and T. Jo. *Orbital Ordering in* $La_{0.5}Sr_{1.5}MnO_4$ *Studied by Soft X-Ray Linear Dichroism.* Physical Review Letters, **vol. 92**(8); 087202, 2004.

[121] A. I. Liechtenstein and I. Mazin. *Quantitative Model for the Superconductivity Suppression in* $R_{1-x}Pr_xBa_2Cu_3O_7$ *with Different Rare Earths.* Physical Review Letters, **vol. 74**; page 1000, 1995.

[122] A. I. Liechtenstein, V. Ansimov, and J. Zaanen. *Density-Functional Theory and Strong Interactions: Orbital Ordering in Mott-Hubbard Insulators.* Physical Review B (Condensed Matter and Materials Physics), **vol. 52**; page R5467, 1995.

[123] N. Stojić, N. Binggeli, and M. Altarelli. *Mn* $L_{2,3}$ *Edge Resonant Scattering in Manganites: Influence of the Magnetic State.* Physical Review B (Condensed Matter and Materials Physics), **vol. 72**; page 104108, 2005.

[124] L. Paolasini, R. Caciuffo, A. Sollier, P. Ghigna, and M. Altarelli. *Coupling between Spin and Orbital Degrees of Freedom in* $KCuF_3$. Physical Review Letters, **vol. 88**; 106403, 2002.

[125] N. Binggeli and M. Altarelli. *Orbital Ordering, Jahn-Teller Distortion, and Resonant X-ray Scattering in* $KCuF_3$. Physical Review B (Condensed Matter and Materials Physics), **vol. 70**(8); 085117, 2004.

[126] Y. Murakami, J. P. Hill, D. Gibbs, M. Blume, I. Koyama, M. Tanaka, H. Kawata, T. Arima, Y. Tokura, K. Hirota, and Y. Endoh. *Resonant X-Ray Scattering from Orbital Ordering in $LaMnO_3$.* Physical Review Letters, **vol. 81**; page 582, 1998.

[127] S. Ishihara and S. Maekawa. *Theory of Orbital Ordering, Fluctuation, and Resonant X-ray Scattering in Manganites.* Physical Review B (Condensed Matter and Materials Physics), **vol. 62**; page R9252, 2000.

[128] A. Koizumi, S. Miyaki, Y. Kakutani, H. Koizumi, N. Hiraoka, K. Makoshi, N. Sakai, K. Hirota, and Y. Murakami. *Study of the e_g Orbitals in the Bilayer Manganite $La_{2-2x}Sr_{1+2x}Mn_2O_7$ by Using Magnetic Compton-Profile Measurement.* Physical Review Letters, **vol. 86**; page 5589, 2001.

[129] H. L. Ju, H.-C. Sohn, and K. M. Krishnan. *Evidence for O_{2p} Hole-Driven Conductivity in $La_{1-x}Sr_xMnO_3$ $(0 \leq x \leq 0.7)$ and $La_{0.7}Sr_{0.3}MnO_z$ Thin Films.* Physical Review Letters, **vol. 79**; page 3230, 1997.

[130] G. Subías, J. García, M. Sánchez, J. Blasco, and M. Proietti. *Soft X-ray Absorption Spectroscopy (Mn $L_{2,3}$ and O K) in Mixed Valence Manganites.* Surface Review and Letters, **vol. 9**; page 1071, 2002.

[131] V. Ferrari, M. Towler, and P. B. Littlewood. *Oxygen Stripes in $La_{0.5}Ca_{0.5}MnO_3$ from Ab Initio Calculations.* Physical Review Letters, **vol. 91**(22); 227202, 2003.

[132] G. Zheng and C. H. Patterson. *Ferromagnetic Polarons in $La_{0.5}Ca_{0.5}MnO_3$ and $La_{0.33}Ca_{0.67}MnO_3$.* Physical Review B (Condensed Matter and Materials Physics), **vol. 67**(22); 220404, 2003.